Spatial distribution maps for benthic communities

A study of common mussels (*Mytilus edulis*), neptune grass (*Posidonia oceanica*), and *Cymodocea nodosa* based on hydroacoustic measurements

Per Settergren Sørensen

Lyngby 1999
Department of Mathematical Modelling
Technical University of Denmark

Ph.d. Thesis

Name	Per Settergren Sørensen, M.Sc.Eng. (CE87)
Ph.d number	96-0169-221
Ph.d programme	Mathematics
Institute	Department of Mathematical Modelling (IMM)
Start date	November 1st, 1996
End date	July 31st, 1999
Supervisor	Professor Knut Conradsen, IMM
Co-supervisor	Associate Professor Bjarne Kjær Ersbøll, IMM

Preface

This thesis has been prepared at the Section for Image Analysis, Department of Mathematical Modelling, Technical University of Denmark, in partial fulfillment of the requirements for acquiring the Ph.D. degree in engineering.

The general framework of this thesis is statistics, in particular geostatistics and statistical image analysis, and the application domain is hydroacoustic marine biology. Reading this thesis requires a basic knowledge of multivariate statistics.

The object of the thesis is the preparation of maps depicting spatial distribution of mussels and seagrasses on the sea floor based on hydroacoustic measurements. The report gives a treatment of some of the statistical challenges arising from the special data types and sampling designs presented by hydroacoustic measurements, in particular echo sounder measurements. The main result is that it is feasible to use hydroacoustic measurements to prepare spatial distribution maps at large scales with a relatively high resolution.

The application of a large and unique collection of hydroacoustic datasets has been a major part of the work, from the planning of observational designs to the data analysis leading to spatial distribution maps. Therefore, the elaboration of a well-founded alignment of methods of geostatistics, image analysis and multivariate statistics in an appropriate data processing scheme has been a main objective. The use of mathematics and statistics in this thesis can be conceived of as a tour around the image modelling marketplace, yet it is my hope that the presentation is coherent and adequate. Hopefully, the results can inspire further developments of data processing methodology for hydroacoustic measurements in regard to sea floor mapping.

Lyngby, November 5th, 1999

Per Settergren Sørensen

Acknowledgements

I am indebted to my supervisor Professor Knut Conradsen, Head of the Section for Image Analysis, for encouraging and guiding many steps throughout this work and for letting me depend on his knowledge of mathematics and statistics. I thank my co-supervisor Associate Professor Bjarne Kjær Ersbøll and Associate Research Professor Allan Aasbjerg Nielsen for their prompt help and many valuable suggestions; during the last 3 years of close collaboration Allan contributed a frank and direct atmosphere that has been stimulating and fruitful. Furthermore, I acknowledge the prompt services by Secretary Helle Welling and the advice on MCMC from Assoc. Professor Jens Michael Carstensen, and the contributions from Ass. Research Professor Nette Schultz and Assoc. Research Professor Anette Ersbøll, all from IMM.

At VKI, my work place, I would like to acknowledge the enthusiasm and energy provided by my marine biologist colleague and close collaborator M.Sc. Kristian Madsen. Words of gratitude go to the head of my department, Arne Hurup Nielsen, and to the director of our division, Kurt Jensen, for their professional and financial support, and to my colleagues for help with the manuscript and with debugging of my Delphi 3 code. I thank M.Sc. Kasper Hornbæk for many valuable comments made during the finalisation of the manuscript. Special thoughts of appreciation go to my former colleague Professor Jes la Cour Jansen, Department of Building and Environmental Technology, Lund University, Sweden, for showing me the entrance to the scientific world many years ago and helping me through the gates.

I acknowledge the geometric approach to statistical image analysis taught me by Assistant Research Professor Mads Nielsen, 3D-Lab, School of Dentistry, University of Copenhagen, during the course in the spring 1998, as well as the energetic work conducted by my fellow student cand.silv. Mads Jeppe Tarp-Johansen from DINA, KVL.

I am grateful to Professor Peter Guttorp, Department of Statistics and director of NRCSE at the University of Washington, Seattle, USA, for giving me the opportunity to visit the National Research Centre for Statistics and the Environment (NRCSE) in September and October 1998. Thanks goes to NRCSE fellows Joel Reynolds and David Caccia for their comments and suggestions and to Professor Paul Sampson and Dean Billheimer for valuable discussions, and to Erik Christiansson and Gerry Goedde for their support during my stay at Bagley Hall.

Thanks to the kind providers of data, Jorge Rey at Estudios Geologicos Marinos (ESGEMAR), Málaga, Patricia Siljeström at IRNASE/CSIC, Sevilla, Ola Oskarsson at MMT, Göteborg, and to Klas Vikgren for providing the video strip-charts. I thank all participants in the BioSonar project for their contributions, which have been inspiring and amending some of the steps taken in this thesis; I am particularly grateful for many hours of good company and inspiring discussions with Kristian, Allan and Knut. The support and funding from the Commission of the European Union under contract no. MAS3-CT95-0026 with the MAST office of DG XII is highly appreciated. The funding received from Øresundskonsortiet is acknowledged.

Finally, I would like to thank my friends and family, Janne, Amanda and Valdemar (arriving in the middle of the study), as well as Katrine and Charlotte for being there and for their support and patience in times of high work load, in particular in the phase of finalising the manuscript.

It goes without saying that without all the fine people mentioned and the funding received I would not have been able to carry out this work.

Abstract

The application of hydroacoustic measurements for preparation of spatial distribution maps of benthic communities is reported. For the present study common mussels (*Mytilus edulis*), neptune grass (*Posidonia oceanica*) and *Cymodocea nodosa*, serving as canonical species of many European marine ecosystems, were selected. These species are supposed to be good indicators of marine ecosystem health. The hydroacoustic measurements comprise preprocessed echo sounder recordings and side-scan sonar data forming a large and unique collection of datasets based on 4 field campaigns in Øresund and the Mediterranean. A combination of geostatistical methods for spatial interpolation of the echo sounder observations and a set of classification rules, based on discriminant analysis of the feature space of the observations, is found to yield reliable distribution maps when compared to groundtruth data. The data-driven methodology developed is shown to be adaptive to instationarities in the echo sounder observations and is recommended as a substantial improvement of existing methods of sea floor mapping based on echo sounder data.

Elaborations of the developed methodology are studied, comprising the use of geostatistical simulation, Markov random fields and Boolean models. Geostatistical simulation provides a means of assessing the variability of random field functionals such as the estimated distribution area of a benthic species. The Markov random field allows the spatial distribution of the benthic communities to be modelled as a less smooth or regular phenomena than assumed when using geostatistical models. The use of Markov random fields in a Markov chain Monte Carlo simulation framework enables an alternative means of assessing variability of image functionals that is based on a sound theoretical basis. The estimates of variability obtained for estimated distribution areas with the two approaches compare satisfactorily. The Boolean models are suggested as a point of departure for embedding models of spatial patterns on the minor scales of observations to be used in up-scaling approaches to enhance the quality of the distribution maps and to be combined with biogeochemical models describing spatiotemporal population dynamics.

Finally, the use of side-scan sonar data is illustrated in a data fusion exercise combining side-scan sonar data with the results based on echo sounder measurements. The feasible use of side-scan sonar for mapping of benthic communities remains an open task to be studied in the future.

The data processing methodology developed is a contribution to the emerging field of hydroacoustic marine biology. The method of penalised maximum pseudo-likelihood for estimation of the Ising model under a huge amount of missing pixel data is a contribution to statistical image analysis. Furthermore, the estimation method developed for non-stationary Boolean models that combines scale-space kernel smoothing with the so-called method-of-moments applied to stationary Boolean models is a contribution to stochastic geometry.

Sammenfatning

Et studie af anvendelsen af hydroakustiske målinger til kortlægning af benthiske samfunds udbredelse beskrives. Blåmuslinger (*Mytilus edulis*), neptungræs (*Posidonia oceanica*) og *Cymodocea nodosa* blev udvalgt, da disse arter er af grundlæggende betydning for mange marine europæiske økosystemer. Disse arter antages således at være gode indikatorer for de marine økosystemers sundhed. De hydroakustiske målinger omfatter præprocesserede ekkolodsmålinger og side-scan sonar målinger, som udgør en enestående samling af datasæt indsamlet under 4 feltkampagner i Øresund og Middelhavet. Studierne viser, at en kombination af geostatistiske metoder til spatiel interpolation af ekkolodsmålinger med klassifikationsregler, som er baseret på diskriminantanalyser af målingernes faserum, resulterer i udbredelseskort, hvis pålidelighed kan verificeres vha. groundtruth data. Det bliver eftervist, at den udviklede data-drevne metodologi er adaptiv mht. manglende stationaritet mellem ekkolodsmålinger, og den anbefales således som en væsentlig forbedring af eksisterende metoder til kortlægning af havbunden vha. ekkolodsmålinger.

Forskellige elaboreringer af den udviklede metodologi er efterfølgende undersøgt, omfattende brug af geostatistisk simulation, Markov felter og Boolean models. Geostatistisk simulation er et redskab til estimering af variabilitet for funktionaler af stokastiske felter såsom estimerede udbredelsesarealer for benthiske samfund. Ved brug af Markov felter er det muligt at modellere benthiske samfunds udbredelse som teksturer, dvs. spatielle stokastiske felter med mindre glathed og regularitet end forudsat, når geostatistiske metoder anvendes. Anvendelse af Markov felt modeller til simulation inden for et såkaldt Markov chain Monte Carlo paradigme er en alternativ metode til estimation af variabilitet for udbredelsesarealer, som har en attraktiv teoretisk fundering. Variansestimater beregnet med de to simulationsmetoder udviser god overensstemmelse. Boolean models foreslås som et middel til at indlejre viden om spatielle mønstre, som er karakteristiske for hvert enkelt benthisk samfund på de mindre skalaer, med sigte på dels at forbedre udbredelseskortenes opløsning og præcision, dels at kunne kombinere udbredelseskortene med biogeokemiske modeller til beskrivelse af spatiotemporal populationsdynamik.

Anvendelse af side-scan sonar data illustreres i en datafusionsøvelse, hvori side-scan sonar data kombineres med resultater baseret på ekkolodsmålinger. Gode anvendelsesmetoder for side-scan sonar data med henblik på at fremstille udbredelseskort for bentiske samfund er et åbent problem, som vil blive studeret fremover.

Den udviklede metodologi for processering af hydroakustiske data er et bidrag til det for tiden fremvoksende felt hydroakustisk marinbiologi. Den udviklede estimationsmetode for Ising modellens parametre under store mængder manglende pixelværdier i et billede, som er baseret på penalised maximum pseudo-likelihood, er et bidrag til statistisk billedanalyse. Den for ikke-stationære Boolean models udviklede estimationsmetode, som kombinerer udglatninger i et skalarum med den såkaldte moment-metode for stationære Boolean models, er et bidrag til metoder inden for stokastisk geometri.

Table of Contents

1 Introduction

This ph.d. thesis investigates the use of various statistical image analysis methods for mapping of benthic communities, and suggests ways of combining data and models at different spatial scales into coherent maps of their spatial distribution. The present chapter gives a short introduction to the background and objectives of the studies, and outlines their scientific and methodological contexts. Furthermore, potential applications are discussed shortly, and a brief introduction to the targeted species is given.

1.1 Background and objectives

The studies reported here aim at the production of reliable, large-scale, high resolution distribution maps for designated benthic communities. The results of the present studies viewed in common with the results of the BioSonar project (MAS3-CT95-0026, 1997; 1998; 1999) yield one of the first tenable bids for a data processing method that complies with these three ambitious objectives, in this author's opinion. The present ph.d. thesis is aimed at the application of a specific spatial data type for particular purposes rather than aiming at a study of a particular mathematical method; hence, the use, description and development of mathematics will be detailed primarily in cases where it is found necessary or desirable. The specific property of the spatial data type under consideration is that it has a particular net-shaped structure of irregular data locations, i.e. what is usually referred to as irregularly spaced data in geostatistics.

1.1.1 Background

The biological material on the sea floor or partly immersed in it is called benthos or benthic material (benthic = at the sea bottom). Benthic habitats are usually divided into a range of types, like it is done in terrestrial biogeography, described by so-called benthic communities characterised by certain species being vital for the structures of benthic ecosystems. Benthic communities constitute the general object of the measurements and methods described here, as opposed to pelagic material (pelagic = in the water phase, above ground), i.e. fish and other swimming organisms. In the world's oceans the benthic biomass at depths greater than 3000 m is probably less than 1 gm^{-2} wet weight, at depths between 200 m and 3000 m the world average is about 20 gm^{-2}, and for waters shallower than 200 m the average is about 200 gm^{-2}; it has been calculated that more than 80% of the marine benthic biomass of the world lives on the continental shelves at depths of 0 - 200 m (Barnes & Mann, 1991). The biological production in these areas is one of the main drivers of global ecological cycles, and very important for humankind too. With the rise of environmental awareness focus on the sustainability and biodiversity of these coastal marine environments is increasing in many public and political contexts.

Thus, monitoring of marine ecosystem health is becoming increasingly important, and new methods must be explored to ensure the sufficient efficacy of environmental surveillance and corresponding mapping of spatial distributions of target species and ecosystems. One group of survey methods selects so-called indicator species, that is species canonical to whole ecosystems, and tries to evaluate the ecosystem health by assessing the state of the indicator

species. In the BioSonar project common mussels (*Mytilus edulis*) and neptune grass (*Posidonia oceanica*) were selected as indicator species. During the project data were also collected for the species *Cymodocea nodosa* in the Mediterranean and eelgrass (*Zostera marina*) in Øresund, creating additional valuable datasets.

Usual marine biological methods for benthic investigations deal with *in situ* sampling of the sea bottom, qualitative reports of diver's findings and occasionally still photos or subsea videos recorded at the sea floor. The BioSonar project explored the opportunities of applying hydroacoustic measurements and sonar recordings for benthic surveys, which was expected to be a promising venture. The BioSonar project concerned how to produce *reliable* and *precise* distribution maps for benthic communities at optimised costs, applying as many automated processes as possible. One of the major challenges of the approach was that there were several chains in the process needing refurbishment and elaboration in order to produce the resulting distribution maps. The list of overall goals of the project included:

- Quantitative detection (ability to detect benthic communities, and the ability to characterise their density with satisfactory precision)
- Reliability (reproducible or traceable, objective methods)
- Automation (computerisation of all possible work processes)
- Change detection (methods for monitoring changes in benthic communities).

Therefore, the goal was to measure precision by quantitative methods, e.g. by use of so-called resubstitution rates for classified images, and the processes should be automated as far as possible. In this context automation means at least computerised as regards the overall processing from the gathering of raw data to the preparation of the distribution maps to be inserted in GIS systems. Some of these processes would possibly require subjective decisions to be carried out during the use of computer programs, and might therefore not be totally objective or independent of the operator.

The present ph.d. thesis was prepared as a part of the work on the BioSonar project, and much of the work was therefore largely overlapping with it. Hence, the overall goals of the of the BioSonar project apply here also, with the qualification that the present thesis is a study of a subset of the data material and the data types collected in the BioSonar project. A specific description of the BioSonar data material and the subset of the data material selected for the present ph.d. study is given in chapter 2.

1.1.2 Objectives

The objectives of the studies can be outlined as follows:

- To determine the feasibility and applicability of hydroacoustic measurements in the form of echo sounder recordings and side-scan sonar images for preparation of distribution maps of benthic communities.
- To develop statistically sound data processing methods for preparation of distribution maps based on hydroacoustic measurements.
- To develop statistical methods for assessment of the uncertainty of distribution maps, in particular of derived coverage area estimates.
- To suggest and estimate stochastic models of the spatial patterns of the selected benthic communities.

Stated in a more pictorial way the objectives are to develop the infrastructure and the black box contents of the general data flow diagram depicted in Figure 1.1.

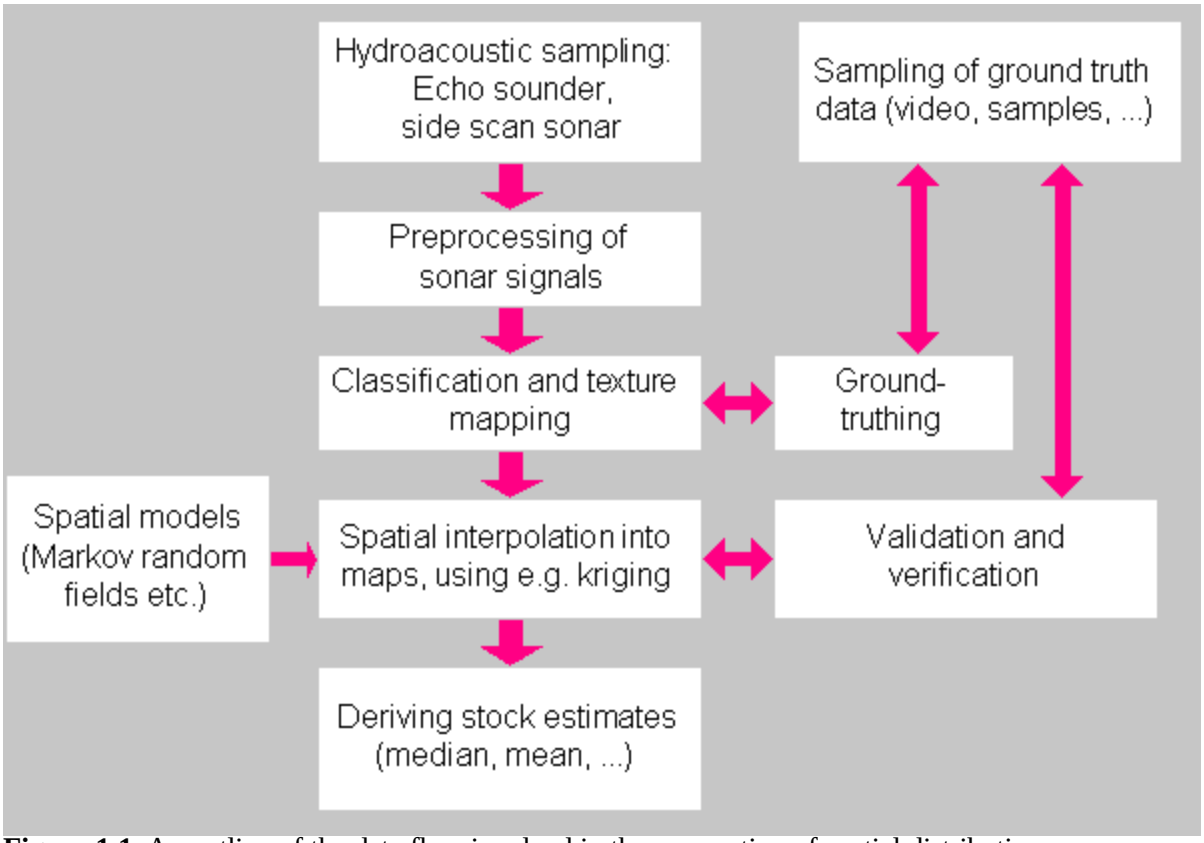

Figure 1.1 An outline of the data flow involved in the preparation of spatial distribution maps based on hydroacoustic measurements.

1.2 Contexts

This section introduces various points of departure for describing the rationale and context of the present study. The contexts sketched in the following comprise an interdisciplinary scientific context, a mathematical context, a marine biological context and an application context, and a list of topics not included is given too.

1.2.1 Interdisciplinary scientific context

To produce spatial distribution maps various disciplines must be brought together. The scientific and methodological fields can be divided into those contributing to the input, i.e. planning of observational designs and collection and acquisition of measurements, to the output, i.e. the production of (end user) spatial distribution maps, and to the intermediate processing linking the output to the input, cf. Figure 1.2.

In the input section remote sensing, marine biology and geostatistics applies to the design of the field campaigns in tasks such as pointing out interesting survey areas and planning sailing transect layouts. Backscatter theory and signal analysis applies to the hydroacoustics considerations of selecting the right instrumentation operating at the right frequencies, etc. and to the collection and preprocessing of electronic sensor signals. Finally, knowledge of underwater video (and photo) is a necessary component in the planning and execution of groundtruth data collection.

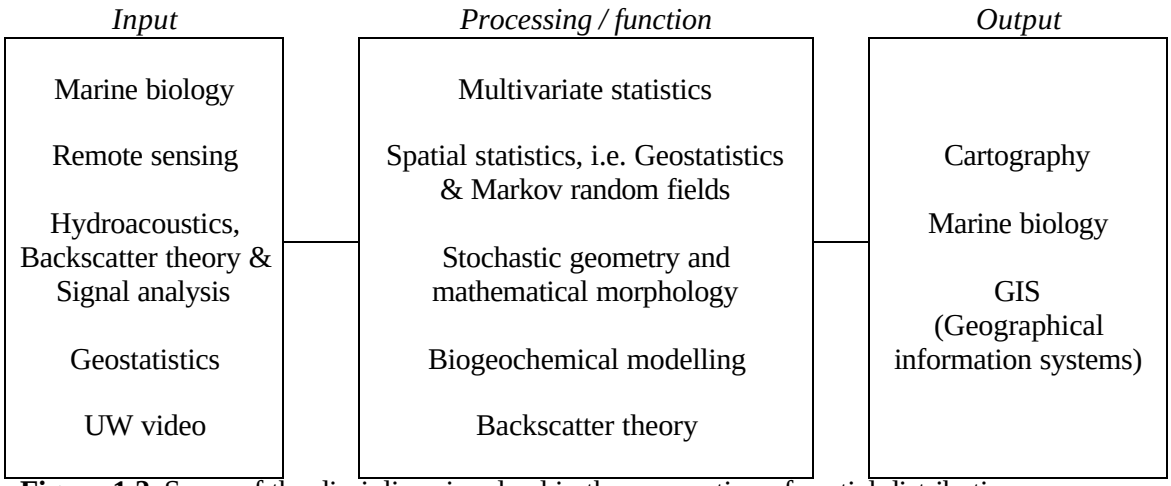

Figure 1.2 Some of the disciplines involved in the preparation of spatial distribution maps on the basis of hydroacoustic measurements. The list of fields given here is not intended to be exhaustive.

In the output section, the production of thematic maps belongs naturally under the field of cartography, and GIS is included in the list to underline the electronic and digital nature of the maps produced. Marine biology enters as a verification means comparing output to groundtruth data.

A selection of mathematically based data processing disciplines links input and output. First and foremost the use of spatial statistics and statistical image analysis, including geostatistics and Markov random fields, is emphasized; in some cases it is advantageous to supplement and elaborate these methods by means of stochastic geometry and mathematical morphology. To provide links to the worldview of biologists and their lines of study a promising path for the future would be to integrate these stochastic models with population dynamics models, the latter often having a principal deterministic content. This would allow the description of growth rates, seasonal behaviour patterns, etc. to enter the modelling; the term biogeochemical modelling in Figure 1.2 is hinting at this. In a more advanced setting, backscatter theory might be applied directly in the data processing when (or if) the measurement techniques reach a level where various species can be differentiated and detected by the hydroacoustic backscatter signatures.

All these jigsaw puzzles can be put into one hat constituting a field that could be labeled hydroacoustic marine biology. The end product is a thematic map, that is a map where subregions have been coloured to indicate properties of interest, like e.g. nations depicted in an atlas; formally, every pixel of a thematic map has been assigned a value from a set of stipulated thematic classes. Thus, a thematic map can be viewed as the product of a topographic map, i.e. a simple map of some measurement variables, and an interpretation of the measurements given by e.g. a set of classification rules.

A few of the fields mentioned above are singled out for further introduction below.

1.2.2 Mathematical-statistical context

A basic dichotomy of mathematical statistics is that of separating signal from noise implicitly defining most statistical models by the following canonical expression:

$$Y = \mu + e \tag{1.1}$$

where Y is a measurement, μ is the deterministic component of the measurement, and e is the random component of the measurement. This dichotomy of a dual (deterministic, random) component is known under various names as e.g. (level, variability), (location, dispersion), (explained, unexplained), and (signal, noise), pertaining more or less to properties of the dual components. These labels are not globally applicable, e.g. explainable components are not necessarily deterministic, levels and locations can be rather fluctuating, noise might be quite explainable, etc. Hence, Tukey (1977) used the terms *smooth* and *rough* to give the notion of this dichotomy in a generic sense. One point of (1.1) is that the delimitation of the explained component μ and the random component e is defined subjectively by the person formulating the model, probably guided by a formulation of the hypothesis to be investigated.

Here, the generic model (1.1) is applied over a 2-dimensional (2D) space, and hence it is written:

$$Z(s) = \mu(s) + e(s) \tag{1.2}$$

extending the random variable Y to the random field Z(s) defined on the underlying 2D space (the index set) containing the point $s = (x,y)'$. The expression (1.2) indicates that the spatial measurements are made up of a smooth spatial component $\mu(s)$ and a random (rough) component e(s).

Another basic observation to make from a statistical point of view is that the datasets studied here represent observational designs, i.e. they are measurements of a state of nature that is not controllable (yet...) by humankind as opposed to experimental designs aimed at studying effects of varying a range of interesting, controllable factors. Observational designs have their own body of design and inference theory, and one of the original introductions to the subject can be found in Cochran (1983).

The random field Z(s) is normally studied by means of geostatistics if the index set is considered to be continuous and by means of theory and methods for random fields with discrete support if the index set is a discretised grid. For simplicity, treatment of the latter will be restricted to Markov random fields.

Geostatistics emerged in the early 1970s and '80s as a hybrid discipline of mining engineering, geology, mathematics, and statistics, primarily elaborated and promoted by G. Matheron at the Ecole des Mines in Paris. Its strength over more classical approaches to ore-reserve estimation lies in the inherent accounting for both large-scale and small-scale spatial variability, where earlier methods like trend-surface methods accounted for large-scale variability only. Much of geostatistics terminology stems from its history of emergence, e.g. the class of optimal linear spatial prediction methods is called *kriging* owing to one of the originators D.G. Krige. Introductions to geostatistics can be found in Journel & Huijbregts (1978) and Isaaks & Srivastava (1989), and to spatial statistics in general in Cressie (1991). Some enlightening remarks on the simultaneous development of computational power and geostatistics can be found in Myers (1999). In the present report, a more detailed introduction to geostatistics is given in section 3.2.1, and an introduction to geostatistical simulation is given in section 3.5.1.

Markov random fields theory is a basic modelling framework for statistical image analysis where images are conceived of as data organised in lattices (the technical term) and represented as pixels. Markov random fields describe small-scale variability by correlation between closely located pixels and provide good means for describing textures of images. Introductions to Markov random fields are given in e.g. Cressie (1991), Carstensen (1992) and Guttorp (1995).

Together, the use of geostatistics and Markov random fields forms the backbone of spatial statistics. A more eloquent definition of spatial statistics is given by Charlie Geyer: "*Spatial statistics, narrowly defined, is the study of stochastic processes in Euclidean spaces, like the locations of trees in a forest or patches of land and water in a satellite image. Broadly defined, it covers any stochastic process with dependence more complicated than a time series, like the inheritance of genetic traits over generations of a family tree or like the network of social interactions in a community.*" (Citation from prof. Geyer's website at University of Minnesota, URL: http://www.stat.umn.edu/booklet/charlie/activities.html)

In the present study the echo sounder data are geostatistical data collected along the sailing trajectories, so-called transects. These data belong to a particular spatial data type belonging to the class of irregular data in the argot of geostatistics (Nielsen, 1994), living on a continuous index set and arranged in a net-shaped pattern.

Finally, it can be mentioned that some elements of stochastic geometry and mathematical morphology are used to analyse patterns formed by mussels and neptune grass by means of Boolean models, and furthermore, that classification methods based on multivariate discriminant analysis are applied as well.

1.2.3 The context of marine biology

In marine biology traditional monitoring methods are based primarily on *in situ* sampling. Hydroacoustic applications in marine biology so far have been dealing mainly with pelagic detection, e.g. distribution mapping of herring (Maravelias & Haralabous, 1995). On the other hand hydroacoustic measurements of the sea floor have been used for more than a decade in oceanographic geology to describe sediments and provide large-scale mapping hereof. Hence, the use of hydroacoustic measurements for mapping of benthic communities lies somewhere in between and is as such an innovative approach.

The hydroacoustic mapping of the benthic communities provides promising options for the execution of large-scale surveys.

In scientific marine biological research a hydroacoustic monitoring methodology of this type would typically apply as a first step in a monitoring campaign to identify interesting sites to be used for in-depth studies. Results produced by this method are (reluctantly) considered to be useful but quite crude by marine biologists, as the resulting maps provide information about presence/absence, where more elaborate parameters must be measured by other means. These views were expressed by several participants at an annual meeting for Danish mussel biologists at VKI in February 1999, where the main results of the studies were presented.

However, in environmental protection and surveillance tasks the options provided are promising, allowing these to be carried out at low costs and yet producing large-scale maps of the selected benthos at the sea floor. Furthermore, the remote sensing perspective is promising, and it might probably be advantageous to integrate investigations of this type with satellite data. In the future, hydroacoustics based maps might provide the groundtruth for larger-scale remote sensing maps of the sea floor.

Until recently, little research has been done on models of spatial patterns formed by benthic communities. An early contribution to *spatial benthic biology* is the seminal paper by Paine &

Levin (1981) where the authors used a stochastic diffusion model to describe the spatio-temporal dynamics of tidal patches of mussels. Snover & Commito (1998) used a fractal model to describe the spatial patterns of tidal patches of mussels recorded in photos.

1.2.4 Scope and field of applications

The hydroacoustic measurements can be used for several purposes:

- Environmental inventories (e.g. in marine conservation areas),
- Environmental impact assessments (e.g. monitoring in relation to construction works), and
- Environmental change detection.

The studies of ways of assessing uncertainty is necessary for use in environmental monitoring in relation to decision support and decision making processes. At present, methods are being developed allowing objective quantitative criteria like a 25% decrease of a certain measure to be included in the design of monitoring campaigns aimed at environmental impact assessments. These planning methods are primarily based on so-called power analysis methods (Green, 1989; Cohen, 1988). Power analysis relates negotiated interesting effect sizes, Δ, to estimates of background variability, σ, and uses power functions, $\pi(\cdot)$, i.e. probabilities of detecting Δ given the size of σ, and the monitoring design(s) in question to assess designs based on $\pi(\Delta/\sigma)$.

Considerations like these were used in the design of the monitoring programmes for the Fixed link between Sweden and Denmark, cf. Sørensen (1994a; 1995).

1.2.5 Scale of spatial distribution maps

The term *scale* is a vague term that is not easily given a rigid formal definition, and this applies also to *large-scale* and *small-scale*. However, an operational definition can be given based on scales of the benthic communities themselves. Mussels do not extend their domain below a maximum water depth of 15-20 metres, and neptune grass does not go below water depths of 80-100 metres. Thus, the maximum water depth of a benthic community defines the extent of the maximum large scale perpendicular to the coastline. At the locations surveyed in the actual field campaigns the maximum water depths corresponded to a maximum scale for mussels at 5-10 km and approximately the same for neptune grass off the coast in the south-eastern part of Spain. It is recommendable that such operational values of large scales are settled upon whenever a similar study is conducted.

1.2.6 Delimitation

The following topics were omitted in the present study, although they might be everything from useful to substantial and interesting in regard to the objectives:

- Hydroacoustic backscatter theory,
- Spatio-temoral population dynamics and their forcing functions,
- General remote sensing theory,
- Aerial primitives, i.e. primitive elements of support and the function hereof is not considered in detail,
- Vector representations of thematic maps, and
- Image segmentation.

Change detection is not fully omitted as minor hints hereat are given e.g. in chapter 5.

1.3 The target species

In this section a very brief introduction to the selected indicator species is given. A general introduction to benthic communities is given in Parsons, Takahashi & Hargrave (1977).

1.3.1 Common mussels

It is common knowledge what a closed or dead common mussel looks like, hence a photo of actively filtrating common mussels is depicted in Figure 1.3.

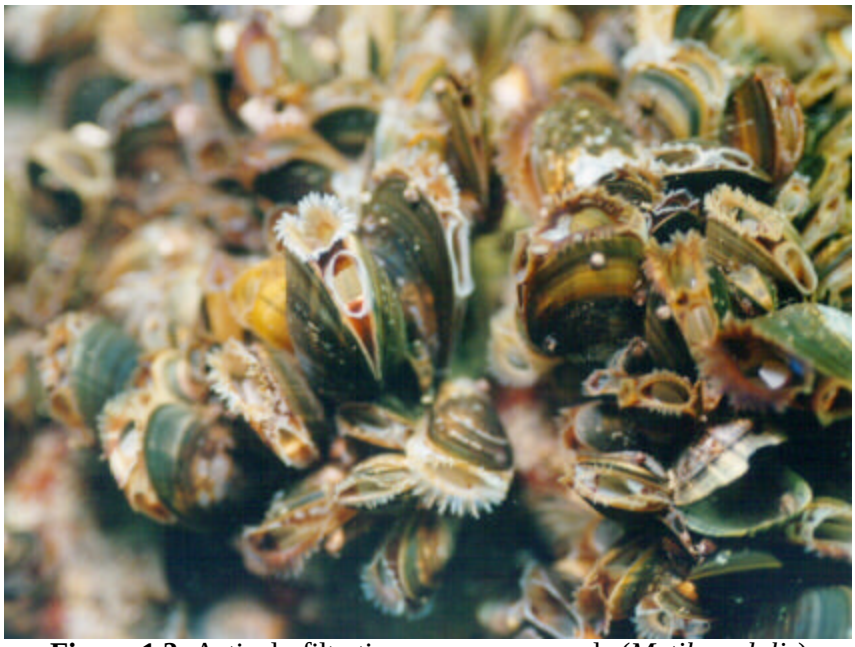

Figure 1.3 Actively filtrating common mussels (*Mytilus edulis*)
(courtesy of Anders Højgård Petersen, VKI).

Mussels begin their life cycle as larvae suspended in the water phase, normally in large swarms. Then they settle, all at about the same time, and attain their wellknown shape beginning as tiny mussels of approx. 1 mm length. Larvae are normally spawned once a year, yet years of 2 spawnings or none have been recorded too, and the generation dynamics of mussels is not well understood. A full-grown mussel reaches a length of 5 - 7 cm.

Mussels tend to form patches to improve their feeding conditions. At larger scales (10 - 100 metres) mussels can either cover the sea floor as a textural distribution known as mussel beds, or they can form dotted patterns of dispersed patches. Only the former was found in Øresund, where the datasets studied here were collected. Mussels are not entirely stationary, they can move about on their foot even though they seldomly do so.

Mussels are often selected as indicator species due their robustness. Mussels can sustain life without oxygen supplies in up to 40 - 50 days. Mussels have specific depth ranges; in Øresund, they are mainly found at water depths between approx. 3 and 15 metres.

1.3.2 Neptune grass (*Posidonia oceanica*)

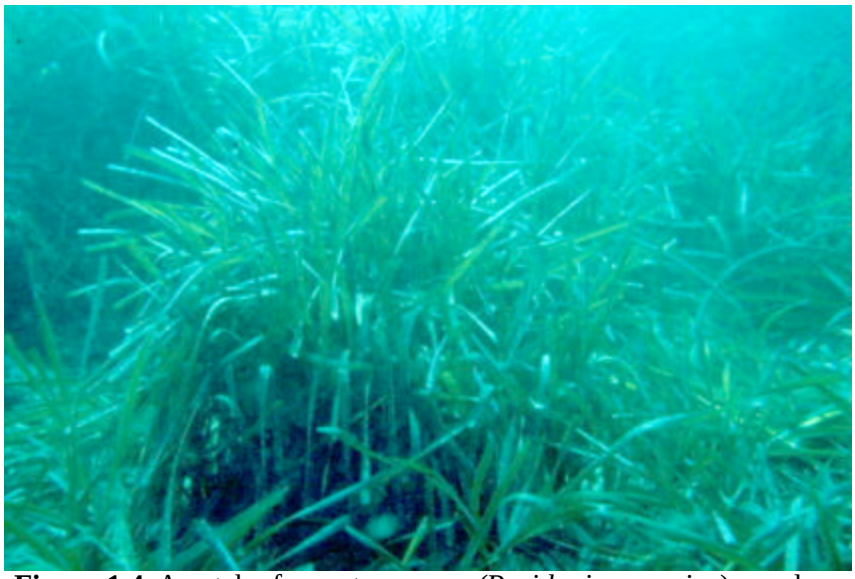

Figure 1.4 A patch of a neptune grass (*Posidonia oceanica*) meadow.

Posidonia is one of the main seagrass genera among *Zostera, Cymodocea, Halodule* and *Thalassia*. Posidonia can go to depths of 60 - 80 metres if the depth of the photic zone allows it. Posidonia forms the basis of many marine ecosystems, and can be present in large neptune grass meadows, cf. Figure 1.4, or be more sparsely distributed in patches separated by sediment. It is abundant and widespread in the Mediterranean where it is the foundation of many benthic ecosystems. Recent years have seen a depletion of the Posidonia meadows caused by the intruding exogenous species *Caulerpa taxifolia* in the northern and western parts of the Mediterranean. The interested reader can find more details on seagrasses and Posidonia in Barnes & Mann (1991).

1.4 Applied software and previous publications

The main vehicle for data processing has been my old workhorse SAS, using here the version 6.12 for Windows95; in particular, some of the more tedious matrix manipulating algorithms were implemented in SAS/IML, both as utility programs and as a means of testing the Delphi programs developed. SAS is a registered trademark of SAS Institute Inc., Cary, North Carolina.

The public domain geostatistical software library GSLIB, version 2.0, and the surface mapping package Surfer, version 6.03, were used to do the geostatistical data processing and production of maps. GSLIB is published by Deutsch & Journel (1998) and copyrighted by Oxford University Press. Surfer is a registered trademark of Golden Software Inc., Golden, Colorado.

The (object) pascal programming environment Delphi, version 3.0, was used to program simulators for Markov random fields as well as a converter, called GRID, to turn GSLIB result files into pixel images in Windows95, using the PGM and PPM image formats, as a parallel to the Postscript converter provided with GSLIB for unix systems. Furthermore, Delphi was used to make a program that conducts the dilations, Gaussian filtering and quadratic regression estimations necessary for the estimation of non-stationary Boolean models. Delphi is a registered trademark of Inprise Corporation, Scotts Valley, California.

Some of the studies reported in this thesis have previously been partially published in:

MAS3-CT95-0026 (1997): "Scientific Report for Year 1 of the BioSonar Project". Report prepared by the BioSonar project partners to the MAST Office of the European Union.

MAS3-CT95-0026 (1998): "Scientific Report for Year 2 of the BioSonar Project". Report prepared by the BioSonar project partners to the MAST Office of the European Union.

MAS3-CT95-0026 (1999): "Final Scientific Report of the BioSonar Project". Report prepared by the BioSonar project partners to the MAST Office of the European Union.

Sørensen P.S., Madsen K.N., Nielsen A.A., Schultz N., Conradsen K. & Oskarsson O. (1998): Mapping of the benthic communities Common mussel and Neptune grass by use of hydroacoustic measurements. 3rd European Marine Science & Technology Conference, Session report of Seafloor characterisation session, European Commission.

1.5 Outline of the thesis

Chapter 3, the basic corner stone of the report, outlines and details the necessary geostatistical data processing steps needed to prepare distribution maps on the basis of echo sounder data. Based on exploratory spatial data analyses summarised in appendix B, this chapter goes through analyses of spatial continuity and classification of feature spaces of echo sounder measurements, to arrive at a hybrid block kriging method employed to prepare classified distribution maps. Furthermore, chapter 3 contains an introductory treatment of spatial change detection, and the results are compared to groundtruth data.

The other chapters follow various paths using the contents of chapter 3 as a point of departure. Chapter 4 describes results of applying the algorithms developed and presented in chapter 3 for mussels (*Mytilus edulis*) to the mapping of neptune grass (*Posidonia oceanica*) and *Cymodocea nodosa* in the Mediterranean. Chapter 5 presents the results of geostatistical simulations conducted to assess variability of distribution maps and derived map functionals like estimated distribution areas of mussels.

Chapter 6 presents Markov random fields as an alternative framework for the simulation based assessment of distribution map variability, and compares the results to those obtained with the geostatistical simulations. A method for estimating the Ising model parameters under presence of major amounts of missing data is discussed, based on penalised maximum pseudo-likelihood.

Chapter 7 gives a short presentation of the use of side-scan sonar data and the fusion hereof with echo sounder data.

Chapter 8 discusses various ways of formulating models of spatial patterns formed by benthic communities and develops a method to estimate localised parameters for a non-stationary Boolean model based on a combination of scale-space theory and Cressie's method-of-moments for stationary Boolean models. The use of the method for estimation of the non-stationary Boolean model is illustrated for the spatial patterns of *Posidonia oceanica*.

Finally, a summary of the thesis is contained in chapter 9, including some suggestions for future research and hints at directions to be taken to develop the field of hydroacoustic marine biology.

This is the plan of the thesis. The present introductory chapter has been sketching some of the contexts of the study, including some very brief details about the indicator species used. The next chapter (chapter 2) presents the data material, the field campaigns and the subsets of the data selected for the ph.d. study.

2 Data Material

This chapter presents the design of the field campaigns, their execution and the resulting datasets including a discussion of data quality issues.

2.1 Field campaigns and data acquisition

The data material was collected during 4 field campaigns executed during the fall of 1996 and 1997 in the southern part of Øresund between Denmark and Sweden and in coastal waters close to Cartagena in the south-eastern part of Spain. The geographical locations of the field campaigns are indicated in Figure 2.1.

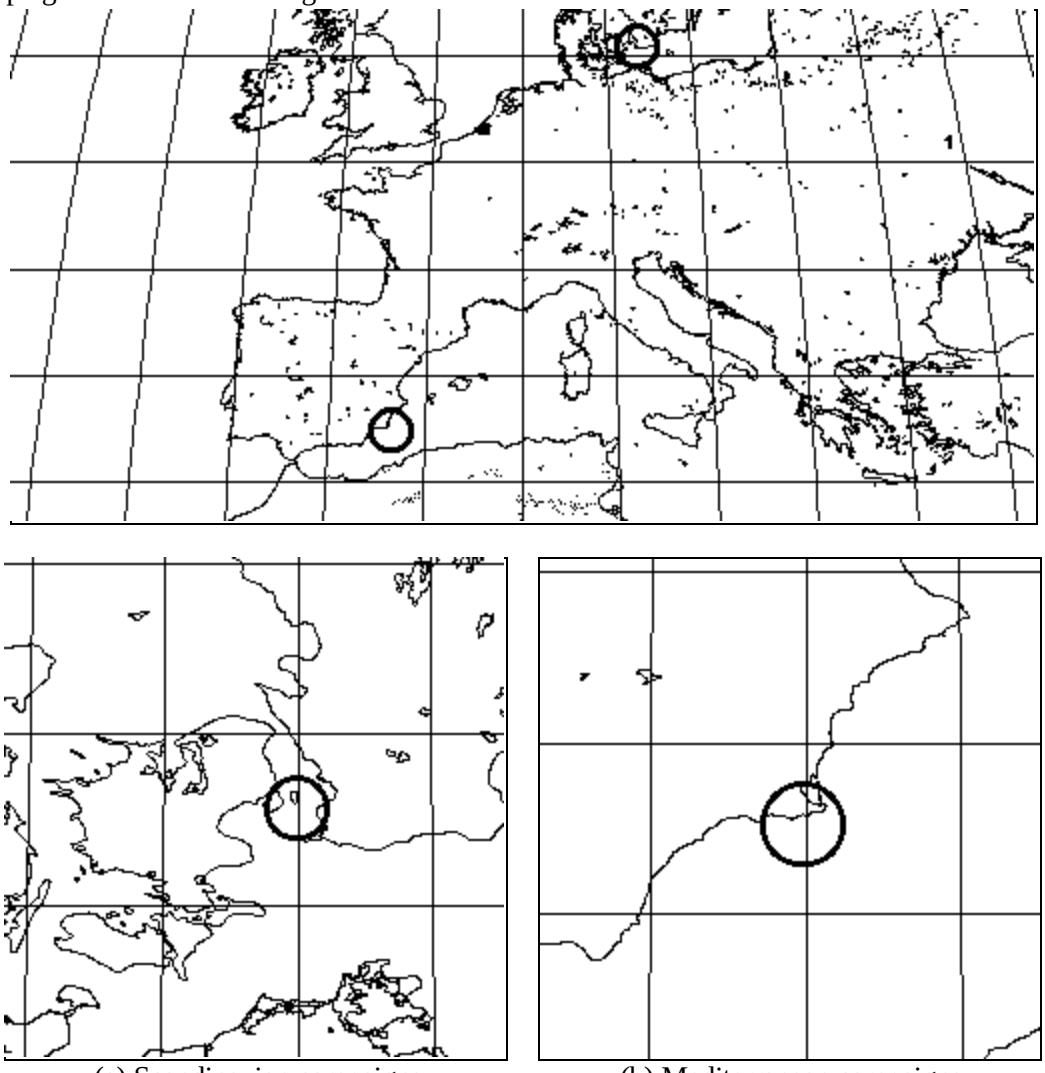

(a) Scandinavian campaigns (b) Mediterranean campaigns

Figure 2.1 Geographical locations of the field campaigns.

In the following sections the what, how, where, when, how much and how good regarding the data material is detailed.

2.1.1 Design of field campaigns

The field campaigns were planned to enable the acquisition of hydroacoustic data, groundtruth data and ancillary data like *in situ* samples of the benthic communities and water samples to be analysed chemically for covariates like turbidity, salinity and oxygen concentration. The hydroacoustic data acquisition comprised the collection of echo sounder data using an echo sounder add-on device called RoxAnn operated at 200 kHz and the collection of side-scan sonar data using a Geoacoustics side-scan sonar at 100 kHz and 500 kHz and an EOSCAN postprocessing device. Specifications of the instrumentation are given in Tables 2.1 and 2.2.

Table 2.1 Components of the GeoAcoustics dual frequency side-scan sonar system.

Unit	Weight /kg
2 Model SS941 Transceiver units containing the key in circuitry, power supply, and analogue processing circuitry.	13.6 x 2= 27.2
1 Model 159 Towed Vehicle containing sub-sea electronics Model SS942. 100/500 kHz ± 1%.	37.5
Coaxial Tow Cable. (50 m).	12
OMS Eoscan Data Acquisition System with five channels EOSCAN Software, version 3.13. Weight includes SVGA monitor.	approx. 45
Auxiliaries: Interconnecting Cables, Rubber Deck Cable, Spare parts case, Interconnecting Cables, Portable Notebook PC	-

Table 2.2 Components of the RoxAnn echo sounder recording system.

Unit
Navigation: Differential GPS Magnavox 200 D
RoxAnn seabed analysis system
Heave compensator Seatex MRU 6
Gyro Robertson RGC11
Echosounder Simrad 300P 200 kHz
Echosounder G101 50 kHz
Main sampling computer MMT ARON System 486 33 Mhz 200 Mbytes 10 serial ports.
Auxiliaries: Plotter, HP 7475B, Parallel printer

The field campaigns in the Mediterranean and in Øresund were carried out in the two consecutive years 1996 and 1997. The areas in Øresund were surveyed in weeks 42 and 43 (last half of October) in 1996 and 1997, and the Mediterranean areas were surveyed in weeks 46 and 47 in 1996 and weeks 47 and 48 in 1997, thus screening out possible effects of seasonal variations in the change detection analyses. The field campaigns were executed under the management of managing director Ola Oskarsson, Marin Mätteknik AB (MMT), Sweden, in Øresund using MMT research vessels, and under the management of technical director Jorge Rey, Estudios Geologicos Marinos (ESGEMAR), Spain, in the coastal waters near Cartagena using ESGEMAR vessels.

How and where

The design of the field campaigns were based on three types of sea bed areas:

- Test areas: Two areas were selected at the locations in Spain and Denmark, respectively, at sizes of 1 - 2 km².
- Bottom type areas: 3 - 6 areas at sizes of 100 x 100 metres were selected.
- Footprint areas: One area was selected for every campaign having a size of 60 x 60 metres.

The purpose of the two test areas was to collect mixed data representing real world cases with the intention that the two test areas should be different. Thus, in Øresund one test area was placed on the southern edge of Drogden, situated southwest of the island Saltholm, and was expected to contain a horizontal density gradient of mussels. The other test area was placed in the northwest part of Flinterenden, an area southeast of Saltholm known to be covered by large mussel beds. In the Mediterranean one test area was placed at Cabo de Palos east of Cartagena expected to represent an area of healthy neptune grass meadows. (This is Palos de Murcia, not to be confused with Palos de la Frontera southwest of Sevilla from where Columbus departed on his first journey in 1492). The other test area was placed at Mazarrón west of Cartagena and was expected to represent an area of degraded meadows.

The purpose of the so-called bottom type areas was to include sea floor areas covered in a practically uniform way by distinct and specific benthic populations. The data from these bottom type areas were planned to apply as reference points when the test areas were studied, and as basic data in preliminary studies of the discriminatory power of the hydroacoustic data.

The measurements made in the so-called footprint area were introduced to be able to assess repeatability and drifts from day to day, i.e. as a possible calibration means.

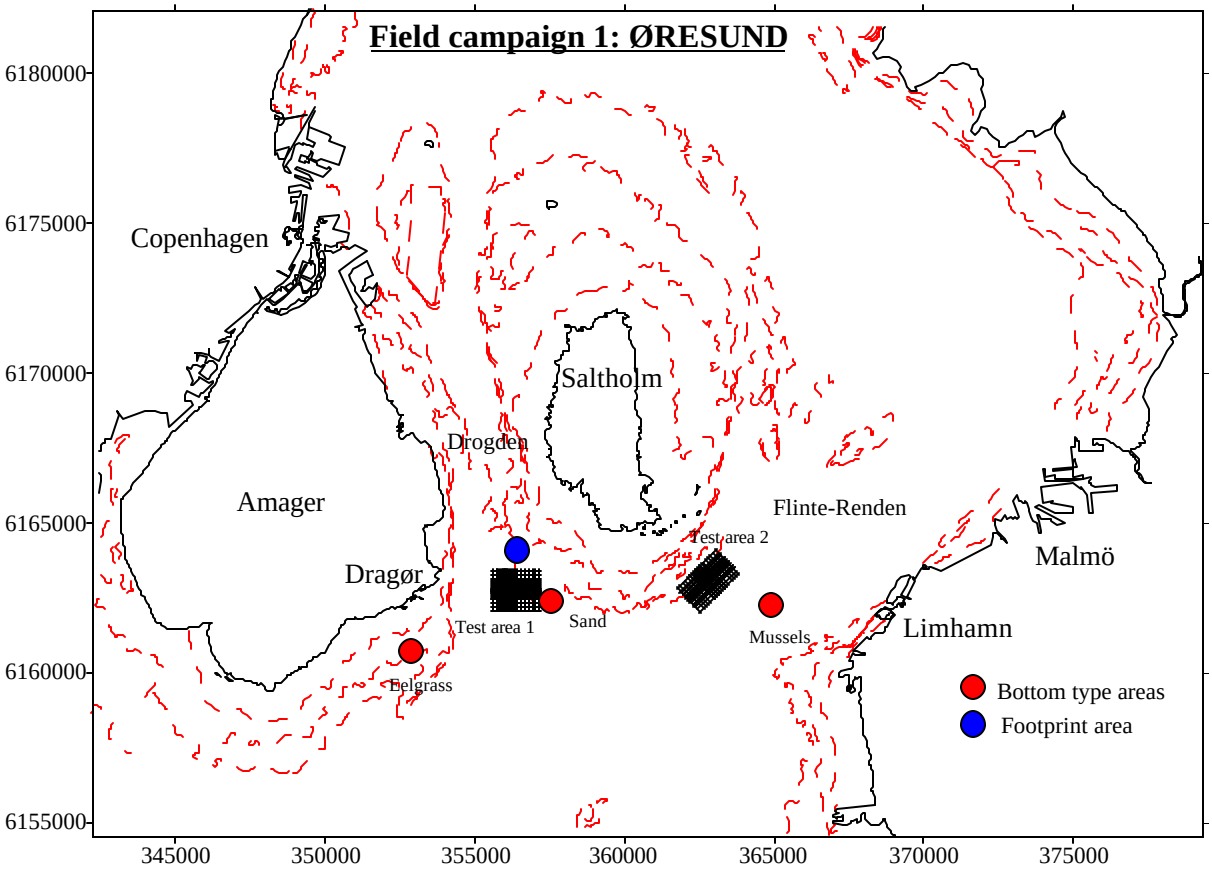

Figure 2.2 Geographical map including test areas etc. in Øresund used in the first field campaign in 1996. The coordinates are UTM 33 Northings and Eastings on the ED50 ellipsoid.

Three bottom type areas were used in the Øresund, namely sand (100% coverage), a mussel bed (100% coverage), and eelgrass (*Zostera marina*) meadows at approx. 100% coverage. The areas of the Øresund field campaigns are depicted in Figure 2.2.

In the Mediterranean five bottom type areas were devised, namely sand (Cabo de Palos), mud (Mazarrón), neptune grass (*Posidonia oceanica*) meadow at a 100% coverage (Cabo de Palos), degraded posidonia meadow (Mazarrón) and a *Cymodocea nodosa* meadow at a 100% coverage (Cabo de Palos).

To study the spatial properties of the hydroacoustic measurements at various scales and directions in the test areas a basic orthogonal transect grid having a distance between transects at 120 metres were applied. The basic transect grid was supplemented by a more dense zone consisting of a cross having 7 transects interspaced by 20 metres in each of the orthogonal directions, and a fringe on the cross consisting of 4 transects separated by distances at 60 metres. This is illustrated for test area 1 in Øresund in Figure 2.3.

Groundtruthing was prepared using video and still photos. Vertical video recordings were taken at fixed stations, primarily at intersection points in the transect grids. The video camera was mounted with a measuring tape. Still images were prepared for fixed stations by means of a photo-sampler. The images cover approx. 2 m² of the sea bottom.

A range of exogenous and supplementary variables were measured, including depth, temperature and salinity profiles, chlorophyll (when feasible), seston and transparency. Sea state was opted for, but the measurements were not implemented.

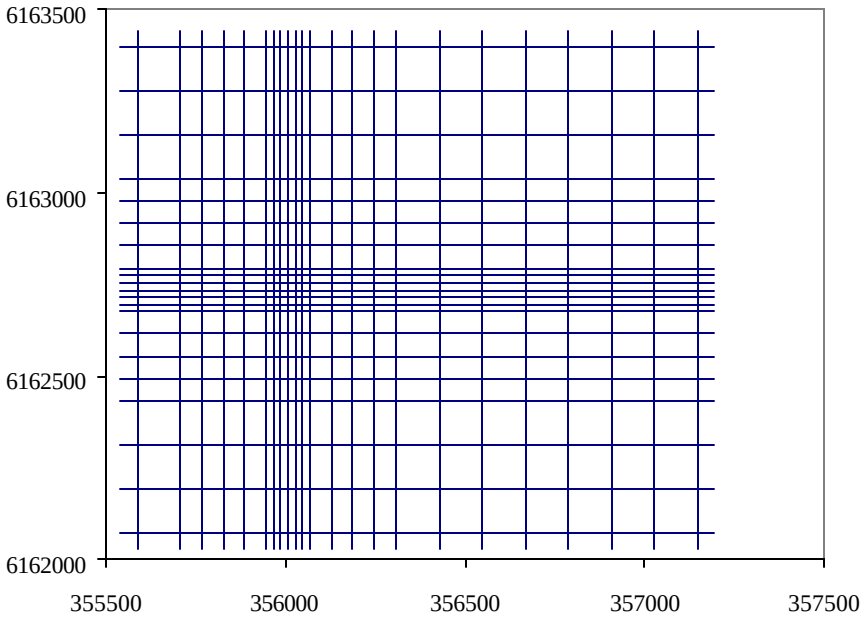

Figure 2.3 Transect grid applied in Test area 1 (Drogden South, Øresund), in 1996 and 1997 with the dense cross positioned at a place presumed to have a potential gradient in mussel density. The coordinates are UTM 33 ED50 Northings and Eastings.

Monitoring grid designs

The footprint area was 60 x 60 m² and was monitored as the first thing every morning during the campaigns. RoxAnn was used along two transects interspaced by 20 metres with a transect in the middle perpendicular to the two others. Side-scan sonar was used along one transect.

The bottom type areas were 100 x 100 m². They were covered by 5 RoxAnn transects interspaced by 20 metres by (10,30,..,90) in two orthogonal directions in 1996, and in 1997 10 transects in either direction were used. For the side-scan sonar three transects were used in each of the four compass directions, with transects starting in 0, 20 and 40 metres from the left end of the bottom axis seen from the direction, where the sailing began.

The test areas were approx. 2 km². For RoxAnn the canonical grid design in the test areas had 7 transects in the centre interspaced by 20 metres. Around these transects 8 transects were placed, 4 on each side, interspaced by 60 metres. On the outside of these transects the rest of the transects were interspaced by 120 metres. An identical grouping of transects was used in the perpendicular direction, cf. Figure 2.3.

According to these monitoring designs an outline of the planned datasets, comprising two types of hydroacoustic data and groundtruth data, can be given in the form of Tables 2.3 and 2.4, for Øresund and the Mediterranean, respectively.

Table 2.3 Outline of planned datasets for the field campaigns in Øresund.

Øresund	Field campaigns	
	1996 - I	1997 - III
Test areas	Drogden South Flinterenden NW	Drogden South Flinterenden NW
Bottom type areas	Mussels Sand Eelgrass	Mussels Sand Eelgrass
Footprint area	near Dragør	near Dragør

Table 2.4 Outline of planned datasets for the field campaigns in the Mediterranean.

The Mediterranean	Field campaigns	
	1996 - II	1997 - IV
Test areas	Cabo de Palos Mazarrón	Cabo de Palos Mazarrón
Bottom type areas	Posidonia, full cover Posidonia, sparse Cymodocea Sand Mud	Posidonia, full cover Posidonia, degraded Cymodocea Sand Mud
Footprint area	at Palos	at Palos

2.1.2 Execution of the field campaigns in 1996

The field campaign in Øresund in the fall of 1996 was executed according to the plan and resulted in a full range of datasets and a collection of groundtruth video recordings.

In the Mediterranean the campaign resulted in full datasets for the Cabo de Palos test area and related bottom type areas, whereas the sea trials in the Mazarrón area were postponed due to bad weather conditions. Parts of these datasets were collected during a supplementary sea trial in the spring of 1997.

2.1.3 Execution of the field campaigns in 1997

The field campaign in Øresund in the fall of 1997 was executed according to the plan and yielded almost all the planned datasets and a collection of groundtruth video recordings. However, the datasets for the eelgrass bottom type area went missing and could not be reestablished, and the majority of the groundtruth transect videos were severely blackened by lack of light thus limiting the scope for groundtruth scrutiny. Due to a need to optimise the time period used for the sea trials, the monitoring of the test area 2 at Flinterenden NW was reduced to a minor part in the centre of the planned test area. The side-scan sonar data acquired with the GeoAcoustics device were supplemented with side-scan sonar recordings made by MMT AB using their Isis equipment.

The field campaign in the Mediterranean in the fall of 1997 was executed according to the plan and resulted in a full range of datasets and a collection of groundtruth video recordings.

2.2 Available and selected data

This section describes the link between the planned datasets and the final selection of datasets among those acquired during the field campaigns, i.e.

$$\text{Planned data} \supseteq \text{Available data} \supseteq \text{Selected data.}$$

2.2.1 Echo sounder data recorded in Øresund

The RoxAnn device, consisting of a head amplifier, a parallel receiver and a software package, records time-integrated parts of the first and the second backscattered echo from the sea floor, called E1 and E2, respectively. The existence of a relation between sea floor morphology and E1 (sea floor roughness) and E2 (sea floor hardness) is detailed on an empirical basis in Chivers, Emerson & Burns (1990) and Chivers & Burns (1991). A theoretical justification for the said interpretation of E1 and E2 is given by Heald & Pace (1996). In the BioSonar field campaigns an echo sounder frequency at 200 kHz was used. Thus, the echo sounder datasets consist of series of bivariate vectors (E1,E2) recorded at series of locations along sailing trajectories, so-called transects. Section 2.4 gives a thorough introduction to the selected echo sounder data from Øresund.

Available data

From the 1996 campaign all planned RoxAnn datasets were available. From the 1997 campaign the eelgrass dataset went missing and could not be recovered.

Data quality and selected data

The RoxAnn datasets were delivered as ASCII files and posed no obstacles regarding collation and preprocessing of the raw data files. By inspection the data were found to be of good quality, with the qualification that some series showed indications of lacking synchronicity between the

GPS logging device and the RoxAnn computer, causing some coordinates to be recorded without proper updating. The treatment of these skips is described in section 2.4.

As the eelgrass bottom type dataset from 1997 went missing it was decided to omit eelgrass from the analyses presented in this thesis.

2.2.2 Echo sounder data recorded at Cartagena

The use of RoxAnn in the Mediterranean was similar to the use in Øresund.

Available data

At Cabo de Palos RoxAnn was used to measure the planned bottom types and test areas, and the additional bottom type characterised by *Cymodocea nodosa*. As mentioned, parts of the datasets from the Mazarrón test area were omitted, and thus this test area was not selected for use here.

Data quality and selected data

The RoxAnn datasets were delivered as ASCII files and posed no obstacles regarding collation and preprocessing of the raw data files. By inspection the data were found to be of good quality.

2.2.3 Side-scan sonar data

The GeoAcoustics dual frequency side-scan sonar device was used in all 4 field campaigns at frequencies of 100 kHz and 500 kHz. Additionally, the Isis side-scan sonar system was used in parallel in the second field campaign in Øresund 1997. Technical details about side-scan sonar devices and their functioning can be found in Blondel & Murton (1997).

Available data

GeoAcoustics data were made available as PCX gray scale images. The raw data, i.e. the voltage measurements aggregated in so-called side-scan sonar pings and stored automatically in a proprietary file format, were made available but not readable, as it proved prohibitively difficult to convert the data. The Isis side-scan sonar recorded pings in the Q-MIPS file format, which is a property of Triton Elics Inc., the manufacturer of the Isis system. The company has made a format description available allowing the raw data to be obtained by conversion of the Q-MIPS files by developing the appropriate software algorithms. The process of converting and geocoding the Q-MIPS side-scan sonar files is described in appendix A.

Data quality and selected data

During inspection of the delivered PCX files some findings cast reasonable doubt on the feasibility of the geocoding algorithms employed. Thus, taking the obstacles caused by the proprietary nature of the GeoAcoustics data into account too, it was decided to omit these data from the present study, with a few exceptions (see chapter 8). The GeoAcoustics side-scan sonar data were used in various other studies reported in the BioSonar reports (MAS3-CT95-0026, 1998; 1999). For illustratory purposes the Isis side-scan sonar from the 1997 field campaign in Øresund were selected here. Due to their restricted and secondary nature, the treatment of them will be likewise.

2.3 Groundtruth data

Video recordings

Along every 5th sailing transect the towfish carried a video camera recording images of the sea floor. An example frame is shown in Figure 2.4. Also, vertical video recordings were taken at fixed stations. Video cameras were mounted with a measuring tape.

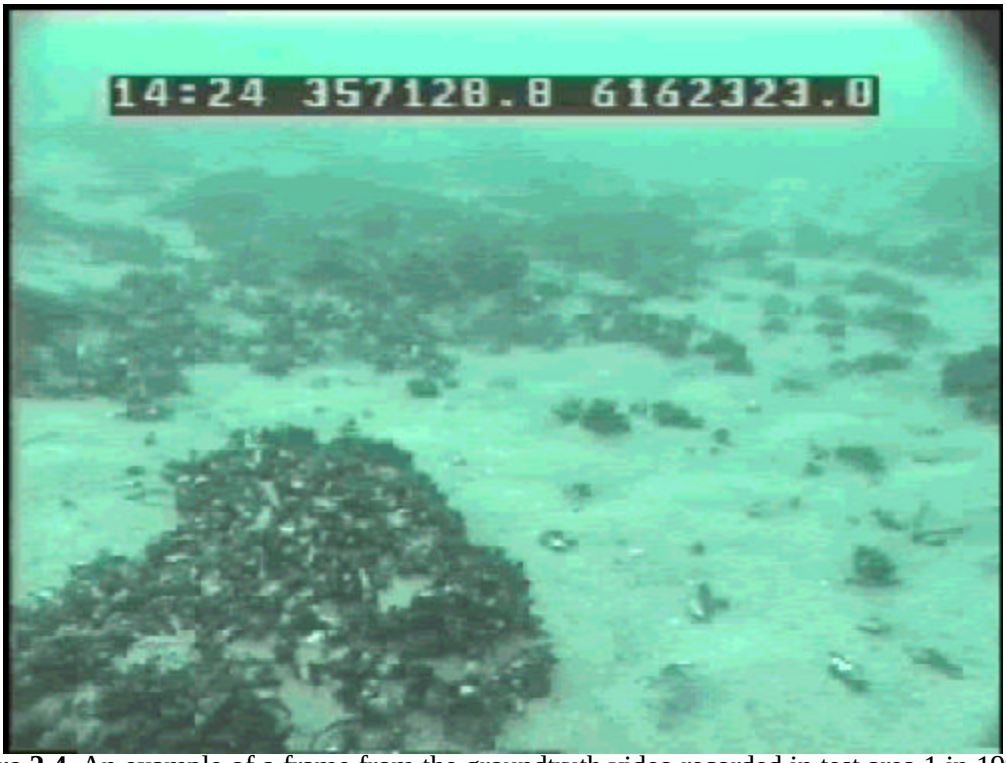

Figure 2.4 An example of a frame from the groundtruth video recorded in test area 1 in 1996.

Apart from videos, series of sea floor photos were taken at fixed stations by means of a photo-sampler. The photos cover approximately 2 m² at the sea floor.

Regarding covariates and *in situ* samples the variables listed in Table 2.5 were recorded.

Table 2.5 Exogenous and supplementary variables.

Variable	**Measurement method**
Water depth	Depth was recorded continuously from the boat.
Temperature	Profiles were measured daily in the footprint area and twice a day in the test area under investigation.
Salinity	Profiles were measured daily in the footprint area and twice a day in the test area under investigation.
Chlorophyll	Water samples were taken at one metre intervals in the footprint area and at three depths in the area under investigation.
Seston	Water samples were taken in one metre intervals in the footprint area and at three depths in the area under investigation.
Transparency	Transparency was measured daily in the footprint area and twice a day in the test area under investigation
Sea state	Sea state was measured by recordings of pitch and roll.

3 Geostatistical distribution maps for mussels

This chapter presents the results of applying geostatistics to the RoxAnn echo sounder measurements made in Øresund to prepare distribution maps for mussels. Appendix B contains an exploratory spatial data analysis illuminating some of the characteristics of the datasets. Section 3.1 gives a short introduction to geostatistics and discusses the measures of spatial continuity and models pertaining to these, and the usage of the models in spatial interpolation, so-called kriging. Methods for transforming measured data into interpreted thematic maps are discussed in section 3.2 based on discriminant analysis of the measurements feature space. Section 3.3 reports on the resulting distribution maps prepared by combining the kriged maps of measured data with the classified regions in feature space derived in section 3.2. Section 3.4 gives a heuristic approach to the use of the distribution maps for change detection, section 3.5 compares the distribution maps with groundtruth data, and section 3.6 contains a summary.

3.1 Semivariograms and kriging

3.1.1 Introduction to the theory of geostatistics

Good introductions to geostatistics are given in Isaaks & Srivastava (1989) and Cressie (1991), on which the following rely even though parts of the notation is adopted from Nielsen (1996) and Rathbun (1998). Although basic knowledge of geostatistics is assumed, this short introduction has been included to allow recapitulation of basic elements.

The term *Geostatistics* comprises methods for dealing with small- and large-scale variations of spatial variables recorded on a continuous index set D (D for domain). This data type is opposed to lattice data living on a discrete 2D (or 3D) grid and having pixel images as their common interpretation in 2D. However, geostatistics is frequently used to deal with lattice data too. The index set D is normally a subset of the Euclidian spaces $\mathbf{R}^2$ or $\mathbf{R}^3$. The random variables studied in geostatistics can be seen as extensions of time series variables, for which one dimension (time) is usually assumed and a random variable Y (without an underlying domain) is generalised to the random function Y(t), which is identified with a stochastic process; the time domain D can be assumed either discrete or continuous. Spatial variables, which are sometimes called regionalised variables (Journel & Huijbregts, 1978), are alike time series variables except for having more dimensions filled into the domain space, and for having symmetrical dimensions, i.e. you can go to the left and to the right in space, but not backwards in time.

As much of geostatistics originated through studies of subsets of $\mathbf{R}^2$ the spatial variable is termed Z thus leaving y free to denote a coordinate identifier rather than a realisation of a random variable Y. The elements in D, i.e. the locations in the region studied, are termed s (vectors and matrices are identified by context, not by use of bold types) for s = (x, y)'.

Some definitions are in place:

Definitions D1-D9.

The set of random variables $Z = \{Z(s) \mid s \in D\}$ defines a *random field* $Z: D \rightarrow \mathbf{R}$. (D1)

$Z(s)$ has the *mean* value $\mu(s) = E[Z(s)]$. (D2)

$Z(s)$ has the *covariance* $\text{cov}\{Z(s),Z(s+h)\} = C(s,h)$, where $h = (h_x, h_y)'$ is a spatial lag vector. (D3)

$Z(s)$ has the *variogram* $\text{var}\{Z(s+h)-Z(s)\} = 2\gamma(s,h)$. (D4)
The function $\gamma(s,h)$ is called the *semivariogram.*

$Z(s)$ is *first-order stationary* if $\mu(s) = \mu$ is constant over D. (D5)

$Z(s)$ is *second-order stationary* if $Z(s)$ is first-order stationary and $C(s,h) = C(h)$ is constant over D. (D6)

$Z(s)$ is said to be *intrinsically stationary* if $2\gamma(s,h) = 2\gamma(h)$ is constant over D. (D7)

$C(h)$ or $2\gamma(h)$ is said to be *isotropic* if $C(h) = C(||h||)$ or $2\gamma(h) = 2\gamma(||h||)$. (D8)

$Z(\cdot)$ is a *Gaussian* random field if $\{Z(s_j) \mid j=1,...,k\}$ is jointly Gaussian distributed for all finite collections of locations $\{s_j \mid j=1,...,k\}$. (D9)

To emphasize the randomness of the random field some authors write the definition as

$$Z = \{ Z(s;\theta) \mid s \in D, \theta \in \Omega)$$

where Ω is an element of a probability space definition given by a triplet (Ω,T,P), T being a topological space of open sets in Ω and P a probability measure defined on T.

The term *random field* is not a unique identifier; other terms applied in presentations of geostatistics are *regionalised variable* (Journel & Huijbregts, 1978), *random function* (Isaaks & Srivastava, 1989; Cressie, 1991; Deutsch & Journel, 1998) and *stochastic process* (Cressie, 1991). In this thesis, *random field* or *spatial variable* is used to explicitly indicate the canonical 2-dimensional nature of the domain D.

The random field is typically denoted by Z or $Z(\cdot)$ rather than $Z(s;\theta)$, leaving $Z(s)$ to denote the random variable at a particular location s. A realisation, i.e. a particular outcome, of the random variable $Z(s)$ is termed $z(s)$. A thorough introduction to random fields is given in Isaaks & Srivastava (1989), where a random field is defined as a set of random variables that have some spatial locations and whose dependence on each other is specified by some probabilistic mechanism (p. 218).

As can be seen from the definitions the basic statistical dichotomy of signal-noise or smooth-rough (Tukey, 1977), cf. section 1.2.2, applies equally well here, using

$$Z(s) = \mu(s) + e(s)$$

to separate large-scale variation $\mu(s)$ and small-scale variation $e(s)$. The mean function $\mu(\cdot)$ can be either deterministic or contain stochastic components and is characterised by the first-order moments. The rough component, $e(\cdot)$, is a zero-mean random field being partially characterised by the second-order moments using, e.g. the covariance $C(s,h)$. Hence, the definitions of first- and second-order stationarity are straightforward, and assumption of these properties are usually stipulated *a priori* to allow a parsimonious description of spatial variability / spatial continuity.

Intrinsic stationarity (D7) defined in the context of the variogram $2\gamma(s,h)$ is a more general concept than second-order stationarity (D6) defined for the covariance $C(s,h)$, as it concerns the increments $Z(s+h)-Z(s)$ only not assuming first-order stationarity of $Z(s)$, i.e.

$$\text{First-order stationarity RFs} \supset \text{Second-order stationary RFs} \subset \text{Intrinsically stationary RFs.}$$

Alternative approaches avoiding *a priori* assumptions of second-order stationarity or intrinsic stationarity include a data-driven attempt to construct a warped metric space in which second-order stationarity can be assumed (Sampson & Guttorp, 1992; Guttorp, Meiring & Sampson, 1994). Given empirical correlation estimates between observation sites, multidimensional scaling was used to transform geographical coordinates into a space where distances correspond to spatial dispersion. The authors then proceed to calculate semivariograms for the transformed locations in the warped space in a traditional fashion.

The lag vectors h are normally embedded in a Euclidian metric space over D. There are cases where a more generalised manifold embedding of D is relevant, allowing other kinds of curved or buckled metric spaces to be induced on the domain D. For example, when geostatistics is applied to variables measured in waters of rivers and estuaries of non-convex shape a natural replacement for Euclidian lag distances would be distances measured in the gauge coordinate system induced by the field of water currents. Thus, the distance measure would take account of bends and curves in the shape of the water body. An approach akin to this was introduced in Rathbun (1998) using a so-called water distance being the shortest distance that may be traversed entirely over water, i.e. the minimum geodesic distance.

Assumptions of Gaussianity of $Z(s)$ are not necessary for the geostatistics machinery, but as in many other fields of statistics estimation and prediction theory is considerably simpler if Gaussianity is assumed. If $Z(s)$ is Gaussian then the random field $Z(\cdot)$ is fully characterised by the first- and second-order moments, i.e. $\mu(s)$ and $C(s,h)$, which is a further simplification.

Stationarity and ergodicity

A random field is not *per se* a very stable or predictable entity. Hence, various assumptions about the random field $Z(\cdot)$ are normally added to the assumptions of first- and second-order stationarity to allow for straightforward interpretation of estimates and predictions. In addition often only one sample $z = (z(s_1), ..., z(s_n))$ is available necessitating the assumption of some regularity conditions. A strong and general assumption to add is that of *ergodicity*.

In a popular phrasing, an ergodic function can go anywhere anytime: It can go anywhere in phase space, i.e. it is not confined to a subspace, and it can go there anytime meaning that it is not bound by periodicity constraints. The term "ergodic" stems from a Greek word denoting wandering. Cressie (1991) states that (p. 53): "*... simply put, this property allows expectations over the W space to be estimated by spatial averages.*" In other words, ergodicity ensures that spatial averages over one realisation approximate a series of parallel spatial averages obtained from many realisations. Where second-order stationarity is a regularity assumption regarding the random field in question, the ergodicity adds regularity assumptions regarding the estimates and predictions that can be made for random fields.

In practice a less ambitious assumption is usually made (often implicitly), namely that of *weak ergodicity* (Cressie, 1991) guaranteeing that the sample mean and covariances converge to their population counterparts. Citing Cressie (1991) again (p. 57): "*Ergodicity is an assumption made to allow inference to proceed for a series of non-independent observations. It might only be verifiable in the sense that one fails to reject it. This should not be too worrisome because scientific discovery generally proceeds in this way.*" The assumptions of stationarity and weak ergodicity are properties of the random field model, not of the underlying spatial distribution. Deutsch & Journel (1998) are suggesting to formulate this as a stationarity *decision* rather than a stationarity assumption, to clear up the matter.

Support

In geostatistics *support* denotes the basic area (or volume) cell represented by a measured value. As an example, the opening angle of the echo sounder used to measure E1 and E2 was 3.5°, yielding the received first echo and hence E1 to represent an elemental circular sea floor area of $\pi(d \cdot \tan 3.5°)^2$ at the water depth d. This so-called footprint area is approximately 0.29 m² (~ 0.542^2 m²) at 5 metres and 1.18 m² (~ 1.08^2 m²) at 10 metres depths. For E2 the signal reverberations travel a distance of 3d to the sea bed (Heald & Pace, 1996), and hence the E2 footprint covers an area of $\pi(3d \cdot \tan 3.5°)^2$, corresponding to 1.63^2 m² and 3.25^2 m² at 5 and 10 metres depth, respectively. Thus, the footprint area size of E2, being a ratio 3^2 larger than that of E1, shows that E2 is a more aggregated measure. The maximum number of mussels in an echo sounder footprint is $[\pi \cdot d^2 \cdot \tan(3.5°)^2/(0.05\text{m})^2]$, e.g. approx. 120 and 1000 mussels in the E1 and E2 footprint at 5 metres, respectively. Various methods exist for considering change-of-support and including support geometry parameters in the expressions for variograms, etc. (Journel & Huijbregts, 1978).

Measures of spatial continuity

The natural measure of the small-scale variation or local correlation of e(s) is the spatial autocovariance cov(Z(s),Z(s+h)) equal to C(h) under assumptions of second-order stationarity. Two other functions apply for the same purpose, namely the correlogram, $\rho(h)$, and the variogram, $2\gamma(h)$ (Isaaks & Srivastava, 1989). These three measures of spatial continuity are related as follows (Isaaks & Srivastava 1989; Rossi *et al.*, 1992; Nielsen, 1996):

$$2\gamma(h) = 2(C(0) - C(h))$$

$$\rho(h) = C(h)/C(0) = 1 - \gamma(h)/C(0),$$

where $C(0) = \sigma^2$ is the variance of the random variable Z(s) and $\gamma(h)$ is the semivariogram. Most applied geostatistics is based on the use of the semivariogram rather than the autocovariance. There are several reasons for this. Firstly, the semivariogram $\gamma(h)$ needs an assumption of intrinsic stationarity only, whereas the covariance C(h) needs an assumption of second-order stationarity to apply. The class of second-order processes is a strict subset of the class of intrinsic stationary processes, hence the semivariogram applies to a larger group of processes. An example of a process that is intrinsically stationary but not second-order stationary, i.e. where $\gamma(\cdot)$ is defined but $C(\cdot)$ is not, is the 2-dimensional isotropic Brownian motion (Cressie, 1991). If $\{W(s) \mid s \in \mathbf{R}^2\}$ is such a process, then

$$\text{var}(W(s+h)-W(s)) = ||h||, \text{ for } h \in \mathbf{R}^2,$$

i.e. a function of h only, and thus $\gamma(\cdot)$ is defined. However,

$$\text{cov}(W(s+h),W(s)) = (1/2) \cdot (||s+h|| + ||s|| - ||h||), h \in \mathbf{R}^2$$

which is not a function of h. Although this difference of properties is a very basic one it is rather exotic, and there are other and more practical reasons for preferring to use semivariograms compared to autocovariances. For example, it can be shown that the semivariogram can be estimated more reliably than the covariance (Cressie, 1991).

Three basic properties, called the *range of influence*, the *sill*, and the *nugget effect* applies to variograms. They can be defined as follows (Isaaks & Srivastava, 1989):

Range (of influence)
As the separation distance ||h|| between pairs of locations increases, the corresponding variogram values will also generally increase. Eventually, however, an increase in the separation distance no longer causes a corresponding increase in the average squared difference between pairs of values and the variogram reaches a plateau. The distance at which the variogram reaches this plateau is called the *range,* cf. Figure 3.1.

Sill
The *sill* is the plateau that the variogram reaches at the range.

Nugget effect
Though the value of the variogram for h = (0, 0)' is strictly 0, several factors, such as sampling error and short scale variability, may cause sample values separated by extremely small distances to be quite dissimilar. This causes a discontinuity at the origin of the variogram. The vertical jump from the value of 0 at the origin to the value of the variogram at extremely small separation distances is called the *nugget effect.* The ratio of the nugget effect to the sill is often referred to as the *relative nugget effect* and is usually quoted in percentages.

Other important concepts like anisotropy, nested structures, and conditional negative-definiteness (Isaaks & Srivastava, 1989) apply also, but the details are skipped here. For simplicity, isotropy will normally be assumed in the following, i.e. that $\gamma(h) = \gamma(||h||)$.

For irregular data the variogram can be estimated by

$$2\gamma^*(h) = 1/N(h,\varepsilon) \Sigma_{(i,j)\in N(h,\varepsilon)} (z(s_i) - z(s_j))^2$$

where $N(h,\varepsilon)$ can be identified without confusion with the set of point pairs

$$N(h,\varepsilon) = \{ (s_i, s_j) \mid s_i - s_j \in O_\varepsilon(h) \}$$

as well as with the number of elements herein; $O_\varepsilon(h)$ is a tolerance neighbourhood of h given by the tolerance vector ε. $O_\varepsilon(h)$ is normally specified by tolerances for the polar representation of h, i.e. by angular tolerances combined with a magnitude tolerance.

To be used in a straightforward manner in the subsequent spatial interpolation (kriging) it is preferred to substitute a model, i.e. an analytical expression, for the sample variogram in the applications. This enables easy calculation of $\gamma(h)$ for any h compared to possibly awkward interpolation of values in the sample variogram.

Three of the mainstream semivariogram models are given in Table 3.1 and depicted in their standardised form in Figure 3.1. For the exponential models and Gaussian models the sill is reached asymptotically, hence the range R is operationally defined as the value of ||h|| where 95% of the sill is reached. This was first proposed by Donald Myers (Myers *et al.*, 1982) and is now common practice.

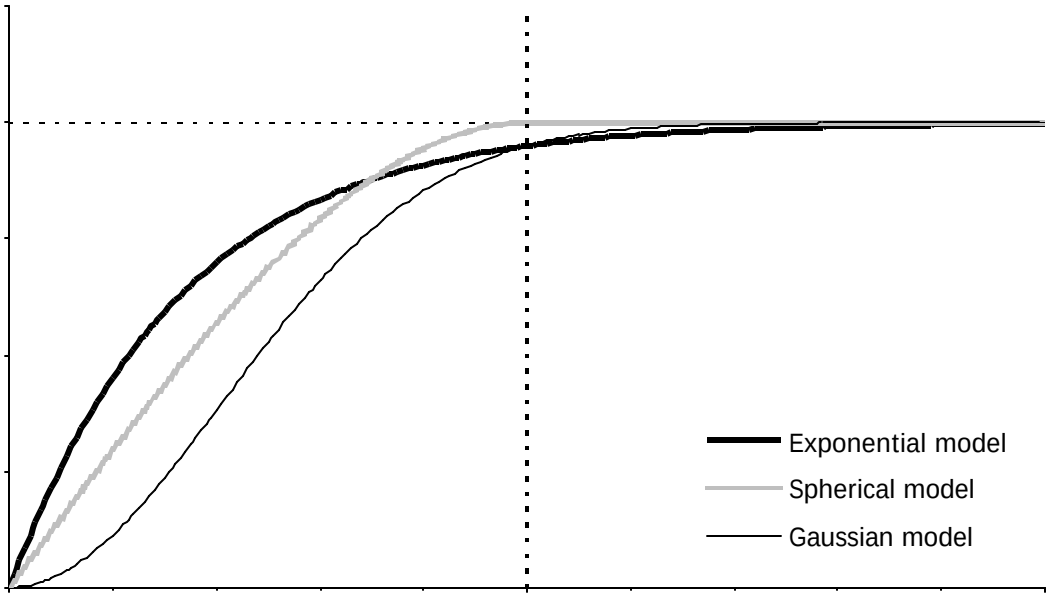

Figure 3.1 An illustration of three semivariogram models with identical values of sill and range. The dotted lines indicate the range and the sill.

Table 3.1 Standardised and generic expressions for selected semivariogram models. The full models including offset (nugget), C_0, and scale (sill if nugget is zero), C_1, are $\gamma(h) = C_o + C_1 \cdot \gamma_s(h)$. The generic expressions $\gamma_g(h')$ are obtained by using α in $h' = \alpha h$ to adjust $\gamma_s(h)$ for the range, R.

Model	Standardised expressions, $\gamma_s(h)$	Generic expressions
Exponential model	$\gamma_s(h) = 1\text{-}\exp(-3h/R)$	$\gamma_g(h) = 1\text{-}e^{-h}$
Spherical model	$\gamma_s(h) = 1.5(h/R) - 0.5(h/R)^3$, if $h \le R$ $\gamma_s(h) = 1$, if $h > R$	$\gamma_g(h) = 3/2 \cdot (h - h^3/3)$
Gaussian model	$\gamma_s(h) = 1\text{-}\exp(-3h^2/R^2)$	$\gamma_g(h) = 1\text{-}e^{-h^2}$

The Gaussian variogram model has a horizontal derivative at the origin, i.e. $\partial\gamma/\partial h(0)=0$, and thus assumes a high degree of smoothness of the spatial continuity. All sample variograms (and other measures of spatial continuity) reported here were calculated using the public domain library GSLIB. Semivariogram models were estimated by use of PROC NLIN in SAS.

Kriging

Spatial interpolation methods devise ways of estimating the expectation $E(Z(s_0))$ of the random field $Z(\cdot)$ at a given location s_0, on the basis of measurements $z(s_1)$, $z(s_2)$, ..., $z(s_n)$. Ordinary kriging is the preferred geostatistical method for linear spatial interpolation, and the *ordinary kriging estimator* $Z^*(s_0)$ for $E(Z(s_0))$ is defined as a linear combination of the data:

$$Z^*(s_0) = E^*(Z(s_0)) = \langle w,z \rangle = \Sigma_i \, w_i \cdot z(s_i) \qquad (3.1)$$

where z is the observation vector, $\langle \cdot,\cdot \rangle$ is the inner product, and w is the vector of weights $w = (w_1, w_2, ..., w_n)'$ subject to the ordinary kriging optimality criteria. Thus, w is found as:

$$\arg\min_{w} V(Z^*(s_0)-Z(s_0)) \tag{3.2}$$

i.e. the weights that minimise the mean squared error of $Z^*(s)$, subject to an unbiasedness constraint

$$E(Z^*(s_0)-Z(s_0)) = 0 \tag{3.3}$$

which amounts to the constraint

$$\langle w,1\rangle = \Sigma_i w_i = 1 \tag{3.4}$$

in case first-order stationarity is assumed, i.e. $\mu(s) = \mu$. If the constraint (3.4) is not applied the interpolation method is called *simple kriging*, as opposed to *ordinary kriging*.

It is an important point to make that the mean squared error of the estimate $Z^*(s_0)$ depends on the structure of the spatial continuity and the geometry of the data points only; *it does not depend on the data values*. This property is a consequence of assumptions of either intrinsic or second order stationarity. Based on axiomatic definitions the kriging variance $\sigma^2_{OK} = V(Z^*(s_0)-Z(s_0))$ can be elaborated as follows:

$$\sigma^2_{OK} = V(Z^*(s_0)-Z(s_0)) \tag{3.5}$$

$$= V(Z^*(s_0)) + V(Z(s_0)) - 2\,\mathrm{cov}(Z^*(s_0),Z(s_0))$$

where $V(Z(s_0)) = \sigma^2$ is the variance of the random variable $Z(s_0)$ assumed to be constant for all s_0, and

$$V(Z^*(s_0)) = \mathrm{var}(\Sigma_i w_i z(s_i)) = \Sigma_i\Sigma_j w_i w_j \,\mathrm{cov}(z(s_i),z(s_j)) \tag{3.6}$$

$$= \Sigma_i\Sigma_j w_i w_j C(s_i-s_j) = \Sigma_i\Sigma_j w_i w_j C(h_{ij}), \tag{3.7}$$

$$2\,\mathrm{cov}(Z^*(s_0),Z(s_0)) = 2\,\Sigma_i w_i \,\mathrm{cov}(z(s_i),Z(s_0)) \tag{3.8}$$

$$= 2\,\Sigma_i w_i C(s_i-s_0)) = 2\,\Sigma_i w_i C(h_{i0}) \tag{3.9}$$

where the steps from (3.6) to (3.7) and from (3.8) to (3.9) are made on basis of the stationarity assumption yielding $C(s_i,h_{ij}) = C(h_{ij})$, hence this is where the data values vanishes from the kriging variance. Thus, the kriging variances provide a comparison of alternative geometric data configurations, but they are usually not measures of local estimation accuracy (Deutsch & Journel, 1998). In other words, the kriging variance $\sigma^2_{OK}(s_0)$ is a function of the local accuracy and can be used to minimise the mean squared error (~local accuracy), even though it is not itself a measure of the local estimation accuracy (as data values have vanished from the expressions).

The expressions in (3.7) and (3.9) can be inserted in (3.5) yielding

$$\sigma^2_{OK} = V(Z^*(s_0)-Z(s_0)) \tag{3.10}$$

$$= \sigma^2 + \Sigma_i\Sigma_j w_i w_j C(h_{ij}) - 2\,\Sigma_i w_i C(h_{i0}). \tag{3.11}$$

In practice the minimisation of σ^2_{OK} under the unbiasedness constraint $\langle w,1\rangle = 1$ is done by including the constraint in the object function using a Lagrange multiplier for $g(w) = \langle w,1\rangle-1$, i.e. $w^* = (w,\lambda)$ is determined as

$$\arg\min_{w^*} [\sigma^2_{OK} - 2\lambda g(w)]$$

The minimising argument w^* is determined by solving the n+1 equations obtained by equating first order partial derivatives of the object function to zero. The kriging equations derived in the fashion illustrated above can be developed using the semivariogram $\gamma(h)$ instead of the covariance C(h), see e.g. Isaaks & Srivastava (1989) for a thorough presentation.

Using kriging for mapping of a 2D region, a series of values $Z^*(s_k)$ are estimated at fixed locations s_k on a grid, G, in the region. Thus, the global kriging result, Z^*, can be written as

$$Z^* = \{ Z(s_k) \mid s_k \in G, k=1..m \}, \qquad (3.12)$$

where Z^* has been calculated by estimating minimising weights w^k locally at all $s_k \in G$. As such, the mapping inherent in the production of Z^* is not constrained to or optimised with respect to any global optimality criteria, it is solely produced by optimising *local* accuracy (unbiasedness and minimum kriging variance). This is a point we will return to in chapter 5. It is in regard to the optimal local accuracy that ordinary kriging is said to provide an optimal linear spatial predictor, known as a BLUE estimator, BLUE for "best linear unbiased estimator".

Other methods of spatial interpolation include (but are not restricted to) Delaunay triangulation, inverse distance weighting, and splines. Delaunay triangulation and inverse distance weighting is described in Isaaks & Srivastava (1989), whereas Laslett (1994) contains an interesting comparison of kriging and splines. However, none of these methods contain any concerns about variance minimisation, wherefore they are less relevant in a statistical setting, although their performances in many circumstances are comparable to ordinary kriging.

Ordinary kriging is extendable in various directions, comprising such extensions as e.g.:

- Indicator kriging, where data values z in $Z^*(s_0) = \langle w,z \rangle$ are replaced by threshold indicators $I[z>c]$ to yield the estimator $Z^*(s_0) = \langle w,I[z>c] \rangle$;
- co-kriging, i.e. simultaneous kriging of multivariate spatial variables using additional cross-covariance models;
- disjunctive kriging, where $Z^*(s_0) = \langle w,z \rangle$ is replaced by $Z^*(s_0) = \langle f(z),1 \rangle$ using the vector f of (possibly different) functions f_i to be applied to the elements $z(s_i)$ in z;
- factorial kriging, which is kriging based on a model containing several stochastic components of the random field, i.e. using the model $Z(s) = Z_1(s) + ... + Z_k(s)$ rather than $Z(s) = \mu(s)+e(s)$, and
- universal kriging, employing a (linear) model of the mean field μ, e.g. allowing covariates to enter the kriging by a linear model $\mu(s) = \langle \beta,x(s) \rangle$.

It remains to introduce the idea of block kriging. The ordinary kriging estimator $Z^*(s_0)$ estimates the value of the random field $Z(\cdot)$ in the (Euclidian) point s_0. Often, it is desirable to estimate the mean value of a basic area element (pixel) B, e.g. a rectangle centered on s_0:

$$Z_B^*(s_0) = |B|^{-1} \int_B z^*(v)\, dv \qquad (3.13)$$

$$\approx 1/n \, \Sigma_i \, Z^*(v_i)$$

where the latter shows that the estimated block mean is normally obtained by using the average of a set of discretisation points v_i within B. Isaaks & Srivastava (1989) give the empirically based observation that $16 \sim 4 \times 4$ discretisation points will suffice in most cases to get a proper precision of the block average.

3.1.2 The practice of semivariograms and kriging

Whereas much of the geostatistical theory has been elaborated to a great extent the practice of geostatistics is still flavored by craftmanship rather than clear-cut consensus procedures. This is mirrored in the reflections of A.G. Journel in the foreword to Isaaks & Srivastava (1989):

"*Applied geostatistics, or for that matter any applied statistics, is an art in the best sense of the term and, as such, is neither completely automatable nor purely objective. In a recent experiment conducted by the U.S. Environmental Protection Agency, 12 independent reputable geostatisticians were given the same sample data set and asked to perform a straightforward block estimation. The 12 results were widely different due to widely different data analysis conclusions, variogram models, choices of kriging type, and search strategy. [...]*

It bears repeating that there is no accepted universal algorithm for determining a variogram/covariance model, whether generalised or not, that cross-validation is no guarantee that an estimation procedure will actually produce good estimates of unsampled values, that kriging need not be the most appropriate estimation method, and that the most consequential decisions of any geostatistical study are taken early in the exploratory data analysis phase."

Regarding the estimation of spatial continuity it is commonly recommended (e.g. Deutsch & Journel, 1998) that several measures be calculated and compared to assess the stability of the results. An example is given below. For the particular irregular data type studied in this thesis, posted as it is on a continuous index set in a netshaped pattern, the choice of search strategy is important. Using a simple search strategy in the interpolation the closest points are selected, and will thus lead to a tiling of the studied area reflected in both the kriging results and in the kriging variances, cf. Figure 3.2. Thus, a quadrant search (or even an octant search) should be preferred for the datasets in question here.

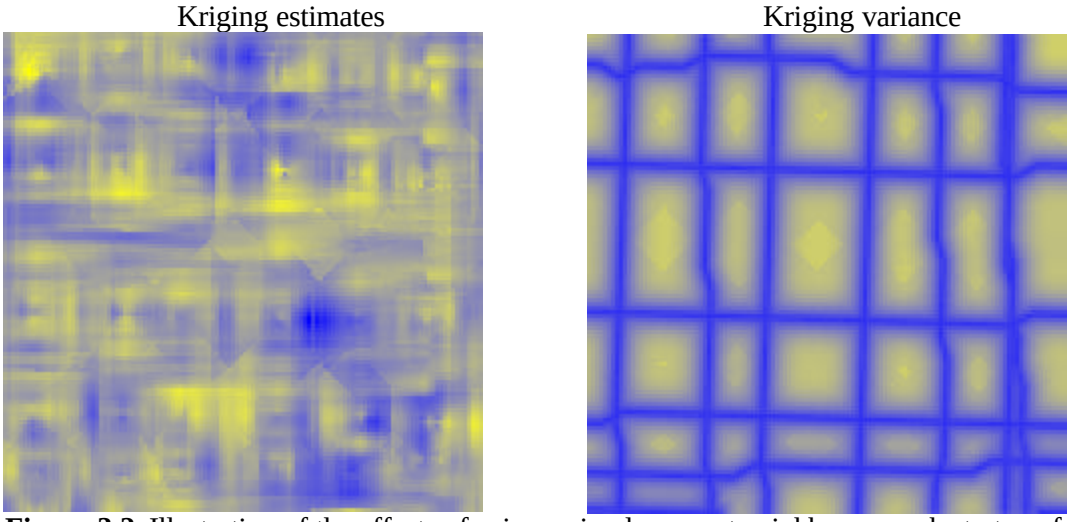

Figure 3.2 Illustration of the effects of using a simple nearest neighbour search strategy for the netshaped data type based on sets of orthogonal transect lines used in the present studies. The striping and discontinuities are clearly visible.

The geostatistical data analysis given herein is based on the widely used software package GSLIB (Deutsch & Journel, 1998). A review of the GSLIB package and handbook is given in Myers (1999).

3.1.3 Semivariograms for the bottom type areas

Semivariograms for the observed values of log E1 and log E2 have been calculated for the bottom type areas by use of the program GAMV from the GSLIB collection, version 2.0, for DOS. Lag sizes of 1 metres were chosen on the basis of the descriptions in section 3.1, as a compromise between the average lag distances found in 1996 and 1997. The SAS procedure PROC NLIN was used to estimate the coefficients of the exponential semivariogram models based on sample semivariogram data for $||h|| < 30$ metres. The estimated coefficients of the variograms are given in Tables 3.2 and 3.3, and the estimated variogram models are illustrated in Figures 3.3 - 3.6.

Table 3.2 Estimated coefficients for exponential variogram models, bottom type areas 1996.

	Mussels, logE1	Mussels, logE2	Sand, logE1	Sand, logE2
c0	0.00444	0.00258	0.00657	0.01170
c1	0.01051	0.01399	0.01541	0.02243
R	9.35	10.01	12.62	16.32
Sill, c0+c1	0.01495	0.01657	0.02198	0.03413
$s_o = \sqrt{c0}$	0.066	0.051	0.081	0.108
Nugget, c0/Sill	29.7%	15.5%	29.9%	34.3%

Table 3.3 Estimated coefficients for exponential variogram models, bottom type areas 1997.

	Mussels, logE1	Mussels, logE2	Sand, logE1	Sand, logE2
c0	0.00180	0.00093	0.00575	0.00288
c1	0.03631	0.02031	0.01452	0.03619
R	8.75	11.64	8.95	11.68
Sill, c0+c1	0.03811	0.02124	0.02027	0.03907
$s_o = \sqrt{c0}$	0.042	0.031	0.076	0.054
Nugget, c0/Sill	4.7%	4.4%	28.4%	7.4%

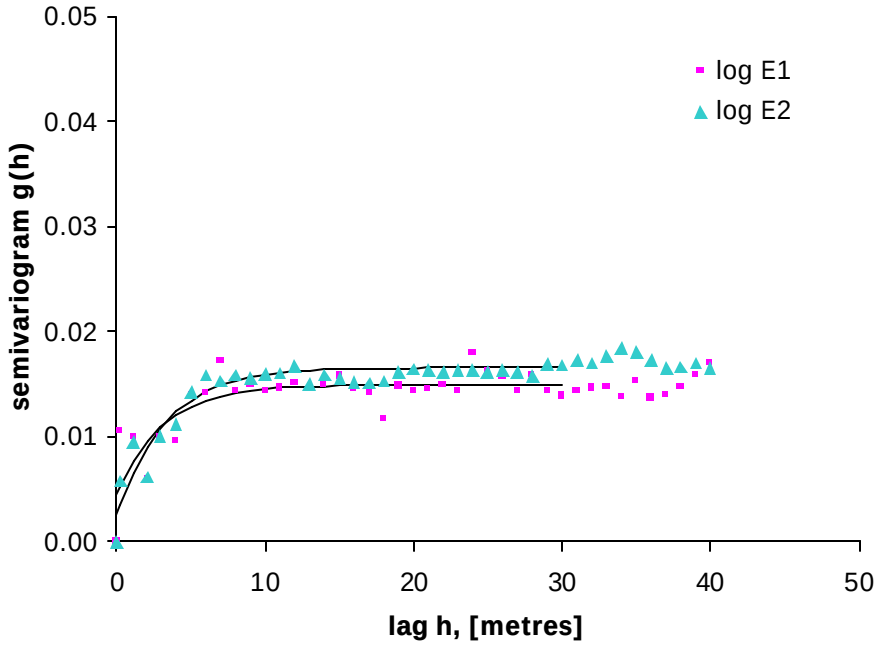

Figure 3.3 Sample omni-directional semivariograms and estimated exponential semivariogram models for the mussel bottom type area, 1996.

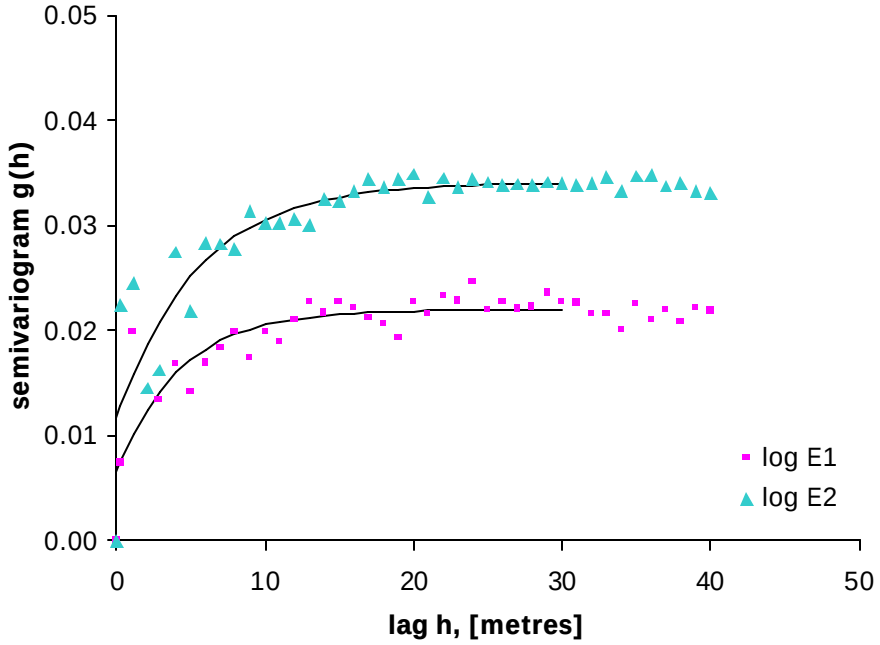

Figure 3.4 Sample omni-directional semivariograms and estimated exponential semivariogram models for the sand bottom type area, 1996.

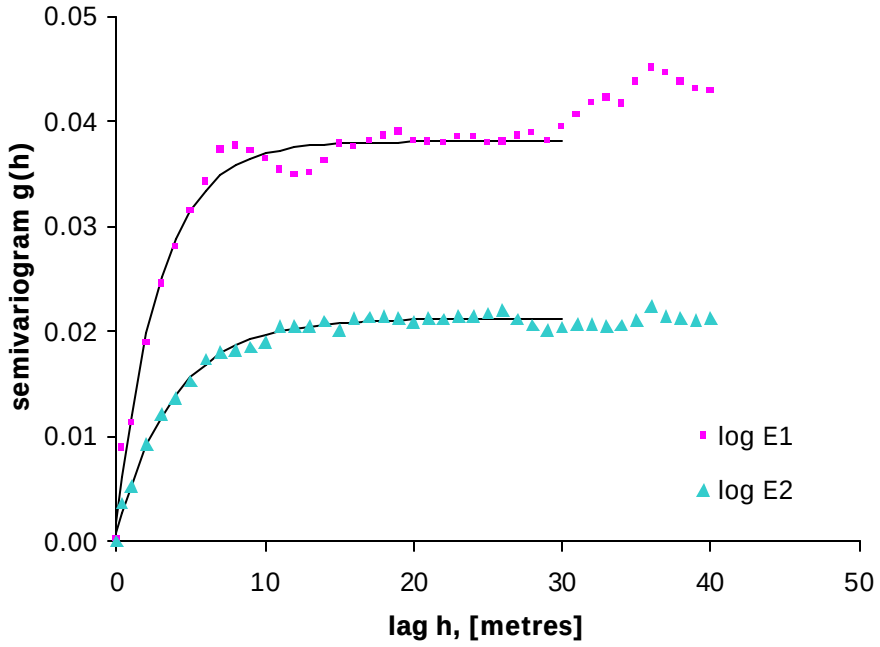

Figure 3.5 Sample omni-directional semivariograms and estimated exponential semivariogram models for the mussel bottom type area, 1997.

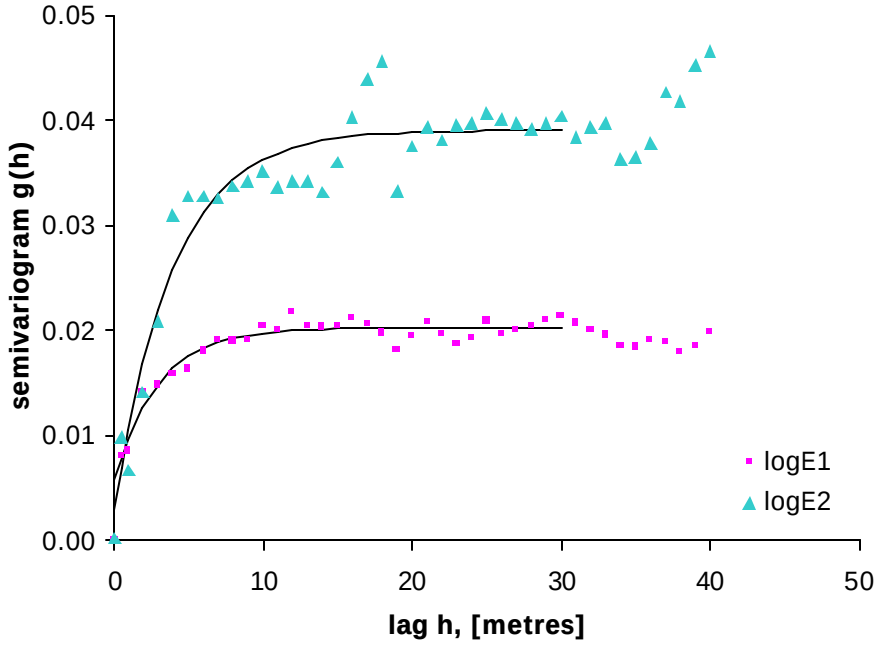

Figure 3.6 Sample omni-directional semivariograms and estimated exponential semivariogram models for the sand bottom type area, 1997.

It was found that:

- Nugget effects compare satisfactorily with the micro-scale variances found in the study of background variability, cf. tables B.1 through B.4 in appendix B.
- The sill of logE1 in the sand area is about unchanged, and the sills of logE2 in both areas are also having approx. stable levels, whereas the sill has increased markedly for logE1 in the mussel area.
- The hole effect present in the sample semivariogram for logE1 in the mussel area in 1997 is supposed to be an effect of the sampling grid used, having a transect interspacing at 10 metres, where the hole effect is seen. The low average separation distance in 1997 is probably a prerequisite for observing such a hole effect.
- The range estimates are rather stable showing no substantial deviations from 1996 to 1997.

The results are consistent as regards the shape of the spatial continuity function, i.e. the semivariogram. Therefore, as an overall assessment, these semivariogram results are found to be consistent taking the differences in the employed sampling grids into account as well as the drift of the voltage signals between 1996 and 1997, cf. appendix B.

As suggested in Isaaks & Srivastava (1989) and Deutsch & Journel (1998) we calculated alternative measures of spatial continuity to discern possible variations and the validity of using the semivariograms as a basis for further studies. The correlogram and the semimadogram were chosen as candidates. Other options include the covariance (equivalent to the correlogram) and the indicator semivariogram, the relative semivariogram and the pairwise relative semivariograms (Deutsch & Journel, 1998), but these are not valid here working on logarithms, and indicator variograms. The semimadogram is a robust estimator using the mean absolute difference (m.a.d.) of the pairs of values in $N_\varepsilon(h)$ as a replacement of the squared difference used in the semivariogram. Other robust estimators exist, e.g. an estimator based on square roots of the absolute difference (Cressie, 1991).

For the mussel bottom area in 1997 sample semivariograms, correlograms and semimadograms were calculated, cf. Figures 3.7 - 3.10, for the NE-SW and NW-SE directions (the area is tilted by 45°) with a tolerance at ±22.5°as well as omni-directional values. Exponential models were estimated for the omni-directional sample measures using PROC NLIN in SAS for the calculated measures. The results are depicted in Table 3.4.

Table 3.4 Coefficients estimated for various measures of spatial continuity.

	measure of	Estimates			Standard deviations		
	spatial continuity	Range	Nugget	Scale	Range	Nugget	Scale
E1	semivariogram	10.45	0.0616	0.8306[1)]	0.96	0.0363	0.0364
	correlogram	19.54	0.1422	-	1.48	0.0383	-
	semimadogram	6.47	0.0166	0.0907	0.64	0.0041	0.0041
E2	semivariogram	11.58	0.0437	0.9788[1)]	0.41	0.0167	0.0168
	correlogram	10.53	0.0286	-	0.35	0.0173	-
	semimadogram	7.41	0.0117	0.0690	0.51	0.0022	0.0022
E1 vs E2	correlogram	41.19	0.8054	-	2.07	0.0064	-

[1)] The sills were standardised for the semivariograms, hence it should ideally not be necessary to estimate both C_0 and C_1, as the identity $C_0+C_1 = 1$ applies. However, data for $h < 40$ m was used having a slightly lower sill.

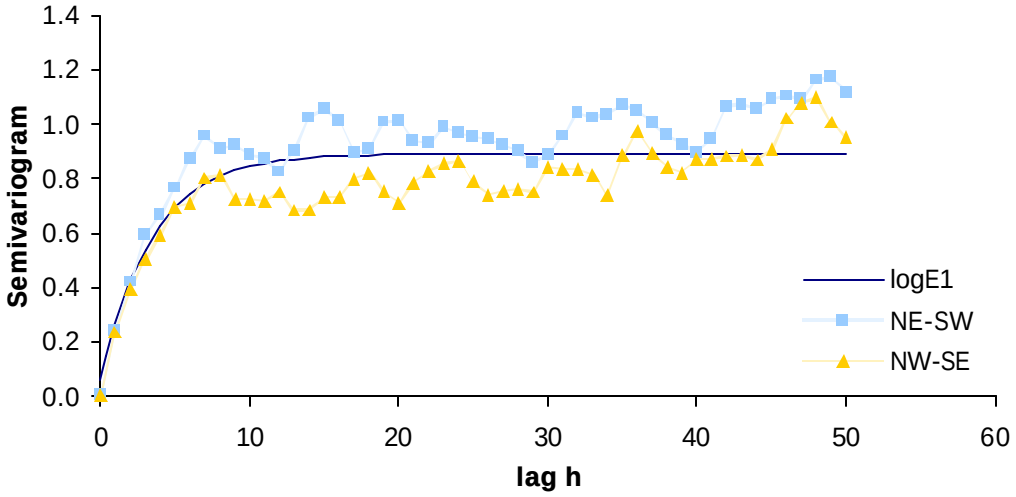

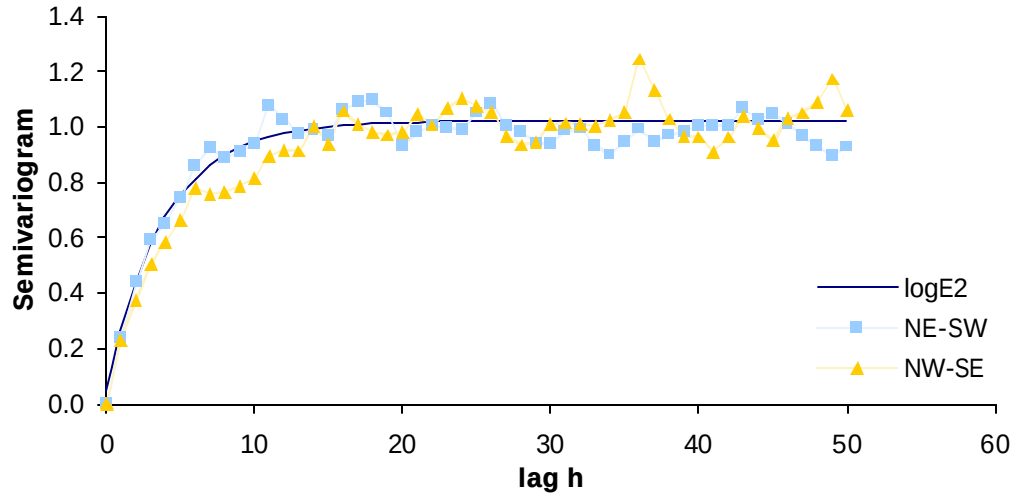

Figure 3.7 Sample northeast-southwest and northwest-southeast semivariograms and estimated exponential models for the mussel bottom type area, 1997.

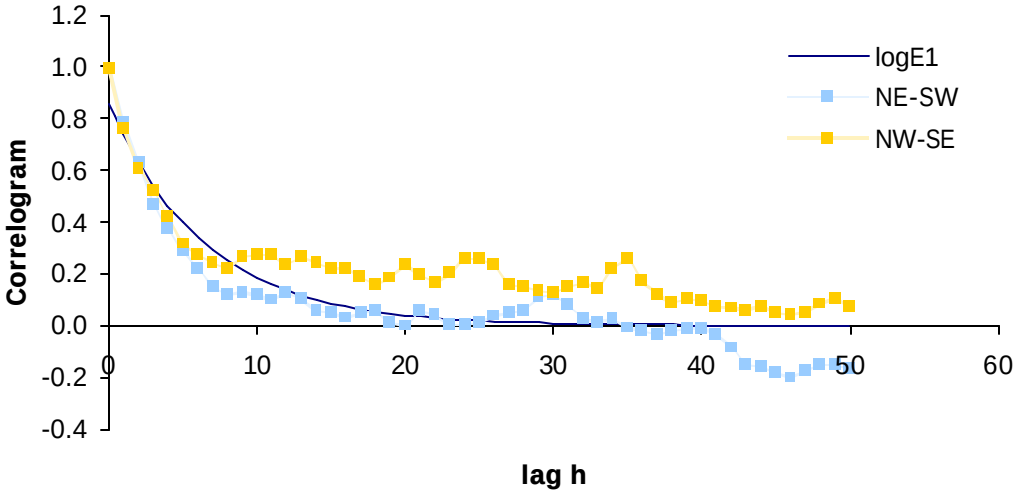

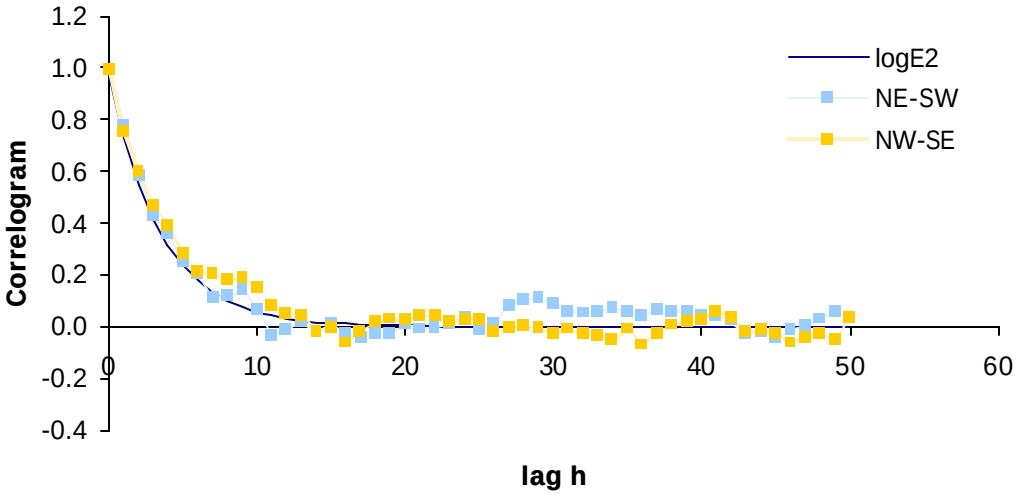

Figure 3.8 Sample northeast-southwest and northwest-southeast correlograms and estimated exponential models for the mussel bottom type area, 1997.

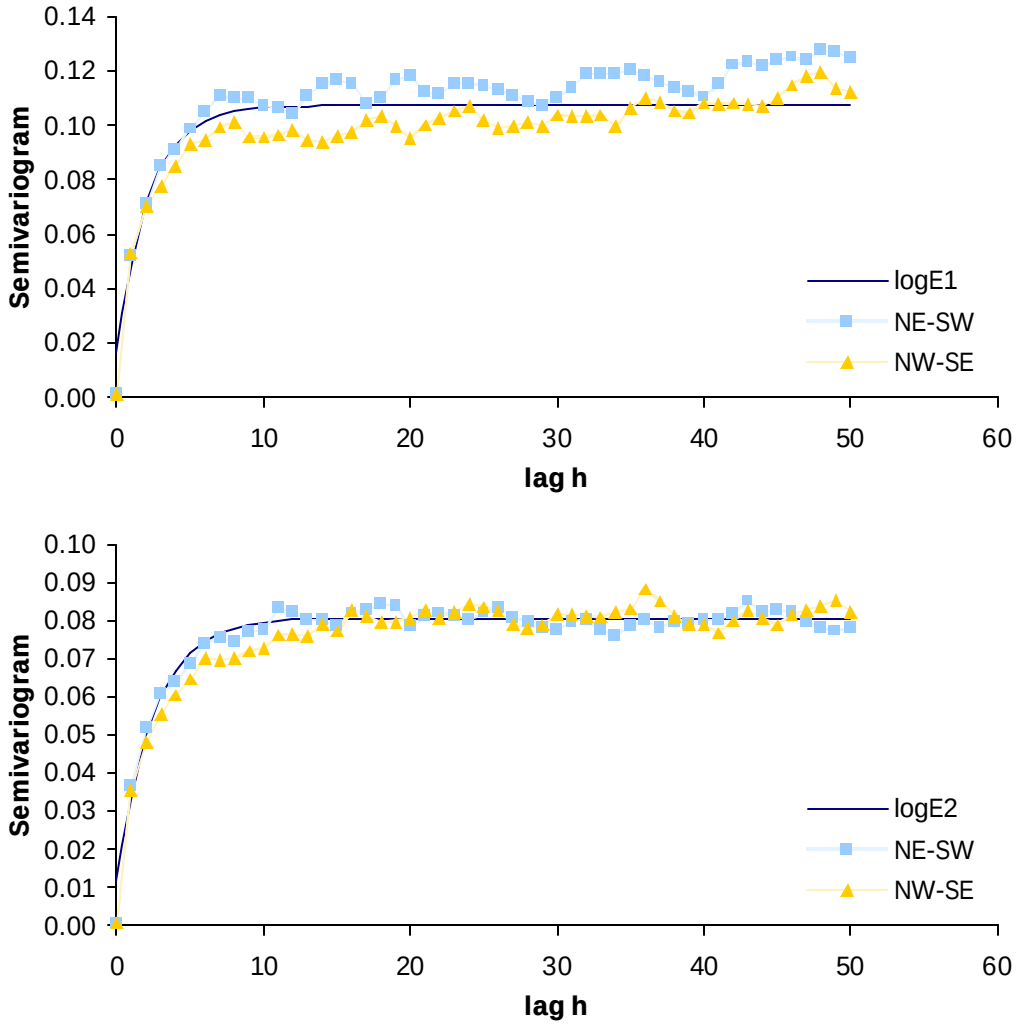

Figure 3.9 Sample northeast-southwest and northwest-southeast semimadograms and estimated exponential models for the mussel bottom type area, 1997.

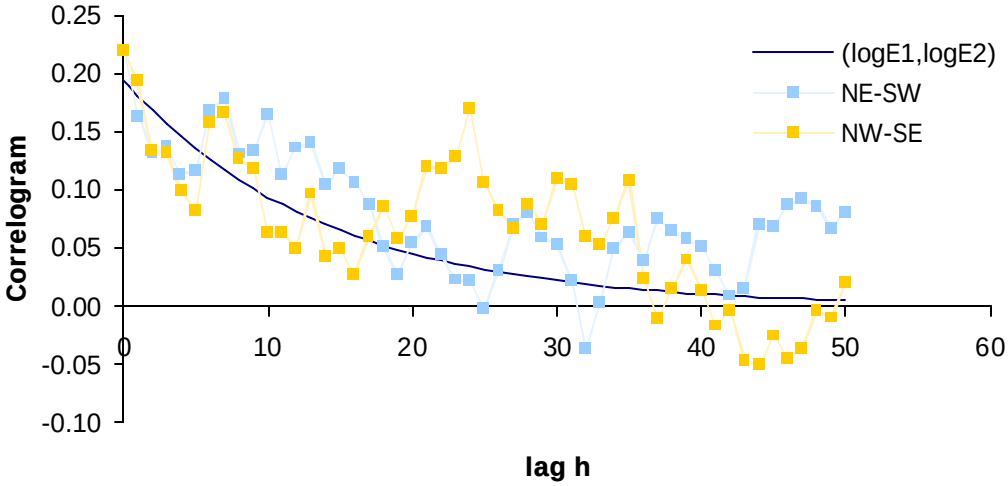

Figure 3.10 Sample northeast-southwest and northwest-southeast cross-correlograms and an estimated exponential model for the mussel bottom type area, 1997.

The ranges estimated for the semimadograms are lower than the ranges found for the semivariograms and the correlograms. However, the semivariograms were found to be in accordance with the semimadograms regarding shape, cf. Figure 3.7 and Figure 3.9, and thus the deviation of the ranges is considered inferior. In all the spatial continuity measures it is clearly visible that logE2 has a more isotropic pattern than logE1 having a slight anisotropy, which however is deemed negligible and therefore not necessary to account for in the sequel. The high range at approx. 40 metres estimated for the cross-correlogram is not surprising as the correlation coefficient $\rho(0) = 0.22$ of logE1 and logE2 is a quite low sill on the outset. Hence, the random fluctuations of the sample cross-correlogram have a substantial biasing influence on the estimation of the model.

The conclusion of the exercise is that the semivariograms provide sufficient information about spatial continuity, thus only semivariograms will be used in the sequel.

3.1.4 Semivariograms for the test areas

Sample semivariograms were calculated for the test areas using lag sizes of 5 metres, and coefficients of exponential semivariogram models were estimated, using sample semivariogram values for $h < 150$ metres. The estimates are given in Tables 3.5 and 3.6, and the estimated semivariogram models are illustrated in Figures 3.11 - 3.14.

For test area 1, 1997, the nugget effect estimates were zero, which is unrealistic. Sample semivariograms were calculated using lag sizes of 0.5 metres up to $h < 30$ metres. However, the estimation procedure (PROC NLIN) did not improve using these values, and alternative estimates of c0 were determined by the following *ad hoc* method. The nuggets have decreased markedly in test area 2 from 1996 to 1997, and, in lack of other quantitative evidence, the relative nuggets of test area 1 are assumed to have decreased by the same rates, i.e. by 0.228 (from 33.3% to 7.6%) and 0.143 (from 32.1% to 4.6%) for logE1 and logE2, respectively. Using these rates on the sills/c1 estimated for test area 1 in 1997 yields the nuggets of 1997 for test area 1 given in Table 3.6. The fit of these *ad hoc* semivariogram models to the 0.5 metres lag size sample semivariograms is depicted in Figure 3.15.

Table 3.5 Estimated coefficients for exponential variogram models, test areas 1996.

	Testarea 1, logE1	Testarea 1, logE2	Testarea 2, logE1	Testarea 2, logE2
c0	0.01114	0.00531	0.01141	0.01512
c1	0.06051	0.03617	0.02284	0.03194
R	42.06	34.90	31.91	66.19
Sill, c0+c1	0.07165	0.04148	0.03425	0.04705
$s_0 = \sqrt{c0}$	0.106	0.073	0.107	0.123
Nugget, c0/Sill	15.5%	12.8%	33.3%	32.1%

Table 3.6 Estimated coefficients for exponential variogram models, test areas 1997.

	Testarea 1, logE1	Testarea 1, logE2	Testarea 2, logE1	Testarea 2, logE2
c0	0.00400	0.00086	0.00429	0.00210
c1	0.11027	0.04707	0.05246	0.04366
R	17.03	18.53	26.36	24.40
Sill, c0+c1	0.11427	0.04793	0.05675	0.04576
$s_0 = \sqrt{c0}$	0.063	0.029	0.065	0.046
Nugget, c0/Sill	3.5%	1.8%	7.6%	4.6%

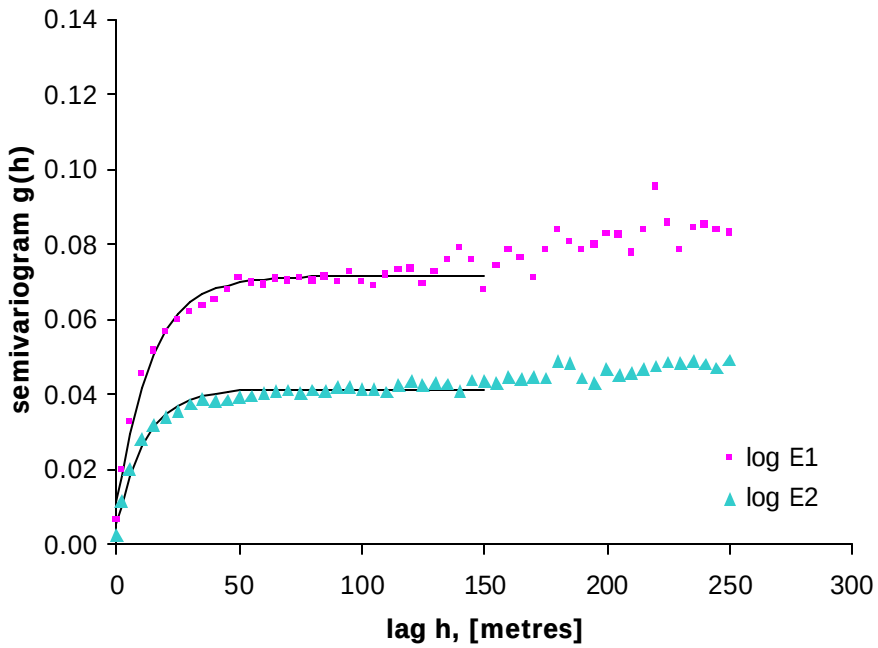

Figure 3.11 Sample omni-directional semivariograms and estimated exponential semivariogram models for test area 1, Drogden South, 1996.

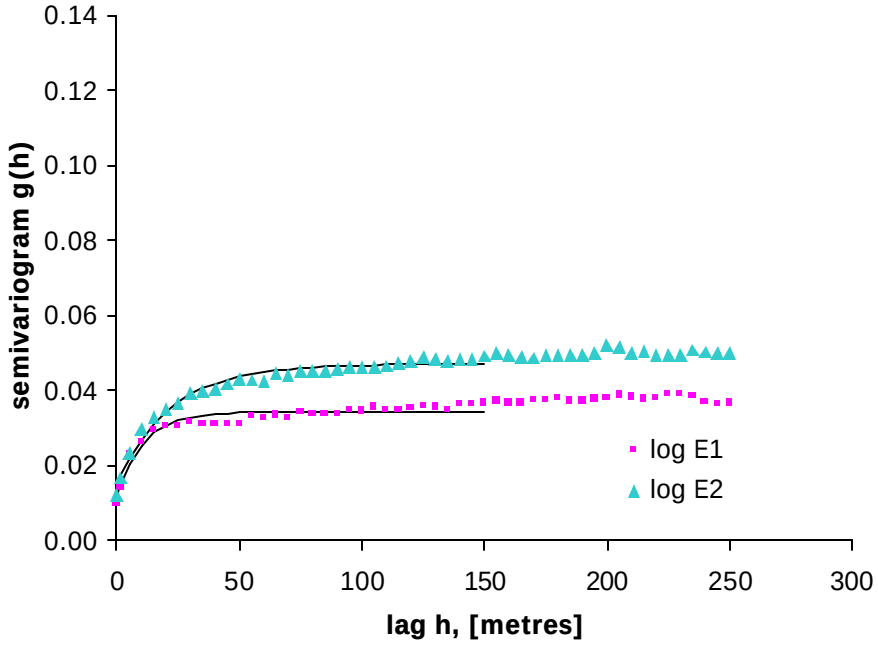

Figure 3.12 Sample omni-directional semivariograms and estimated exponential semivariogram models for test area 2, Flinterenden NW, 1996.

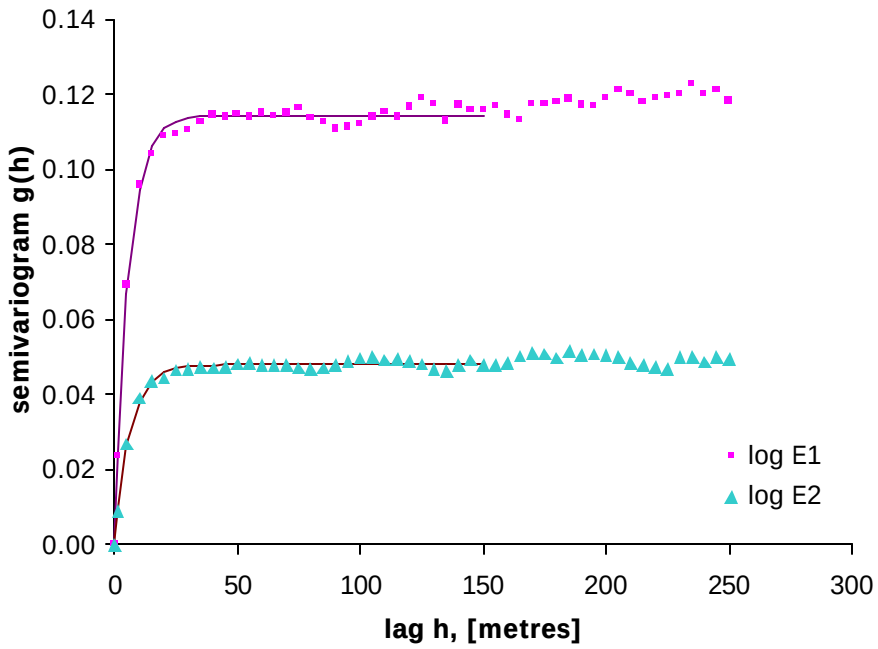

Figure 3.13 Sample omni-directional semivariograms and estimated exponential semivariogram models for test area 1, Drogden South, 1997.

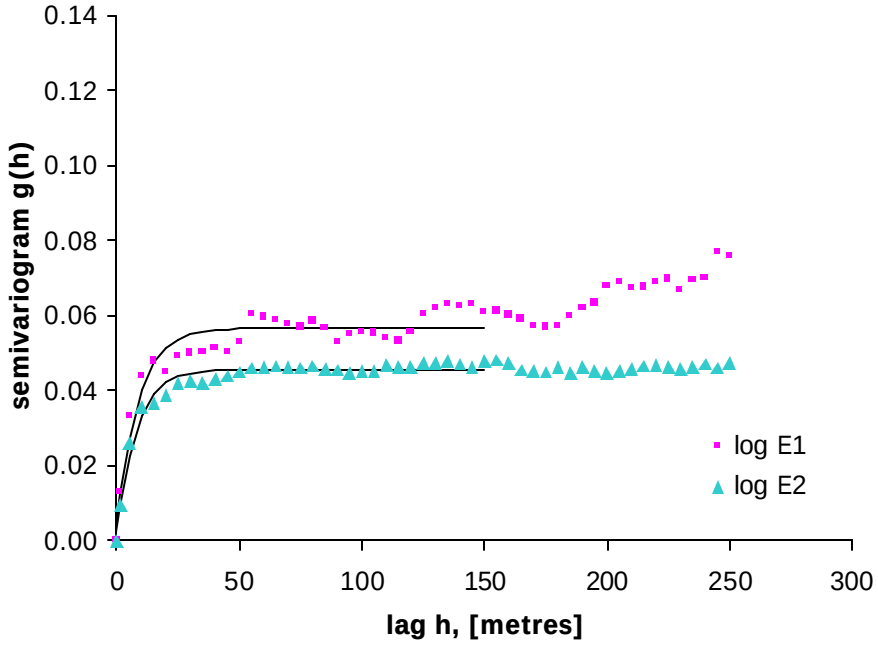

Figure 3.14 Sample omni-directional semivariograms and estimated exponential semivariogram models for test area 2, Flinterenden NW, 1997.

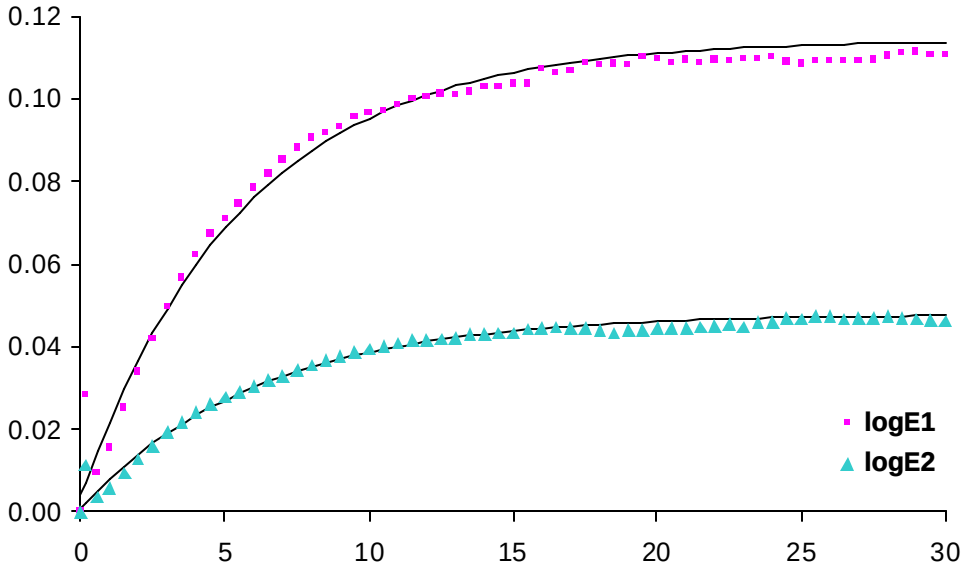

Figure 3.15 Sample omni-directional semivariograms for lag sizes at 0.5 metres, and estimated exponential semivariogram models for test area 1, Drogden South, 1997, using the *ad hoc* estimated nugget effects.

Based on the semivariogram estimations the following findings were made:

- The estimated nugget effects have decreased markedly from 1996 to 1997. The pattern of test area 1 exhibiting the lower nugget effects is maintained in both years. The nugget effects are in concordance with the micro-scale variances found in the background variability study.
- The sills have increased from 1996 to 1997, except for logE2 in test area 2 keeping a constant sill. The ratios of the sills for logE1 and logE2 in the test areas seem to be stable in both years, being approx. 2 for test area 1 and 1.2 for test area 2, cf. Figures 3.11 - 3.14.
- There is a slightly disturbing decrease in the range values from the 1996 to the 1997 datasets. It could be suggested that it is caused by the instationarity observed between 1996 and 1997, but it is not possible to give any supporting evidence.

The results are consistent as regards the shape of the spatial continuity function, i.e. the semivariogram, and with the findings for the bottom type areas, apart for the shrinking of the ranges. Thus, as an overall assessment, it is maintained that these semivariogram results are consistent measures of spatial continuity taking the drift of the signal voltages between 1996 and 1997 into account.

3.2 Classification of feature spaces

Features are certain properties expected to enable or enhance the detection of objects of interest. In many image analysis applications the generation and extraction of features is a task in its own right. For the echo sounder data it could be relevant to conduct a feature extraction exercise provided that the full, digitised signal was available. However, it is not; what is at hand is the roughness and hardness features extracted by the RoxAnn device, called E1 and E2. Hence, the feature space consists of these two variables, and the classification hereof is aimed at establishing quantitative and computational rules for assigning a sea bottom class to a measurement Y = (E1, E2)'.

3.2.1 Classification and discriminant analysis

Modern development of classification algorithms during the last 2 decades has shaped modern adaptive classifiers based on neural networks, deformable templates, and other semiparametric methods. Several decades before that, classical discriminant analysis based on multivariate Gaussian distribution theory and some subsequent nonparametric elaborations were developed. Classical Gaussian discriminant analysis will be employed here, too, leaving modern classification methods to be pursued in other settings. For a presentation of the application of deformable templates to the mussel and sand feature spaces analysed in the sequel, the reader is referred to Schultz (1995; 1998; 1999) and to her contributions in the BioSonar reports (MAS3-CT95-0026, 1997; 1998; 1999).

An introduction to (multivariate) Gaussian discriminant analysis is given in Conradsen (1984). The classification is based on a statistical discrimination between k Gaussian populations

$$\pi_1, \pi_2, ..., \pi_k, \qquad \pi_i \sim Gau_p(\mu_i, \Sigma_i).$$

To classify an observation x means to assign it to a population π_i, which is done by calculating a vector $u = (u_1, ... , u_k)'$ of scores u_i for every population by use of

$$u_i(x) = -1/2 \log(\det S_i) - 1/2(x-y_i)'S_i^{-1}(x-y_i) + \log(p_i), \qquad (3.14)$$

where y_i and S_i are estimates of the population mean μ_i and dispersion Σ_i, and p_i is a prior probability of x being a member of population π_i. The observation x is then assigned to the class i for which u_i attains the maximum value in the set of u_i's. This classification rule is known as the Bayesian solution, as the posterior probability of x being a member of π_i given the value of x, is

$$p(\pi_i \mid x) = \exp(u_i) / \Sigma_j \exp(u_j),$$

thus the maximum u_i corresponds to the maximum posterior probability $p(\pi_i \mid x)$. If prior knowledge is unavailable, i.e. it is not possible to assign reasonable values to p_i, the all-equal principle is usually used, and the term $\log(p_i)$ is then removed from (3.14), as all p_i are equal. Other classification strategies than the maximisation of posterior probability can be applied, e.g. the minimax (= minimisation of maximum loss) solution choosing a strategy that makes all misclassification probabilities identical.

In the present feature space there are only two populations, and the third class, the reject class, is comprised of all observations lying outside the two 95% Gaussian confidence ellipsoids. The use of the 95% confidence ellipsoids was decided as a compromise between covering the sample populations and securing a minimal overlap of the two confidence ellipsoids.

Thereby, the following decision rule for the x assignment applies:

class 0, **if** $||x-y_1||_1 > \chi^2(2)_{0.95}$ and $||x-y_2||_2 > \chi^2(2)_{0.95}$

class 1, **if** $u_1(x) > u_2(x)$ and $||x-y_1||_1 \leq \chi^2(2)_{0.95}$

class 2, **if** $u_1(x) \leq u_2(x)$ and $||x-y_2||_2 \leq \chi^2(2)_{0.95}$,

where the norms $||z||_i$ are given by $||z||_i = z'S_i^{-1}z$. The code 1 is used for the mussel class, and 2 is used for the sand class.

3.2.2 Estimation of classification regions

The classification of the mussel and sand feature spaces for 1996 and 1997 was carried out in two steps. First, a discriminant analysis was carried out based on bigaussian descriptions of the mussels and sand samples with different dispersion matrices. Secondly, to introduce a reject class describing areas far away from the samples, 95% confidence ellipsoids were used to delimit the mussel and sand classes, leaving the area outside to be classified as an 'other' bottom type.

In 1996, the two datasets for the mussel and the sand bottom type area contain 709 and 1011 observations, respectively. To provide a cross-classification dataset approximately one third of both datasets have been put aside for test datasets, leaving 451 and 697 observations for the estimation datasets. Table 3.7 shows the sample averages, y, and dispersions, S, for (log(E1), log(E2))' for the mussels and sand estimation datasets.

Table 3.7 Descriptive statistics for the 1996 estimation datasets (from the bottom type areas) for the bigaussian measurements Y = (logE1, logE2)'.

	Mussels , 1996	Sand, 1996
N	451	697
average, y	$\begin{bmatrix} -1.73100 \\ -0.78987 \end{bmatrix}$	$\begin{bmatrix} -2.23279 \\ -0.64862 \end{bmatrix}$
dispersion, S	$\begin{bmatrix} 0.01745 & 0.00350 \\ 0.00350 & 0.01540 \end{bmatrix}$	$\begin{bmatrix} 0.02225 & 0.00758 \\ 0.00758 & 0.03232 \end{bmatrix}$

The two datasets for the mussel and the sand bottom type areas from 1997 contain 3094 and 1624 observations respectively. As for 1996 approximately one third of either dataset have been put aside for cross-validation datasets, leaving 2021 and 1126 observations for the estimation dataset. The descriptive statistics for the estimation datasets from 1997 are given in Table 3.8.

Table 3.8 Descriptive statistics for the 1997 estimation datasets for the bigaussian measurements Y = (logE1, logE2)'.

	Mussels, 1997	Sand, 1997
N	2021	1126
average, y	$\begin{bmatrix} -2.52213 \\ -2.11986 \end{bmatrix}$	$\begin{bmatrix} -3.12155 \\ -2.16624 \end{bmatrix}$
dispersion, S	$\begin{bmatrix} 0.04519 & 0.00704 \\ 0.00704 & 0.02110 \end{bmatrix}$	$\begin{bmatrix} 0.01964 & 0.00556 \\ 0.00556 & 0.04283 \end{bmatrix}$

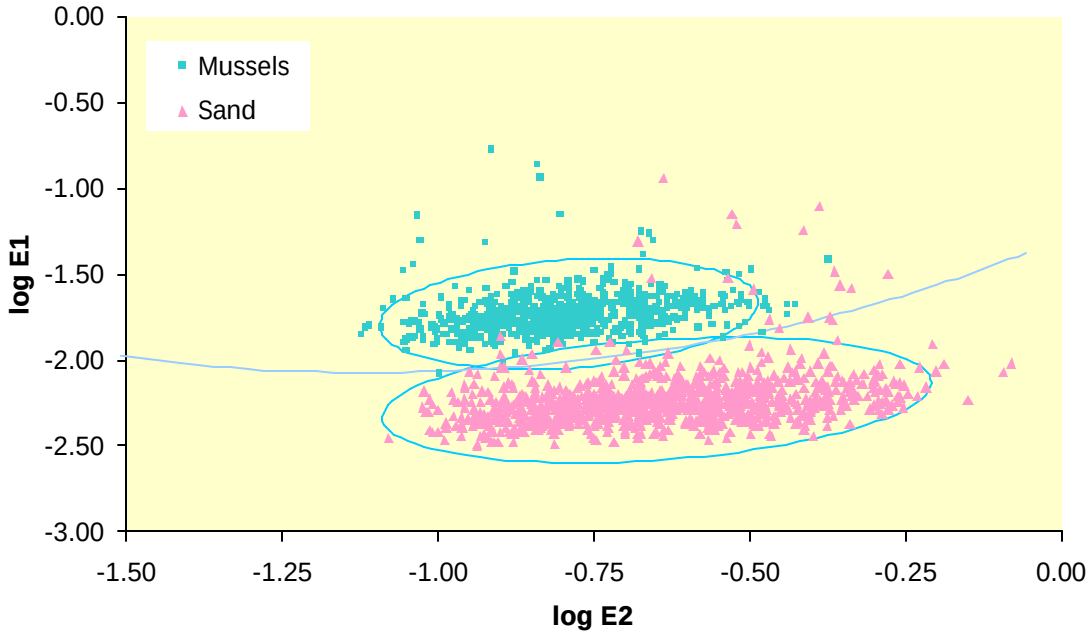

Figure 3.16 (a) The feature space of 1996 with illustrations of the regions used in the classification: The quadratic border line between the mussel and sand regions, and the 95% approximated confidence ellipsoids for the mussel and sand observations. The separating line, the discriminator curve, is an ellipsoid.

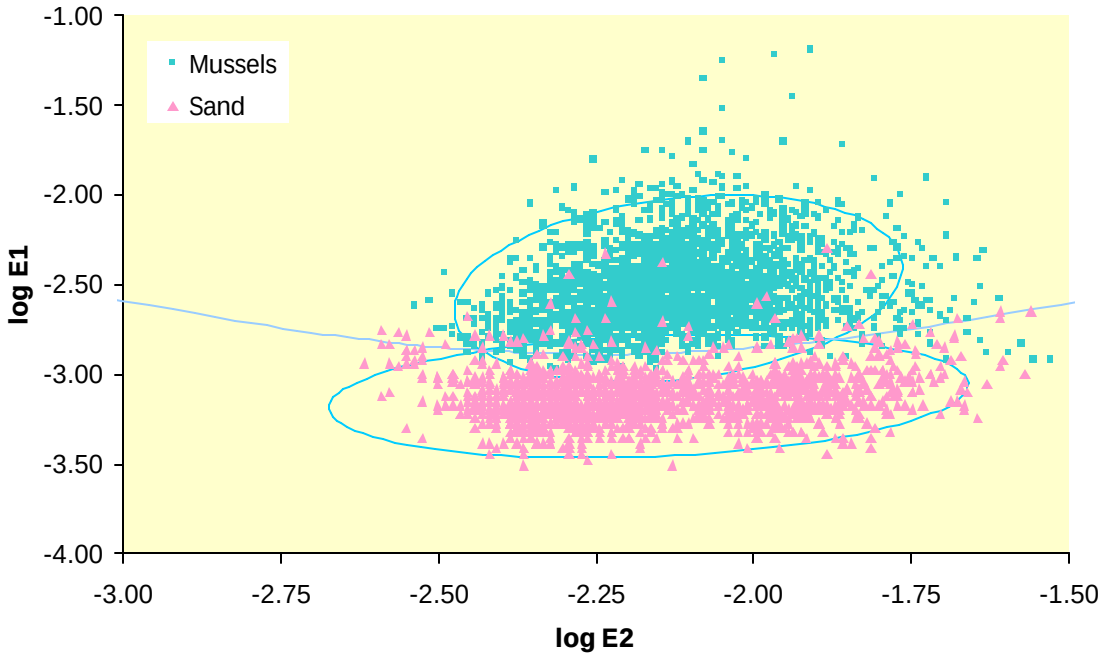

Figure 3.16 (b) The feature space of 1997 with indications of the regions used in the classification: The quadratic border line between the mussel and sand regions, and the 95% approximated confidence ellipsoids for the mussel and sand observations. The quadratic discriminator function is a hyperbola.

It is noted that the variances found for logE1 and logE2 and listed in Tables 3.7 and 3.8 are in good concordance with the sills found for the variograms in the bottom type areas in 1996 and 1997, cf. Tables 3.2 and 3.3.

The quadratic discriminator functions derived from setting $u_1(x) = u_2(x)$ in 1996 and 1997, respectively, and thus separating the two classes, are given by the polynomials

$$P_{1996}(x,y) = -5.5996x^2 -17.2096y^2 +2.1964xy +8.4739x -33.8822y +20.1880 = 0$$

$$P_{1997}(x,y) = 14.759x^2 -12.882y^2 +0.924xy +107.783x -55.275y +122.998 = 0,$$

where positive values $P(x,y) > 0$ indicates the mussel region having the line $P(x,y) = 0$ as boundary; note that $(x,y)'$ is $(\log E1, \log E2)'$ here, even though the plots in Figure 3.16 (a) and Figure 3.16 (b) are depicted in accordance with the tradition of putting E2 on the abscissa. The conics described by $P(x,y)$ for 1996 and 1997, respectively, are an ellipsoid and a hyperbola. (Easily checked for $P(x,y) = ax^2+by^2+cxy+ ...$, as $ab > c^2/4$ implies an ellipsoid and $ab < c^2/4$ a hyperbola).

The distance functions $d_\pi(v)$ used to compute the 95% confidence ellipsoids for the populations $\pi \in \{\pi_{mussels}, \pi_{sand}\}$ are given by the norms listed above, i.e.

$$d_\pi(v) = ||v-x_\pi||_\pi = (v-x_\pi)'S^{-1}_\pi(v-x_\pi),$$

where x_π and S_π are the estimates of the mean μ_π and the dispersion Σ_π. For simplicity of notation we let $(x,y)' = (\log E1, \log E2)'$:

1996

$$d_{Mussels}(x,y) = 60.0383x^2 +68.0471y^2 -27.3007xy +186.2886x +60.2391y + 185.0233,$$

$$d_{Sand}(x,y) = 48.8391x^2 +33.6278y^2 -22.9079xy +203.2364x -7.5253y +224.4515,$$

1997

$$d_{Mussels}(x,y) = 23.3456x^2 +50.0050y^2 -15.5855xy +84.7221x +172.699y +289.889,$$

$$d_{Sand}(x,y) = 52.8645x^2 +24.2400y^2 -13.7343xy +300.287x +62.1474y +535.994.$$

Hence, $d(x,y) < \chi^2(2)_{0.95} = 5.99$ is the inequality supplemented to discriminate the reject class from the mussels and sand regions in the classification. The classifications using $u_1(x)$ and $u_2(x)$ to assign a mussel or sand class to observations was conducted using PROC DISCRIM in SAS, and a subsequent postprocessing SAS program was used to filter distant observations into the reject class.

The classification results (before the assignments to the reject class) from PROC DISCRIM are given in Tables 3.9 and 3.11 for the estimation datasets, and Table 3.10 and 3.12 give the cross-validation results.

Table 3.9 Classification Summary for Calibration Data, 1996.

Number of Observations and Percent Classified into CLS:

From CLS	To CLS=1	To CLS=2	Total
1	449	2	451
2	19	678	697
Total	468	680	1148
1	99.56%	0.44%	100.00%
2	2.73%	97.27%	100.00%
Total	40.77%	59.23%	100.00%

Table 3.10 Classification Summary for Cross-validation Data, 1997.

Number of Observations and Percent Classified into CLS:

From CLS	To CLS=1	To CLS=2	Total
1	257	1	258
2	7	307	314
Total	264	308	572
1	99.61%	0.39%	100.00%
2	2.23%	96.18%	100.00%
Total	46.15%	53.85%	100.00%

Table 3.11 Classification Summary for Calibration Data, 1997.

Number of Observations and Percent Classified into CLS:

From CLS	To CLS=1	To CLS=2	Total
1	1982	39	2021
2	38	1088	1126
Total	2020	1127	3147
1	98.07%	1.93%	100.00%
2	3.37%	96.63%	100.00%
Total	64.19%	35.81%	100.00%

Table 3.12 Classification Summary for Cross-validation Data, 1997.

Number of Observations and Percent Classified into CLS:

From CLS	To CLS=1	To CLS=2	Total
1	1052	21	1073
2	19	479	498
Total	1071	500	1571
1	98.04%	1.96%	100.00%
2	3.82%	96.18%	100.00%
Total	68.17%	31.83%	100.00%

The cross-validation results given in Tables 3.10 and 3.12 supplemented by the contents of Figures 3.17 and 3.18, showed that the results of the classification of the feature space are fairly robust and reliable. Feature space inspection and the estimated variogram models underpin the finding that the magnitude of the E1 and E2 values cannot be used directly in a reliable estimation procedure, wherefore it is recommendable to use the classification method described here in an adaptive fashion.

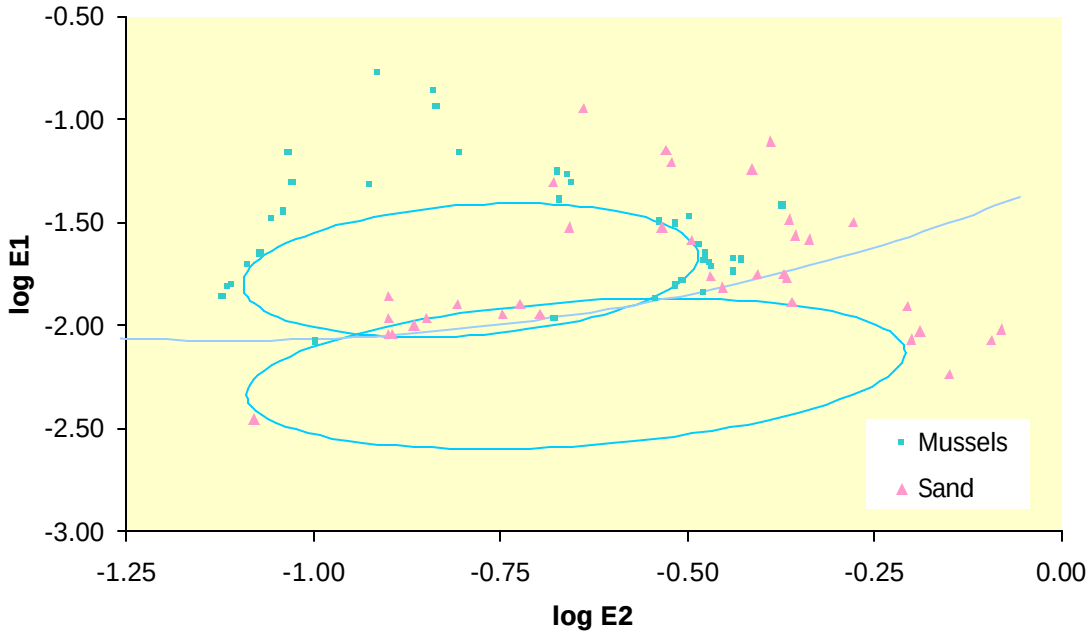

Figure 3.17 The rejects and misclassified observations from the bottom type areas of 1996, 36 observations from the sand area and 36 from the mussel area.

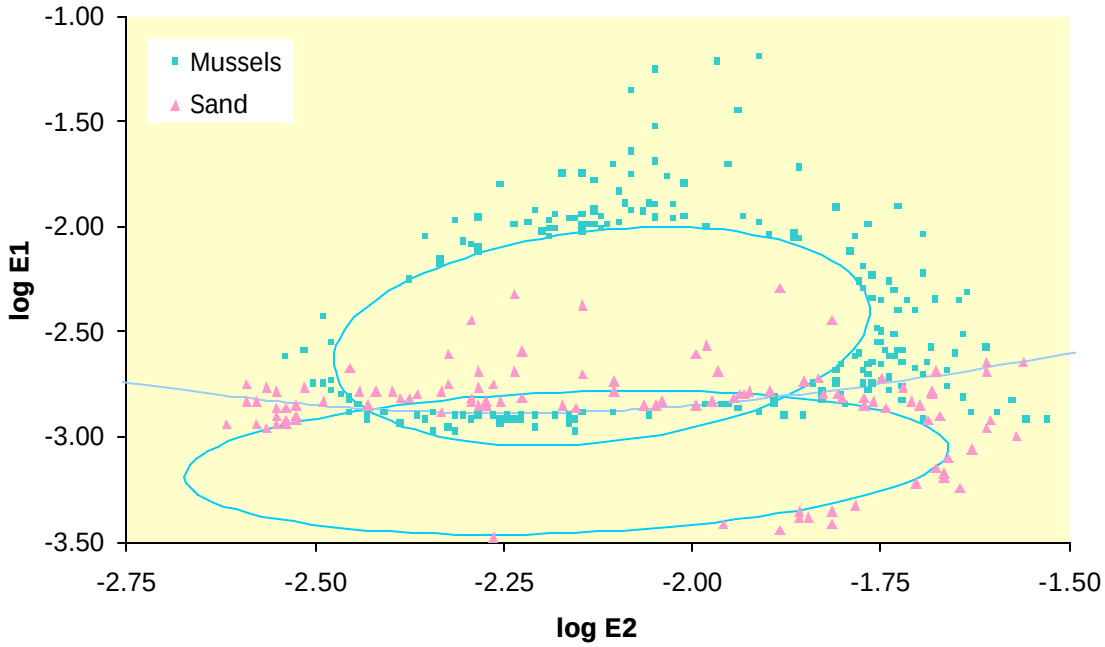

Figure 3.18 The rejects and misclassified observations from the bottom type areas of 1997, 109 observations from the sand area and 201 from the mussel area.

3.2.3 Classification of the test areas

To give an impression of the configurations of datasets from the test areas in feature space the Figures 3.19 - 3.22 have been prepared.

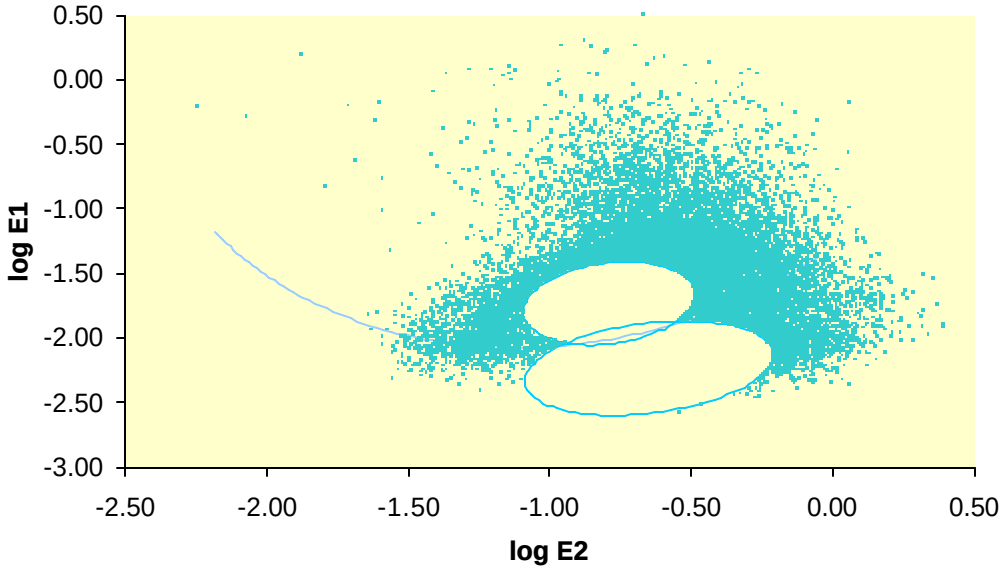

Figure 3.19 The 17401 rejects (~ 52.2%) among the observations from test area 1 in 1996.

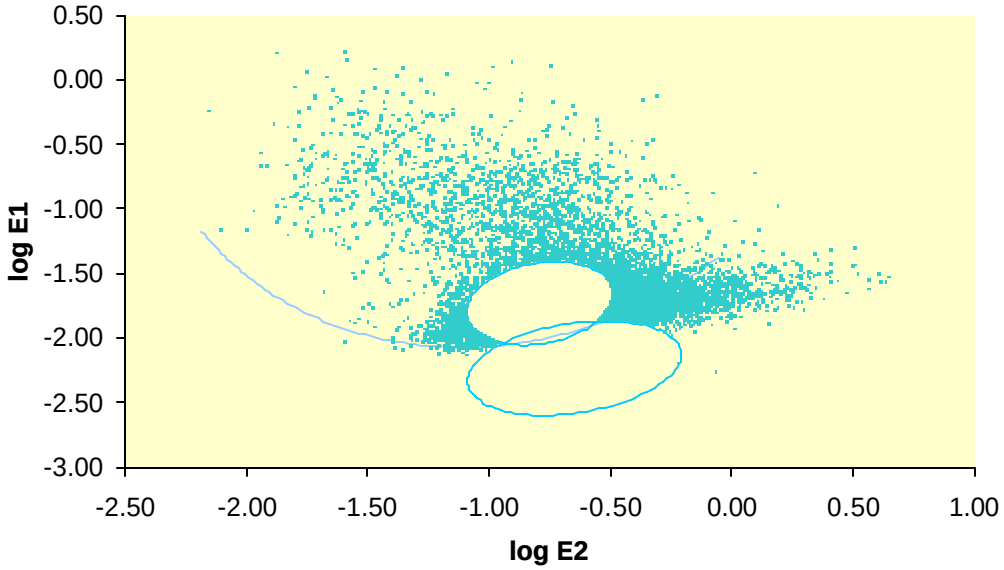

Figure 3.20 The 6877 rejects (~22.7%) among the observations from test area 2 in 1996.

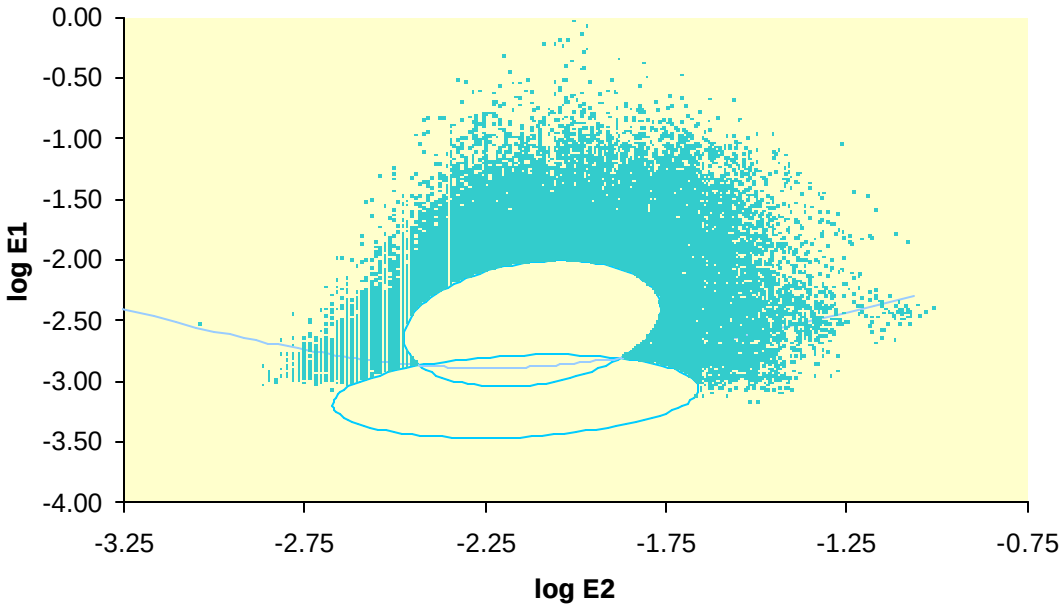

Figure 3.21 The 35468 rejects (~ 45.9%) among the observations from test area 1 in 1997.

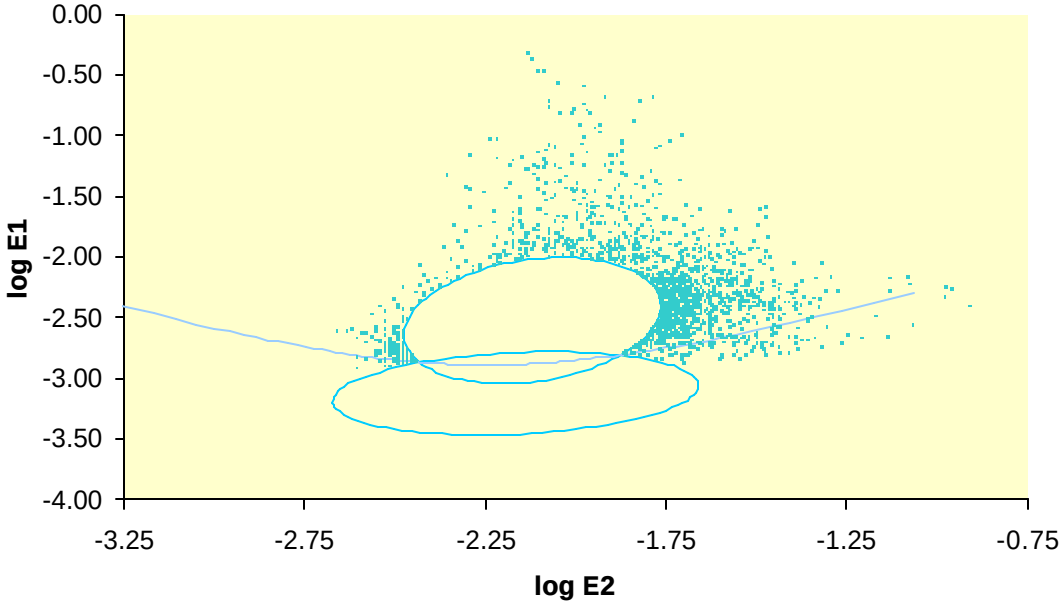

Figure 3.22 The 1623 rejects (~15.5%) among the observations from test area 2 in 1997.

Table 3.13 Classification summary for the test areas in 1996 and 1997.

	frequency			percent		
	mussels	sand	reject	mussels	sand	reject
1996, test area 1	13109	2640	17401	39.5	8.0	52.5
1996, test area 2	22849	521	6877	75.5	1.7	22.7
1997, test area 1	39299	2481	35468	50.9	3.2	45.9
1997, test area 2	8747	76	1623	83.7	0.7	15.5

The classification results for the test areas are summarised in Table 3.13. Very small fractions of the observations are classified as sand, whereas the mussels as expected are clearly dominant in test area 2, which is also reflected by Figure 3.20 and 3.22. In test area 1 the expected heterogeneous pattern is mirrored in the feature space.

3.2.4 Interpretations

A word on the interpretation of the feature space classification is in place. The interpretation offered in this thesis is conservative as it uses a binary scale for assigning mussel or sand classes to the observations. Several like studies operate with trinary or quaternary scales, the trinary scale containing a class corresponding to the middle gray region of undecidedness (50/50), and the quarternary scale using 4 classes corresponding to the quartile intervals of 0-25%, 26-50%, etc. However, here the aim is to lay a reliable corner stone for future developments, and as long as there is no supporting evidence that warrants further divisions of the mussel-sand scale it will not be discussed here.

Other approaches could be envisioned, e.g. an approach using the Mahalanobis distances from an observation to the sample averages of the mussel and sand populations in feature space to assign a probability vector to the observation by inverting the quantile of the corresponding contour line into a probability. However, such approaches can only be qualified by certain types of datasets, e.g. bottom type areas having a fixed coverage rate of mussels below 100%, and as these are not at hand, it will be superfluous to embark on such a venture here.

What is really at stake is the challenge of identifying (link) functions $\mu(c;\theta)$ and $e(c;\psi)$ for the relation between RoxAnn measurements $Z(s) = (E1(s), E2(s))'$ and the mussel coverage rate $c(s)$ at the location s:

$$Z(s) = (E1(s), E2(s))' = \mu(c(s);\theta) + e(c(s);\psi)$$

where θ and ψ are auxiliary parameters describing other properties that the mean field and the small-scale variation might depend upon, like the pattern of the mussels, e.g. patches or smooth texture. Even in a very simple form,

$$Z(s) = \mu(c(s)) + e(s) \qquad (3.15)$$

this functional relation is not identifiable from the datasets produced during the BioSonar field campaigns. Based on the existing datasets the following statistics of the function (3.15) were estimated:

$$E(Z(s) \mid c \approx 0) \text{ and } V(Z(s) \mid c \approx 0)$$

and

$$E(Z(s) \mid c \approx 1) \text{ and } V(Z(s) \mid c \approx 1)$$

for the sand and mussel bottom type areas, respectively. That is, knowledge about the function at the endpoints of the coverage rate scale has been obtained (and it was found that these endpoints seem to be instationary although maintaining the same relative positions in feature space). Future scrutiny of the function $\mu(c;\theta)$ could involve tank experiments with controlled / designed mussel textures, which would be very interesting.

3.3 Preparation of distribution maps and estimates of distribution areas

This section describes in detail how the calculated variograms and classified regions of feature space are used intertwined to produce spatial distribution maps by kriging of the observations followed by classification of the kriged values.

3.3.1 Validation maps for the bottom type areas

For the bottom type areas spatial distribution maps have been prepared mainly to validate the use of the classification rule given in section 3.3. It is expected that they will reflect the presence of a homogeneous sea bottom covered either by mussels or sand.

The distribution maps were prepared in a simple and straightforward fashion by kriging the observations of logE1 and logE2 to estimate point values on a grid where points are separated by 1 metre in vertical and horizontal directions. The kriging was based on the variogram models given by the coefficients listed in Tables 3.2 and 3.3. The maps were produced using Surfer, version 6.0, and the grids containing the results of the point kriging were postprocessed with a SAS program to provide the classified maps using the classification rule given in section 3.3. The resulting classification codes are given as:

1 ~ mussels, 2 ~ sand, and 0 ~ reject class.

The mussel codes are depicted as blue (the darker colour in gray scale), the sand codes are yellow (the lighter colour in gray scale), and the reject codes are white throughout this section. The resulting maps are depicted in Figures 3.23 - 3.26, where the kriged map of the water depth has been included to allow scrutiny of potential deviations, etc.

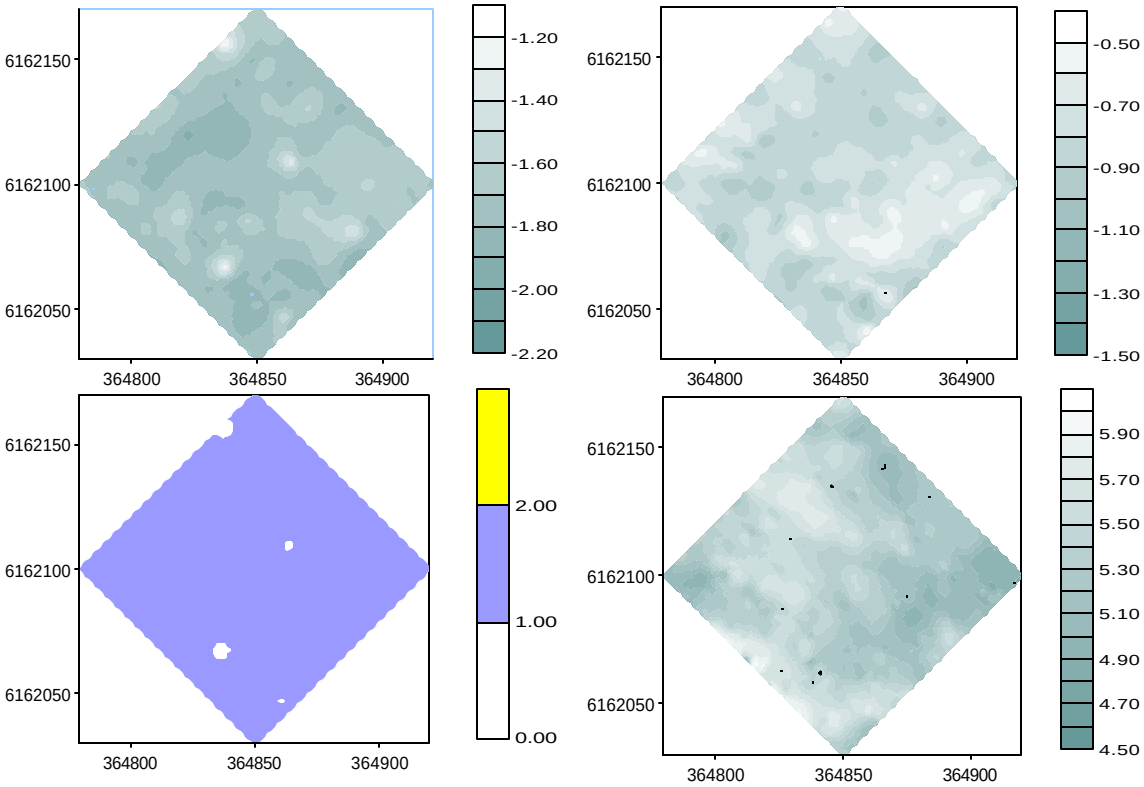

Figure 3.23 Mussel bottom type area, 1996. LogE1 is mapped upper left, logE2 is mapped upper right, depth is mapped lower right, and lower left depicts the classified distribution map.

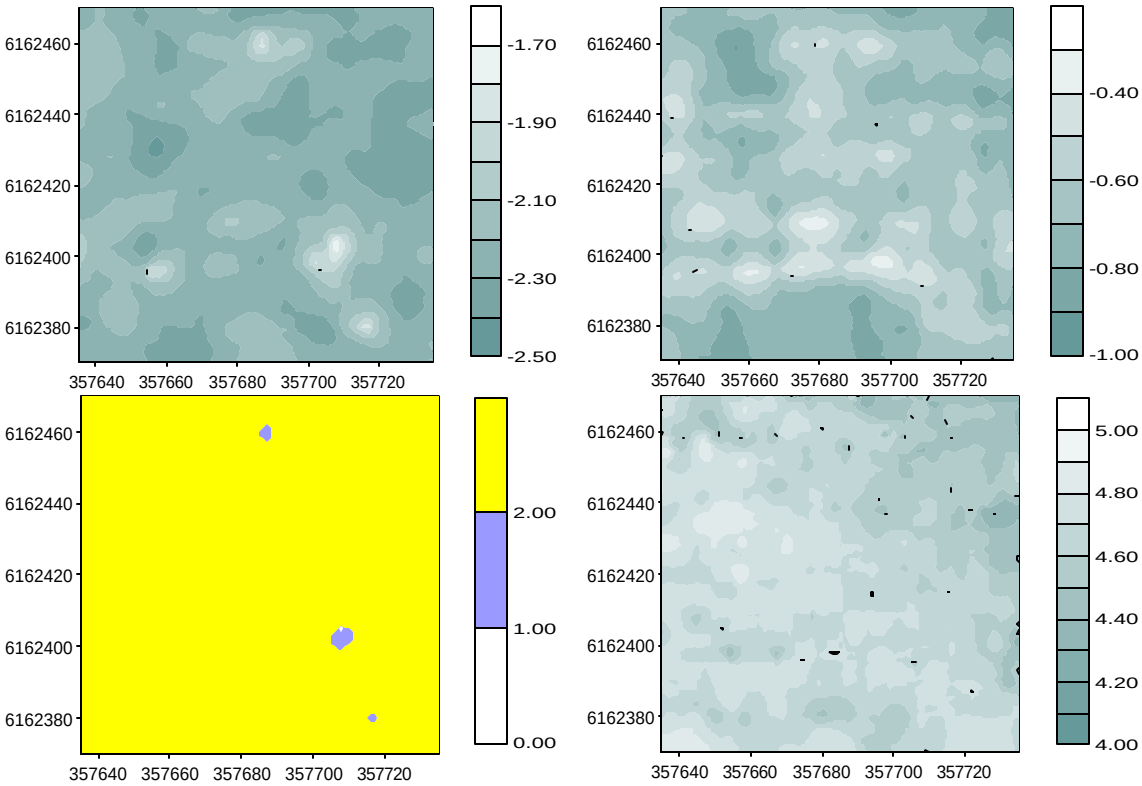

Figure 3.24 Sand bottom type area, 1996. LogE1 is mapped upper left, logE2 is mapped upper right, depth is mapped lower right, and lower left depicts the classified distribution map.

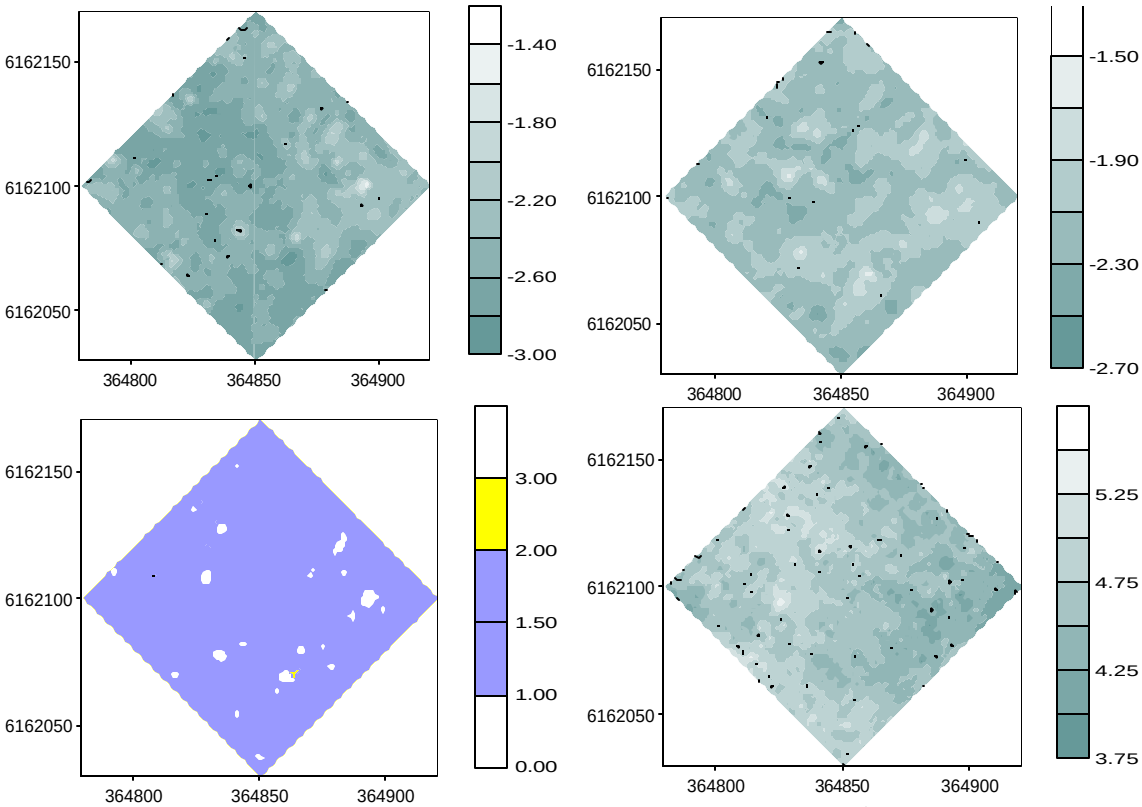

Figure 3.25 Mussel bottom type area, 1997. LogE1 is mapped upper left, logE2 is mapped upper right, depth is mapped lower right, and lower left depicts the classified distribution map.

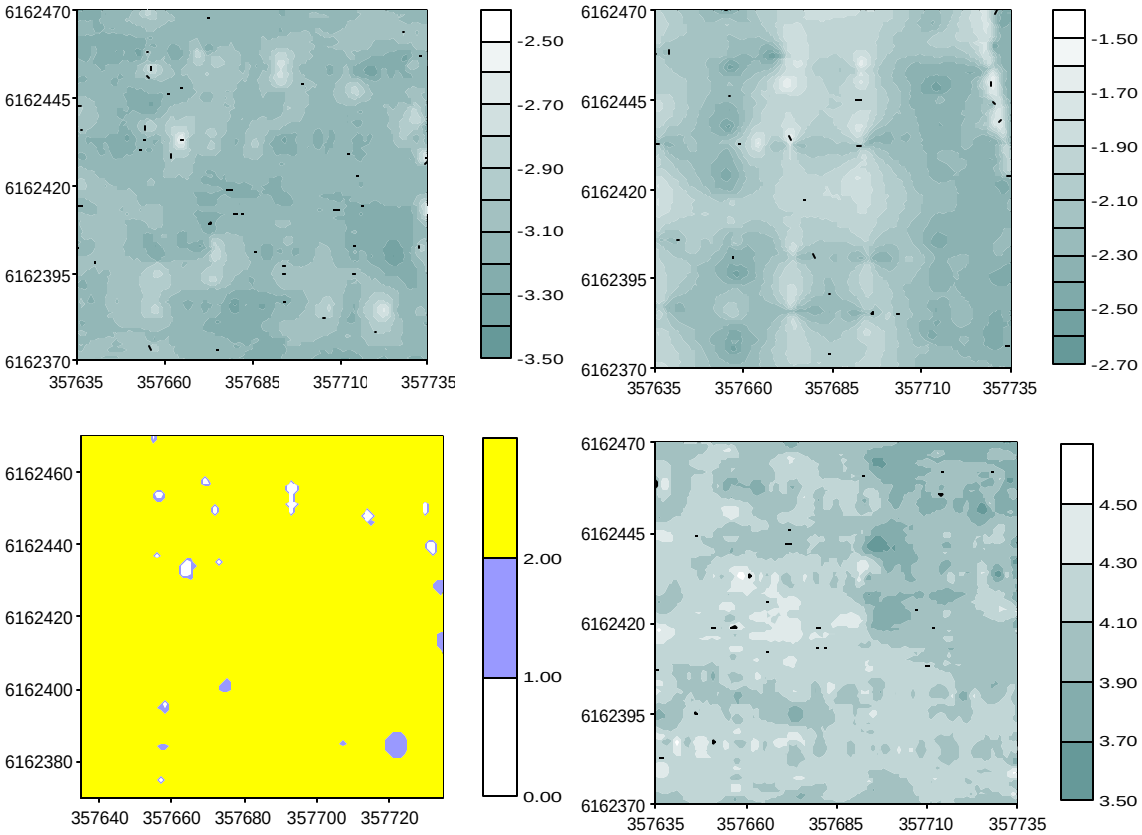

Figure 3.26 Sand bottom type area, 1997. LogE1 is mapped upper left, logE2 is mapped upper right, depth is mapped lower right, and lower left depicts the classified distribution map.

A short summary of the classification results for the kriged points is given in Table 3.14. The following observation can be made in Figures 3.23 - 3.26 and Table 3.14:

- The 1996 maps of logE1 and logE2 appear smoother than the maps for 1997, which is an effect of the lower data density and the lower transect density.
- In the 1997 maps the data along transects are clearly reflected in the kriged maps, wherefore it could be argued that the side length of the square grid cells should have been greater (than 1 metres) for the 1997 data. This is particularly apparent in the maps of the water depths; however, the grid cell size being identical in both years allows comparisons to be made without qualifications regarding differences in cell size.
- The patterns of the depth maps, i.e. the topography, are reproduced fairly well from 1996 to 1997, which is a good underpinning of the validity of the data.
- Mussels are represented as a strong majority in the mussel bottom type area, and sand is *vice versa* in the sand areas. The positions and number of blank spots containing complementary bottom classes are not reproduced from 1996 to 1997, which can be attributed to random variation inherent in the measurement process, or, at least in the mussels case, a result of restructuring of mussel beds, i.e. wandering and settling of mussels.

Table 3.14 A summary of the classification of the kriged values for the bottom type areas, given in percentages of the total number of grid points.

	Mussels	Sand	Reject	Total
Mussels, 1996	99.4	0.0	0.6	100.0
Mussels, 1997	98.6	0.2	1.2	100.0
Sand, 1996	0.3	99.7	0.0	100.0
Sand, 1997	0.6	98.9	0.5	100.0

Regardless, the main observation is that the fractions of grid points classified as mussels in the mussel area and those classified as sand in the sand area, given in Table 3.14, seem pretty convincing and provide a proper validation of the outlined classification scheme. The classified maps evidently support this impression.

3.3.2 Distribution maps for test area 1, Drogden South

The maps of the spatial distribution of mussels should provide this information lending itself to clear and unambiguous interpretation. Thus, the following considerations applied to the method chosen for preparing the maps. It is considered desirable, that the maps depicted in raster format contain directly interpretable figures, hence every pixel should represent an average of the part of the region it covers. In other words block kriging is more suited for this task than point kriging.

For the block kriging a discretisation of the pixel interior by use of 4 x 4 points was chosen on the basis of the recommendation by given Isaaks & Srivastava (1989), where 4 x 4 points is recommended as a minimum limit for ensuring stability of the results. One way to go about this would be to form block averages directly from the 4 x 4 values obtained from point kriging and then classifying the block averages using a modified dispersion matrix S adjusted for the averaging of 16 spatially dependent point estimates from Z(s). Alternatively, the variogram model could be adjusted for the change of support from points to the pixel blocks and then used in a "point" kriging that would produce the block averages directly. Journel & Huijbregts (1978) give a thorough discussion of how to adjust variogram models for change of support.

Either way, the result will be a binary variable, and therefore a hybrid approach was chosen to gain a little more resolution. Thus, an ordinary point kriging system is used to estimate the 16 points, which are then classified individually. Afterwards, mussel and sand proportions are calculated as the marginal ratios hereof within every pixel. The classification rule for the block is set to use a 50% thresholding rule, i.e. if one of the proportions p_{mus} or p_{sand} are greater than 0.5, the pixel will be classified accordingly, otherwise it will be assigned to the reject class. Suppose c is a 16-valued vector containing the classification results c_i at all the 4 x 4 subgrid points, then p_{mus}, p_{sand} and class are assigned values as follows:

$$p_{mus} = \Sigma_{i=1..16} I[c_i=<\text{mussels}>]/16$$

$$p_{sand} = \Sigma_{i=1..16} I[c_i=<\text{sand}>]/16$$

$$\text{class} = \begin{cases} <\text{mussels}>, & \text{if } p_{mus} > 0.5 \\ <\text{sand}>, & \text{if } p_{sand} > 0.5 \\ <\text{reject}>, & \text{otherwise.} \end{cases}$$

If $p_{mus} = p_{sand} = 0.5$ a coin is flipped (this didn't occur anywhere).

Other considerations concern the choice of pixel size in the grid to be used. An upper limit is indicated by the magnitude of the range of influence, R. Hence, going substantially higher than R a very smoothed result can be expected as then the spatial continuity is smoothed at the global level, and thus will be close to the overall kriged average. As a rule-of-thumb a lower limit is

set by the minimum distance between data, as the purpose of kriging is to estimate the mean field by smoothing out small-scale spatial variation which cannot be observed below the minimum distance between observations. Sometimes a similar concern is phrased as "the data are visible in the kriged map", not implying the obvious, but rather that deviating small-scale patterns are seen in regions of high data density; an observation like that would indicate that the grid size should be increased. These concerns have been combined with a rationale of keeping a fixed relative data density thereby making use of the three distinct grid sizes used in the sampling of the areas to obtain maps in various scales of resolution. Thus, maps have been prepared for the total outstretch of the test areas having gross transect distances at 120 metres using the hybrid block kriging and proportion calculation of pixels at 30 x 30 m² pixels. For the center part of the test areas containing transects 60 metres apart the size of the pixels were chosen at 15 x 15 m², and for the core part of test area 1 where transects are 20 metres apart the pixel size was chosen at 5 x 5 m². Thus, the relative data density is maintained (approximately) by choosing pixel sizes at a ratio 30: 15: 5 similar to the transect distances at 120: 60: 20.

The specifications of the geographic boundaries for the maps prepared for test area 1 are given in Table 3.15.

Table 3.15 Specifications of the geographic boundaries for the total area and subareas in test area 1, Drogden South.

Area	side length of square pixels /m	map boundaries in UTM coordinates	image dimensions (height x width)
Total area	30	[355520, 357200] x [6162000, 6163440]	48 x 56
Center area with transects 60 m apart	15	[355700, 356330] x [6162420, 6163050]	42 x 42
Core part with transects 20 m apart	5	[355940, 356060] x [6162680, 6162800]	24 x 24

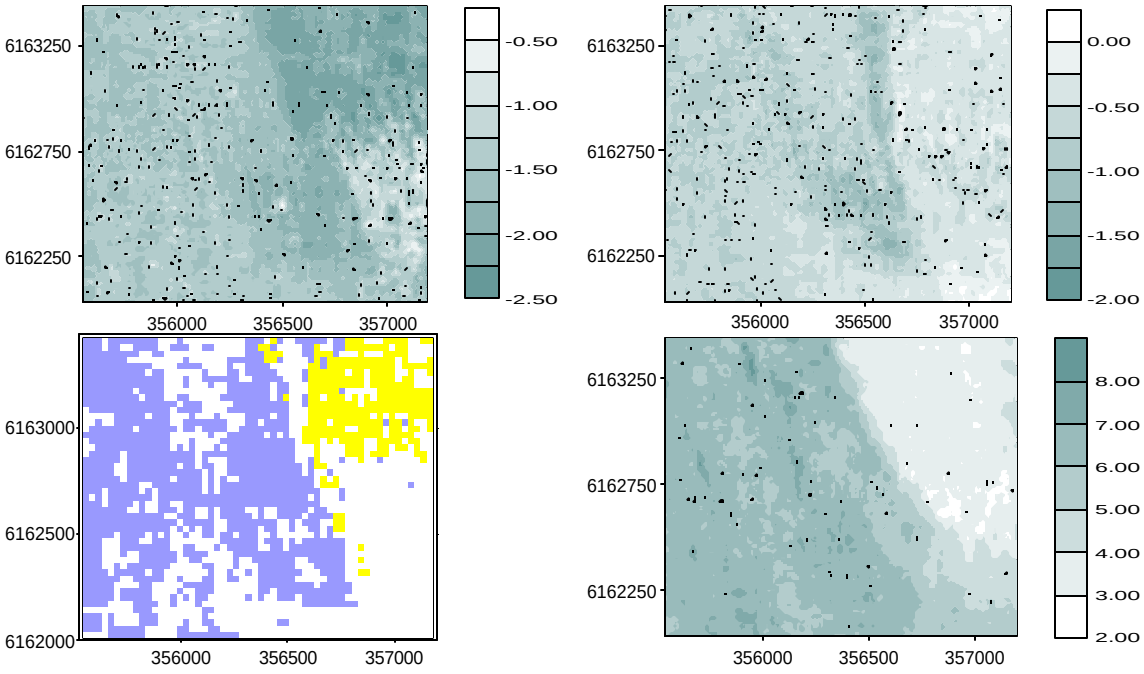

Figure 3.27 Kriged observation maps and the distribution map containing classified 30 x 30 m blocks for test area 1, 1996. LogE1 is mapped upper left, logE2 upper right, and depth lower right. The lower left depicts the classified distribution map, where blue is mussels and yellow is sand.

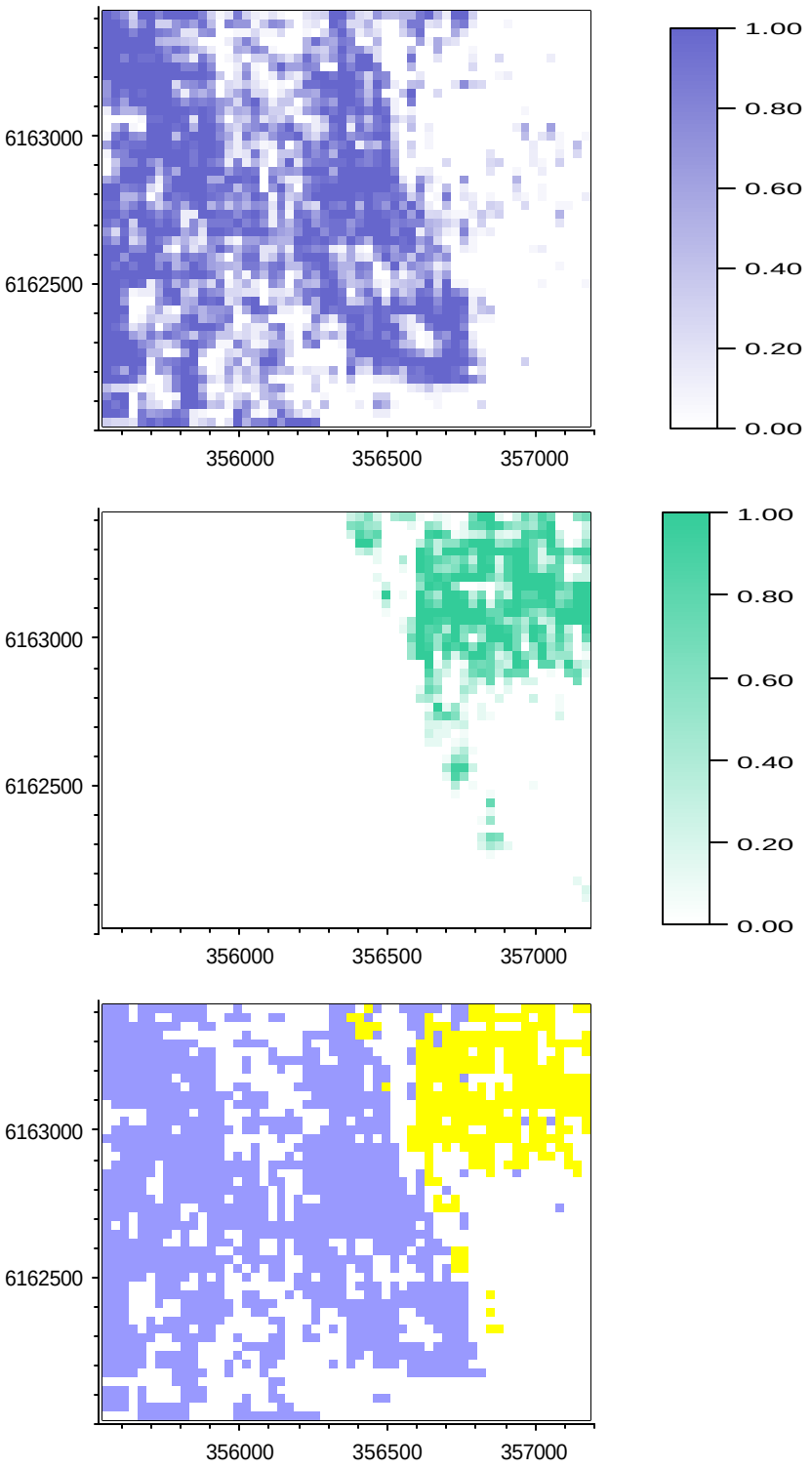

Figure 3.28 Maps for the total test area mainly covered by transects 120 metres apart, for test area 1, 1996. At the top the mussel proportions map is depicted, the middle depicts the sand proportions map, and the lower is the classified map. The total area is 1680 x 1440 m^2 = 2.4192 km^2.

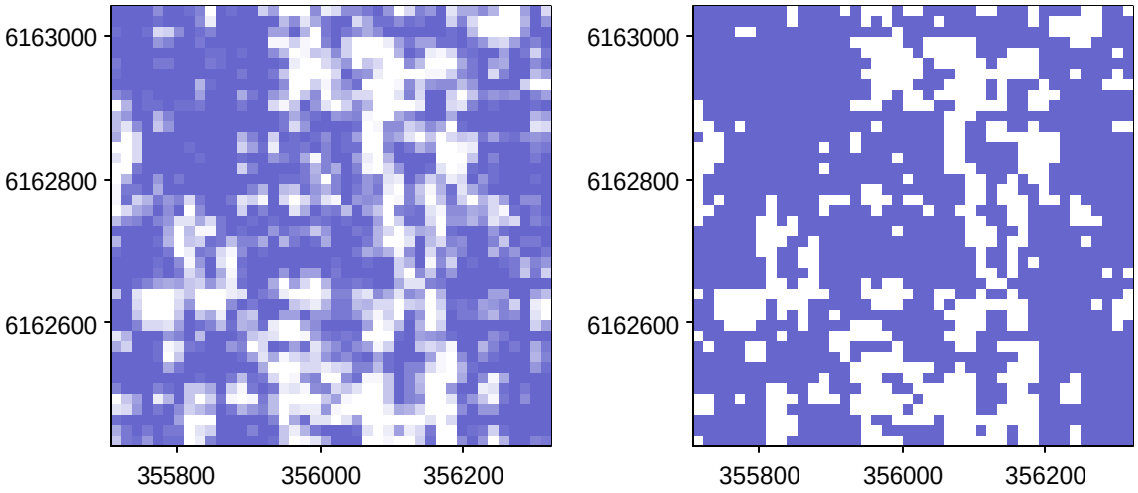

Figure 3.29 Maps for the centered area covered by 60 metres interspersed transects, for test area 1, 1996. The left map shows the mussel proportions, and the right contains the classified map. The total area is 630 x 630 m² = 0.3969 km².

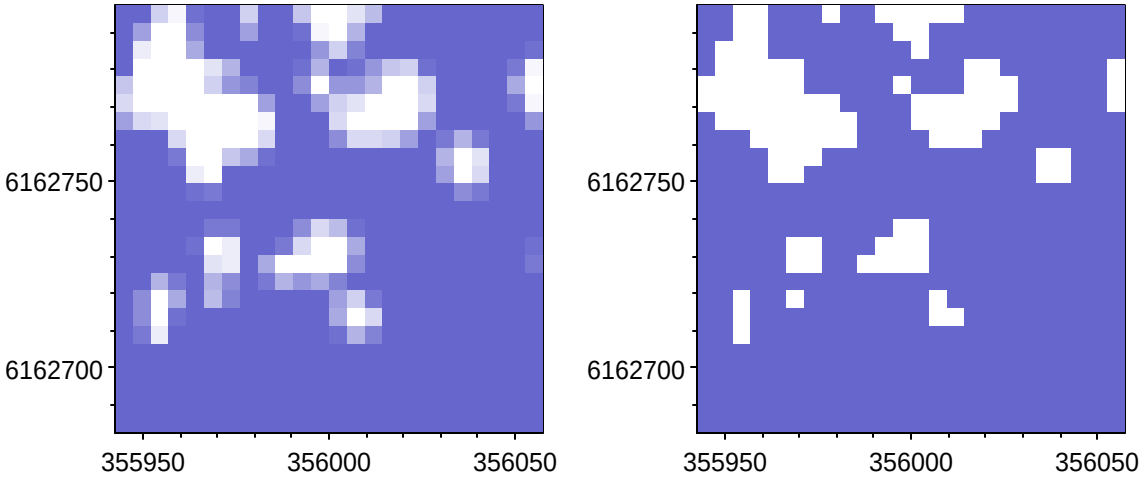

Figure 3.30 Maps for the core area covered by transects 20 metres apart, for test area 1, 1996. The left map contains the mussel proportions, and the right map holds the classified map. The total area is 120 x 120 m².

The block kriging was carried out using Surfer to prepare the point kriging results on the 4 x 4 subgrids, followed by a calculation of the proportions within blocks and the block class using a SAS program. The results are pixels of 900 m², 225 m² and 25 m² having assigned values of a sea bottom class, and assigned proportions of mussel and sand coverage rates in a resolution of unity at 2^{-4}, i.e. {0, 1/16, 2/16, ..., 1}.

The maps for logE1, logE2 and depth contained in Figure 3.27 and 3.31 were prepared using point kriging to a 10 metres grid. This was done to give an indication of their patterns of spatial variation at a higher resolution than provided by the 30 m grid.

The resulting maps for mussel and sand proportions and the derived classified maps are depicted in Figures 3.28, 3.29 and 3.30 for the total area, the center area and the core area, respectively. The sand bottom type was not detected in the center and core areas, hence sand proportions are not depicted in Figure 3.29 and 3.30.

The coincidence between low water depths and lack of mussels is clearly visible as the lower depth limit is approx. 2 - 3 metres. The lack of mussels even allows for larger parts of the upper right in test area 1 to be classified as sand, which is a rare circumstance here, as sand is almost totally lacking from all other classified maps of test area 1. The mussel distribution found in Figure 3.28 is centered in two columns with a vertical band in the middle were mussels are more sparse than at the left and in the middle of the area, yielding a specific area at 44.1% corresponding to approx. 1.07 km² of mussels. All estimates of distribution areas are collected in Table 3.16.

The center and core areas contain no sand and an increasing specific area covered by mussels in 1996. They are depicted in Figures 3.29 and 3.30, which could have been smoothed by using contours or interpolation splines to produce smoother maps, however the raw pixels are depicted "as is" to make explicit reference to their interpretation.

It is interesting to note the indication of a mesoscale for spatial variability of mussels presented by the range of maps in Figure 3.28 - 3.30. Disregarding the change of scale the granularity or ruggedness of the classified maps in Figure 3.28 and 3.29 seems quite similar, whereas this granularity is smaller for the classified map of the core area in Figure 3.30. These grids have approx. identical relative data density, and hence this is not as obvious as it might seem. However, it is a qualitative affirmation of the estimated ranges of influence as the pixel length of 5 metres is far below these ranges and thus a high degree of spatial correlation of the mussel patches must be expected in Figure 3.30. This is masked to some degree by the large coverage exhibited by the mussels in the core area.

Table 3.16 Summary of estimated distribution areas for test area 1 and subareas hereof.

	selected		specific areas [%]			distribution areas /km²		
	area	#pixels	mussels	sand	reject	mussels	sand	reject
1996	total	2688	44.1	11.1	44.8	1.0669	0.2685	1.0838
	total[b)]	2049	56.4	1.4	42.3	1.0401	0.0258	0.7801
	center	1764	70.2	0.0	29.8	0.2786	0.0000	0.1183
	core	576	82.5	0.0	17.5	11880[a)]	0	2520[a)]
1997	total	2049	73.5	1.7	24.9	1.3554	0.0313	0.4592
	center	1764	71.8	0.0	28.2	0.2850	0.0000	0.1119
	core	576	69.4	0.0	30.6	9994[a)]	0	4406[a)]

[a)]: For the core areas the distribution areas are given in m².
[b)]: For comparison with 1997, estimates for 1996 were calculated for an area being clipped like the 1997 area.

The results for test area 1 in 1997 were prepared in the same fashion as described above, but with a slight twist due to the lack of observations in the upper right part of the total area. The results for logE1, logE2 and depth are depicted in Figure 3.31, and the sequence of mussel proportion maps and classified maps for the total area, the centered area and the core area is given in Figures 3.32 - 3.34.

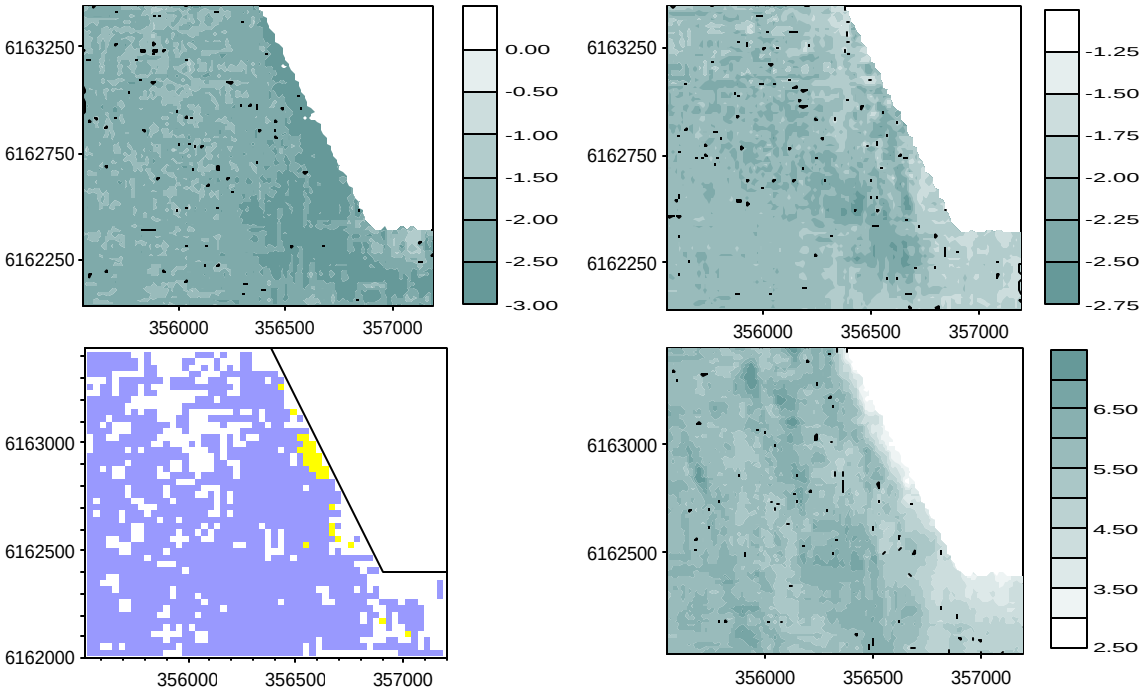

Figure 3.31 Kriged observation maps and the distribution map containing classified 30 x 30 m blocks for test area 1, 1997. LogE1 is mapped upper left, logE2 upper right, and depth lower right. The lower left depicts the classified distribution map, where blue is mussels and yellow is sand.

The coincidence between low water depths and lack of mussels cannot be reproduced in the 1997 maps due to the lack of data in the upper right. However, in the vicinity of the upper right sloped edge bordering to that part of the area, there are traces of sand in the classified map in Figure 3.32. The general pattern of the mussel distribution found in 1996, cf. Figure 3.28, is reproduced to some extent, i.e. the description of the mussel distribution centered in two columns with a sparser vertical band in the middle still applies. The 1997 map indicates that the mussels have spread into the southern part of the area, indicating a general increase in the abundance of mussels in test area 1, from 1996 to 1997. The corresponding estimates of mussel distribution area are 1.04 km² and 1.36 km² for 1996 and 1997, respectively, corresponding to an increase in specific area from 56.4% to 73.5%, cf. Table 3.16.

The indication of a (meso-)scale for spatial variability of mussels discussed for the 1996 maps is visible for the 1997 maps too. In 1997 the mussel distribution in the core area, cf. Figure 3.34, has decreased markedly compared to 1996, from 82.5% to 69.4% measured by the specific area. Most of the blank spots from the 1996 core area map, cf. Figure 3.30, are recaptured by the 1997 map of the core area, and many more blank spots have appeared in the meantime, indicating that an erosion of the mussel beds in the area has taking place.

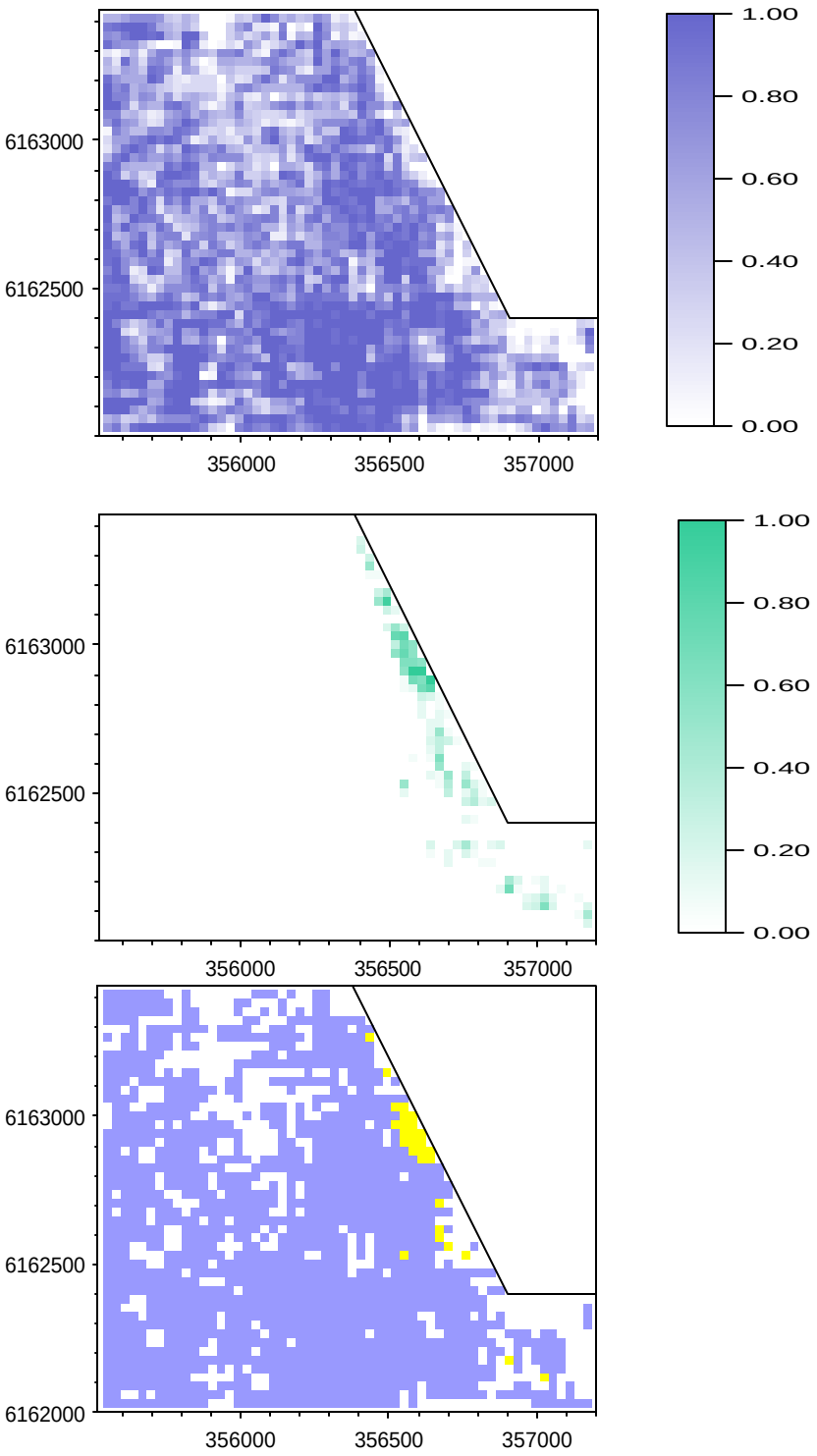

Figure 3.32 Maps for the total test area mainly covered by transects 120 metres apart, for test area 1, 1997. At the top the mussel proportions are depicted, the middle contains the sand proportions map, and at the bottom the classified map is depicted. The total area is 1680 x 1440 m^2 - 1040 x (280+820)/2 m^2 = 1.8472 km^2, and the pixel size is 30 x 30 m^2.

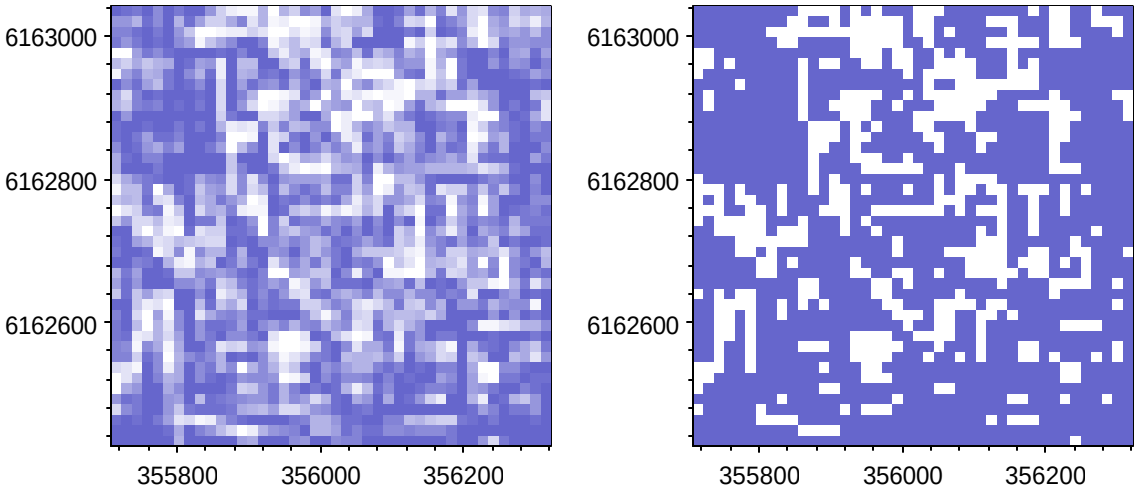

Figure 3.33 Maps for the centered area covered by transects 60 metres apart, for 1997. The left map shows the mussel proportions, and the right the classified map obtained by thresholding the left map at 0.5. The total area is 630 x 630 m² = 0.3969 km², and the pixel size is 15 x 15 m².

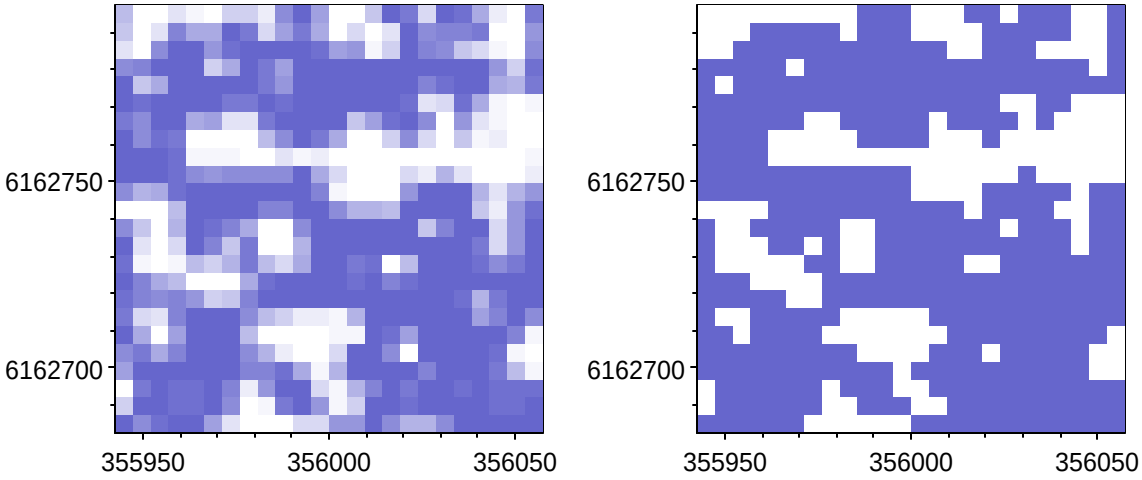

Figure 3.34 Maps for the core area covered by transects 20 metres apart. The left map shows the mussel proportions, and the right map contains the classified map. The total area is 120 x 120 m², and the pixel size is 5 x 5 m².

3.3.3 Distribution maps for test area 2, Flinterenden NW

Distribution maps for test area 2 in 1996 and 1997 have been prepared by the same method as described for test area 1 above, i.e. using square pixels with a side length of 30 metres to form a hybrid block kriging of mussel and sand proportions. The distribution maps for test area 2 in 1996 are depicted in Figures 3.35, 3.36 and 3.37, indicating huge amounts of mussels at the seabed. In particular, the degree of pixels having coverage rates at 100% or just below 100% is remarkable in Figure 3.36, indicating a large and homogeneous mussel bed in the area. At the upper western edge the depth delimitation of the mussels is reflected.

In 1997, having confirmed the abundant distribution of mussels in test area 2, the field campaign was redesigned to put emphasis on more interesting matters than monitoring large, homogeneous patches of mussels, cf. Figure 3.36. Thus, only the core part of the area was sampled in 1997. To enable some comparison between 1996 and 1997 the core part of the area was mapped for 1996 as well using square pixels with a side length at 15 metres. The estimated distribution areas and specific areas are given in Table 3.17.

Table 3.17 Estimates of distribution areas in test area 2.

	selected area		specific area			distribution area /m²		
			reject	mussels	sand	reject	mussels	sand
1996	total	2448	18.1	81.8	0.1	398779	1802218	2203
	core	595	0.2	99.8	0	268	133607	0
1997	core	595	2.9	97.1	0	3882	129993	0

In the specific areas given in Table 3.17 the abundant mussel beds in test area 2 are evident, and even more so in the core part of the areas in 1996 and 1997 having specific areas at 99.8% and 97.1%, barely a decrease worth mentioning. However, although the majority of the average coverage rates obtained for the 15 x 15 m² pixels in the maps in Figures 3.38 and 3.39 are greater than 0.5, there is a visible tendency in the mussel proportions maps of some decreases in the coverage rates.

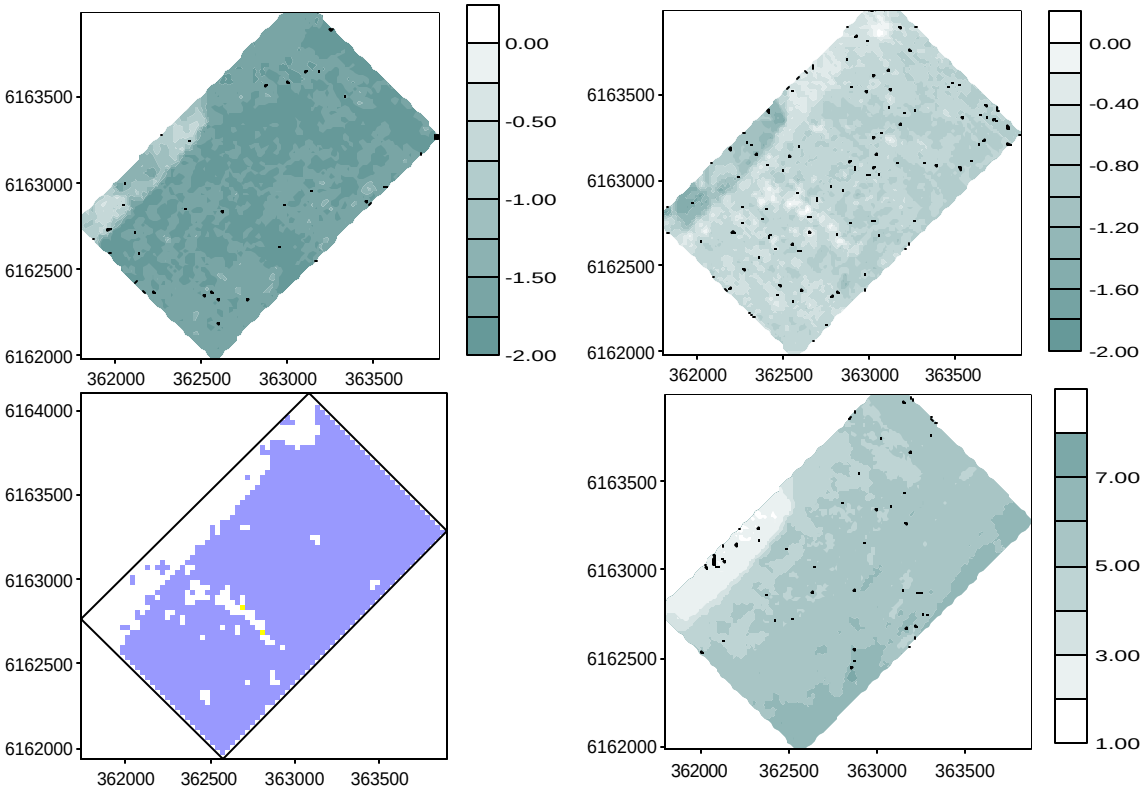

Figure 3.35 Distribution map for test area 2, 1996. LogE1 is mapped upper left, logE2 is mapped upper right, depth is mapped lower right, and lower left depicts the classified distribution map.

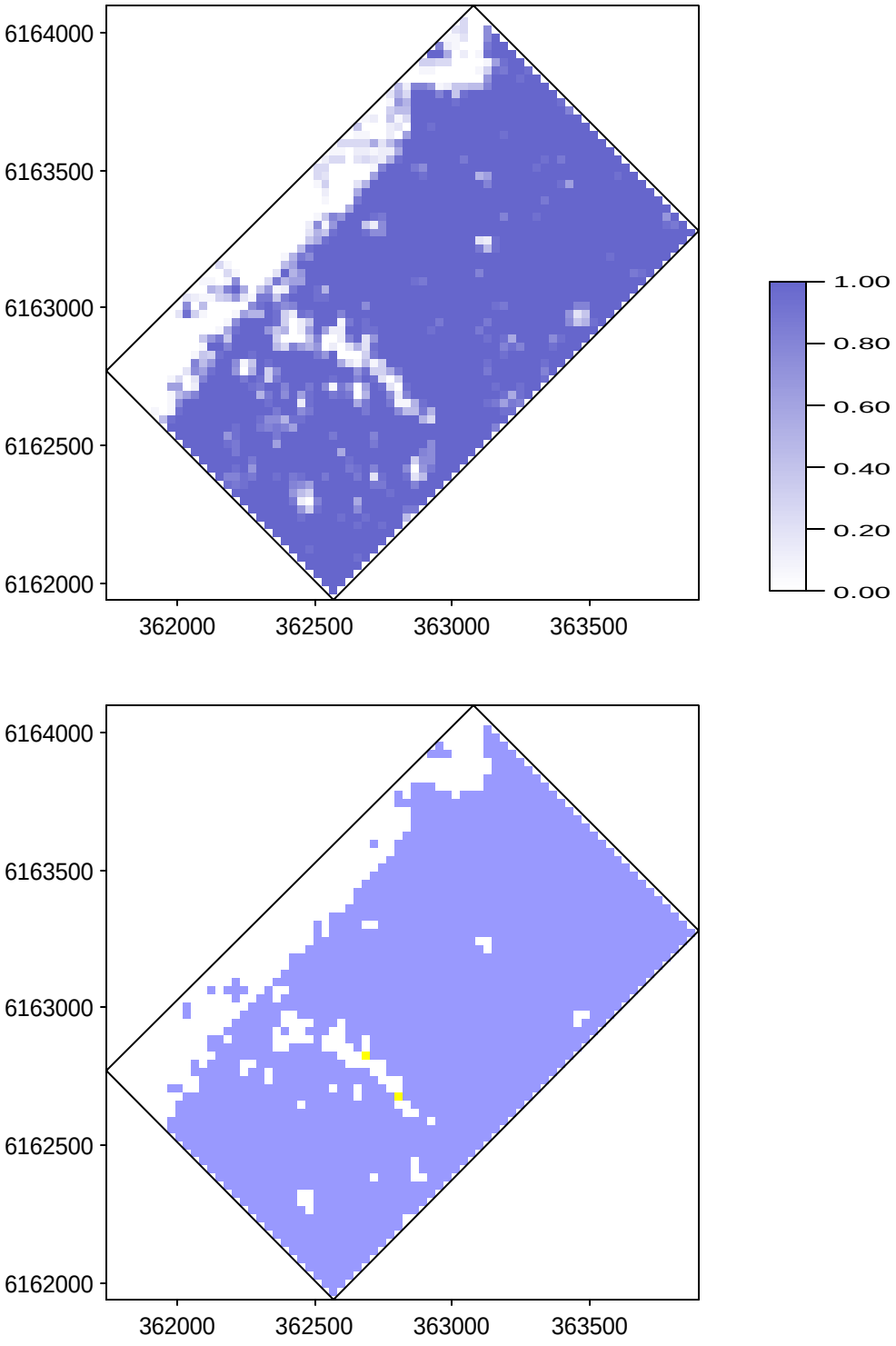

Figure 3.36 Maps for test area 2 in 1996 mainly covered by transects 120 metres apart. The upper map depicts the mussel proportions, and the lower is the corresponding classified map. The total area is 2.2032 km², and the pixel size is 30 x 30 m².

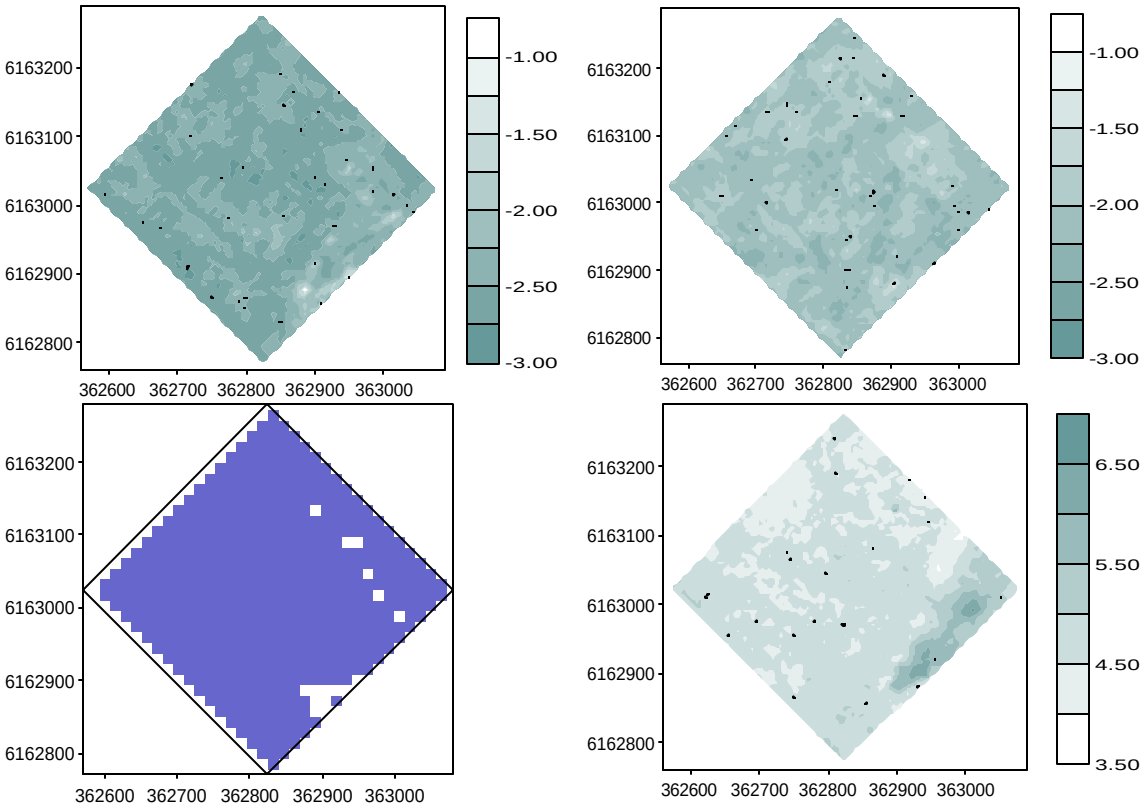

Figure 3.37 Distribution map for test area 2, 1997. LogE1 is mapped upper left, logE2 is mapped upper right, depth is mapped lower right, and lower left depicts the classified distribution map.

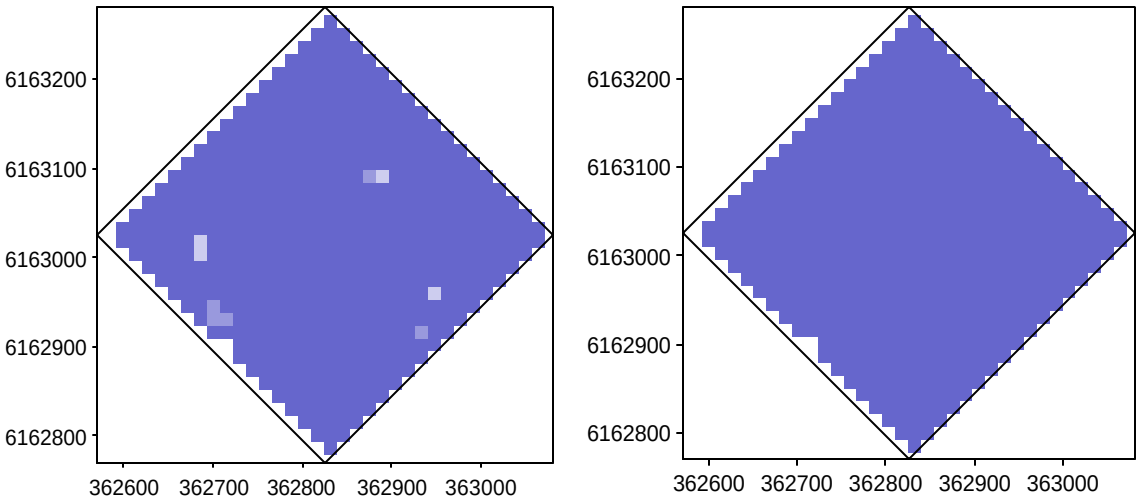

Figure 3.38 Maps for the core part of test area 2, 1996, mainly covered by transects 60 and 20 metres apart. The left map depicts the mussel proportions, and at the right the classified map is depicted. The total area is 0.1339 km², and the pixel size is 15 x 15 m².

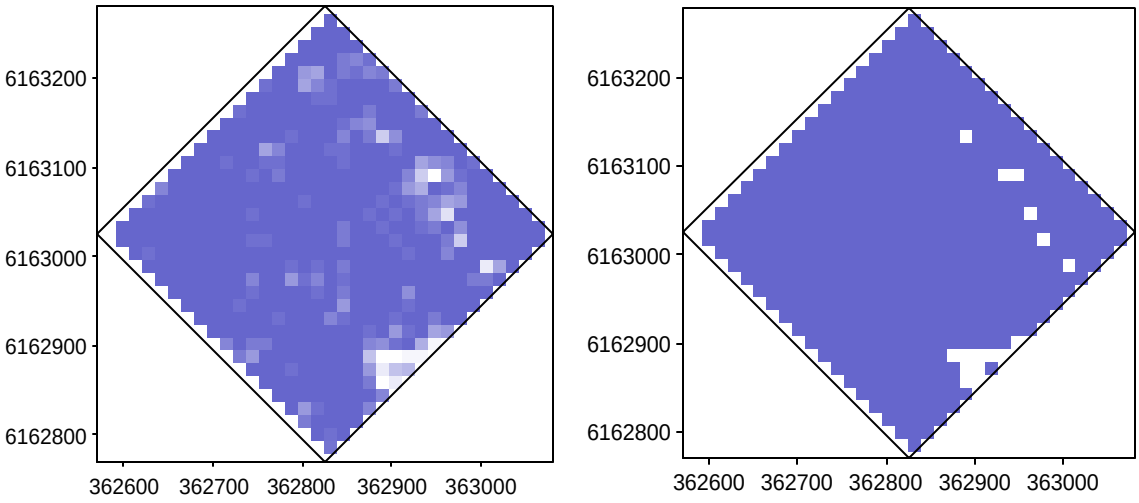

Figure 3.39 Maps for (the core part of) test area 2, 1997, mainly covered by transects 60 and 20 metres apart. The left map depicts the mussel proportions, and at the right the classified map is depicted. The total area is 0.1339 km², and the pixel size is 15 x 15 m².

3.4 Change detection in mussel distribution maps

This section illustrates a few heuristic ways of assessing the changes in mussel distribution based on the maps presented in section 3.3. Some common sense basics of spatial change detection and related hypothesis testing is discussed in Martin & Scott (1995).

One of the objectives of the BioSonar project has been to study the opportunities for change detection in the developed map preparation and data processing methodology. These opportunities can be illustrated by use of the observations recorded for test area 1, Drogden South, in Øresund. Having employed the thorough data processing scheme described and developed in the preceding sections one finally arrives at maps depicting locations of mussels, sand and the so-called reject class, representing all other bottom types. On the basis of these distribution maps it is elementary to subtract the maps of 1996 from those of 1997 to form difference maps, which have been done for test area 1 in total, for the center area, and for the core part. The resulting maps are depicted in Figures 3.40, 3.41 and 3.42, respectively, along with the distribution maps of 1996 and 1997.

As noted above it seems that the mussels have been increasing their abundance in the southern part of the area while maintaining large parts of their distribution in particular in the center of the total area bordering to the sloping edge at the upper right. To assess whether the expected correlation between the locations of sea bottom classes of 1996 and 1997 is present, a 2-way frequency table was generated using SAS, cf. Table 3.18. A χ^2-test was used to test whether the contents of the table can be assumed to be random, i.e. that the pixels of 1996 are independent of the pixels in 1997. The test result shown in the lower part of Table 3.18 strongly indicates that this is not the case here, and that indeed the pixels classified as mussels in 1996 to a large extent are classified as mussels in 1997 too, and *vice versa*.

The postulated spread of mussels in the southern part of the area in 1997 was quantified likewise by separating the area into a northern and a southern part at UTM Northings of 6162700, and then producing the 2-way tables in each part of the area. The results are depicted in Table 3.19 and show that the migration between the reject and mussel classes is about equal in the northern part, as 164 mussel pixels have vanished and 140 new mussel pixels have appeared in 1997. In the southern part, there is a marked increase in the number of mussel pixels, 46 have gone and 416 new mussel pixels have appeared, strongly underlining the visual impression of the distribution maps and their changes.

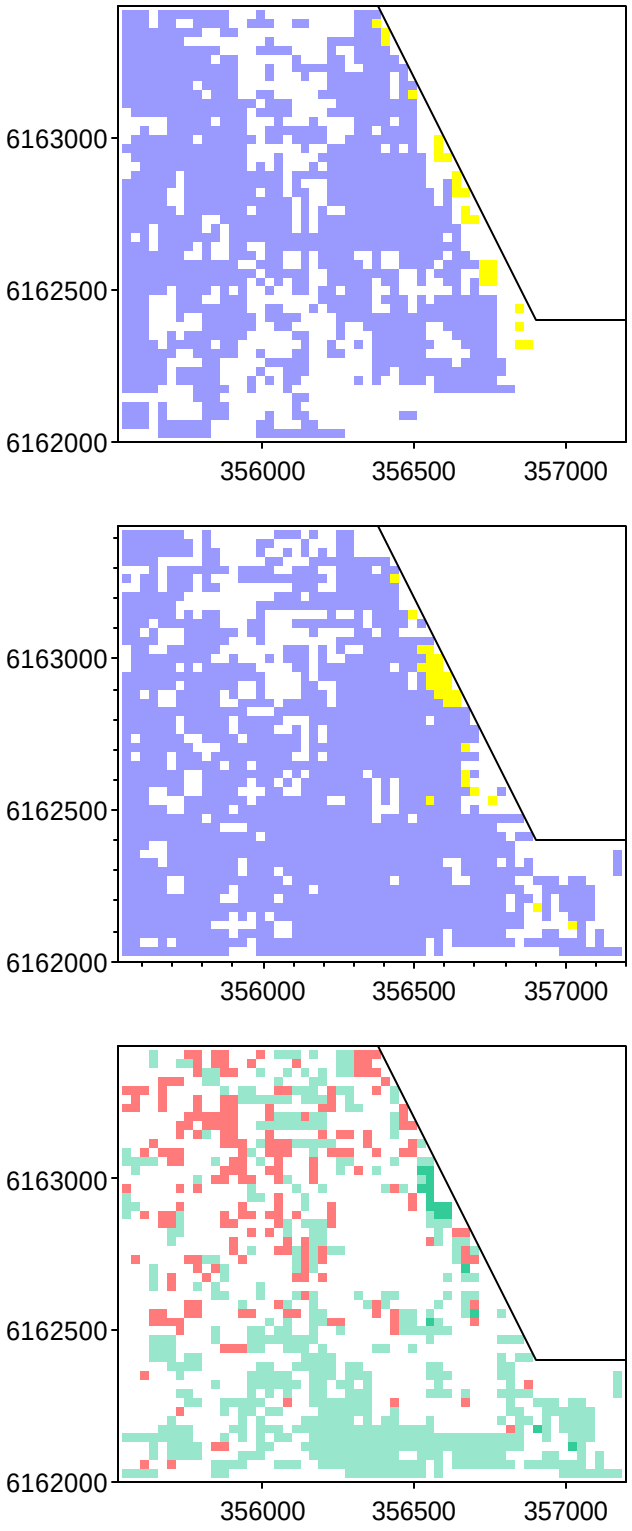

Figure 3.40 Graphical change detection for test area 1. In the map at the bottom, red (the darker colour in grayscale prints) is the color of decreases from 1996 to 1997, and green (the lighter colour) indicates increases from 1996 to 1997. At the top, the 1996 distribution map is depicted, in the middle the 1997 map is shown.

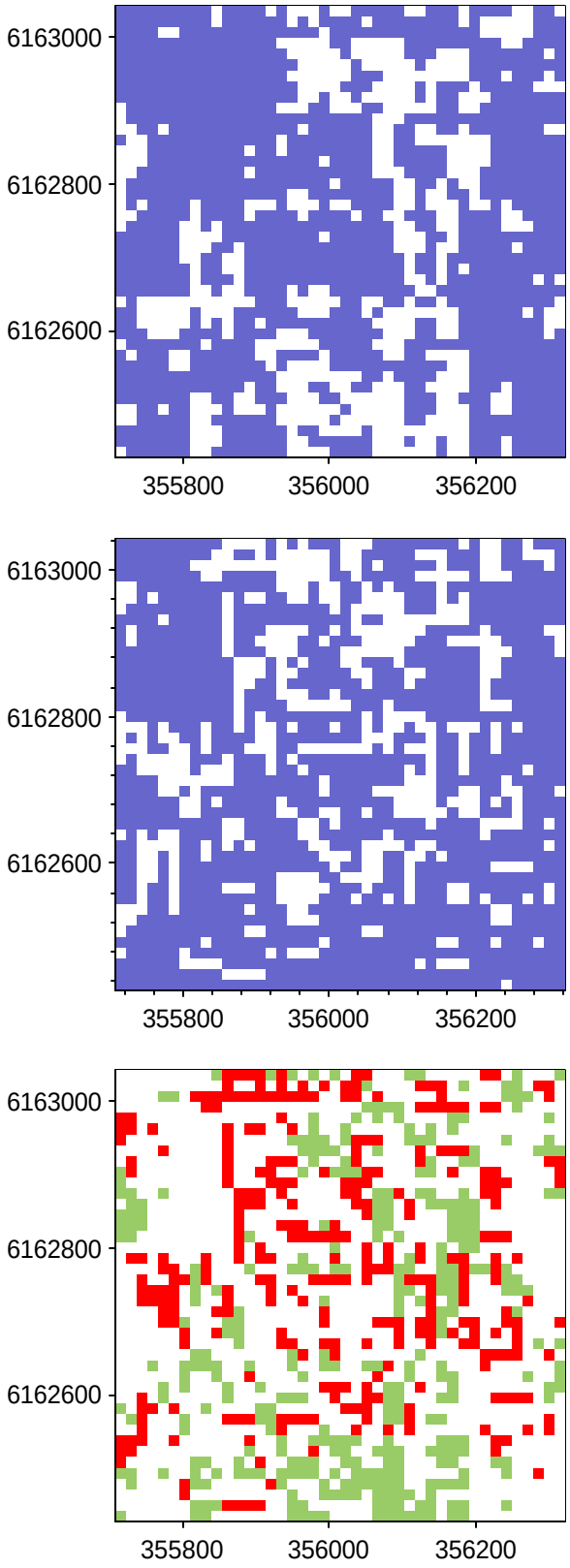

Figure 3.41 Graphical change detection for the center part of test area 1 containing transects 60 metres apart, illustrated by the classified maps. In the map at the bottom, red (the darker colour in grayscale prints) is the color of decreases from 1996 to 1997, and green (the lighter colour) indicates increases from 1996 to 1997. At the top, the 1996 distribution map is depicted, in the middle the 1997 map is shown.

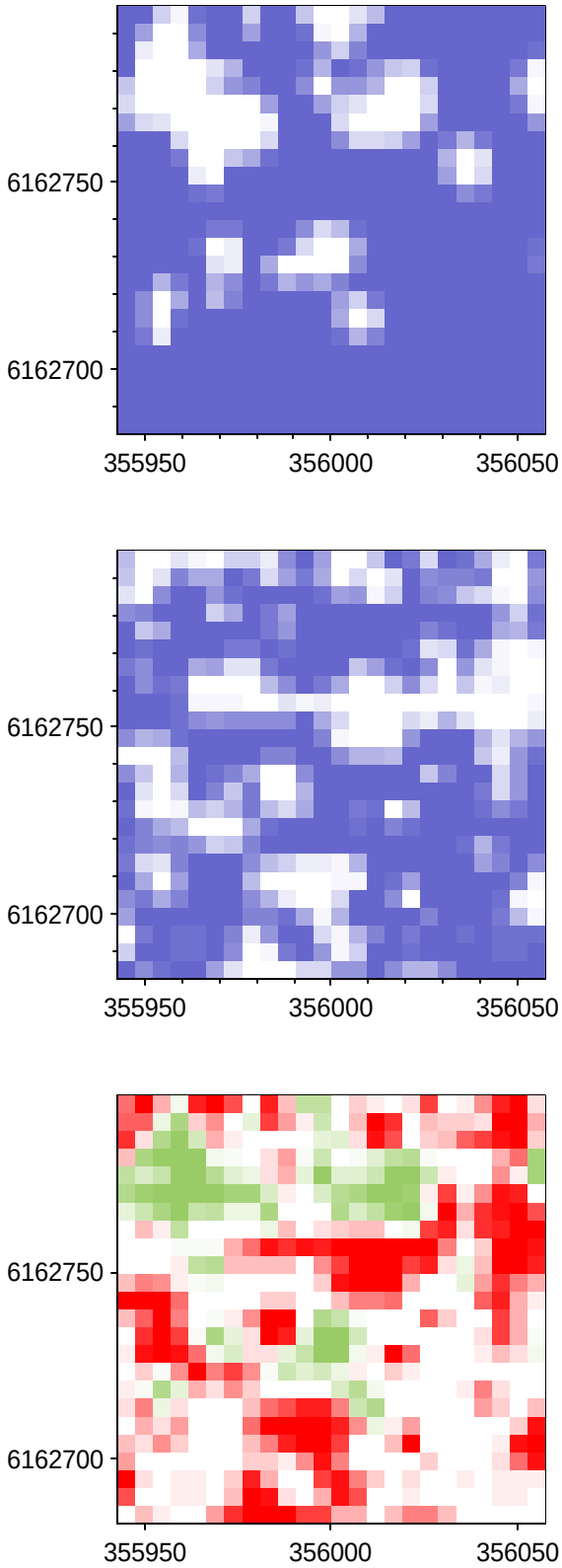

Figure 3.42 Graphical change detection for the core part of test area 1 containing transects 20 metres apart, illustrated by the mussel proportion maps. In the map at the bottom, red (the darker colour in grayscale prints) is the color of decreases from 1996 to 1997, and green (the lighter colour) indicates increases from 1996 to 1997. At the top, the 1996 distribution map is depicted, in the middle the 1997 map is shown.

Table 3.18 A categorical table of the classified pixels in the clipped test area 1 in 1997 versus the classes in 1996 (output from PROC FREQ in SAS) for the same pixels. A χ^2-test of cell independence is included in the lower part of the table.

TABLE OF CLS97 BY CLS96

CLS97 / CLS96	0	1	2	Total
0	290	210	10	510
	14.15	10.25	0.49	24.89
	56.86	41.18	1.96	
	33.49	18.18	35.71	
1	556	941	8	1505
	27.14	45.92	0.39	73.45
	36.94	62.52	0.53	
	64.20	81.47	28.57	
2	20	4	10	34
	0.98	0.20	0.49	1.66
	58.82	11.76	29.41	
	2.31	0.35	35.71	
Total	866	1155	28	2049
	42.26	56.37	1.37	100.00

STATISTICS FOR TABLE OF CLS97 BY CLS96

Statistic	DF	Value	Prob
Chi-Square	4	285.696	0.001
Likelihood Ratio Chi-Square	4	139.801	0.001
Mantel-Haenszel Chi-Square	1	48.634	0.001
Phi Coefficient		0.373	
Contingency Coefficient		0.350	
Cramer's V		0.264	

Sample Size = 2049

Table 3.19 Categorical tables of classified pixels from 1997 versus classified pixels from 1996, for the northern part (UTM Northing above 6162700) of test area 1 (the upper table) and the southern part of test area 1 (the lower table).

TABLE OF CLS97 BY CLS96

CLS97	CLS96			
Frequency, Percent, Row Pct, Col Pct	0	1	2	Total
0	98 11.15 37.12 38.58	164 18.66 62.12 27.02	2 0.23 0.76 11.11	264 30.03
1	140 15.93 23.81 55.12	441 50.17 75.00 72.65	7 0.80 1.19 38.89	588 66.89
2	16 1.82 59.26 6.30	2 0.23 7.41 0.33	9 1.02 33.33 50.00	27 3.07
Total	254 28.90	607 69.06	18 2.05	879 100.00

TABLE OF CLS97 BY CLS96

CLS97	CLS96			
Frequency, Percent, Row Pct, Col Pct	0	1	2	Total
0	192 16.41 78.05 31.37	46 3.93 18.70 8.39	8 0.68 3.25 80.00	246 21.03
1	416 35.56 45.37 67.97	500 42.74 54.53 91.24	1 0.09 0.11 10.00	917 78.38
2	4 0.34 57.14 0.65	2 0.17 28.57 0.36	1 0.09 14.29 10.00	7 0.60
Total	612 52.31	548 46.84	10 0.85	1170 100.00

3.5 Groundtruthing and verification

Having all the prepared distribution maps at hand it is stimulating to turn to reality for a while. In the following a small selection of the groundtruth data is presented, with a primary focus on the sea bottom imagery obtained during the field campaigns.

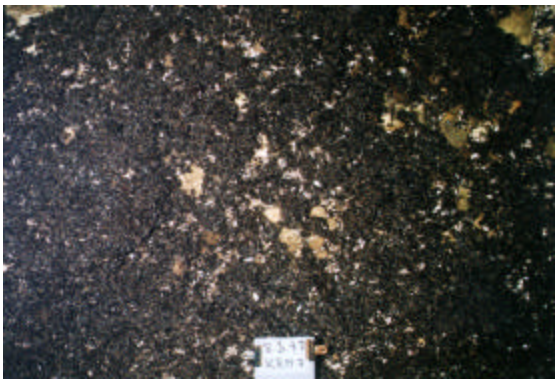

7a: (364822, 6162142)

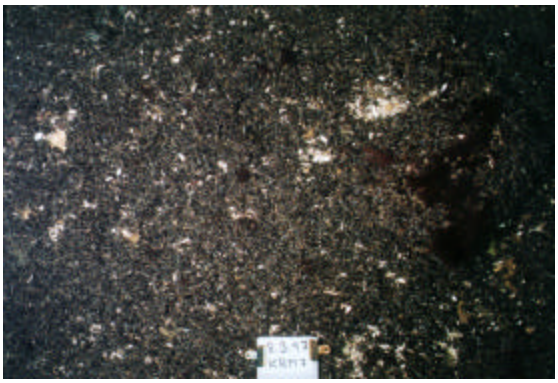

7b: (364822, 6162142)

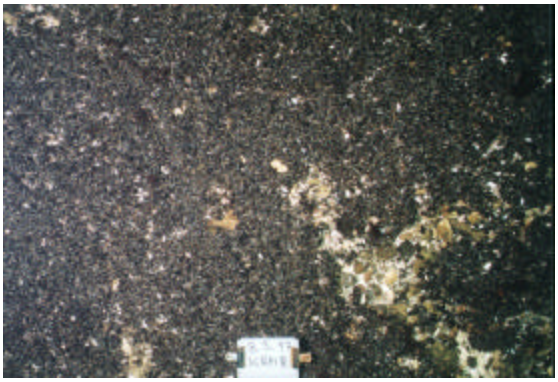

8a: (364829, 6162149)

8b: (364829, 6162149)

Figure 3.43 Groundtruthing photos from the mussel bottom type area, taken at the upper left rim of the area. Locations 7 and 8 were classified as mussels.

For the bottom type areas the photos taken at the bottom fulfilled the expectations of a smooth and homogeneous bottom coverage of mussels and sand, respectively. Figure 3.43 depicts photos taken at the locations 7 and 8 in the mussel bottom type area and the mussels are clearly abundant in these locations. All photos were made in duplicate by lowering the photo sampler twice through the water column onto the seafloor. Differences in duplicate photos are caused by the drift of the vessel in the time interval between the two photos were taken.

The size of the bottom covered by the photo sampler is approx. 2 m^2, which is quite close to the pixel size used for the bottom type areas, whereas for the test areas the basic pixel size is 30 x 30 m^2. Hence, the photos can merely give indications of the sea floor in their close surroundings in the test areas, wherefore it would be preferable to have a selection procedure for the groundtruthing sites that could adapt to proposed pixel sizes for the resulting maps. These could in turn be derived from investigations of spatial continuity based on preliminary investigations. Having a proposed pixel size at hand photos could be recorded in selected pixels at all of the 4 x 4 discretisation points used for block kriging.

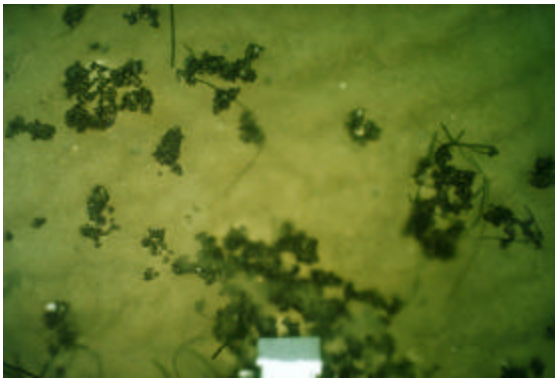

12a: (356908, 6162320)

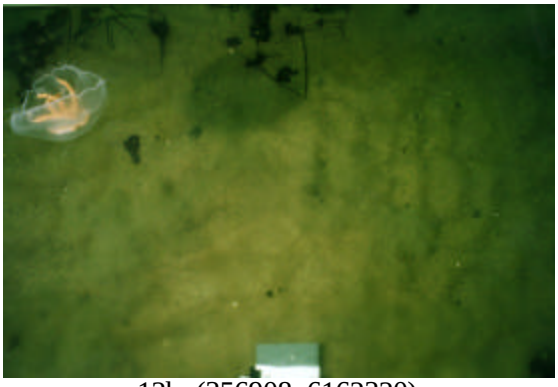

12b: (356908, 6162320)

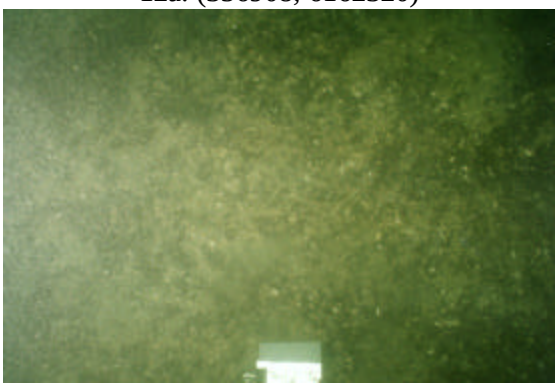

13a: (356311, 6162078)

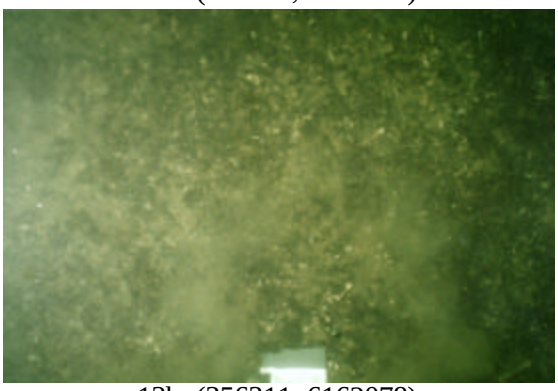

13b: (356311, 6162078)

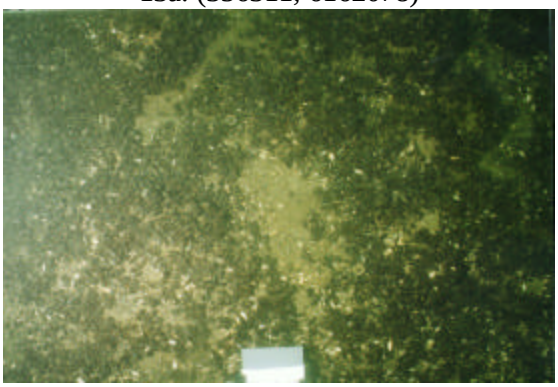

16a: (355589, 6162316)

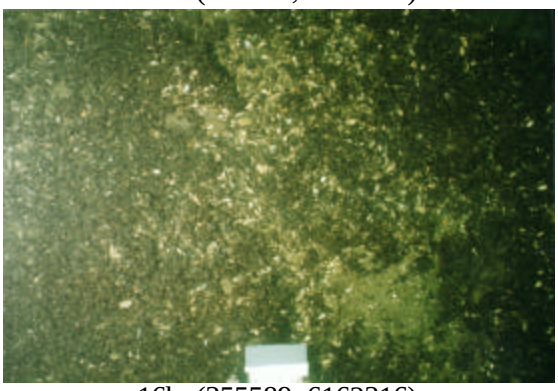

16b: (355589, 6162316)

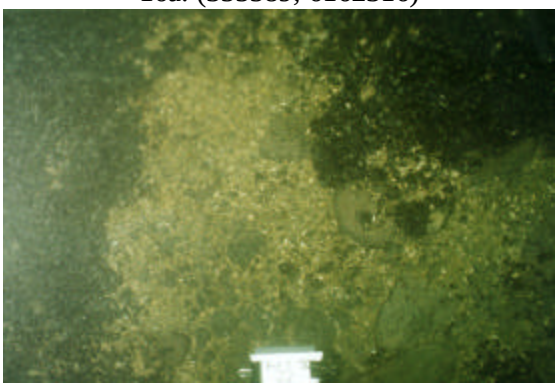

22a: (356048, 6163407)

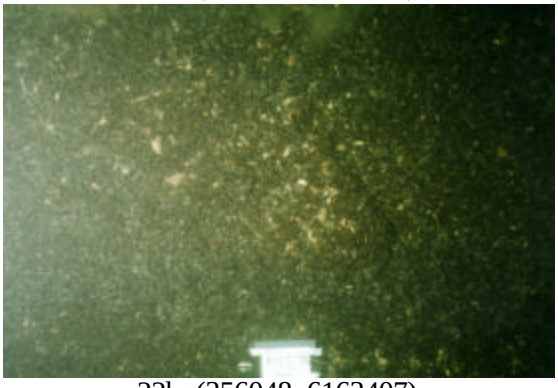

22b: (356048, 6163407)

Figure 3.44 Selected groundtruthing photos from test area 1, 1996. The locations 12, 13 and 22 were classified as rejects, i.e. neither mussels nor sand, and the location 16 was classified as a mussel seafloor, cf. Figure 3.28.

In Figure 3.44 a selection of photos from test area 1 in 1996 is shown. Three of the four locations depicted are classified as rejects on the basis of estimates of the proportion of the 900 m² pixel in which they are contained, cf. Figure 3.28. Nevertheless, the photos and the classification of the aerial elements to which they belong does make good sense, although interpretations based hereon for the larger pixels must be made with caution. Location 12 is contained in a reject pixel close to a set of pixels classified as sand in the south-eastern part of test area 1. Location 16 contained in a mussel pixel does indeed have the highest cover of mussels in the photos shown. However, the gross difference between 22a and 22b hints at the micro-scale variation exhibited by mussel beds. Thus, it is considered satisfactory to verify that the photos do not lead to rejection of the mapping results but rather support the classification results, although the difference in aerial coverage between 2 m² and 900 m² prohibits any confirmatory statements to be made.

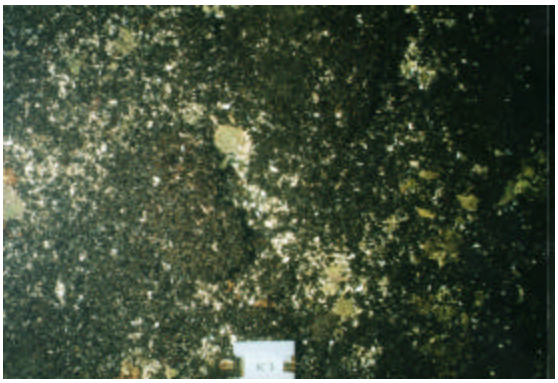

7a: (362670, 6163119)

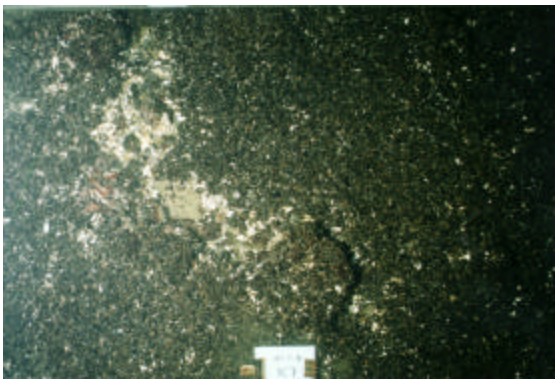

7b: (362670, 6163119)

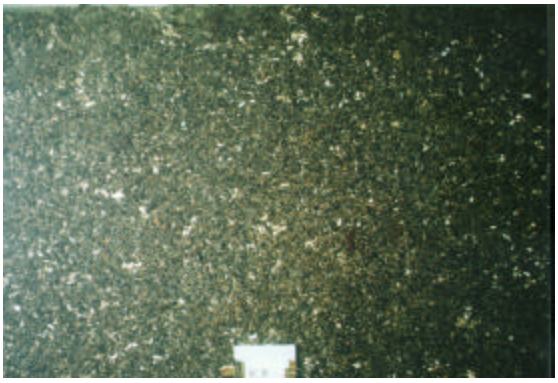

8a: (363336, 6163113)

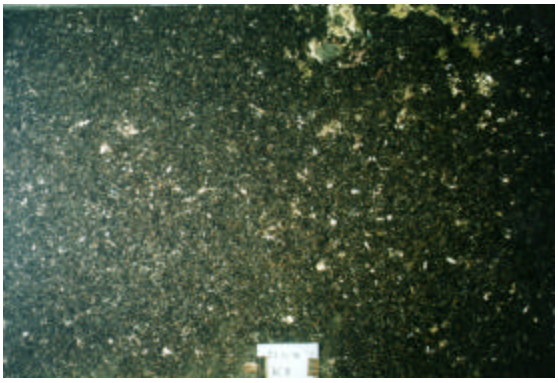

8b: (363336, 6163113)

Figure 3.45 Selected groundtruthing photos from test area 2. Locations 7 and 8 were classified as mussels, cf. Figure 3.36.

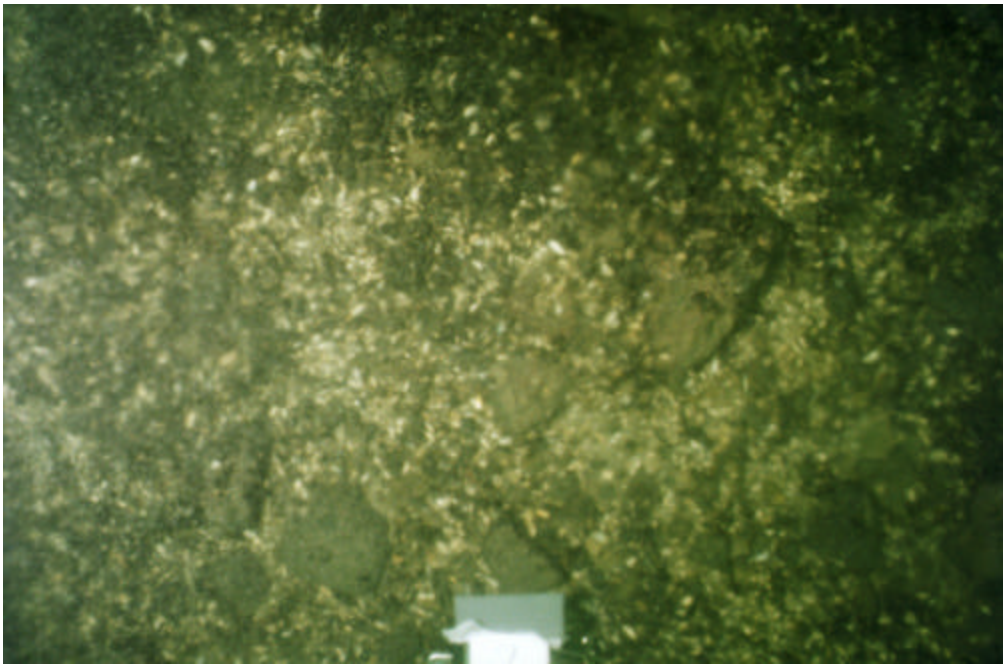

Figure 3.46 Photo from the core part of test area 1, 1996, taken at position (356046, 6162696), classified as mussels.

The selected photos from test area 2 in 1996 depicted in Figure 3.45 underpins the classification results, as they are covered entirely by mussels, except for the little sandy stripe in the middle of the photos from location 7. Finally, for the photo in Figure 3.46, the difference in aerial cover is an order of magnitude less as it was taken in the core part of test area 1, where it can be compared to the charted 5 x 5 m² pixel in which it is contained. The classification of that pixel as having more than 50% of the sea floor covered by mussels seems to be tenable.

Other means of groundtruthing are represented by video strip charts and selected video clips, that can be found in the BioSonar website (see appendix E), as well as manual transcripts of interpretations of the video contents. Table 3.20 shows a transcript example.

Table 3.20 Excerpts from a transcript of a video interpretation for tape 2, recorded October 17, in test area 1, 1996. Sand, Stones, Zostera, and Mytilus have been estimated by coverage abundance in ranks from 1-4.

Time	X	Y	Sand	Stones	Zostera	Mytilus	Comment
.....							
1405	357212	6162196	3	1	1	1	
1422	357183	6162327	2	1	3	2	Patchy
1423	357173	6162330	2	1	0	2	
1423	357165	6162332	3	1	3	1	Patchy
1423	357154	6162333	2	1	0	2	Patchy
1423	357147	6162332	4	0	0	0	
1423	357143	6162331	3	1	0	1	Patchy
1424	357128	6162323	2	1	0	2	Patchy
1424	357125	6162320	1	2	0	3	Patchy
1424	357119	6162317	3	1	1	1	
1425	357104	6162314	3	1	3	1	
1425	357080	6162316	3	1	1	1	Patchy

Transcripts like that shown in Table 3.20 are very useful in the establishing phase of the monitoring and the development of the methodology. They do not lend themselves easily to automation and/or quantification, wherefore the transcripts has the qualification that all interpretation is based on qualitative estimates made once by an operator for the purpose of a quick estimation only; multiple runs made by different operators may give quite different results.

To shed some light on the appropriateness of the proposed mapping procedure a small validation exercise was conducted in the style of Isaaks & Srivastava (1989). A vertical transect centered on an UTM Easting of 356015 was selected, and the data in the 30 x 30 m² pixels centered on this transect were compare to the results of the hybrid block kriging. For every 30 x 30 m² pixel all observations Y = (logE1, logE2)' were classified using the classification rules stipulated earlier, and the marginal proportions of mussels and sand in the observation sets were calculated. These observation based proportions were compared to the proportions obtained from kriging and classification of the 4 x 4 block discretisation points.

The results are depicted in Figure 3.47 and 3.48. In Figure 3.47 it is indicated that the kriging procedure tends to yield more polarised estimates than is indicated by the observations. For the 1997 datasets this is a valid interpretation of the results as the data density is approx. 48 observations / pixel being markedly greater than the 16 point values / pixel used in the mapping procedure. The upper left rectangles in Figure 3.47 indicates some deviation in the proportion estimates leading to differences in the classification results, which amounts to 7 / 48 = 14.6% for the 1997 dataset, and 6 / 47 = 12.8% for the 1996 dataset.

This tendency of the hybrid block kriged proportion estimates to be heavier tailed than the observation based proportion estimates is clearly visible in Figure 3.48 too. As long as the pixels contain a greater amount of data locations than discretisation points, the coarseness of the discretisation can be expected to drive the polarisation of the kriged estimates. Increasing the resolution by adding more discretisation points will not remove the polarisation, unless a scale is reached that reflects the scale of the spatial variability. This is analogous to the polarisation effect of using a winner-take-all voting system in democracies compared to the substantially smaller bias introduced by proportional representation voting systems.

Although there is some bias present, the results of this one-transect validation are considered satisfactory as the curves nevertheless exhibit the same patterns in Figure 3.48 and hence the kriging results can be relied upon to reflect to sea floor state in most cases. The earlier observation of mussels spreading south from 1996 to 1997 is underlined by the rise of the plots in the left side in 1997.

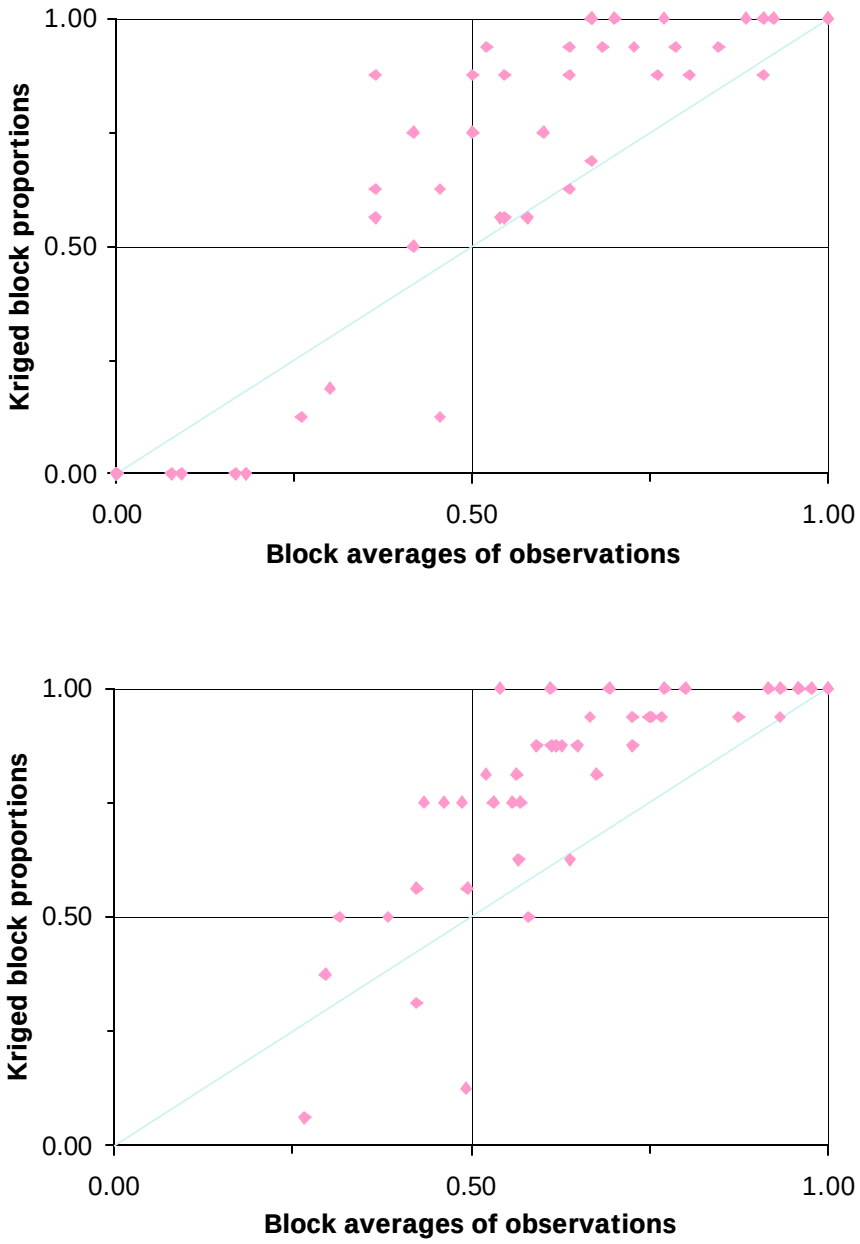

Figure 3.47 Scatter plots for kriged block proportions versus block proportions calculated by averaging of observations for the pixels centered on the vertical transect at UTM Eastings of 356315 m. The upper plot depicts the results for 1996, the lower depicts the results for 1997.

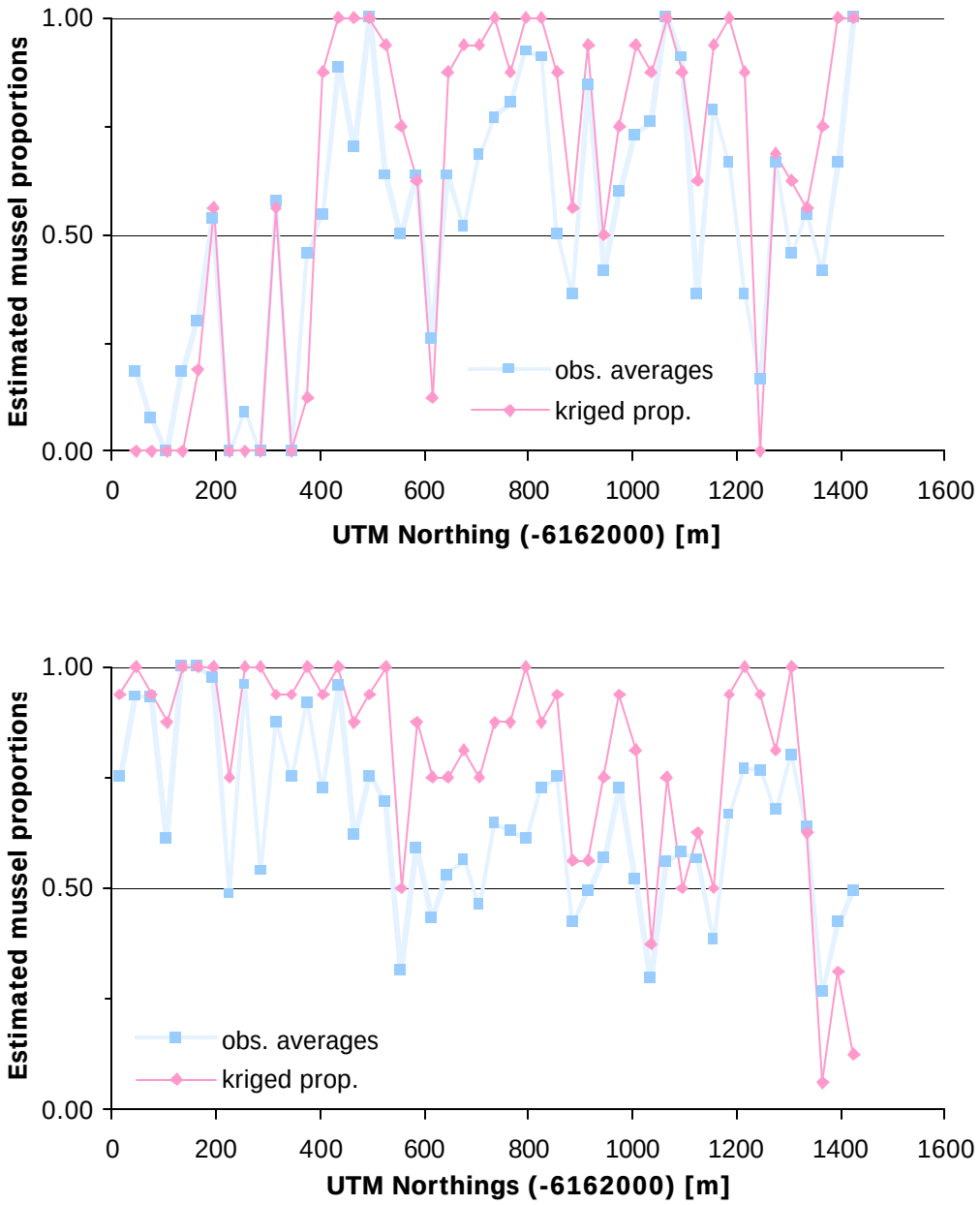

Figure 3.48 Transect line series for kriged block proportions versus block proportions calculated by averaging observations. The upper plot depicts results from 1996 and the lower reflects the 1997 results.

3.6 Summary and discussion

Let us recapitulate for a moment the path travelled through this chapter. In the spring of 1996 the field campaigns were designed to allow for enhanced results of the distribution mapping based on hydroacoustic measurements. The field campaigns were executed in the fall of 1996 and 1997, and the datasets were preprocessed to remove artefacts arising from lacks in the navigation data, etc.

The obtained datasets allowed the estimation over several scales of spatial continuity and possible anisotropy hereof. Exploratory spatial data analyses and studies of the spatial continuity established that data are basically stationary within areas, that logarithms of the observations in most cases yield good approximations to Gaussian distributions, and that actually measured values and ranges of the measurements differ markedly between 1996 and 1997 (details are given in appendix B). However, the structure of the spatial continuity was similar for the two years, and the relative positions of data in feature space were similar too. Studies of the feature spaces of data from the bottom type areas established that the hydroacoustic observations allow basic discrimination between seafloors covered with mussels, eelgrass, and sand, respectively. Thus, the data are considered reliable and the methodology is thought to be resistant to long-term instationarities emerging over years or months; it is of course vulnerable to short-term instationarities causing discrepancies between measurements made in a bottom type area and a test area within the same sea trial.

Kriging was used to interpolate maps of logE1 and logE2, which were combined and classified using the regions derived from the feature spaces of the bottom type areas. This type of classification using groundtruth and observations representing distinct classes is referred to as supervised classification in the pattern recognition literature. The devised methodology was adapted to the need for clear interpretations of the maps by using block kriging to produce (block) averages over map pixels. The kriged values representing a 4x4 points discretisation of the blocks were classified and used to calculate marginal proportions for mussels and sand for every block. This procedure makes better use of the information contained than forming block averages of logE1 and logE2 straightforwardly and classifying the single value obtained. Comparisons to results based on a transect containing data at high densities indicate that the methodology produces viable results, although tendencies towards a polarisation bias in the estimated proportions were found, i.e. estimated proportions were more frequent in the tails at approx. 0% and 100% than the observations.

To the best of this author's knowledge, the methodology to prepare spatial distribution maps developed here is unique, as regards the use of advanced data-driven methods of geostatistics in combination with selected bottom type areas and groundtruthing data. Related approaches include the traditional use of RoxAnn, and the methodologies developed and presented by the survey companies BioSonics Inc. and Quester Tangent Corp.

In the traditional use of RoxAnn (Chivers, Emerson & Burns, 1990; Chivers & Burns, 1991) users can interpret results in feature space (E1, E2) by use of a fixed classification map provided by the manufacturer Marine Microsystems Ltd. In many cases this can be expected to lead to gross misclassification rates as the fixed division of feature space using disjoint rectangles is rigid and insensitive to behaviour of actual observations, not to mention the inexorable problems encountered if the instationarities found in the BioSonar field campaigns are a widespread property of the RoxAnn measurements (which they might very well be). Therefore, although the original RoxAnn methodology presented a breakthrough making large scale sea bed classifications workable, several elaborations have been developed in acknowledgement of the shortcomings of the rigid classification procedure used in the original approach.

The contributions made by BioSonics Inc., Seattle, WA, lie in the development of more flexible feature extraction algorithms and development of the necessary hardware and software enabling this enhanced flexibility. Thus, BioSonics has developed alternative hardware devices, like e.g. the ESP Echo Signal Processor, enabling users to store digitised echo envelopes at a (user-specified) high sampling frequency. Having the full echo signal at hand allows subsequent analysis and feature extraction to be made on a qualified basis, rather than by use of two hardwired chips producing E1 and E2 in the RoxAnn device (Sabol & Burczinski, 1998). This is a promising component to include in future sea bed classification methodologies, where it is likely that adaptation of feature extraction algorithms to the domain under study as well as the objectives of the study will be a step forward.

The contributions from Quester Tangent Corporation, Sydney, Canada, lie mainly in the development of a more fine-grained classification procedure. Thus, a hardware component parallel to RoxAnn was developed by QT, which uses the digitised signal from an echo sounder to generate a feature vector containing 150 - 166 feature elements. These feature vectors are subsequently compressed into 3 feature variables by use of principal components analysis, and the 3 feature variables are then used for classification purposes (Collins & McConnaughey, 1998; Collins, Gregory & Anderson, 1996). The classifications can be either unsupervised if no groundtruth is available or supervised in the presence of training data sets (Collins & McConnaughey, 1998). Based on the experience of the present study unsupervised classification is not recommendable, at least not for the goals pursued here.

The contributions from these two companies go hand in hand focusing on separate links in the data processing chain. However, the end results are typically presented as maps containing classified transects shown as appropriately coloured line segments to depict the classification. No attempts are apparently made to let the classified transect observations enter a geostatistical framework in order to produce exhaustive thematic maps of investigated regions, and here is the link in the data processing chain where the methodology described in this chapter enters as a contribution. The approach developed here is simple, transparent and makes good use of geostatistics to produce full coverage maps with clear interpretations.

Meanwhile, RoxAnn remains the most used device for sea bed classification despite the limited resolution and precision provided, mainly because it has gained widespread use for mundane purposes like e.g., finding coral reefs or pipelines, and detecting lobsters and schools of fish. At present several of the companies mentioned are directing their research into the field of dual frequency echo sounders as a promising way of supplying an extended set of features to the sea bed classification algorithms. Alternative devices are multibeam echo sounders and side-scan sonars, which are discussed briefly in chapters 8 and 9.

As regards the inner workings of the methodology developed in this chapter the following comments can be put forth.

The kriging results rely heavily on the estimated variogram parameters which exhibited substantial degrees of uncertainty in some cases, cf. the estimation of the variograms for test area 1 in 1997, in section 3.1.4. This uncertainty could be propagated to the kriging results simultaneously with the uncertainty inherent in data by embedding the kriging in a Bayesian framework by use of Markov chain Monte Carlo methods (Diggle, Tawn & Moyeed, 1998).

The hard classification values applied here might alternatively be replaced by probability fields describing the somewhat crude proportion measures derived above. Alternatively, a probability vector for each pixel might be obtained by transforming the vector of distances from each class center (normalised by the dispersion norm) into a probability assigned to the corresponding contour ellipsoid, maybe employing some degree of thresholding at a certain quantile. Subsequently, a probability field kriging (Deutsch & Journel, 1998) could be applied and postprocessed using a threshold value like the 40% coverage rate (i.e. pixel probability value)

used in the Fixed Link studies (Sørensen, 1994b; Sørensen, 1995) to produce a binary distribution map. Another approach could be to use the reverse of linear mixture modelling, called linear unmixing (Nielsen, 1997; Settle & Drake, 1993).

Because the echo sounder data are very dense along transects and very sparse in the orthogonal directions, the order of first conducting the block kriging (by discretisation with 4x4 points for logE1 and logE2) and then subsequently classifying these points and forming proportions (by marginal frequencies within classes) might be reversed. Thereby, the dense trails of observations could be classified within a subgrid corresponding to the aforementioned 4x4 discretisation points yielding local proportion estimates based on averages of classified observations. These data derived proportions could then be subjected to block kriging, probably after use of a logit transform ($\text{logit}(p) = \log[p/(1-p)]$) on the data derived proportions to have the input to the kriging being closer to Gaussianity.

Regarding the benthic communities in question, it is seen that the separation occurs mainly along the E1 axis, i.e. the ruggedness scale (this is even more apparent when eelgrass is included, as the eelgrass observations enter the feature space in a cluster above mussels on the E1 axis). Thus, it can be argued that the echo sounder discriminates the different textures by means of the dominating grain size being reflected in the ruggedness measure. The feature space classifications are not exact, bias and variability are introduced by e.g. mussels hiding beneath seaweeds being classified as rejects, or stone and gravel at the same grain size as mussels (~ 5 cm length) being classified as mussels. Furthermore, there is no evidence that the features used here enable the discrimination between live and dead mussels. Although these qualifications should be recognised when using the spatial distribution maps, the method remains a substantial improvement for the preparation of large scale, high resolution mapping.

Regarding the size of mussel beds, the preparation of distribution maps at varying scales adapted to the varying transect densities indicated that one of the characteristic scales of mussel beds might lie in the range of 80 - 100 metres, cf. the maps for the core part of test area 1. This is a reproduction of a finding from an earlier study using another and less refined methodology (Sørensen, 1995).

Finally, methods to match the support of groundtruth data to the support of hydroacoustic observations, so-called footprints, and/or to the kriging results, e.g. based on up-scaling, should be a priority for future studies. A comparison of the hybrid block kriging method based on a winner-take-all block voting of the discretisation points within a pixel with a more traditional approach based on adjusting the variograms models to the change of support, as described in detail in Journel & Huijbregts (1978), would be interesting too.

Several benefits could be gained from a study intended to reproduce the results reported here. The drift between years could be checked, and monitoring designs could sample selected bottom type areas twice to enable a broader assessment of the precision, i.e. repeatability and reproducibility, of the measurements. Furthermore, execution of sea trials with complete navigation data rendering the pre-smoothing of coordinates within transects obsolete, would remove one of the concerns about the studies reported in this thesis.

An increase of the estimated mussel distribution area in test area 1 from 1.04 km² in 1996 to 1.35 km² in 1997 was observed. Whether this is attributable to random fluctuations or to an actual structural change cannot be judged on a statistical basis given the results at hand. The chapters 5 and 6 are devoted to addressing this question by use of geostatistics and image analysis methods.

Before moving on to that, the next chapter gives a short description of a distribution mapping study based on the Mediterranean data.

4 Spatial distribution maps for seagrasses

This chapter describes attempts made to prepare spatial distribution maps for neptune grass (*Posidonia oceanica*) and *Cymodocea nodosa* based on the Mediterranean data.

The exposition here will be based on the 1997 echo sounder data only. For a description of the 1996 datasets and attempts to use these for spatial distribution mapping the reader is referred to Schultz & Ersbøll (1998), where some inherent problems with these datasets are illustrated.

4.1 Descriptive statistics and variograms

This section gives a brief introduction to the datasets collected in the bottom type areas at Cabo de Palos in the fall of 1997 and in the test area placed in the same region, and presents the estimated semivariograms to be used in the spatial interpolation.

4.1.1 The datasets from the bottom type areas at Cabo de Palos

The monitored bottom type areas at Cabo de Palos in 1997 comprise a bottom type area with *Posidonia oceanica* at the sea floor, one covered by *Cymodocea nodosa*, and three different sand bottom type areas, covering various water depths at 13, 16 and 23 metres, respectively. The locations of the transect observations are depicted in Figure 4.1 and 4.2.

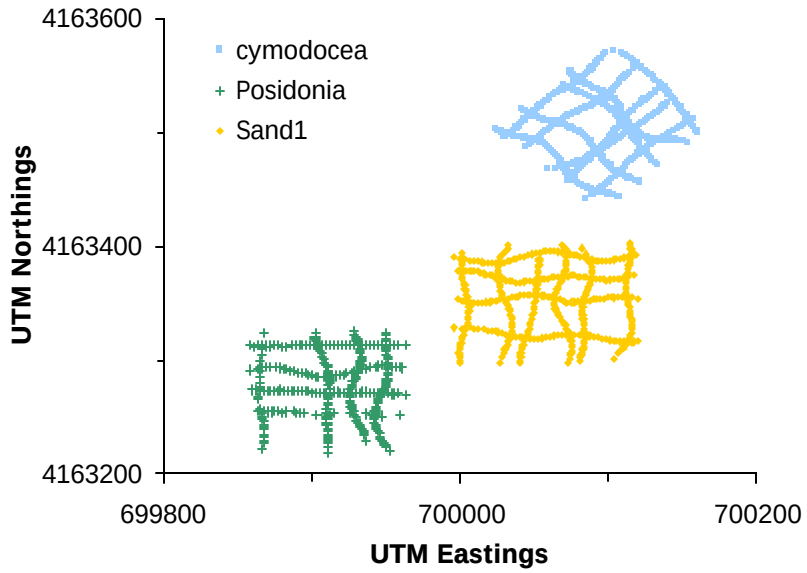

Figure 4.1 Transect grids for the bottom type areas of Cymodocea, Posidonia and sand no. 1.

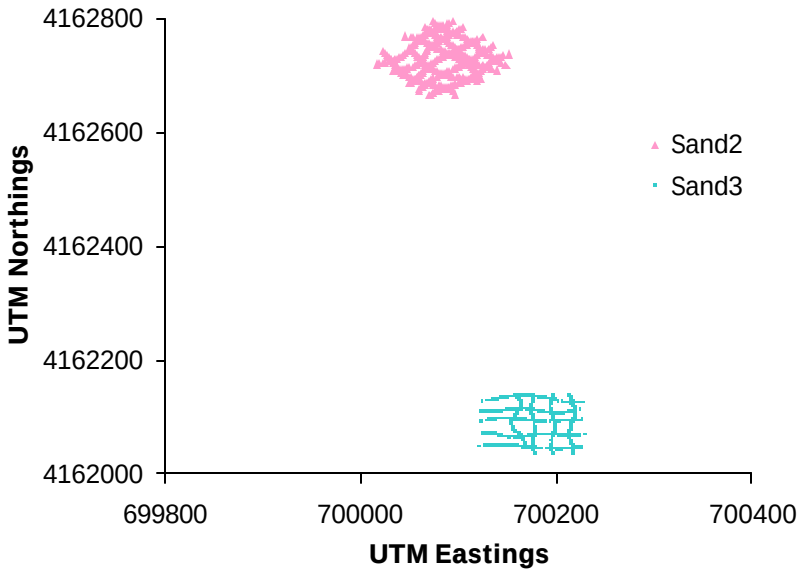

Figure 4.2 The transect grids used for the sand bottom type areas no. 2 and 3.

A collection of basic descriptive statistics are tabulated in Tables 4.1 - 4.5 for the bottom type areas. A scatter plot depicting all the bottom type datasets is shown in Figure 4.7. A few observations can be made herein:

a) The Posidonia dataset has standard deviations for logE1 and logE2 at 0.4114 and 0.6007, respectively, which are substantially greater than the standard deviations for the other bottom type areas, perhaps with s(logE2) = 0.5366 in sand area no. 2 as an exception. Whether the Posidonia dataset has been subject to (excess) noise during the collection of the observations or it is reflecting actual sea floor characteristics was not settled.
b) The skewness of logE1 is generally quite small, except for sand area no. 2. This finding is at variance with the finding in Øresund, where the skewness of logE1 was clearly greater than zero, with a few exceptions.
c) The depths are very stable, cf. the coefficients of variation in the tables, except for the Posidonia bottom type area and the sand area no. 2, where the depth variation is markedly higher than in the other areas. To investigate whether these two factors were connected descriptive statistics similar to those in Tables 4.1 - 4.5 were calculated for low depths only, but yielded no reduction in the dispersion of these datasets.
d) Figure 4.7 shows that some of the Posidonia observations have logE1 values that are lower than those found in any sand area. This was considered one of the main problems in the analyses of the 1996 data, and it is here too. Very low logE1 values correspond to a sea floor that absorbs the echo sounder pulse and returns a considerably reduced echo. It might be postulated that the morphology of some Posidonia plants having leaves spreading out at many angles could explain this absorption, yet the matter remains an open question to be investigated in the future.
e) The standard deviations of logE1 and logE2 in the Cymodocea area and sand area no. 3 are relatively low, and therefore these datasets can be expected to be nicely localised in feature space, and thus giving good opportunities for classification.

Table 4.1 Descriptive statistics for the Cymodocea bottom type area in 1997.

	E1	E2	Depth	logE1	logE2
N	396	396	396	396	396
Mean	0.2414	0.1751	12.4356	-1.4314	-1.7666
Std.dev.	0.0339	0.0394	0.3027	0.1419	0.2177
Skewness	0.1435	0.7412	-0.1028	-0.1504	0.2942
CV	14.1%	22.5%	2.4%	-	-
Range	0.164	0.211	1.8	0.7024	1.077
Q3-Q1	0.055	0.060	0.4	0.2278	0.3524
Max	0.325	0.320	13.4	-1.1239	-1.1394
Q3	0.270	0.202	12.6	-1.3093	-1.5995
Median	0.240	0.167	12.4	-1.4271	-1.7898
Q1	0.215	0.142	12.2	-1.5371	-1.9519
Min	0.161	0.109	11.6	-1.8264	-2.2164

Table 4.2 Descriptive statistics for the Posidonia bottom type area in 1997.

	E1	E2	Depth	logE1	logE2
N	311	311	311	311	311
Mean	0.2165	0.0913	13.204	-1.6071	-2.5589
Std.dev.	0.0788	0.0502	1.2537	0.4114	0.6007
Skewness	-0.0074	0.704	-4.5139	-0.6117	-0.3419
CV	36.4%	55.0%	9.5%	-	-
Range	0.334	0.260	15.29	1.8146	2.9741
Q3-Q1	0.130	0.083	0.5	0.6211	1.0312
Max	0.399	0.274	17.39	-0.9188	-1.2946
Q3	0.281	0.129	13.5	-1.2694	-2.0479
Median	0.214	0.082	13.2	-1.5418	-2.5010
Q1	0.151	0.046	13.0	-1.8905	-3.0791
Min	0.065	0.014	2.1	-2.7334	-4.2687

Table 4.3 Descriptive statistics for the sand bottom type area no. 1 in 1997.

	E1	E2	Depth	logE1	logE2
N	454	454	454	454	454
Mean	0.1558	0.094	12.9051	-1.8709	-2.426
Std.dev.	0.0239	0.0284	0.2262	0.1511	0.3814
Skewness	0.5458	-0.6415	-0.1608	0.123	-1.3586
CV	15.3%	30.2%	1.8%	-	-
Range	0.153	0.127	1.2	0.9104	1.9129
Q3-Q1	0.034	0.037	0.3	0.2202	0.3924
Max	0.256	0.149	13.5	-1.3626	-1.9038
Q3	0.172	0.114	13.1	-1.7603	-2.1716
Median	0.153	0.0995	12.9	-1.8773	-2.3076
Q1	0.138	0.077	12.8	-1.9805	-2.5639
Min	0.103	0.022	12.3	-2.273	-3.8167

Table 4.4 Descriptive statistics for the sand bottom type area no. 2 in 1997.

	E1	E2	Depth	logE1	logE2
N	345	345	345	345	344
Mean	0.2963	0.0557	16.1203	-1.2371	-3.0079
Std.dev.	0.0771	0.029	1.3684	0.1858	0.5366
Skewness	5.7205	0.7261	-0.7532	2.2568	-0.7148
CV	26.0%	52.1%	8.5%	-	-
Range	0.892	0.294	6.7	2.2946	3.0706
Q3-Q1	0.045	0.029	2	0.1552	0.5632
Max	0.992	0.194	18.3	-0.008	-1.6399
Q3	0.313	0.068	17.2	-1.1616	-2.6809
Median	0.286	0.054	16.5	-1.2518	-2.9188
Q1	0.268	0.039	15.2	-1.3168	-3.2442
Min	0.1	-0.1	11.6	-2.3026	-4.7105

Table 4.5 Descriptive statistics for the sand bottom type area no. 3 in 1997.

	E1	E2	Depth	logE1	logE2
N	387	387	387	387	387
Mean	0.3958	0.1712	23.3641	-0.9323	-1.7719
Std.dev.	0.0403	0.0197	0.4314	0.1057	0.1168
Skewness	-0.4394	0.0594	-0.0575	-0.7679	-0.3234
CV	10.2%	11.5%	1.8%	-	-
Range	0.24	0.122	2.8	0.6503	0.7187
Q3-Q1	0.047	0.026	0.6	0.1175	0.1523
Max	0.502	0.238	24.6	-0.6892	-1.4355
Q3	0.424	0.184	23.7	-0.858	-1.6928
Median	0.396	0.171	23.3	-0.9263	-1.7661
Q1	0.377	0.158	23.1	-0.9755	-1.8452
Min	0.262	0.116	21.8	-1.3394	-2.1542

4.1.2 The dataset for the test area at Cabo de Palos

A summary of descriptive statistics for this dataset is given Table 4.6. The standard deviations for logE1 and logE2 are at the same level as found for the Posidonia bottom type dataset, which is not surprising as the area is large and covered with a heterogeneous blend of sea floor types.

Table 4.6 Descriptive statistics for the test area at Cabo de Palos in 1997.

	E1	E2	Depth	logE1	logE2
N	19789	19789	19789	19789	19789
Mean	0.3098	0.1447	16.402	-1.227	-2.1245
Std.dev.	0.1101	0.0954	4.5337	0.3265	0.6235
Skewness	1.6471	1.6973	0.0572	0.275	-0.0602
CV	35.5%	65.9%	27.6%	-	-
Range	1.308	0.861	23.5	2.6264	5.663
Q3-Q1	0.127	0.104	8	0.4336	0.84
Max	1.41	0.864	27.7	0.3436	-0.1462
Q3	0.361	0.183	20.6	-1.0189	-1.6983
Median	0.287	0.117	15.2	-1.2483	-2.1456
Q1	0.234	0.079	12.6	-1.4524	-2.5383
Min	0.102	0.003	4.2	-2.2828	-5.8091

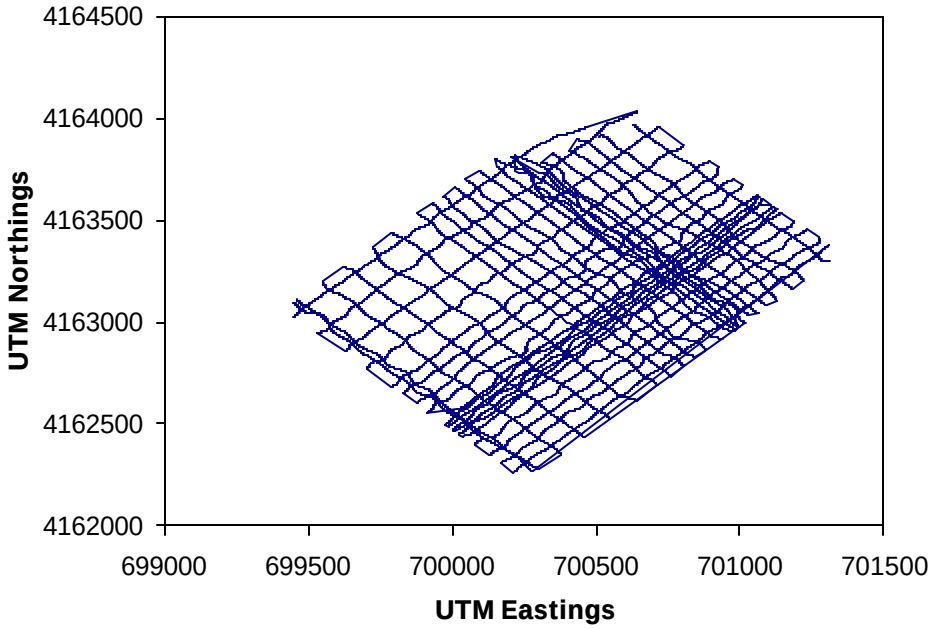

Figure 4.3 The transect grid applied in the Cabo de Palos test area in 1997.

The transects used in the test area in 1997 are depicted in Figure 4.3, and a scatter plot of all observations is depicted in Figure 4.4.

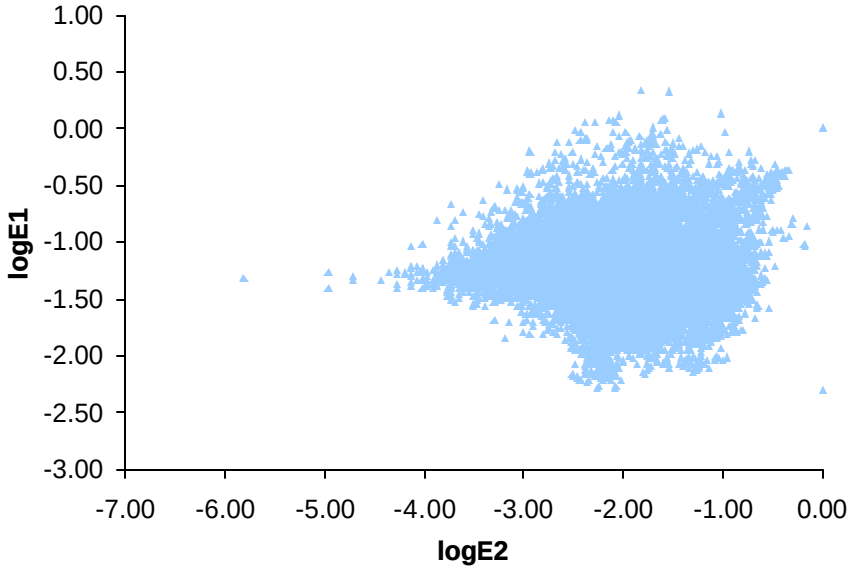

Figure 4.4 A scatter plot of logE1 versus logE2 for the Cabo de Palos test area 1 in 1997.

The contour of the scatter cloud in Figure 4.4 is shaped like a droplet much alike the shapes seen for the test areas in Øresund. It is a curiosity that the droplet shape in Figure 4.4. is tilted by 90° compared to those found in Øresund, cf. Figure B.9, suggesting that the variables have been swapped. However, several checks verified that this was not the case.

4.1.3 Semivariograms

Semivariograms for the observed values of log E1 and log E2 in the test area were calculated by use of the program GAMV from the GSLIB collection, version 2.0. Lag sizes of 5 metres were chosen. The SAS procedure PROC NLIN was used to estimate the coefficients of the exponential semivariogram models based on sample semivariogram data for ||h|| < 150 metres. The estimated coefficients of the variograms are given in Table 4.7, and the estimated variogram models are illustrated in Figures 4.5 and 4.6.

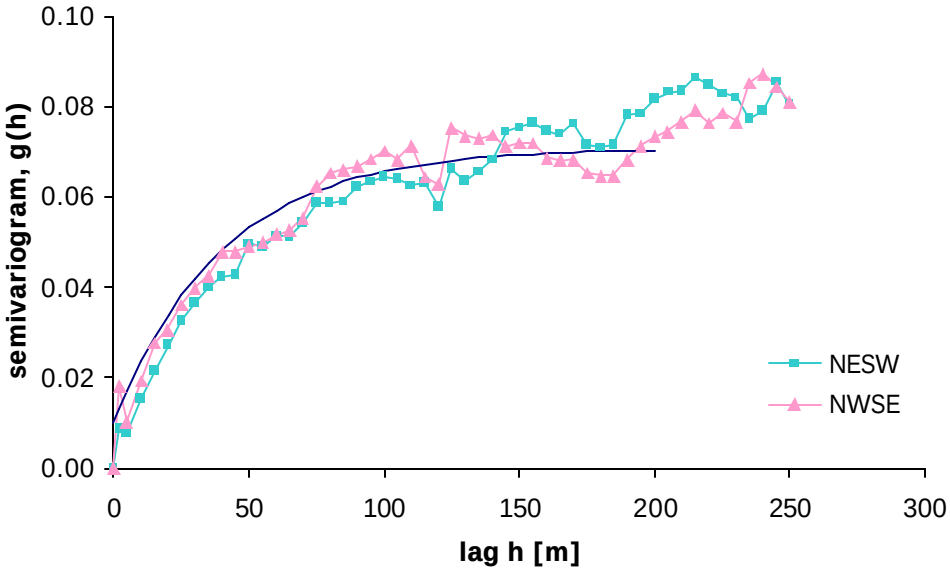

Figure 4.5 Sample semivariograms for NW-SE and NE-SW directions and the estimated exponential model for log E1 in the Palos test area.

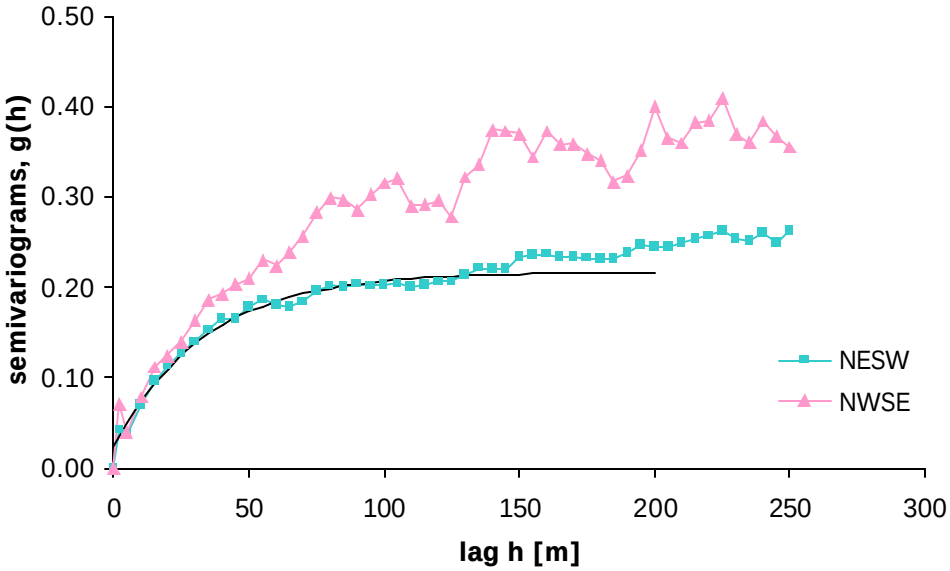

Figure 4.6 Sample semivariograms for NW-SE and NE-SW directions and the estimated exponential model for log E2 in the Palos test area.

Table 4.7 Estimated parameters for exponential variogram models for logE1 and logE2 in test area 1 in Cabo de Palos.

	log E1	log E2
C0	0.0102	0.0235
C1	0.0606	0.1934
R	121.4	100.7
sill	0.0708	0.2169
nugget	14.4%	10.8%

For logE1 the variogram model was estimated using the omni-directional sample variogram, as the semivariograms in Figure 4.5 seem quite isotropic. For logE2 there is a solid zonal anisotropy for lags above 50 metres in that the sill in the direction from north-west to south-east is clearly higher than the sill for the perpendicular direction. As the mesoscale (and microscale) contributions to the spatial continuity are important to model here, the semivariogram model was fitted to the sample semivariogram for the lags along the north-east to south-west orientated transects.

The ranges found for the variogram model, cf. Table 4.7, are remarkably high compared to the ranges found in Øresund lying at values of 10 - 40 metres with one exception at 66 metres.

4.2 Feature space classification

An introduction to classification based on discriminant analysis is given in section 3.3. The feature space containing observations from the five selected bottom types areas is depicted in Figure 4.7, in which it is evident that the Posidonia observations are represented as a large, diffuse cloud surrounding the population of Cymodocea measurements and the 3 scatter clouds obtained from sand bottom type areas. Thus, they cannot be discriminated from the localised scatter clouds of the other bottom types, and it is not considered feasible to use the Posidonia observations in a classification based on traditional discriminant analysis.

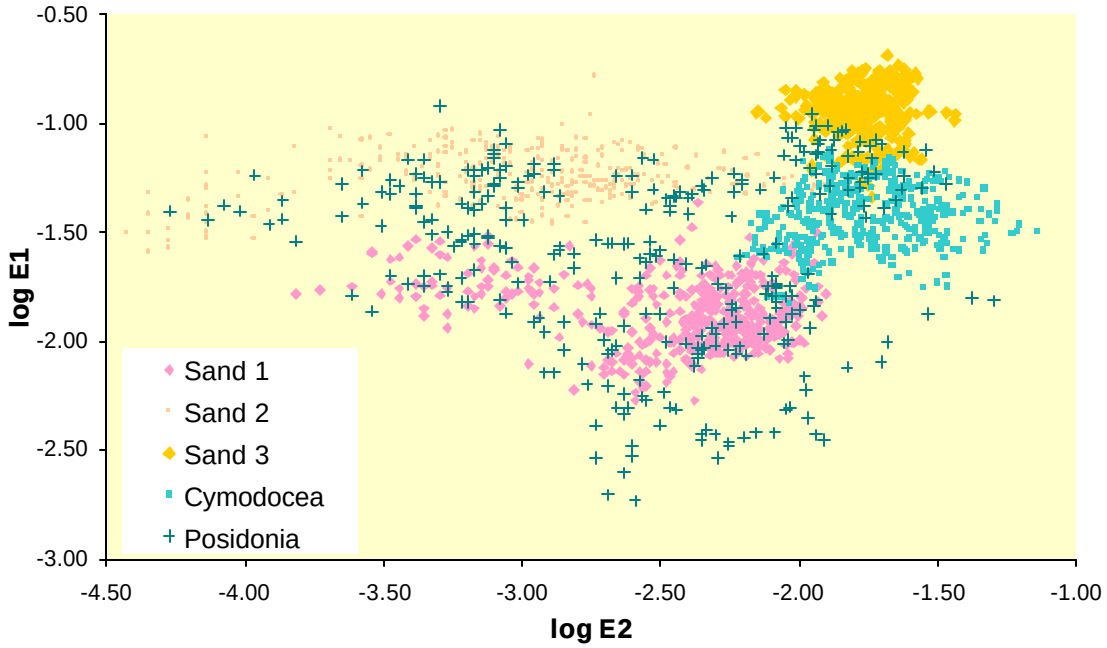

Figure 4.7 The feature space for the Mediterranean RoxAnn data from 1997 at Cabo de Palos.

Alternative methods of classification were sought that would accommodate the Posidonia dataset, and the minimum/maximum autocorrelation factors (MAF) transformation was tested. Introductions to the MAF transform are given in Ersbøll (1989) and Nielsen (1994), the seminal paper being that of Switzer & Green (1984). The MAF transform minimises the autocorrelation rather than maximising the data variance, as is done by principal components. A calculation of the MAF transforms for logE1 and logE2 was prepared by Associate Research Professor Allan Aasbjerg Nielsen, IMM, based on an adaptation of the MAF transform to irregular data given in Nielsen (1994). The results are shown in Figure 4.8.

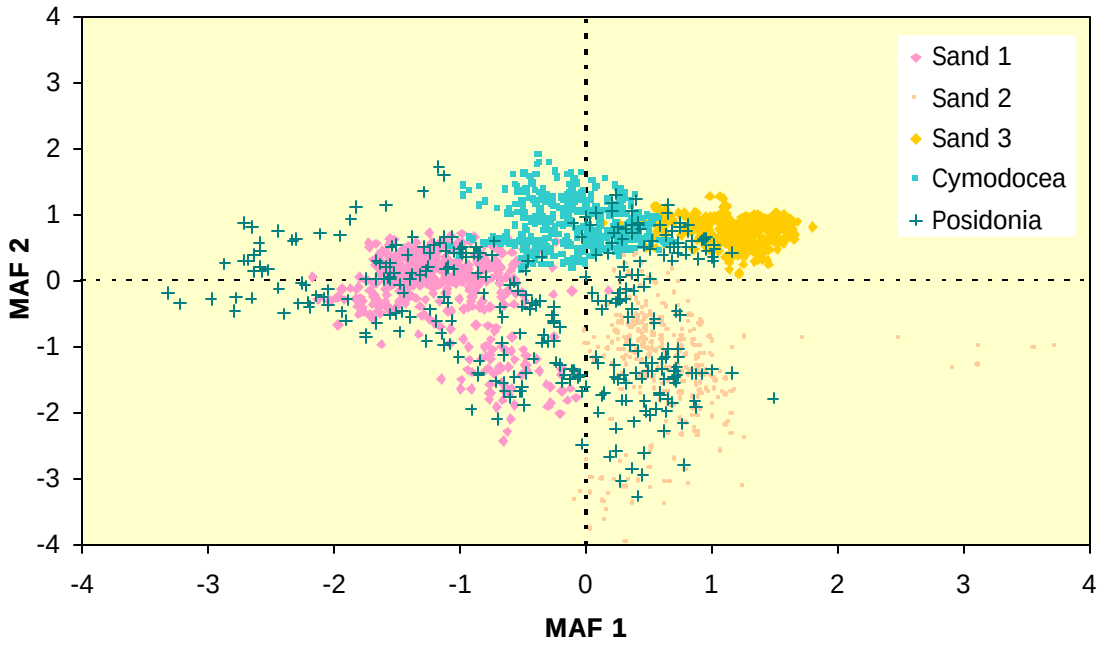

Figure 4.8 MAF_2 vs. MAF_1 for the bottom type areas at Cabo de Palos, 1997.

The results were not encouraging, and the aim of including Posidonia in the classification and subsequent distribution mapping was not pursued any further. A possible next step could be to adapt the Owen-Hjort-Mohn (OHM) classification algorithm to irregular data and test it on the Posidonia dataset. OHM classification (Ersbøll, 1989) forms feature vectors by transforming any observation vector x into the expanded vector

$$x_{OHM} = (x', x_L', x_R', x_A', x_B')'$$

where x_L, x_R, x_A, x_B denotes the neighbour observations at the left, right, above, and below the observation x. If x has d dimensions then x_{OHM} will have 5d dimensions and therefore the use of x_{OHM} extend the scope for classification considerably. However, the extension of this algorithm from usage on a regular lattice to irregular data is not a simple task.

It is evident in Figure 4.7 that the population of Cymodocea measurements is sufficiently separated from the 3 sand populations, and therefore a classification based an usual quadratic discriminant analysis was carried out after exclusion of the Posidonia dataset, using PROC DISCRIM in SAS with uninformed priors, i.e. all being equal. The resulting resubstitution rates, given in Table 4.8, are quite satisfactory indicating that this is a feasible way to proceed.

Table 4.8 Resubstitution rates for the four bottom types used in the classification. Class 1 is Cymodocea, and classes 2, 3, and 4 correspond to sand areas no. 1, 2, and 3, respectively.

From CLS	1	2	3	4	Total
1	381 96.2%	9 2.3%	0 0.0%	6 1.5%	396 100%
2	13 2.9%	424 93.4%	17 3.7%	0 0.0%	454 100%
3	13 3.8%	0 0.0%	331 96.2%	0 0.0%	344 100%
4	13 3.4%	0 0.0%	3 0.8%	371 95.9%	387 100%
Total Percent	420 26.6%	433 27.4%	351 22.2%	377 23.9%	1581 100%

4.3 Spatial distribution maps for *Cymodocea nodosa*

A spatial distribution map for *Cymodocea nodosa* and sand has been prepared based on ordinary point kriging of log E1 and log E2 in the test area followed by a classification of the pixels by entering logE1 and logE2 into the classification conducted by PROC DISCRIM in SAS. Figure 4.9 depicts the resulting map comprising 2 classes, viz. sand and Cymodocea, i.e. the 3 sand classes have been merged in the map, and Table 4.9 holds the pixel counts for the 4 classes.

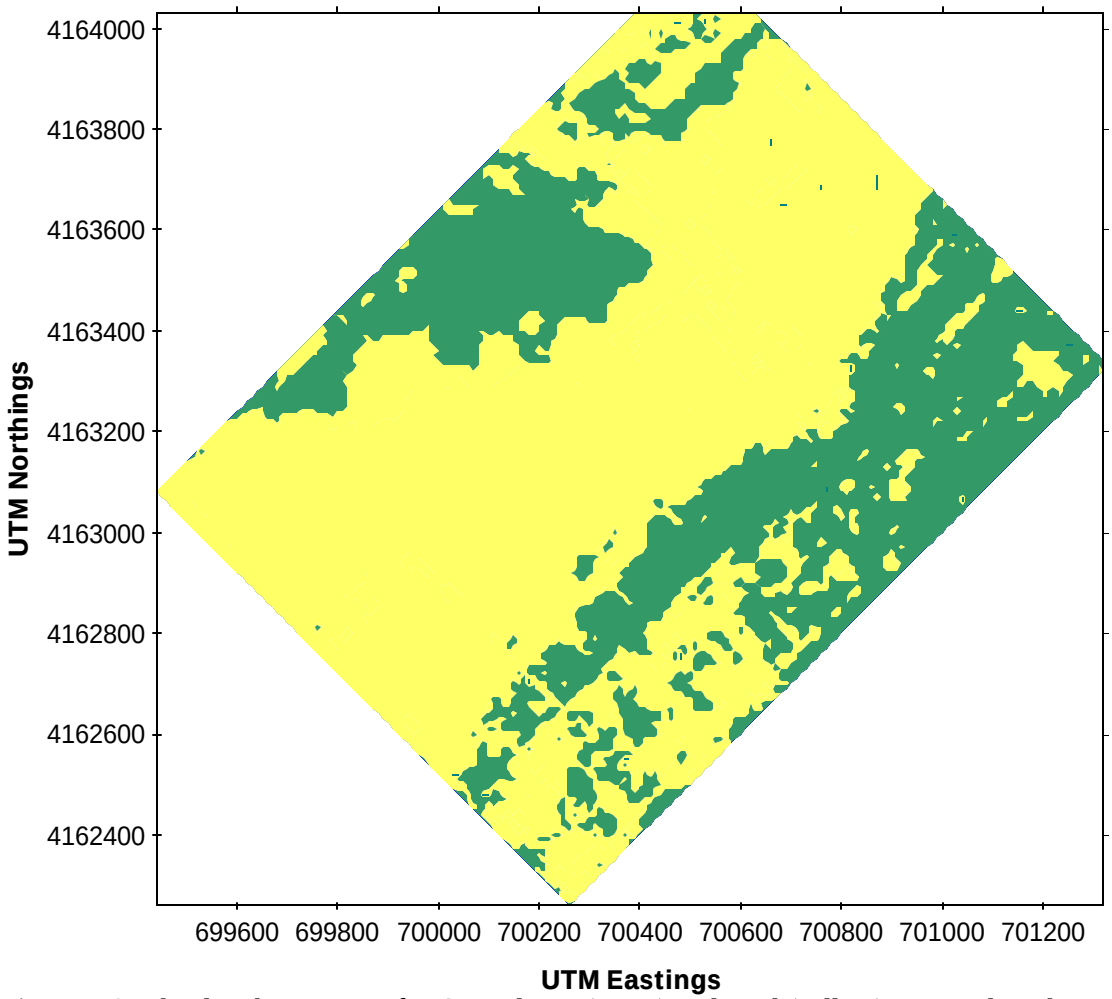

Figure 4.9 The distribution map for Cymodocea (green) and sand (yellow) prepared on the basis of RoxAnn measurements. In grey scale yellow is lighter and green is the darker colour.

Table 4.9 The counts of pixels for the four populations entering the sea bed classification.

CLASS	Frequency	Percent	Cumulative Frequency	Cumulative Percent
Cymodocea	5707	32.4	5707	32.4
Sand 1	1347	7.7	7054	40.1
Sand 2	8909	50.6	15963	90.7
Sand 3	1630	9.3	17593	100.0

The pixel colour counts in Table 4.9 were multiplied by the pixel size of 10 x 10 m² yielding a distribution area estimate at 0.5707 km² of the spatial distribution of *Cymodocea nodosa*.

Comparison with side-scan sonar based maps

The distribution map in Figure 4.9 can be compared to the distribution map for the same area prepared on the basis of side-scan sonar mosaics by Patricia Siljeström and Adela Moreno at IRNASE in Sevilla. This map is depicted in Figure 4.10 and contains segmentations of Posidonia, Cymodocea and sand. It is clearly visible how the contour of the area classified as

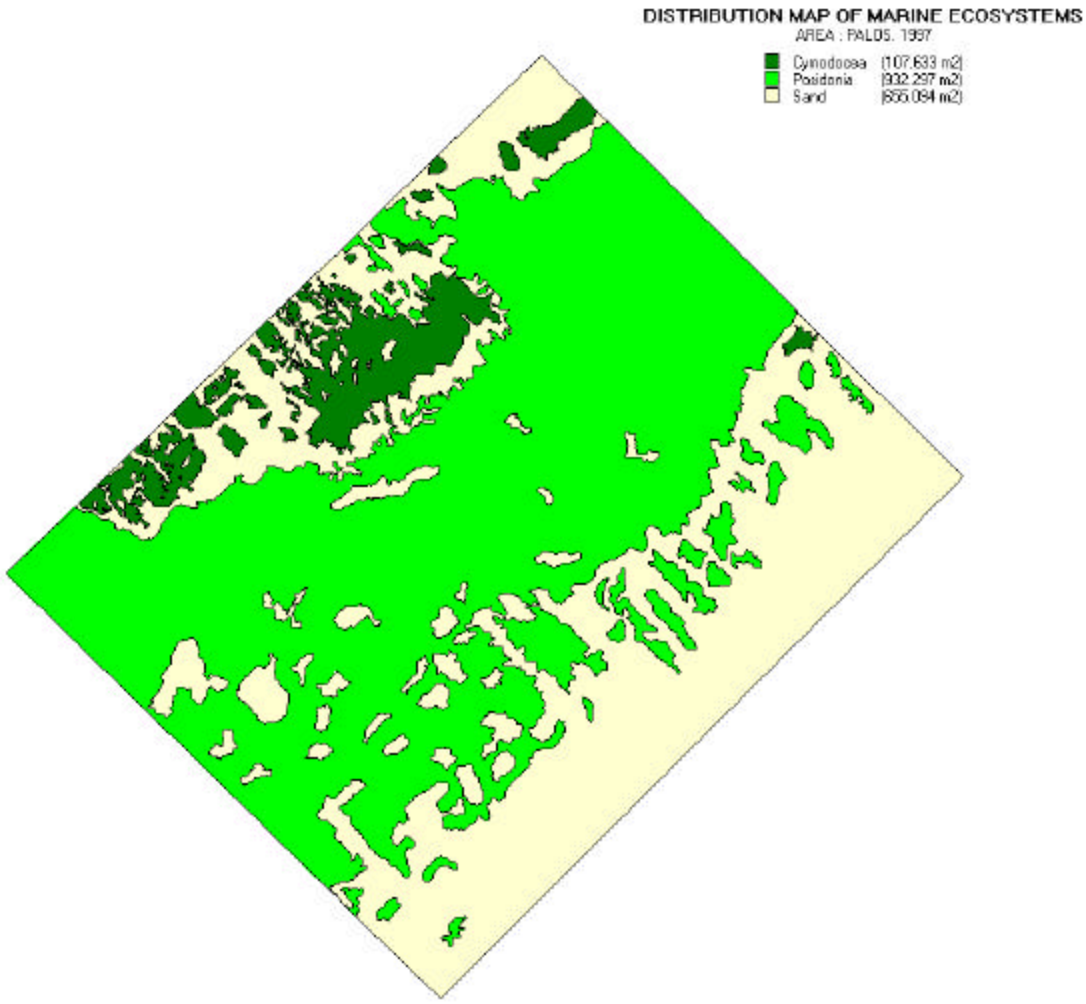

Figure 4.10 The distribution map for Cymodocea and Posidonia at Cabo de Palos, 1997, prepared on the basis of side-scan sonar mosaics.

sand based on echo sounder measurements in Figure 4.9 resembles the contour of the area classified as Posidonia in the side-scan sonar based distribution map. This is quite understandable, as the Posidonia class was excluded from the analysis of the RoxAnn data.

4.4 Discussion

The spatial distribution map for Cymodocea can be regarded as being tentatively groundtruthed by the corresponding side-scan sonar map, thus indicating that the methodology combining kriging and classification is feasible for Cymodocea too. This is said with the qualification that the discrepancy between the two maps concerning Posidonia must be resolved in other ways.

As such, the results given here and in the data report for the 1996 data (Schultz & Ersbøll, 1998) for *Posidonia oceanica* are not immediately encouraging. However, the lack of success here might be overcome by similar research sea trials, and it might regardlessly stimulate elaborations of sea bed classification methods for the class of ragged textures that Posidonia seems to be a member of. Like mussels, Cymodocea is known to have a rather small characteristic scale, and therefore forms a smooth texture at the seafloor, whereas Posidonia meadows consist of large plants that can have many shapes and form a large variety of sea bed textures. Hence, the results are perhaps not that surprising after all. Pursuance of this matter by refining the classification algorithms is another option, either by testing the said Owen-Hjort-Mohn algorithm on these data, or by using some of the other modern classification methods like deformable templates or neural networks.

It is this author's belief that the results for Posidonia reported here should be sought reproduced in other areas, largely repeating the designs used here too, to verify the problems encountered. Should they so prevail, other methods of detecting *Posidonia oceanica* can be pursued, like for example in Bozzano *et al*. (1998), where the acoustic backscattering signature of *Posidonia* is used for detection purposes.

5 Geostatistical simulation of mussel distribution maps

This chapter provides a means of assessing the uncertainty of the spatial distribution maps for mussels. Geostatistical simulation is used to derive estimates of coverage areas and accompanying variance estimates. It is argued that simulated maps are valuable supplements to kriged maps of mussel distributions.

5.1 Introduction to geostatistical simulation

The need for geostatistical simulation arises when it is necessary to estimate the spatial variability for some purpose, for example when the variability of a random field functional is requested. An example of a random field functional is the distribution area, D, of a specific sea floor type, C, measured by the random field $Z(\cdot)$:

$$D[Z(\cdot)] = \int_A I[Z(s) \in C]\, dA.$$

An example

In the present context, monitoring of the abundance of mussels within a larger region where environmental impacts are anticipated could be an example (abundance is the biological term for numbers obtained by counting individuals of a species). Suppose mussels have been selected as an indicator species by an Environmental Protection Agency (EPA), and some moderating actions are planned in case environmental impacts reach a certain level, which is expected to be matched by a decrease in mussel abundance at 10%. The EPA would then need an assessment of the feasibility of the 10% threshold value, and - on a statistical basis - this would amount to whether such a decrease would be detectable in the presence of random variation of the mussel abundance estimate, which could be derived from mussel distribution area estimates derived in chapter 3. Geostatistical simulation would then be needed to quantify the variance of estimated mussel abundances.

Rationale

The interpolation procedure of kriging provides the optimum local estimates $Z^*(s)$ of the random field over a designated grid G, i.e. $\{ Z^*(s) \mid s \in G \}$, in terms of unbiasedness, i.e. $E[Z^*(s)]=Z(s)$, and minimum mean square error, i.e. $Z^*(s)$ minimises $E[(Z^*(s)-Z(s))^2]$. Therefore, the kriging estimator $Z^*(s)$ is a smoother that estimates the mean field $\mu(s)$ in $Z(s) = \mu(s) + e(s)$ and ignores $e(s)$, maintaining the unbiasedness as $E[e(s)] = 0$. Hence, the univariate variability as well as the spatial variability of $Z^*(s)$ will normally be smaller than for the random field $Z(s)$ under study. This is simply a more complex manifestation of the phenomenon that a mean value estimator like the arithmetic average will tend to have a variance that is less than the variable it is averaging. Geostatistical simulation is needed to provide estimators that include the small-scale random field $e(s)$.

5.1.1 Basic theory of conditional geostatistical simulation

The following introduction is based on Journel & Huijbregts (1978) and Deutsch & Journel (1998). Geostatistical simulation aims at reproducing global properties of the spatial dataset under investigation, primarily univariate distributions, patterns of spatial continuity and observed values in the data locations: A) Univariate distributions are reproduced in terms of first and second order moments as well as empirical histograms, B) patterns of spatial continuity are maintained by using models of the empirical variograms in the kriging of the simulated values, and C) the data values are maintained by conditioning of the simulated values to the data points. Other kinds of specific global properties can be reproduced in the simulations too, but will not be dealt with here.

A) The univariate distributions are reproduced by transforming data appropriately before use, and then back-transforming simulation results afterwards, signified by the transformation function ψ in Figure 5.1. In GSLIB practice (Deutsch & Journel, 1998), the transform ψ is produced with a separate program that produces a histogram file to be used in the back-transformation too.

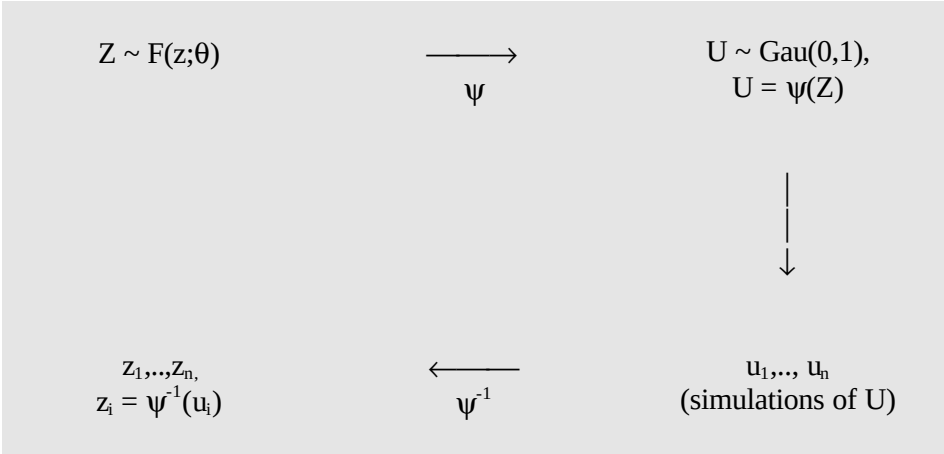

Figure 5.1 Transform and back-transform applied in simulating n instances of the random variable Z having the (possibly empirically determined) cdf. $F(z;\theta)$.

B) The pattern of spatial continuity is maintained by calculating local conditional expectations and variances by use of simple kriging (SK):

$$E[Z(s) \mid z(s_i), i=1,..,k] = Z_{SK}^{*}(s) = m(s) + \Sigma_{i=1..k}\, w_i(z(s_i)-m(s_i))$$

$$V[Z(s) \mid z(s_i), i=1,..,k] = C(0) - \Sigma_{i=1..k}\, w_i C(s-s_i),$$

where $z(s_i)$ are k data values in a relevant neighbourhood of s, m(s) is the expected value of the random variable Z(s), and the k weights w_i are given by the k equations (Deutsch & Journel, 1998, p. 140) in the SK system:

$$\Sigma_{j=1..k}\ w_i C(s_i-s_j) = C(s-s_i),\ \ i=1..k.$$

This local conditioning to maintain spatial continuity holds provided the random variables are Gaussian, hence the need for the initial transformation.

C) The conditioning to data values is made by the following trick. Suppose that an unconditional simulation has been conducted yielding results $z_s(s)$ in grid nodes $s \in G$ and in data locations $z_s(s_i)$, i=1..n, using s as a subscript to indicate simulation. Pretending the

simulated values $z_s(s_i)$ at the data locations are observed and fixed values (like the real data), the kriging of the real data is mimicked at the grid nodes to produce kriged estimates $z_s^*(s)$, $s \in G$. Having the simulated values $z_s(s)$ at hand already, the kriging error $e^*(s)$ at the grid nodes $s \in G$ can be estimated by $e^*(s) = z_s(s)-z_s^*(s)$. Using an exact interpolator $Z^*(s)$ will ensure that the kriged value is equal to the observed value at data locations, i.e. $z^*(s_i) = z(s_i)$, and therefore $z_s^*(s_i) = z_s(s_i)$, because the same vector of kriging weights w apply to $z^*(s_i)$ and $z_s^*(s_i)$ as they stem from identical data configurations.

Keeping in mind that the ordinary kriging estimator $Z^*(s)$ is estimating the mean field it might be termed $\mu^*(s)$, and the conditional simulation estimator can then be expressed as

$$z_{sc}(s) = \mu^*(s) + e^*(s)$$

$$= z^*(s) + (z_s(s) - z_s^*(s)).$$

The conditional simulation estimator $z_{sc}(s)$ is thus composed of the ordinary kriging estimate providing the mean field contribution and the simulated error estimate constructed to retain data values while maintaining the univariate distributions and the spatial continuity as well. Journel & Huijbregts (1978) proves that the estimator $z_{sc}(s)$ has the same variogram $2\gamma(h)$ as the dataset used for conditioning (in terms of the variogram model provided for the simulation), and therefore fits its purpose.

It is required that the error estimates $e^*(s)$ and the mean field estimates $\mu^*(s)$ are independent (or orthogonal), which is proved in Journel & Huijbregts (1978), p. 497. On p. 496 the authors prove that the estimation variance of $z_{sc}(s)$ is twice the kriging variance, and goes on to state: "*In terms of estimation variance, kriging is twice as good an estimator as conditional simulation: Estimation is not the object of simulation*".

Thus, it is clear that conditional simulation cannot take the place of kriging under normal circumstances. However, Deutsch & Journel (1998) discuss objectives that could qualify the use of conditional simulation for estimation, and mention estimation of global features like large-scale heterogeneity or textures, and estimation of extreme values, i.e. tail quantiles. In the latter case kriging is not an optimal choice as the kriging estimator is a mean squared error minimiser targeted at local levels of the mean field, and hence suboptimal for extreme values.

Geostatistical simulation is a growing field according to Deutsch & Journel (1998), although it seems to be slightly controversial judged by the arguments given on page 4: "*Recent applications of geostatistics have de-emphasized the mapping application of kriging. Kriging is now used to build models of uncertainty that depend on the data values in addition to the data configuration. The attention has shifted from mapping to conditional simulation, also known as* stochastic imaging*. Conditional simulation allows drawing alternative, equally probable realizations of the spatial distribution of the attributes(s) under study. These alternative stochastic images provide a measure of uncertainty about the unsampled values taken* altogether *in space rather than one by one. In addition, these simulated images do not suffer from the characteristic smoothing effect of kriging.*"

5.1.2 The practice of conditional geostatistical simulation

The GSLIB manual (Deutsch & Journel, 1998) gives the following recipe for conducting conditional geostatistical simulations, p. 144 (Deutsch & Journel uses **u** for locations instead of s, "cdf" for a cumulative distribution function, i.e. a c.d.f., and "ccdf" for a conditional c.d.f.):

"*The conditional simulation of a* continuous *variable z(**u**) modeled by a Gaussian-related stationary RF Z(**u**) proceeds as follows:*

1. *Determine the univariate cdf $F_Z(z)$ representative of the entire study area and not only of the z sample data available. Declustering may be needed if the z data are preferentially located; smoothing with extrapolation may also be needed.*

2. *Using the cdf $F_Z(z)$, perform the normal score transform of z data into y data with a standard normal cdf; [the program nscore from GSLIB is mentioned]*

3. *Check for bivariate normality of the normal score y data; […] If the multivariate Gaussian model cannot be retained, then consider alternative models such as a mixture of Gaussian populations [197] or an indicator-based algorithm for the stochastic simulation.*

4. *If a multivariate Gaussian RF model can be adopted for the y variable, proceed with program sgsim and sequential simulation, i.e.,*
   - *Define a random path that visits each node of the grid (not necessarily regular) once. At each node **u**, retain a specified number of neighboring conditioning data including both original y data and previously simulated grid node y values.*
   - *Use SK with the normal score variogram model to determine the parameters (mean and variance) of the ccdf of the RF Y (**u**) at location **u**.*
   - *Draw a simulated value $y^{(l)}$ (**u**) from that ccdf.*
   - *Add the simulated value $y^{(l)}$ (**u**) to the data set.*
   - *Proceed to the next node, and loop until all nodes are simulated*

5. *Backtransform the simulated normal values { $y^{(l)}$ (**u**), **u** Î A} into simulated values for the original variable {$z^{(l)}(u) = j^{-1}(y^{(l)}($ **u**$))$, **u** Î A}. Within-class interpolations and tail extrapolations are usually called for; […]"*

This recipe will be used in the next section to evaluate the uncertainty of the mussel distribution area within the core part of test area 1 in 1997.

5.2 Simulation-based assessment of variability

The selected area

The core part of test area 1 from 1997 was chosen to illustrate the use of geostatistical simulation to assess variability of distribution maps. The core part of test area 1 contains transects 20 metres apart, thus having a large data density, and it has an interesting blend of mussels and non-mussels (rejects) at the sea floor, cf. Figure 3.34.

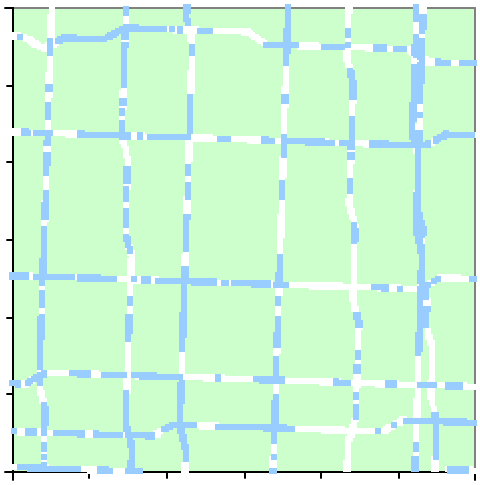

Figure 5.2 An illustration of classified observations in the core part of test area 1 from 1997. The darker symbols represent mussels and the lighter symbols non-mussels. The area is 120^2 m^2.

As in section 3.4 the core part is defined as the 120 x 120 m² area given by the UTM Eastings and Northings [355940, 356060] x [6162680, 6162800]. The dataset from 1997 contains 2008 observations herein. Using the classification function described in section 3.3 to divide all observations into the binary classes of mussels and non-mussels, the total number of mussel observations is 1008 (~ 50.2%). The classified observations are illustrated in Figure 5.2.

5.2.1 The steps of the simulation

Since the simulations in GSLIB are performed on standardised Gaussian data, a first preparatory step is to transform the variables in question, logE1 and logE2, into normal deviates by use of the program NSCORE. The resulting transformation curves based on empirical histograms are depicted in Figure 5.3, and a scatter plot of the resulting transformed variables is depicted in Figure 5.4.

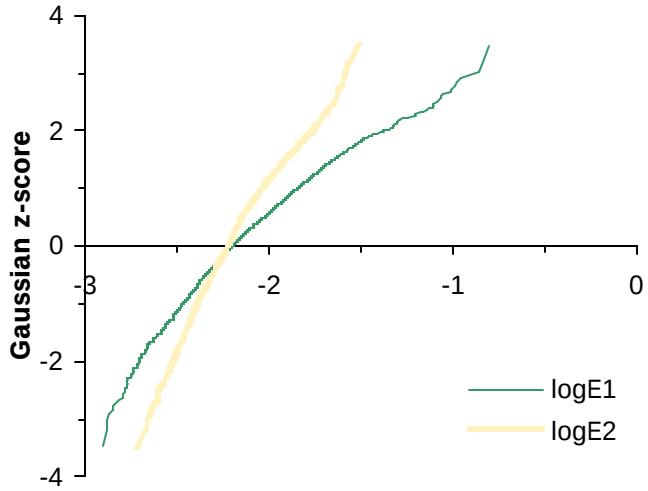

Figure 5.3 Transformation curves for logE1 and logE2 calculated by NSCORE.

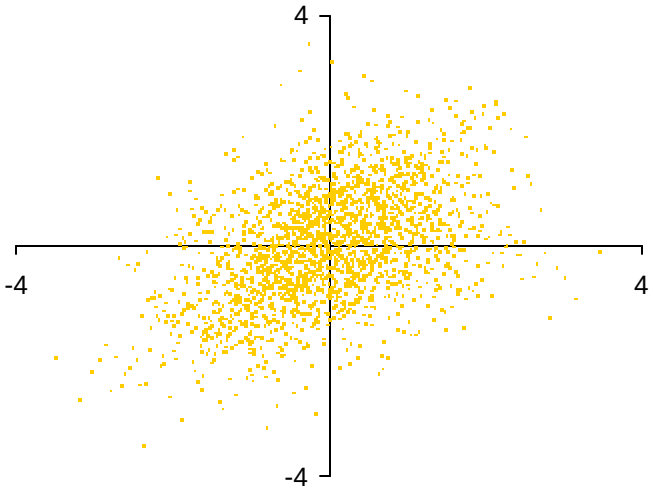

Figure 5.4 Scatter diagram of transformed logE1 and logE2 values.

Before commencing to the geostatistical simulation using SGSIM, semivariograms were prepared for the standardised Gaussian transforms of logE1 and logE2, cf. Figures 5.5 and 5.6.

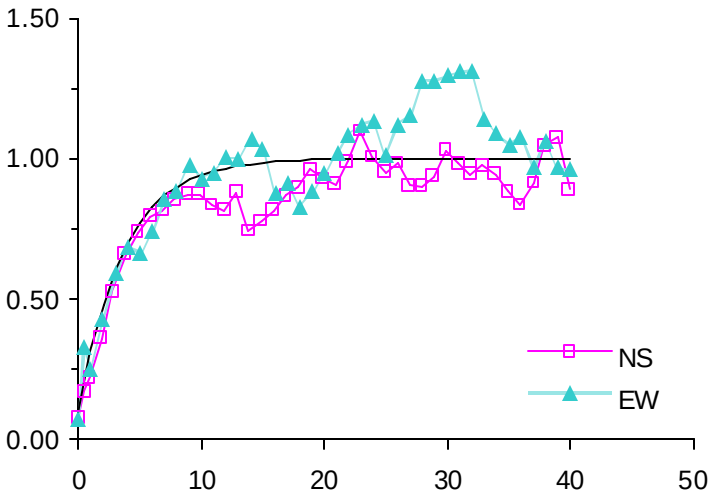

Figure 5.5 Semivariogram for the transformed variable z(logE1), the standardised Gaussian deviate of logE1.

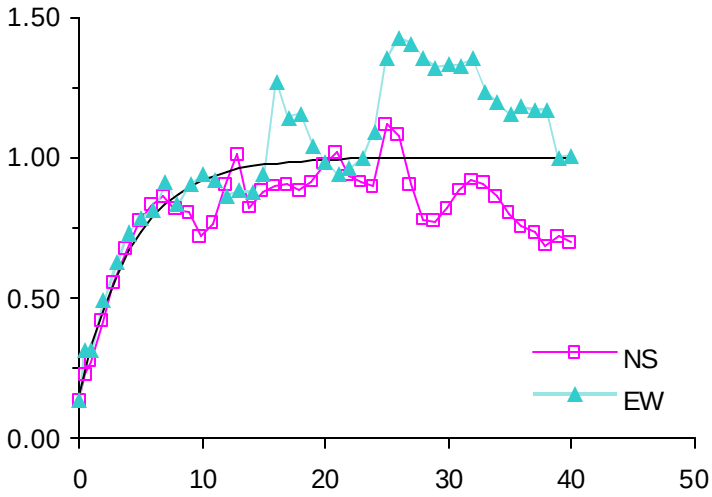

Figure 5.6 Semivariogram for the transformed variable z(logE2), the standardised Gaussian deviate of logE2.

Table 5.1 Estimated coefficients for exponential semivariogram models for the transformed variables. As the standardised values have a sill at 1, only the nugget,C0, and the range, R, were estimated. C1 is then 1-C0.

	z(logE1)	*z(logE2)*
C0	0.0984 ± 0.0404	0.1512 ± 0.0529
C1	1-C0	1-C0
R	10.83 ± 0.89	12.72 ± 1.23

For simplicity the values (10.8, 0.10) and (12.7, 0.15) of (R, C0) for z(logE1) and z(logE2), respectively, were used for exponential variogram models.

A simulation was conducted to produce 10 instances of the z(logE1) and z(logE2) random fields conditional on the transformed data on a grid with nodes 1 metre apart, i.e. containing 120 x 120 nodes. Check statistics of the 10 simulations are given in Table 5.2. The deviations from the ideal values 0 and 1 of average and standard deviation for a standardised variable are relatively small, except perhaps the averages of simulation no. 1, which might optionally be discarded as representing an initial phase before stationarity is reached.

Table 5.2. Check statistics for the 10 conditional simulations generated.

simulation	zE1		zE2	
no.	average	std.dev.	average	std.dev.
1	-0.1274	1.0052	-0.1284	0.9886
2	-0.0328	0.9791	-0.0219	0.9733
3	-0.0041	0.9916	0.0110	1.0126
4	-0.0473	0.9706	-0.0301	1.0095
5	-0.0463	1.0115	-0.0381	1.0457
6	-0.0240	0.9812	-0.0128	1.0308
7	0.0021	0.9978	0.0097	0.9892
8	-0.0043	0.9834	0.0037	0.9760
9	0.0096	0.9848	0.0250	0.9914
10	-0.0647	0.9752	-0.0483	0.9998

The simulated 10 maps of logE1 and logE2 were classified by use of the rules outlined in chapter 3, and their class counts are summarised in Table 5.3. Subsequently, due to the very low amount of sand pixels, these were identified with rejects in the images to yield the binary maps depicted in Figure 5.7.

Table 5.3 Class counts and relative frequencies for the 10 simulated maps distribution maps. The average of the specific mussel coverage areas is 59.87% for the 10 simulations with a standard deviation at 1.12%. The class counts sum to $120^2 = 14400$.

	class counts			specific areas / relative frequencies		
simulation no.	mussels	sand	reject	mussels	sand	reject
1	8915	3	5482	61.9%	0.02%	38.1%
2	8712	0	5688	60.5%	0.00%	39.5%
3	8485	1	5914	58.9%	0.01%	41.1%
4	8708	0	5692	60.5%	0.00%	39.5%
5	8375	0	6025	58.2%	0.00%	41.8%
6	8483	0	5917	58.9%	0.00%	41.1%
7	8560	1	5839	59.4%	0.01%	40.6%
8	8533	2	5865	59.3%	0.01%	40.7%
9	8678	2	5720	60.3%	0.01%	39.7%
10	8759	1	5640	60.8%	0.01%	39.2%

The simulated images where merged into an average image, which was then thresholded at 0.5 amounting to a simple majority decision among the 10 images about the value of the merged pixel. This is the so-called MPM estimate (MPM = marginal posterior modes) introduced in e.g. Besag (1989). The MPM estimate of the distribution map is seen in the lower right corner of Figure 5.7.

For comparison with the simulated maps a series of maps of logE1 and logE2 were kriged using 1, 2, 4, and 8 metres as side lengths in the pixels. For the maps based on 2, 4 and 8 metres pixels cubic splines were used to interpolate the maps onto a 1 metre grid. The sequence 1, 2, 4, and 8 was applied to illuminate the degree of smoothing as a function of block size as well as the amount of artefacts introduced by interference between the highly irregular data geometry and the relatively high resolution of 1 x 1 m^2 grid cells. The sequence of classified maps prepared from the logE1 and logE2 maps is shown in Figure 5.8.

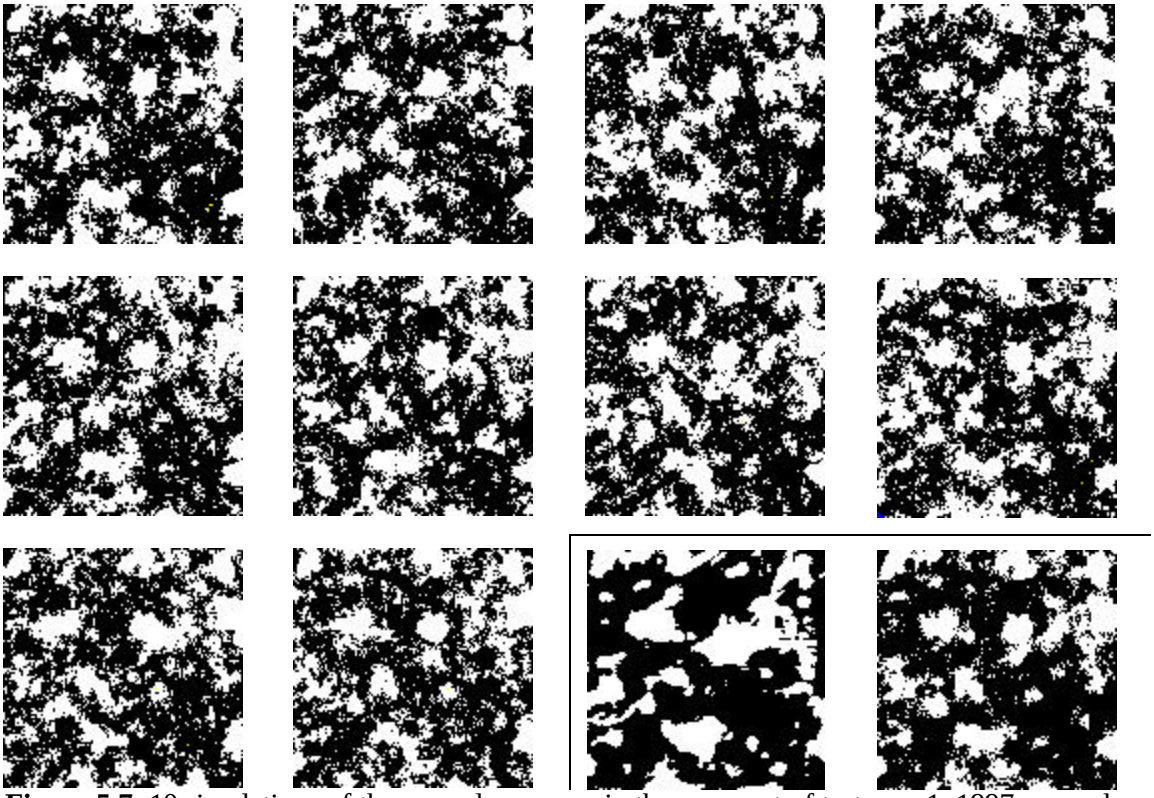

Figure 5.7 10 simulations of the mussel coverage in the core part of test area 1, 1997; mussel pixels are black, rejects are white. The lower right corner depicts the coverage map derived from a smoothed kriging (left) and the MPM estimate of the same map (right) derived by thresholding the average of the 10 images at 0.5.

5.2.2 Results and subsequent analyses

It is the impression of the simulated maps that they reproduce the mean field consistently with the kriged map in the lower right corner of Figure 5.7 (left), with the addition of the simulated errors embedding a certain amount of diffusion in the maps. The average map given by the MPM estimate in the lower right corner of Figure 5.7 (right) is more similar to the kriged map than the individual simulations as the error component is dampened by the averaging, yet it still contains many traces of small-scale diffusions, which the kriged map does not.

The small-scale variation in the MPM estimated map can be interpreted as a reflection of a real world phenomenon rather than an estimation error, as mussel beds are known to have some degree of patchiness when the mussel cover (specific area) is markedly lower than 100%, i.e. far from saturation. Some self-similarity of mussel pattern geometry within the scales of 5 cm - 5 m would allow the conjecture that the diffused MPM map has a closer resemblance to the state of nature than the kriged maps. The self-similarity assumption over a limited range of scales would allow the scaling of inference from mussel dimensions of 5 cm length to the map pixel dimensions of 1 m², even though the pixels might contain more than 400 mussels each. Snover & Commito (1998) describe a field study of these self-similar (fractal) patterns of *Mytilus edulis* in a soft-bottom system, and conclude that the mussel beds studied exhibited fractal qualities over a two orders of magnitude range of spatial scales, approx. 5 mm to 50 cm.

Assuming the small-scale heterogeneity is a real world phenomenon the MPM map could be used to point to verification sites by selecting sites fully surrounded by mussel pixels or reject pixels, respectively. In these sites, there should be a high probability of finding a high coverage respectively a low coverage of mussels within 1 x 1 m² pixels, which could be covered by the photo sampler used in the BioSonar field campaigns.

It must be underlined that the MPM estimate is based on simulation and is therefore not the best estimator, as mentioned earlier. Hence, individual pixels in highly diffused local regions cannot be interpreted as optimal estimators of the sea floor class and therefore cannot apply for verification measures. However, for a joint interpretation of local regions, i.e. local sets of pixels, the amount of small-scale diffusion seen is probably more realistic than the sharp edges between the mussel regions and reject regions seen in the kriged map, as judged by transect videos and photos from the groundtruthing data.

1 m, 67.6% 2 m, 69.0% 4 m, 69.6% 8 m, 71.1%

Figure 5.8 Kriged distribution maps for square pixel side lengths of 1, 2, 4 and 8 metres, postprocessed by cubic splines to interpolate the maps onto 1 m² grids. The specific areas of mussel coverage are given below the maps.

Another view to the estimation of small-scale variation can be discussed by looking at the kriged map sequence in Figure 5.8. As kriging is a mean field estimator the resolution of the kriged grid is sufficiently low as long as data values are not visible in the kriging results, as such a visibility of data would reflect a small-scale variation intended to be smoothed to inferiority. This principle can be used to judge the feasibility of the resolutions used in the map sequence in Figure 5.8. Thus, the maps kriged to grid cells having side lengths of 1 m and 2 m contain clearly visible traces of data, in particular along the intertwined double transect close to the right edge of the area. Therefore, these maps are judged to have a resolution that is too high to allow kriging to estimate the mean field alone. The maps based on 4 metres and 8 metres could both be argued to reflect the mean field. The map based on 8 m pixels was compared to the MPM estimated map yielding the 2 x 2 frequency table given in Table 5.4.

Table 5.4 Two-way frequency table for the pixels in the binary maps obtained by kriging and simulation. The specific areas are 67.6% for the MPM estimated map and 71.1% for the kriged map.

		MPM estimated map			
		frequencies		percentages	
		0	1	0	1
Kriged map based on 8 m pixels	0	2934	1230	20.4%	8.5%
	1	1729	8507	12.0%	59.1%

The correlation coefficient of the two maps is 0.519, indicating the marked influence of the small-scale heterogeneity on the MPM estimated map. It should be underlined that the MPM estimated map is not a realisation of the hypothetical random field $Z(\cdot)$ describing mussel proportions within 1 metre pixels as are the individual simulations. Rather, it is an intermediate map lying between the kriging results and the individual realisations. This is confirmed by the consistency with which the specific mussel area increases with increased degrees of smoothing. For the individual simulations, the specific areas lie around 60%, cf. Table 5.3, whereas the specific area of the MPM estimated map, 67.6%, is markedly biased. The increasing degree of smoothing in the kriged map sequence in Figure 5.8 increases the specific area monotonically from 67.6% to 71.1% for the highest degree of smoothing.

Having the specific mussel areas increasing consistently with increased smoothing, i.e. having similar effects as averaging, suggests that the population of measurements y = (logE1, logE2)' within the core part of test area 1 has its centre of gravity placed within the 95% confidence ellipsoid for mussels used in the classification. (The derivation of this ellipsoid is described in section 3.2). This would explain how the smoothing would tend to contract the bivariate envelope onto a centroid posted inside this ellipsoid and hence the overlap of the ellipsoid and the bivariate envelope of kriged results would increase as the degree of smoothing increases.

The scatter plot of logE2 versus logE1 for the core part of test area 1 in 1997 is depicted in Figure 5.9, where the centre of gravity - the centroid - is indicated with a cross.

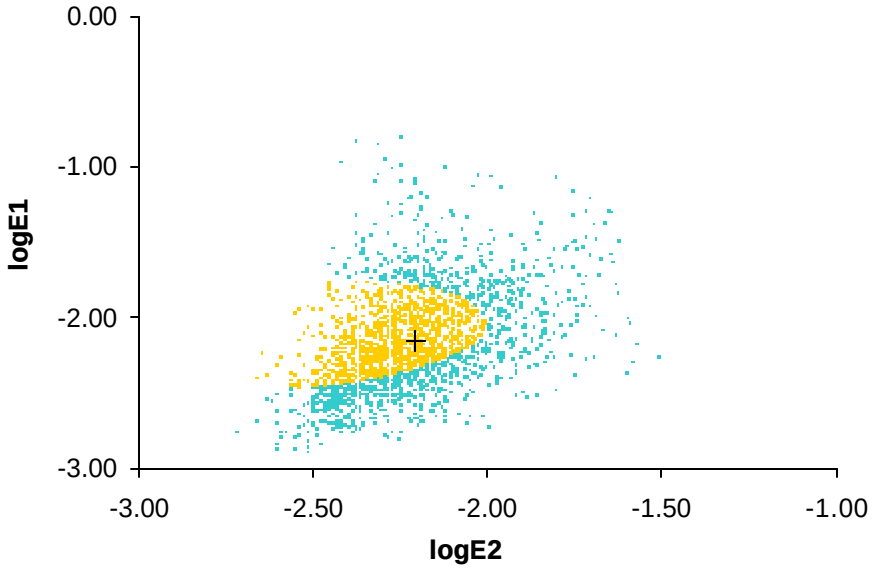

Figure 5.9 The feature space for the core part of test area 1 in 1997, i.e. logE1 vs. logE2. The observations within the mussel ellipsoid are indicated by the lighter (ocre) colour, and the observations with the blue (darker) colour are the rejects. The cross indicates the average of the observations.

The bivariate envelope depicted in Figure 5.9 verifies this explanation of the increasing specific areas, as the centroid is clearly within the mussel ellipsoid, and the rejects are posted at the fringe of (the right part of) the ellipsoid.

In Figure 5.10 the relative frequencies of fractions of mussel classifications assigned to every individual pixel are depicted. The bias of the MPM estimate is reflected by the slope of the relative frequencies from low proportions of mussel classifications to high proportions of mussel classifications. That is, mussel pixels that are assigned to the reject class in 1 - 4 of the simulations are much more frequent (by about a factor 3) than reject pixels that are assigned to the mussel class in 1 - 4 of the simulations. Assuming that the simulations are ergodic this property is a characteristic of the individual simulations too, and indeed the simulations depicted in Figure 5.7 indicate that there is a higher tendency to have spurious reject pixels within mussel areas than to have spurious mussel pixels within reject areas.

This is a textural feature that cannot be reproduced by kriging, and hence it is another argument for the case of simulation based estimation of maps for the present case. This textural feature is an observation that is coherent with the basic knowledge that mussels in Øresund tend to form clusters (Mussels normally cluster, but occasionally they form regularly distributed smaller patches, e.g. in Limfjorden in the northern part of Denmark).

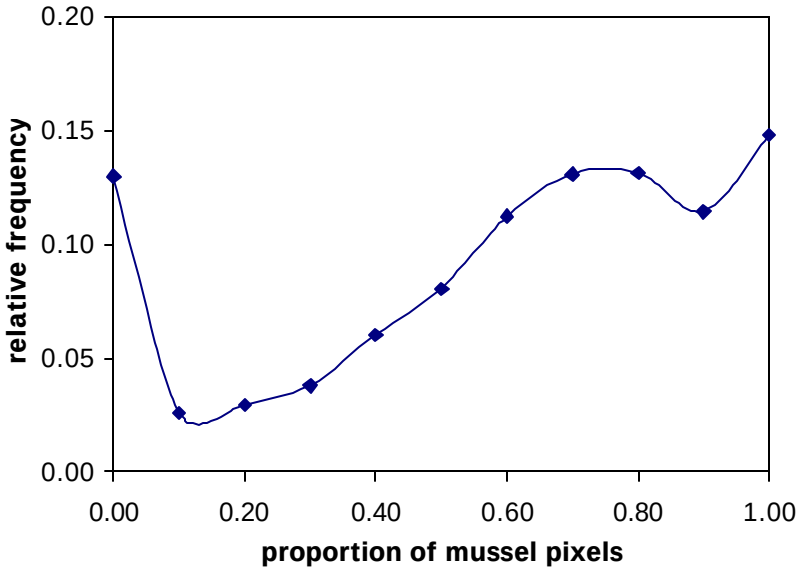

Figure 5.10 The distribution of the relative number of mussel classifications within pixels in the simulated images.

What is then the conclusion on this bias discussion, i.e. what is the best guess at the true mussel distribution area? The distribution area is a joint feature of the whole map and therefore the estimate must be based on the individual simulations. Certainly, the kriged map is a locally optimal estimator, but here the subsequent classification step depends on an extreme quantile, i.e. the 95% confidence ellipsoid, and therefore the smoothing provided by kriging is not optimal for joint estimation. Higher credibility must therefore be assigned to the average specific area at 59.87% for the individual simulations than to the estimates based on smoothing, including the MPM map.

5.3 Discussion

On the outset the present chapter was not intended to make the case for simulation based estimates of maps, but rather to concentrate on the variability estimation issue. However, the presentation given above indicates that simulated maps are valuable supplements to kriged maps as regards mapping and visual exposition of regions in question, and as a means to ensure optimality of values of random field functionals. Whereas kriging is the best local estimator as it is targeted on the mean field, the simulated maps are the best means of illuminating such features as texture and diffusion in local regions of a map. One does not have to choose, the two approaches are complementary by satisfying different objectives of description. Hence, the estimated map derived as the MPM estimate formed from an array of simulated random fields is suggested as a supplement to mussel distribution maps. Regarding the computation of random field functionals, like e.g. a sea floor distribution area for a specific bottom class, simulation is preferable in terms of unbiasedness and as a means of estimating variability of functionals.

A simulation based MPM map could be used to point to good candidates for verification sites in the studied region by pointing to regions where the local diffusion is low. These candidates could then be selected for monitoring provided they are situated on an edge in the kriged map.

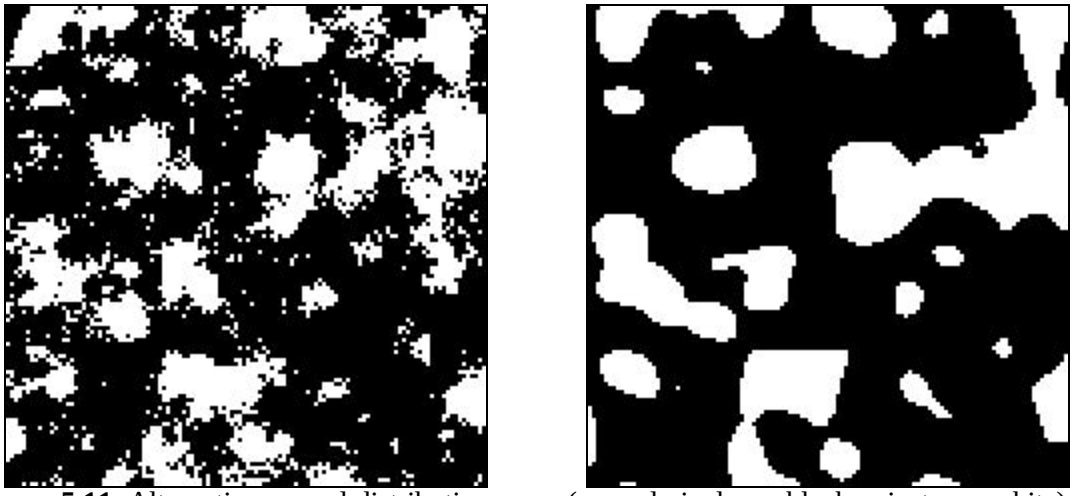

Figure 5.11 Alternative mussel distribution maps (mussel pixels are black, rejects are white): The simulation based MPM estimated map (left) containing smoothed traces of small-scale heterogeneity, and the kriged mean field map (right).

There are other arguments for the use of simulated maps than the smoothing versus extreme values schism. The data geometry is highly irregular due to the transect based monitoring design, thus the simulated maps might be the only realistic way of producing maps at high resolutions, i.e. close to the resolution of the transects. Furthermore, the exploratory spatial data analysis in appendix B indicated that logE1 is not strictly Gaussian, which is another reason why kriging might perhaps not be the optimal estimator.

There are interesting pathways to study further in relation to simulated maps. For example, it would be interesting to use the simulation approach to assess the effect of removing transects from the grid on the resulting variance of the specific areas. Properly designed, such studies would provide valuable input to future optimisation of monitoring designs for hydroacoustic measurements. Another interesting pathway could be to study the properties of the simulated maps in scale-space to elucidate possible characteristic spatial scales of mussel beds. If successful, results from such a study might be combined with a self-similarity model ranging over 2 or 3 orders of magnitude to be used in e.g. up-scaling of groundtruth data to reflect the resolution of kriged maps.

Returning to the question given in the opening of the chapter, the feasibility of a 10% decrease of the mussel distribution area can now be evaluated for the core part of test area 1 in 1997. Making the assumption that the standard deviation at 1.12% applies to the next year too, the rate of decrease of the mussel distribution area could be estimated as

$$r = 1 - A_1/A_0,$$

where A_0 and A_1 are mussel distribution areas of the current year and the next year, respectively. The hypothesis testing should preferably be conducted in log space (Lyngby & Sørensen, 1994; Green, 1989; Roberts, 1993), and the hypothesis for testing the true decrease rate ρ against the stipulated value of 10% = r_0 would then be

$$H_0: \log(1-\rho) \geq \log(1-0.1),$$

against $$H_1: \log(1-\rho) < \log(1-0.1).$$

Underlying assumptions are

$$\log A_0 \sim \text{Gau}(\mu_0, \sigma^2)$$

$$\log A_1 \sim \text{Gau}(\mu, \sigma^2)$$

where $\mu = \mu_0(1-\rho)$, and the σ^2 of the logarithms of estimated areas could be derived from the average and standard deviation above by using that var(logX) = log(1+CV(X)) holds approximately if CV(X) is not too high (i.e. clearly below 100%). Thus, we estimate

$$\sigma^2 = \log (1 + 1.12\%/59.87\%) = 0.13614,$$

and would then reject H_0 for values of Z such that

$$Z = (\log(1-\rho) - \log(1-r_0))/\sigma < \Phi(0.05) = -1.6445,$$

assuming that σ^2 is known, which yields a critical limit at $\rho = 0.2805$ using a traditional significance level at 5%. When the true relative decrease is above 28.1% there is less than 5% probability of missing this incidence by testing against a decrease threshold at 10%. In a real application context further considerations would apply, including power calculations, etc., but based on experience a setup like that given here would often be deemed feasible and practicable.

The point is that these calculations are made on a reliable basis provided by geostatistical simulation. Another point is that the variability estimates provided by the simulation make use of the data values, whereas the variances obtained by kriging depend solely on the geometry of the data locations.

There are some qualifications of the use of geostatistical simulation results; some of them related to possible lacks of ergodicity are discussed in Deutsch & Journel (1998). Furthermore, it is not known to this author whether it is possible to formulate results akin to central limit theorems for geostatistical simulations.

Therefore, in the next chapter we turn to a more simplistic random field model, that has nice theoretical properties in terms of ergodicity and a framework providing central limit theorems etc., thereby providing a better theoretical foundation for statistical inference of random field functionals.

6 A Markov Random Field approach to distribution maps of mussels

This chapter applies an alternative and very simple random field model for simulation of distribution maps, the so-called Ising model living on a discrete index set as opposed to the models living on continuous index sets used so far. First, an introduction is given to Markov random fields and the Ising model, and the estimation and simulation of the Ising model is outlined. By interpreting a rectangular region containing transect data as an image with a massive amount of missing data, an adaptation of an existing estimation method that accounts for the missing data, called penalised maximum pseudo-likelihood, is presented. The model is estimated for the core part of test area 1 in 1997 and then used for simulation. The results, as regards texture and variability of image functionals, are compared to the results from the geostatistical simulations.

6.1 Introduction

So far the objectives of mapping the distribution of benthic communities and estimating their distribution area, as well as finding accompanying uncertainty measures, have been based on random field models living on a continuous index set, i.e. $\mathbf{R}^2$ in a generic sense. However, a rich variety of methods has been developed over the last two decades for random fields living on a discrete index set (a lattice), i.e. $\mathbf{N}^2$ in a generic sense, called Markov random fields. The spatial continuity is defined by the dependency on the neighbourhood of the marginal distributions over individual points, which is conceptually similar to the use in geostatistics of spatial autocovariances for random fields living on $\mathbf{R}^2$ to describe spatial continuity.

One of the main problems in dealing with coverage estimates based on distribution maps prepared by means of classification (or segmentation) of processed echo sounder or side-scan sonar data, is the lack of explicit information about uncertainty of the estimates. This stems mainly from the fact that the distribution map normally constitutes one solitary observation, wherefore no replicates are present to be used for assessment of variability.

To overcome this obstacle several theoretical frameworks contribute means of combining a single observation, i.e. a 2D map in this case, with a model to allow for estimation of uncertainties by simulations. A range of synthetic datasets are produced by simulating the model conditional on the observed map data, and used subsequently as synthetic replicates to calculate variability measures. In the traditional geostatistical framework this can be done by simulations based on the geostatistical model as illustrated in chapter 5. In this chapter the methodology known as Markov chain Monte Carlo simulation (MCMC) is illustrated as an alternative approach, using the so-called Ising model as a model of the patterns of mussel pixels in the map. One advantage of the MCMC methodology is that it is directly applicable to maps produced by either geostatistical processing of echo sounder data or maps produced by image processing of side-scan sonar data.

The Ising model (or Ising field) belongs to the family of Markov Random Fields (MRF). Being one of the simplest MRFs, the Ising model does not involve smoothing and might therefore be a feasible alternative description of mussel beds, at least as a first approximation.

The presentation in this chapter relies on Cressie (1991), Carstensen (1992), Higdon (1994), Guttorp (1995), Gilks, Richardson & Spiegelhalter (1996), Rosholm (1997), and Green (1998).

6.1.1 Markov random fields

A Markov random field is a 2D sibling to the 1D Markov chain defined by the lack of memory property, i.e. for the time series $Y = (Y_1,...,Y_t)'$ to be a Markov chain it is sufficient that the value of Y_{t+1} depends on Y_t, but not the Y_i for $i < t$, that is

$$p(Y_{t+1}|Y) = p(Y_{t+1}|Y_t).$$

Giving the t-axis a spatial rather than a temporal interpretation the Markov property states that Y_{t+1} depends on the neighbour Y_t only. The following is straightforward, taking notice of the notation used in image analysis and MRF theory having a tradition for using one index i only for the image pixels, without loss of interpretability. The idea of Y_t as a neighbour of Y_{t+1} can be generalised a bit by defining a neighbourhood system N on the 2D lattice G:

$$N = \{ \partial i \mid i \in G \},$$

where ∂i is such that

$$i \notin \partial i,$$

and

$$i \in \partial j \iff j \in \partial i,$$

whereby N defines a topology on G consisting of the neighbourhood sets ∂i. For digital images the lack of memory property is stated as:

$$p(X_i \mid X_{-i}) = p(X_i \mid \partial_i)$$

i.e. the value of the i^{th} pixel conditional on the rest of the image, $X_{-i} = \{X_1,...X_{i-1}, X_{i+1},...,X_n\}$, depends on the neighbouring pixels only. This is often termed the *local property* of Markov random fields, i.e. that they (by definition) allow the probability distribution of the image X to be specified by local pdf.'s for pixels conditioned on their neighbourhood. (The random field must also satisfy a condition stating that all configurations of pixels X must have a probability above zero, a technical condition that basically ensures ergodicity).

The random fields can describe Gaussian distributions for individual pixels, i.e. be Gaussian Markov random fields, and can be assigned many other distributions as well. In the sequel the simplest possible type of random variable will be used, namely a binary variable, said to have a Bernoulli distribution B(1,p), e.g. X_i is fully specified by p:

$$Pr\{X_i = 1\} = p, \quad Pr\{X_i = 0\} = 1-p.$$

Their number of elements orders the neighbourhood systems and thus the neighbourhoods containing the smallest possible neighbourhood sets are called 1. order neighbourhoods, etc. For square pixels on a rectangular grid (as opposed to triangular and hexagonal grids) a 1. order neighbourhood is given by the four closest pixels, one at the left, one at the right, one above, and one below the current pixel. This yields the definition of the Ising model, as it is identical to a 1. order binary Markov random field.

Detailed introductions to Markov random fields are given in Guttorp (1995), Carstensen (1992) and Conradsen & Carstensen (1998), where the equivalence with Gibbs random fields is discussed as well as the celebrated Hammersley-Clifford theorem proving this equivalence. For a general exposition of the theory of stochastic processes underlying MRFs, see e.g. Cox & Miller (1965).

6.1.2 Markov chain Monte Carlo

Markov chain Monte Carlo (MCMC) is a very general methodology used to simulate distributions that could otherwise not be obtained due to complexity. The complexity can stem from e.g. the distributions being hypervariable, that is containing a huge number of mutually dependent variables, or from causal links and networks of high complexity in models. Gilks, Richardson & Spiegelhalter (1996) give examples of the many different statistical areas in which MCMC can solve hitherto computationally impracticable problems. MCMC is still an exciting new research area in 1999, cf. the words of Peter Guttorp (1995) in the preface: "*...I try to emphasize the importance of Markov chain Monte Carlo methods, which are having as profound an impact on statistics in the nineties as did the bootstrap in the eighties.*"

The basic idea of MCMC can be stated as follows (Green, 1998). Given a distribution of interest $\pi(\theta)$, $\theta \in \Omega$, a Markov chain $\theta_1, \theta_2, ...$, is constructed having π as its limiting distribution, and the chain is then simulated and the realisations treated as a sample from π. The construction of a Markov chain $\{\theta_t\}$ implies the definition of a transition kernel $P(\theta_t,\theta_{t+1})$ over Ω^2 whereby the probabilities of state transitions are given for all θ_t and θ_{t+1}. The transition kernel P is a generalisation of the transition matrix for discrete Markov chains.

Having produced a sample from $\pi(\theta)$ by MCMC, estimates can be calculated. For example, the probability $\pi(\theta \in A \subseteq \Omega)$ is estimated by $\#\{t \le N: \theta_t \in A\}/N$ and the expectation of a function $g(\theta)$ is estimated by $1/N \cdot \Sigma_{t=1..N} g(\theta_t)$. Note the Bayesian flavour of the terminology, where e.g. $\pi(\theta)$ is a Bayesian posterior in most cases. MCMC can be used in other frameworks, but most MCMC theory has been developed with a view to the Bayesian paradigm and therefore applies naturally in a Bayesian setting.

MCMC can be used even where static simulation cannot, as all simulation methods rely on the law of large numbers, which remains true due to the ergodic theorem when Markov chains are used instead of an i.i.d. sequence (i.i.d. = independent identically distributed).

To be applicable for MCMC a Markov chain must be ergodic, that is it must be *aperiodic* and *irreducible*. Irreducibility ensures that the Markov chain will not get trapped in a subspace of Ω, and aperiodicity allows any point in Ω to be reached in the next step of the chain with a probability higher than zero (regardless of how small it might actually be). The ergodic properties are needed for the basic MCMC limit theorems, which state that (Green, 1998):

1) If $\{\theta_t\}$ is an irreducible Markov chain with transition kernel P and invariant or limiting distribution π, and g is a real valued function with $\int|g(\theta)|\pi(d\theta) < \infty$, then

$$1/N \, \Sigma_{t=1..N} \, g(\theta_t) \rightarrow \int g(\theta)\pi(d\theta).$$

for π-almost all θ_0.

2) If the chain is also aperiodic, i.e. fully ergodic, there is a stronger result implying convergence in distribution as well, that is

$$||P_t(\theta_0,\cdot) - \pi(\cdot)|| \rightarrow 0$$

as $t \rightarrow \infty$, for π-almost all θ_0.

MCMC is relevant to image processing, where for example the neighbourhood dependency described for MRFs allow transition kernels P to be defined as local transitions making it straightforward to construct Markov chains that simulate images. As will be shown later, MCMC can play a special role in the estimation of image models under presence of missing data. Furthermore, the basic limit theorems of MCMC ensure that functionals derived from the MCMC simulated images are themselves stable in the sense of having a limiting distribution, and thus the MCMC framework ensures the existence of first-order and second-order statistics for derived image functionals as well.

Thus, whereas the image model used in this chapter might be too parsimonious, its embedding in an MCMC framework guarantees some mathematically sound and defendable results on the other hand.

Peter Green discusses some strengths and weaknesses of MCMC in his presentation (Green, 1998), mentioning the following strengths:

- MCMC gives a large freedom in modelling being, in principle, unlimited and because it is well adapted for models defined on sparse graphs.
- MCMC gives freedom in inference as well, giving opportunities for simultaneous inference and allowing one to address questions posed after simulations are completed, like e.g. ranking and model selection.
- It is the only available method for complex problems.
- MCMC integrates uncertainty coherently and allows for model comparisons, -criticism, and -choice and also encourages sensitivity analysis.

He is also listing the following weaknesses and dangers:

- MCMC implies the risk that fitting technology runs ahead of statistical science.
- There are difficulties in validating computer code.
- There are risks of MCMC leading to undisciplined, selective presentations.
- Possibilities of slow convergence that might not be diagnosable.

Good introductions to MCMC can be found in Gilks, Richardson and Spiegelhalter (1996), and in Guttorp (1995), and a good overview of the application of MCMC with four detailed examples is given in Besag *et al*. (1996).

6.2 The Ising model

This section introduces the Ising model and some of its characteristics, followed by outlines of how to simulate and estimate Ising models.

6.2.1 Basic properties of the Ising model

The Ising model originated within statistical mechanics as a model to describe magnetisation. A two-dimensional grid or lattice is supposed to contain one of two values in every cell (originally

positive or negative magnetic spin) and the cells are assumed to be correlated to their nearest neighbours adjacent to the four cell edges. (The rectangular grid based on squares is just one of several basic grids, other grid types like the hexagonal can be applied). The value of the i^{th} pixel, X_i, is thus influenced by the neighbours $j \in \partial i$, a relation that defines the local conditional probabilities

$$p(X_i = x_i \mid \partial i) = \exp(x_i \cdot [\alpha + \beta_1(x_w + x_e) + \beta_2(x_n + x_s)]) / (1 + \exp(\alpha + \beta_1(x_w + x_e) + \beta_2(x_n + x_s))),$$

where the members of $\partial i = \{x_w, x_e, x_n, x_s\}$ are the neighbours of x_i at the west, the east, the north and the south. In this parameterisation, which is common in image processing, β_1 controls the number of horizontal 1-1 neighbours and β_2 controls the number of vertical 1-1 neighbours. This interpretation is valid under the assumption that the set {0,1} was used for the binary coding of pixels. When $\beta_1 = \beta_2 = \beta$ the Ising model is said to be *isotropic*. The parameter α controls the amount of 1-pixels, assuring a mean fraction at 0.5 when $\alpha = -(\beta_1 + \beta_2)$. If the mean fraction of 1-pixels is 0.5, the Ising model is said to be *symmetric* or having a *zero field*. Denoting the local conditional probability of X_i being a 1-pixel by p, we write

$$p = p(X_i = 1 \mid \partial i) = \exp(\alpha + \beta_1(x_w + x_e) + \beta_2(x_n + x_s)) / (1 + \exp(\alpha + \beta_1(x_w + x_e) + \beta_2(x_n + x_s))),$$

and hence

$$\text{logit } p = \log(p/(1-p)) = \alpha + \beta_1(x_w + x_e) + \beta_2(x_n + x_s),$$

which can be averaged over all 16 combinations of pixel values for the neighbours to yield

$$\text{logit } p = \log(p/(1-p)) = \alpha + \beta_1 + \beta_2,$$

from which it is evident that we can set p equal to 0.5 locally and obtain $\alpha = -(\beta_1 + \beta_2)$ as the condition for symmetry. It is my conjecture that the relation

$$\log \text{OR}(\mu) = \text{logit } \mu = \langle \theta, 1 \rangle = \alpha + \beta_1 + \beta_2 \qquad (6.1)$$

where μ is the global mean fraction of 1-pixels, i.e. the image mean value, and θ is the parameter vector $(\alpha, \beta_1, \beta_2)'$, holds too, but it has not been within my reach to consult the relevant papers, e.g. Martin-Löf (1973), which might contain the relevant proof. The symbol OR indicates that the figure is the odds ratio of the mean, known from logistic regression (Kleinbaum, 1994). In some contexts the Ising model is described as a spatial logistic model (Cressie, 1991). Log odds ratios will be used as indirect measures of the external fields, i.e. the mean fractions, in the following sections.

If (6.1) holds globally, it can be used to compute the mean fraction, μ, when the parameter vector $\theta = (\alpha, \beta_1, \beta_2)'$ is known or estimated.

The joint probability of an image $X = \{X_1, ..., X_n\}$ for the isotropic model is

$$P(X = x) = 1/c(\alpha,\beta) \cdot \exp(\alpha \Sigma_i x_i) \exp(\beta \Sigma_i \Sigma_{j \in \partial i} x_i x_j) \qquad (6.2)$$

where $c(\alpha,\beta)$ is a normalisation constant, sometimes referred to as the partition function (Carstensen, 1992; Guttorp, 1995).

The original parameterisation assumed that pixels be coded from the set {-1,1} of spins. In that case the *interaction parameters*, β_1 and β_2, control the number of identical neighbours in either direction, and α controls the mean fraction.

The parameterisation of the isotropic Ising model can be generalised to read (Higdon, 1994)

$$P(X = x) = 1/c(\alpha,\beta) \cdot \exp(\alpha\Sigma_i x_i) \exp(\beta \Sigma_i\Sigma_{j\in\partial i} I[x_i=x_j]) \quad (6.3)$$

allowing α to control the mean fraction, μ, as α = logit μ, and letting the β coefficient control adjacencies of identical pixels, regardless of the coding of the pixels. Both parameterisations are used in this chapter. The first given by (6.2) will be referred to as the Carstensen-parameterisation and the second given in (6.3) will be referred to as the Higdon-parameterisation. When not explicitly stated, the Carstensen-parameterisation is assumed. In the Higdon-parameterisation α is called the external field, and the β's are called interaction parameters (as mentioned above).

The Ising model got its name from the original work in 1923 by the graduate student Ising, who showed that the 1-dimensional model had no phase transition, i.e. the magnetization varied continuously. The other main contributor is Onsager (1944) who gave the exact solution to the 2-dimensional problem in 1944, showing that it had a phase transition of the type seen in real ferromagnets. This led to great advances in the theory of phase transitions and critical phenomena.

The phase transition is illustrated in the example images in Figure 6.1 simulated for a symmetric and isotropic Ising model. For $\beta = 0$ a binary white-noise image is obtained, and for β at 0.5, 1.0, 1.5 and 1.7 it is seen that the size of clusters containing identical pixels increase while retaining the symmetry, i.e. having about an equal number of 1-pixels and 0-pixels in the images. When the β coefficient approaches the percolation limit of $2\cdot\sinh^{-1}(1) \approx 1.7627$ (half this value, ≈ 0.88, for the Higdon-parameterisation), percolation begins to emerge, i.e. pixels of the same colour begin to form very large clusters that tend to have a global outreach. For β above 1.7627 it is seen that the image is covered almost solely by one of the two kinds of pixels, leaving just a few speckles of the other pixel type in the images. In the phase transition the mean fraction of a symmetric joint distribution is still 0.5, but the mean is now divided image-wise instead of pixel-wise locally in the images. This is graphed in Figure 6.2, showing the bifurcation of the mean fraction in a sample image, i.e. a realisation from the joint distribution.

Onsager (1944) showed that the phase transitions occur for values above the so-called *criticality limit* and that this limit is defined for the anisotropic model by the equation

$$\text{crit}(\beta_1,\beta_2) = \sinh(\beta_1/2)\sinh(\beta_2/2) = 1. \quad (6.4)$$

Coefficients β_1 and β_2 for which $\text{crit}(\beta_1, \beta_2) > 1$ are said to be *supercritical*, whereas those corresponding to $\text{crit}(\beta_1, \beta_2) < 1$ are said to be *subcritical*. The state of supercriticality or phase transition is also referred to as long-range correlation, as it can be shown that any image pixel is correlated to the border pixels when the coefficients are supercritical, independently of the size of the image.

There are many similarities to random fields with continuous support. The external field described by α is stationary for α being a single, global variable (using the Higdon-parameterisation here). It is straightforward to introduce an external field by specifying α locally, i.e. α is replaced by the matrix $A = \{ \alpha_i \}$ describing the external field at every site. This is similar to geostatistical applications where kriging of a stationary field can be augmented by an external field, which is presumably described by some smooth function; in simple cases a quadratic polynomial will suffice. The same idea could be used to fill in A with a smooth external field. A more stochastic approach would be to use an underlying data image as a prior thereby letting α_i depend on y_i in the data image without fixing the site value x_i in the estimated image, i.e. $\alpha_i < \infty$. Higdon (1994) contains several examples of applications of these ideas.

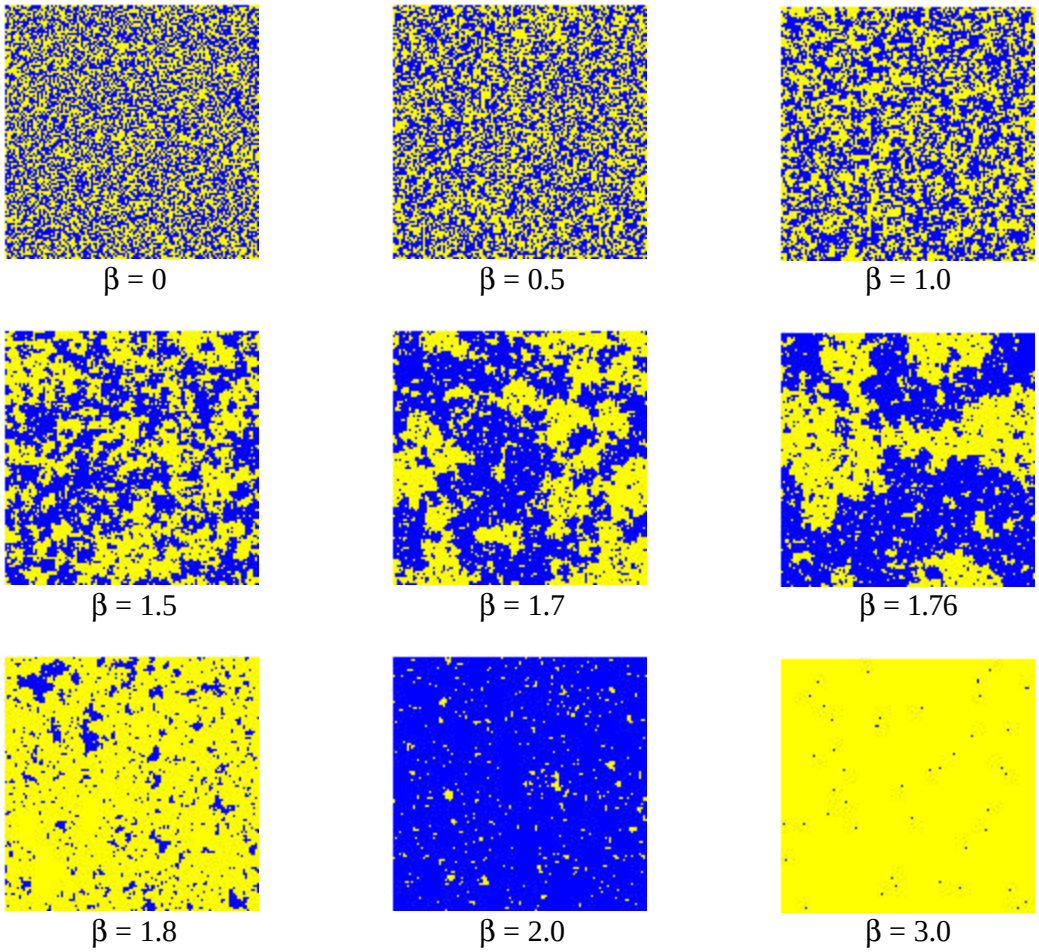

Figure 6.1 Example configurations for the symmetric isotropic Ising model for an increasing sequence of β values.

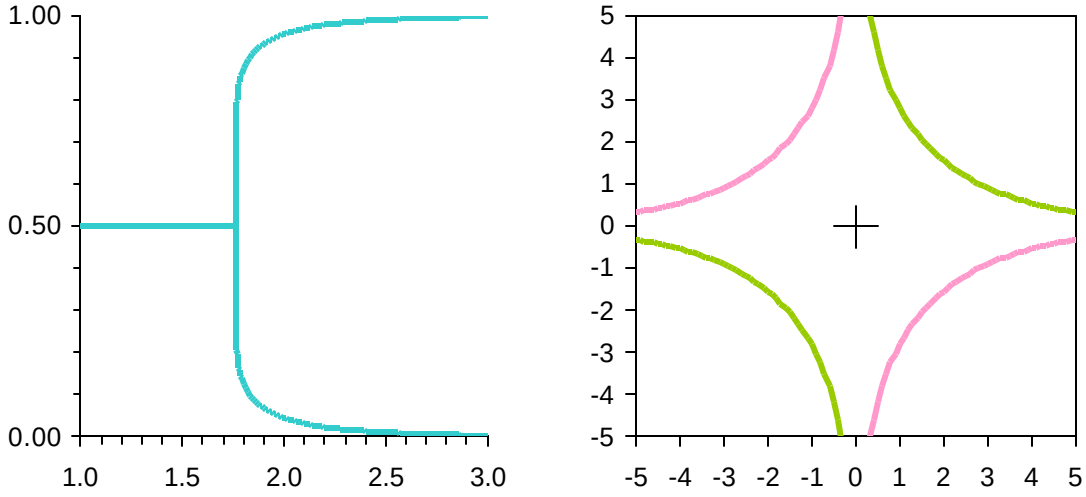

Figure 6.2 Illustrations of the phase transition in the Ising model. At the left, the mean fraction, μ, of 1-pixels is depicted for the symmetric isotropic Ising model as a function of β. The phase transition occurs at $\beta = 2\sinh^{-1}(1) = 1.762747$. At the right, the phase transition boundaries given by (6.4) are depicted for the anisotropic model.

The Ising model is aperiodic and irreducible, hence an ergodic theorem applies and it can be used in an MCMC framework. Applications of the Ising model and binary MRFs in image analysis comprise image restoration, texture simulation, etc. For more details about MRFs and their use in image modelling the reader is referred to Carstensen (1992) and Higdon (1994).

6.2.2 Simulation of the Ising model

The early methods of simulating Ising models relied on single site updates like Metropolis sampling (Hastings, 1970) and Gibbs sampling (Geman & Geman, 1984). These algorithms visit every individual pixel and use smart ways of expressing the local conditional probability, i.e. (6.1) or (6.2), with regard to simulation purposes. This has evolved into a subfield of its own within the MCMC framework, where updating and mixing algorithms are studied in the framework of the Metropolis-Hastings-Green (MHG) update mechanisms (Geyer, 1998) for use in other types of models.

For Ising models the single-site updates were succeeded by the cluster updating methods, now known under the name of *auxiliary variable methods.* The first and seminal algorithm was the Swendsen-Wang cluster update (Swendsen & Wang, 1987), which has formed the basis for a variety of elaborations. Being one of these, the *partial decoupling* algorithm was introduced by Higdon (1994) and works like a very user-friendly version of the Swendsen-Wang algorithm. A short sketch of the Swendsen-Wang and the partial decoupling algorithms is given in the following.

The Swendsen-Wang algorithm (SW) is sketched in Table 6.1. An auxiliary "bond" variable, u, is used to form bonds between sites, i.e. $u_{ij} = 1$ means that x_i and x_j are connected, while $u_{ij} = 0$ means that they are not. The rationale is that by specifying bonds by the variable u it is possible to decouple the interaction terms from the external field term. We define $\pi(u|x)$ to let the u_{ij}'s be independent and uniformly distributed. The interaction coefficients enter the realisations of the u variable by controlling the probability of bonding, i.e.

$$p(u_{ij}=1| x) = 1-\exp(-\beta_{ij})$$

where $\beta_{ij} = \beta_1$ for horizontal neighbours and *vice versa*. Subsequently, the bonds can be traversed to form clusters of bonded pixels and the clusters can then be assigned a value using the external field only, i.e. with a probability proportional to $\exp(\alpha\Sigma_{i\in C} x_i)$ over the cluster C. In other words, when each cluster has been assigned a colour the sweeping step is done. This procedure gave a tremendous speed up of computation time, in particular for larger images.

Table 6.1 Swendsen-Wang algorithm (SW).

```
for every sweep of the image:
        { given x, update u:
                setup bonds between sites using β1 and β2
                label clusters and assign cluster IDs to sites
          given u, update x:
                assign colours to clusters using α
                assign cluster colour to all sites }
```

The SW algorithm speeds up computations by a high rate. However, some deficiencies arise when e.g. the SW algorithm is used with an external field and strong interactions, i.e. having the mean fraction μ differing from 0.5, or when SW is sought used for sophisticated simulation purposes like simulating images conditional on partial data. If some of the pixels of the image are fixed, as they would be when simulating conditional on data, the SW algorithm may move

slowly through the sample space, when a majority of the clusters contain data and therefore have a zero probability of changing colour. Elaborations of the Swendsen-Wang that allowed for conditional simulation and good mixing when used with external fields were sought and Higdon (1994) suggested the partial decoupling algorithm as a generalisation of the Swendsen-Wang that can be adapted easily to a range of application purposes.

Table 6.2 Partial decoupling algorithm.

```
Setup decoupling weights λ_ij

for every sweep of the image:
    { given x, update u:
        setup bonds between sites using β_1 and β_2
        label clusters and assign cluster IDs to sites
      given u, update x:
        determine cluster borders
        assign colours to clusters using α, β_1 and β_2
        assign cluster colour to all sites }
```

The partial decoupling algorithm is sketched in Table 6.2. A user-specified matrix containing the decoupling weights λ_{ij} as fixed constants is used to direct the simulations. The decoupling weights enter the simulations the expression of the bonding probabilities for u_{ij} now read

$$p(u_{ij}=1|\, x) = 1-\exp(-\lambda_{ij}\beta_{ij})$$

and the price for introducing these weights is that the clusters are no longer independent of one another, conditional on the bond variables, u. Hence, it is necessary to update clusters conditionally on their neighbours. The theoretical details of the conditional probabilities involved are given in Higdon (1994). That partial decoupling is a generalisation of the SW algorithm is easily seen as it is identical to Gibbs sampling when all $\lambda_{ij} = 0$ and identical to the SW algorithm when all $\lambda_{ij} = 1$.

Partial decoupling is easily used for simulations conditional on data. Setting $\lambda_{ij} = 0$ for $j \in \partial i$ for all data pixels x_i and setting all other $\lambda_{ij} = 1$ will prevent any neighbouring pixel from bonding with the data pixel while using the SW updates away from the data pixels.

In the simulations prepared here, a guard region at 10% width was added to the images and then a so-called periodic boundary was used, meaning that the image is simulated on a torus, letting leftmost and rightmost pixels in a row be neighbours, as well as topmost and bottommost neighbours.

6.2.3 Maximum likelihood estimation for the Ising model

The full likelihood for the Ising model is not computable in practice, hence the traditional solution to parameter estimation prescribes to maximise the so-called pseudo-likelihood instead (Cressie, 1991; Carstensen, 1992). The pseudo-likelihood is given by assuming that pixels are independent, wherefore the expression

$$PL = \prod p_i^{xi} (1-p_i)^{1-xi}$$

can be maximised leading to the maximum pseudo-likelihood (MPL) estimate. In practice the logarithm of PL is maximised, i.e. the function $f(\theta)$ is used:

$$f(\theta) = \log PL = \Sigma_i [x_i T_i - \log(1+\exp(T_i))], \quad (6.5)$$

where $\theta = (\alpha, \beta_1, \beta_2)'$, $s_i = (1, x_w+x_e, x_n+x_s)'$, $T_i = \theta' s_i$, and $p_i = \exp(T_i)/(1+\exp(T_i))$.

Feeding $f(\theta)$ and the gradient

$$\nabla f(\theta) = \Sigma_i [x_i - p_i] s_i \quad (6.6)$$

and Hessian matrix

$$\nabla^2 f(\theta) = -\Sigma_i p_i/(1+\exp(T_i)) \cdot s_i s_i' \quad (6.7)$$

to a computerised maximisation routine (like e.g. NLPQN in SAS/IML) an estimate of θ can be obtained. It is not straightforward to derive an initial starting guess $\theta_0 = (\alpha_0, \beta_{10}, \beta_{20})'$ from the sufficient statistics of the image $(t_0, t_1, t_2)'$, where

$$t_0 = 1/N \Sigma_i x_i, \quad (6.8)$$

$t_1 = 1/N \Sigma_i \Sigma_{j \in \partial i} x_i x_j$ for horizontal neighbours, and

$t_2 = 1/N \Sigma_i \Sigma_{j \in \partial i} x_i x_j$ for vertical neighbours,

however, the relation

$$\alpha_0 + \beta_{10} + \beta_{20} = \text{logit } t_0, \quad (6.9)$$

can be combined with reasonable isotropic initial values for β in the range of 1.0 - 1.5 with good results because the MPL algorithm is rather robust as regards avoiding falling into local maxima (Carstensen, 1992).

Other methods apply, e.g. Besag's coding set method (Besag, 1974), but the MPL method has gained widespread use due to its simplicity and its ability to produce good estimates (Cressie, 1991; Carstensen, 1992).

6.3 Ising model estimation for images with missing data

The MPL estimation outlined in the section above is implicitly assumed to work on images where all pixels are known, i.e. given by a measured value in some sense. However, the transect data only account for a small fraction of the pixels, leaving the rest as unknowns. The Ising model would not be estimable if the data were scattered all over the field as in traditional geostatistical datasets, leaving no data pixel pairs to be used in the estimation of the interaction coefficients, β (unless a very coarse discretisation is applied to the data). The one-dimensional nature of the transect data ensures that a feasible number of pixel pairs is present and allows the MPL estimation to be carried out. However, when the transect data are discretised and filled into an image, the fraction of missing data pixels is still rather high, typically at least 90%. Naturally, the actual fraction of missing data for a dataset depends on the size of the pixels used for the discretisation of the image.

In acknowledgement of the crude accuracy (accuracy comprising bias and precision) of MPL estimates under these circumstances, the plan was to use the MPL estimate as an initial good starting guess for a refined and complex maximum likelihood algorithm called MCL. Charles Geyer discusses MCL in several papers, e.g. Geyer & Thomson (1992) and Geyer (1998), and

Guttorp (1995) gives a good basic introduction to the MCL method as well. Geyer (1998) describes in detail how the method might be used for cases of missing data to obtain good estimates within a MCMC framework.

It turned out that the MPL estimates tend to break down when the fraction of missing pixels lies somewhere between 80% and 90% and, moreover, vast numerical difficulties were encountered when the MCL method was implemented, due to its highly non-linear properties. The breakdown properties of the MPL estimates were studied and lead to a penalised version of the pseudo-likelihood algorithm, by which penalised maximum pseudo-likelihood estimates (PMPL) can be obtained. This section gives the details of the studies leading to the PMPL method and presents the theory behind the MCL estimation procedure.

6.3.1 Maximum pseudo-likelihood for images containing missing data

Preliminary attempts to produce MPL estimates for images containing binary coverage data as well as missing data indicated that the MPL estimates get inflated when the fraction of missing data reaches a certain level in the interval of 80% - 90%. Thus an experiment was conducted to study the properties of this breakdown using sequences of images derived from an initial full image by removing an increasing fraction of the pixels, i.e. assigning them to the class of missing values. The removal of pixels was done by removing an identical number of columns and rows leaving equidistant rows and columns of data pixels in the image, thereby producing a sequence of increasingly thinned images, cf. Figure 6.4.

In the thinning experiment described in the sequel the fraction of missing data is used as the critical measure for the breakdown of the MPL estimation. The most accurate measure to use would be the number of missing pixel pairs, as this is the critical number for the estimation of the interaction coefficients. However, as this fraction is considered to be proportional to the fraction of missing pixels due to the strict one-dimensional geometry of the transect data, the latter is used in the sequel.

The image thinning experiment

In order to emulate the properties of an image given by classified transect data containing a major amount of missing data, i.e. void pixel values, an image thinning experiment was carried out. A set of 7 images containing 128 x 128 pixels were simulated to closely mimic the area to be studied, i.e. the core part of test area 1 being 120 x 120 m². A symmetric Ising field was assumed with isotropic β values at 1.5, which are values anticipated to be close to the end results, i.e. the parameter vector $\theta = (-3.0, 1.5, 1.5)' = (\alpha, \beta_1, \beta_2)'$ was used. An interaction coefficient, β, at 1.5 ensures that clusters (mussel patches) can be contained by the model while maintaining a local nature of the clusters, as an isotropic $\beta = 1.5$ is subcritical. The 7 simulated images are depicted in Figure 6.3.

For every image a sequence of increasing thinning was generated by retaining the values in every k^{th} row and column for k = 4, 8, 10, 12, 14, 16, 18, and 20 corresponding to fractions of missing pixels at 0.562, 0.766, 0.821, 0.850, 0.864, 0.879, 0.894, and 0.908. One of the resulting image sequences are illustrated in Figure 6.4 for the first image (a) in Figure 6.3, and bear good resemblance to the geometry of the real world transect data.

The image sequences were fed to a maximisation routine (NLPQN in SAS/IML) to obtain MPL estimates θ^* of $\theta = (\alpha, \beta_1, \beta_2)'$ for k = 4, 8, and 16 initially, to be checked for recovery of the true values of $\theta = (-3.0, 1.5, 1.5)'$, cf. Figure 6.5 and Figure 6.6. Figure 6.5 depicts inflation measured by $\|(\beta_1,\beta_2)'\|/\|(1.5,1.5)'\|$ and the relative criticality $crit(\beta_1,\beta_2)/crit(1.5,1.5)$, where β_1 and β_2 are estimated values. Figures 6.5 and 6.6 show that instabilities occur at k = 16, i.e. at a fraction of missing data at 0.879.

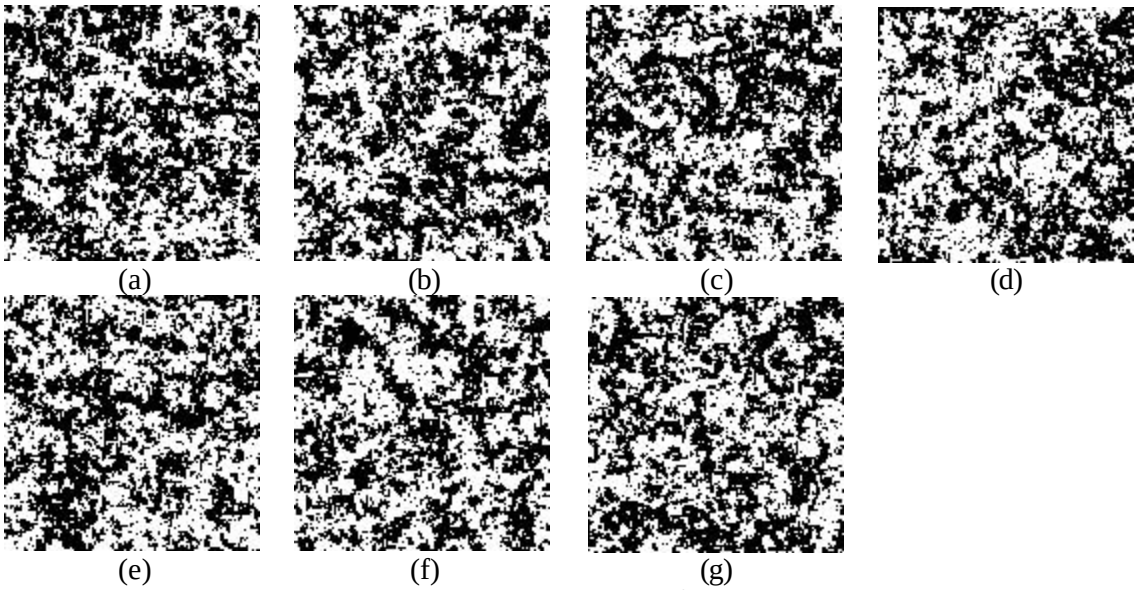

Figure 6.3 The 7 simulated images employed as a basis for the thinning experiment.

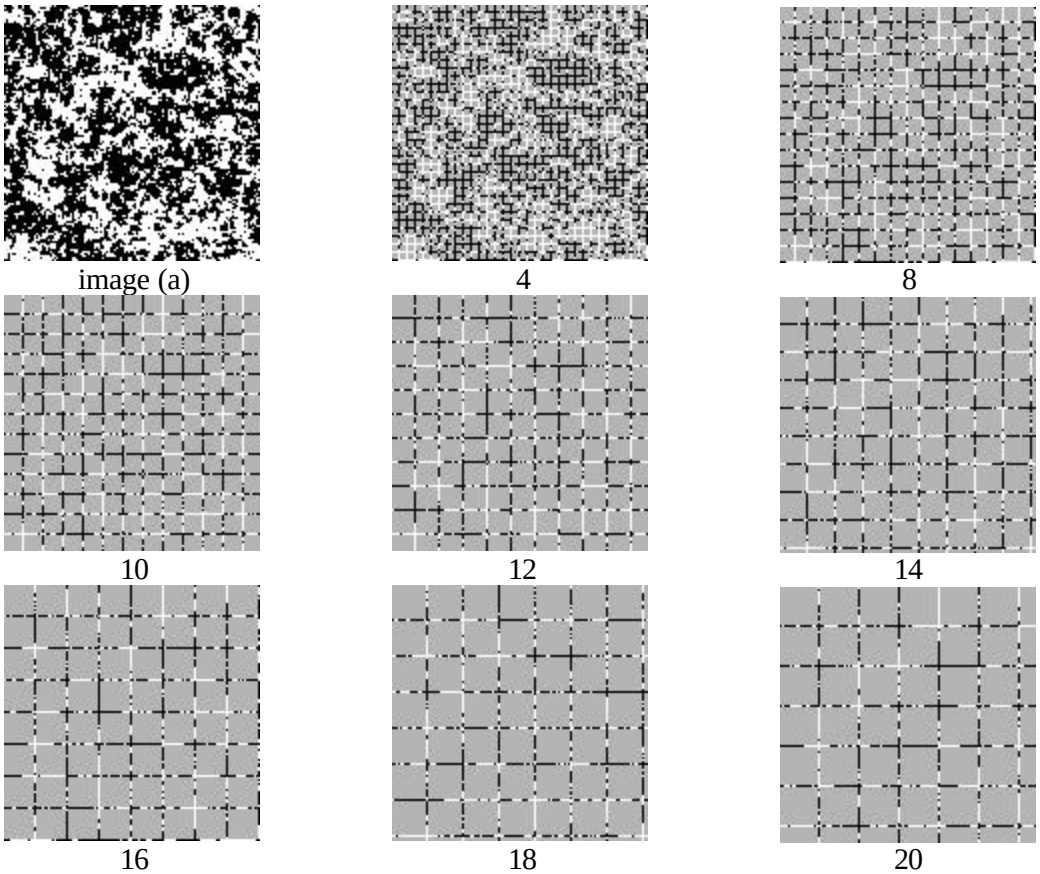

Figure 6.4 The image thinning sequence for image (a) in Figure 6.3, retaining every k^{th} row and column for k = 4, 8, 10, 12, 14, 16, 18, 20. Grey pixels indicate missing values.

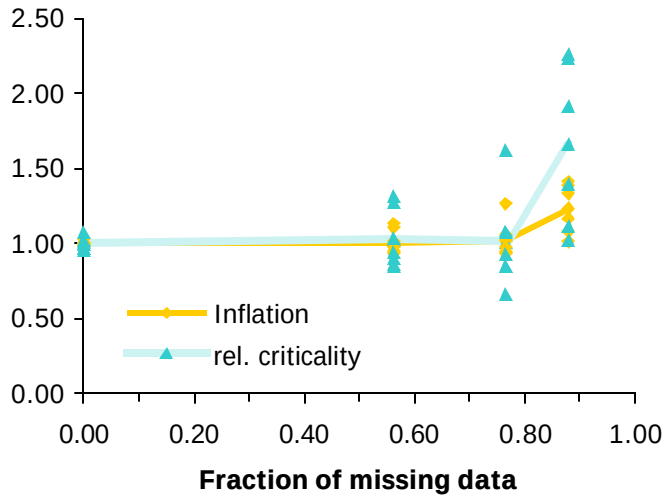

Figure 6.5 Inflation and relative criticality for the interaction coefficients, β_1 and β_2, for thinned images given by k = 4, 8, and 16. The inflation is measured as the length of (β_1,β_2) relative to the true vector (1.5,1.5), i.e. by $||(\beta_1,\beta_2)'||/||(1.5,1.5)'||$, where β_1 and β_2 are estimated values. The relative criticality is measured by $\text{crit}(\beta_1,\beta_2)/\text{crit}(1.5,1.5)$. The markers indicate results for individual image sequences and the lines indicate the averages of the measures.

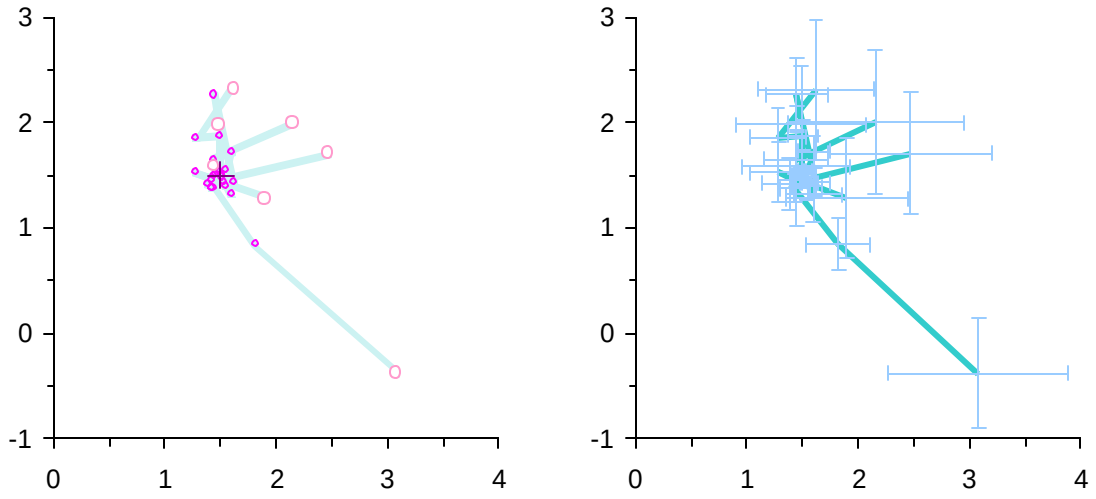

Figure 6.6 Trajectories of (β_1,β_2) estimates for increased thinning rates in the β phase space, showing a clear inflation at the high end of the interval of thinning rates. At the right the trajectories are depicted with error bars indicating the standard deviations of the β's derived from the Hessian matrix. Abscissas and ordinates are β_1 and β_2, respectively.

Subsequently to the initial experiment, extra thinnings k = 10, 12, 14, 18, and 20 were added to the image sequences as an effort to locate the limiting fraction of missing data pixels above which the inflation occurs in the interval between 80% and 90%. The biases found in the MPL estimates for criticality, mean fraction and anisotropy for the extended image sequences are depicted in Figures 6.7 - 6.9, which depict the odds ratios, the relative criticalities, and the anisotropy biases, respectively. The latter is given as $\max(|\beta_1/\beta_2|, |\beta_2/\beta_1|)$.

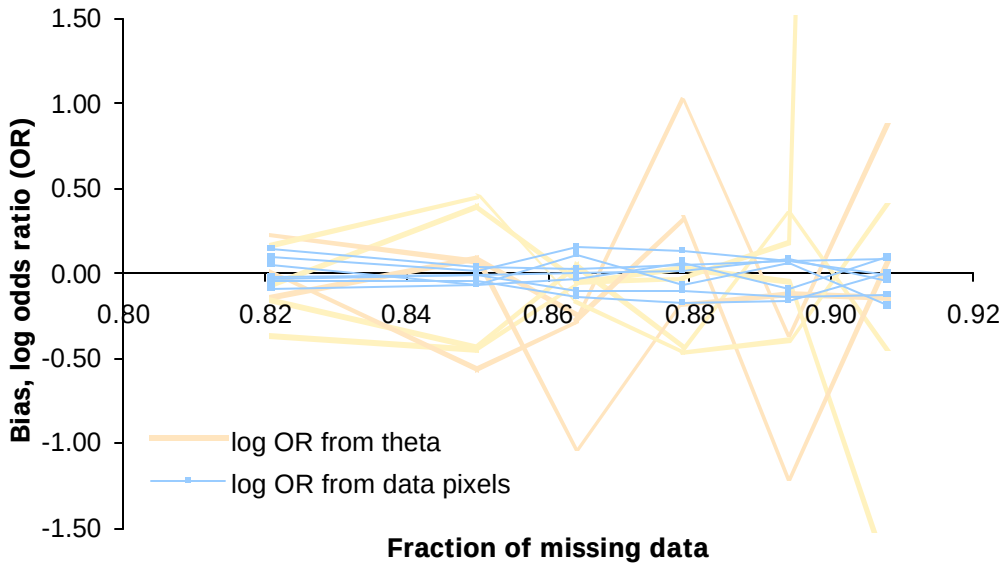

Figure 6.7 Bias in log odds ratio (OR), in the MPL estimates θ and in the log OR derived from data pixels. The true log OR is 0 for a symmetric Ising field.

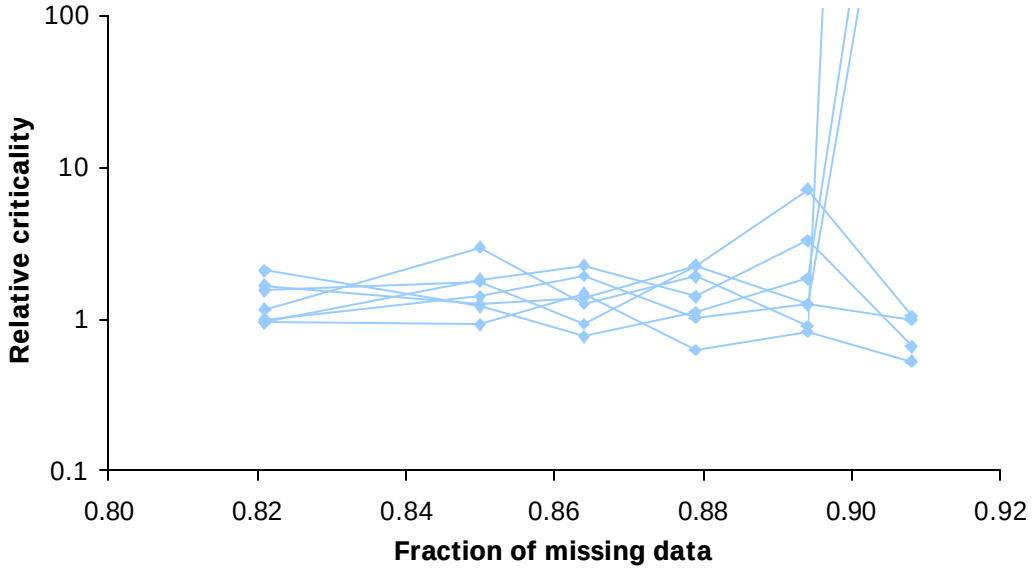

Figure 6.8 Criticality bias for MPL estimates, measured as crit(β_1,β_2)/crit(1.5,1.5).

The simulations underpin the bias and inflation introduced by thinning an image successively into line segments, and indicate that the breakdown limit where loss of accuracy due to inflation is no longer negligible, is close to 90% for the MPL estimation algorithm. This is stated here as an empirical observation based on the described thinning experiment and there is no doubt that this finding can be elaborated theoretically and experimentally to get closer to the truth. However, the evidence from the thinning experiment supporting these observations is considered substantial enough to point to the elaboration of the MPL algorithm given in the next subsection.

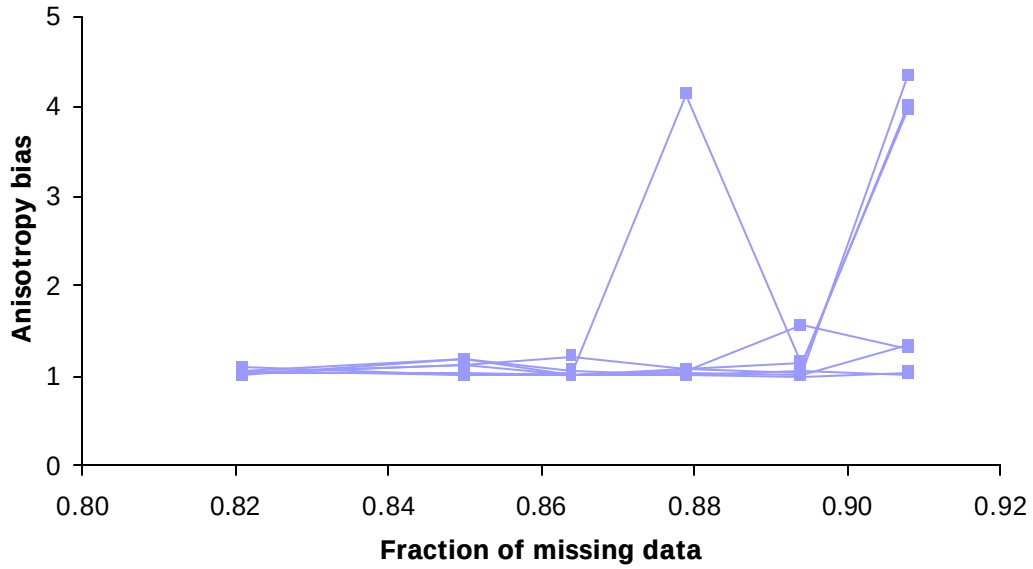

Figure 6.9 Anisotropy bias for MPL estimates measured by $\max(|\beta_1/\beta_2|, |\beta_2/\beta_1|)$.

The development of bias as a function of the amount of missing data in the log odds ratio, log OR(θ), given by (6.1) is displayed in Figure 6.7, which also indicates that the log OR derived from the data still left in the image is more stable than the estimated log OR. Thus, the image statistic for the OR can be used to provide a good initial value θ_0 and to penalise large fluctuations in the OR(θ). Thus, the next subject is introduced as it is evidently required to repair the MPL algorithm for the inflation and related loss of accuracy encountered when the fraction of missing pixels is high, i.e. above 80% - 90%. These high fractions apply to the dataset to be studied from test area 1.

What is needed is a way of supporting the estimation by imposing certain regularity measures, such that the optimality of θ will depend on the pseudo-likelihood and on the regularity criteria as well. Adding such regularity criteria to an estimation procedure is known as penalisation, i.e. the secondary criterion is specified as a penalty on the object function of the maximisation. The setup of a penalty vector and a comparison of the penalised MPL with the ordinary MPL is described in the next section.

6.3.2 Penalised maximum pseudo-likelihood

In some frameworks the following elaborations are termed regularisation (Nielsen, 1998). However, it is preferred to reserve the word 'regularisation' for cases of massively multivariate estimation problems, where some smoothness condition, normally expressed as a penalty on first- or second-order derivatives, is applied in the elementary approaches (Green, 1998a). Here we deal with an estimation vector θ containing three elements and the general term 'penalised likelihood' will apply. In usual maximum likelihood θ is estimated as the argument value where a maximum of the likelihood function L(θ) is found, i.e.

$$\theta_{ML} = \arg\max [L(\theta)],$$

whereas in penalised maximum likelihood a penalty criterion P(θ) is added to obtain the penalised maximum likelihood estimate θ by:

$$\theta_{PML} = \arg\max [L(\theta) - \lambda P(\theta)]$$

where λ is a multiplier either to be included in the maximisation as an auxiliary parameter or to be assigned a fixed value before the optimisation is carried out.

A simple example of penalised likelihood is in model selection likelihood, where the penalty adjusts the likelihood function for the number of parameters entering the model(s) by use of e.g. the Akaike information criterion, AIC, or the Bayes information criterion, BIC. Green (1998a) gives another example, describing how the optimal selection of splines for empirical curve fitting leads to selection of the well-known cubic splines when a penalty on the lack of smoothness of the second-order derivative is added to the minimisation of the sum of squares.

Thus, a penalty vector was applied to regularise or calibrate the estimation to the condition of a massive amount of missing data. The penalty vector,

$$P(\theta) = (p_1^2(\theta), p_2^2(\theta), p_3^2(\theta))'$$

is usually specified by quadratic penalty elements, making inference and derivatives easy to handle and interpret. Some authors prefer to use a linear criterion $P_i(\theta) = |p_i(\theta)|$ rather than a quadratic $P_i(\theta) = p_i^2(\theta)$, and Green (1998a) suggests a generalisation using $P_i(\theta) = \log \cosh(p_i(\theta)/\partial)$, where ∂ can be used to calibrate the power of the expression in the interval between 1 and 2.

Three penalty elements have been defined to penalise departures in θ regarding supercriticality, mean fraction or log odds ratio, and anisotropy.

Criticality

The penalty for supercriticality is based on considerations of the phenomenon that is modelled with the Ising field, i.e. it is partly based on a domain-specific argument. If the images cover sufficiently large areas and the data indicate that the area is not totally covered by mussels (i.e. that the mean fraction of the data pixels is clearly less than 1), then it can be assumed that mussel patches will exhibit a local structure and not be globally connected. Furthermore, it can be argued that supercritical interaction coefficients are generally undesirable for mussel beds because they would imply that mussel beds are bimodal in the large global areas studied. Mean fractions of mussel beds close to 1 (or 0) are thus better modelled by imposing a strong external field and keeping the interaction coefficients in the subcritical region.

Apart from these domain specific arguments, the thinning experiment showed that the interaction coefficients have some tendency to inflate markedly and thus a criticality penalty is reasonable as a means to control the inflation hereof. The inflation of the interaction coefficients could alternatively be controlled by a penalty on the Euclidean length of the vector (β_1,β_2). However, it was found recommendable to use the penalty for the criticality measure as it applies at a higher qualitative level due to the domain-specific arguments given above.

In operational terms it is assumed that the interaction coefficients comply with the inequality

$$\text{crit}(\beta_1,\beta_2) = \sinh(\beta_1/2)\sinh(\beta_2/2) < 1.$$

A straightforward penalty would be $p_1(\theta) = \text{crit}(\beta_1,\beta_2)$, as this would assume high values for supercritical β values. However, this criterion was found to be too weak for practical purposes and something more akin to thresholding of supercritical values was searched for, while maintaining simplicity of the penalty expression. Thus, to make this penalty behave like a blend of a penalty and a thresholding, a quartic penalty, i.e. a double squared penalty, was used:

$$p_1(\theta) = [\text{crit}(\beta_1,\beta_2)]^2. \qquad (6.10)$$

Mean fraction

A simple linear penalty was used to control the departures from the log odds ratio, which is simply logit(t_0), where t_0 is the mean fraction estimated from the data pixels by use of (6.8):

$$p2(\theta) = \langle\theta,1\rangle - \log OR = \alpha + \beta_1 + \beta_2 - \text{logit}(t_0).$$

Anisotropy

It is not the intention to impose isotropy on the interaction coefficients with this penalty. If that was the case, it would be much simpler to estimate an isotropic Ising field directly. The intent is to counteract the tendency to get highly artificial anisotropic coefficients due to the inflation, which was observed in the thinning experiment. To penalise anisotropy the following expression was used:

$$p_3(\theta) = (\beta_1/\beta_2 + \beta_2/\beta_1)/2.$$

The maximisation function, $f(\theta)$, the derivative and the Hessian given by (6.5), (6.6), and (6.7) are then supplemented with the penalty vector to yield the following maximisation system:

$$g(\theta) = f(\theta) - \langle\lambda,P(\theta)\rangle,$$

$$\nabla g(\theta) = \nabla f(\theta) - \langle\lambda,\nabla P(\theta)\rangle,$$

$$\nabla^2 g(\theta) = \nabla^2 f(\theta) - \langle\lambda,\nabla^2 P(\theta)\rangle,$$

and the penalised pseudo-maximum likelihood (PMPL) estimate θ^* of θ is the argument value where $g(\theta)$ is maximised.

The PMPL method has the flavour of an *ad hoc* method, yet the calibration results are quite satisfactory. Based on a subjective trial and error process it was found that a $\lambda = (1,3,5)'$ yielded stable and consistent results not departing very much from the full-image estimates. In Figure 6.10 the trajectories in the phase space for the interaction coefficients obtained with PMPL are compared to the trajectories obtained with MPL, giving the clear impression that the inflation has vanished with the introduction of the penalties. Figures 6.11 - 6.13 are the PMPL counterparts to Figures 6.7 - 6.9, and indicate the improvements in accuracy obtained by using PMPL, cf. the scaling of the axes.

Standard deviations of the estimates of α, β_1, and β_2 obtained for the 7 sample images were calculated for every thinning level to quantify the precision of the MPL and the PMPL estimates. These values are collected in Table 6.3. Likewise, the average of the absolute differences between estimates and true values over the 7 sample images were calculated at every thinning level to quantify the bias of the MPL and the PMPL estimates. The bias estimates are collected in Table 6.4.

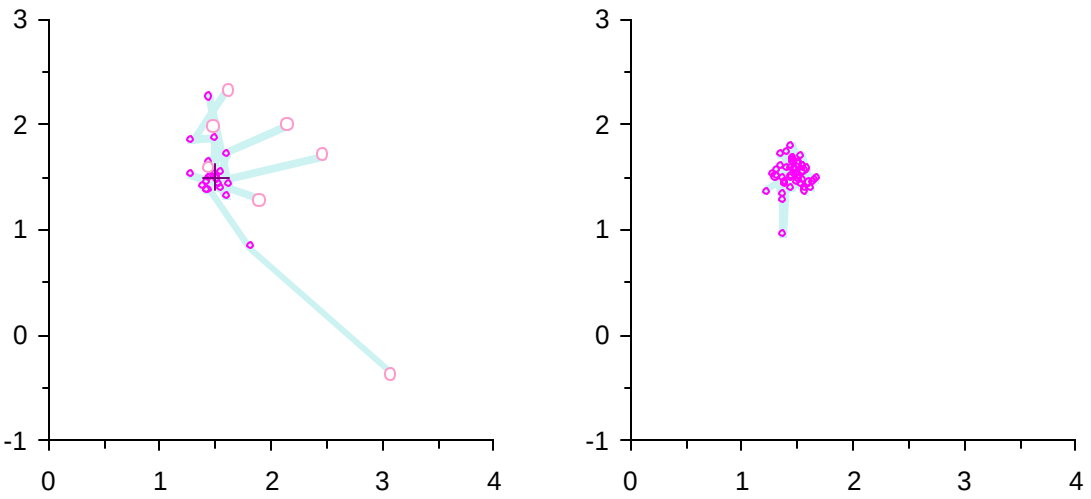

Figure 6.10 Phase spaces for the betas before and after penalising the pseudo-likelihood. Estimates of the interaction coefficients β_1 and β_2 obtained by MPL are depicted to the left, and estimates obtained by PMPL are depicted to the right. Abscissas and ordinates are β_1 and β_2, respectively. The true value is $(\beta_1,\beta_2) = (1.5,1.5)$.

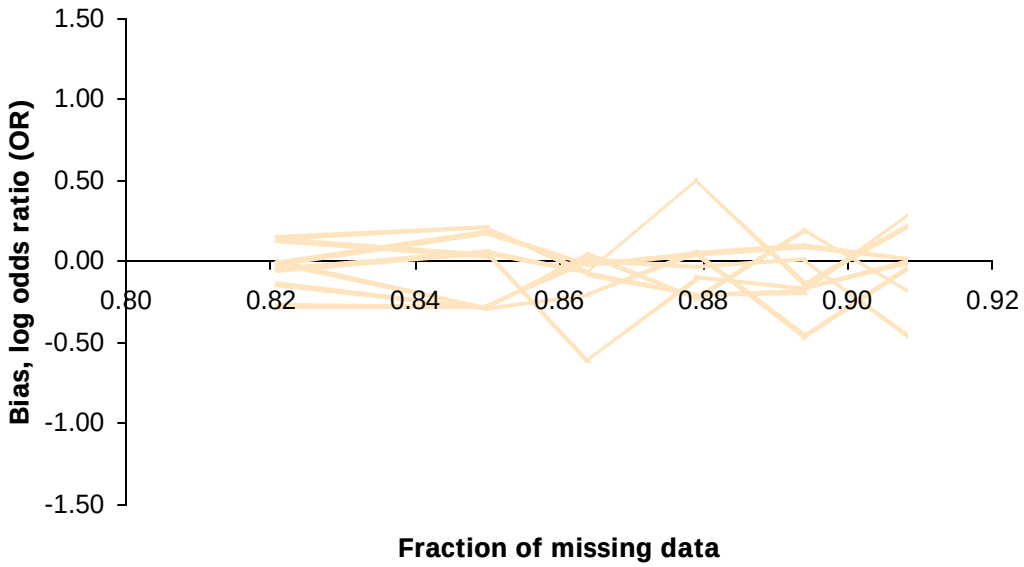

Figure 6.11 Log odds ratio bias for PMPL estimates, cf. Figure 6.7.

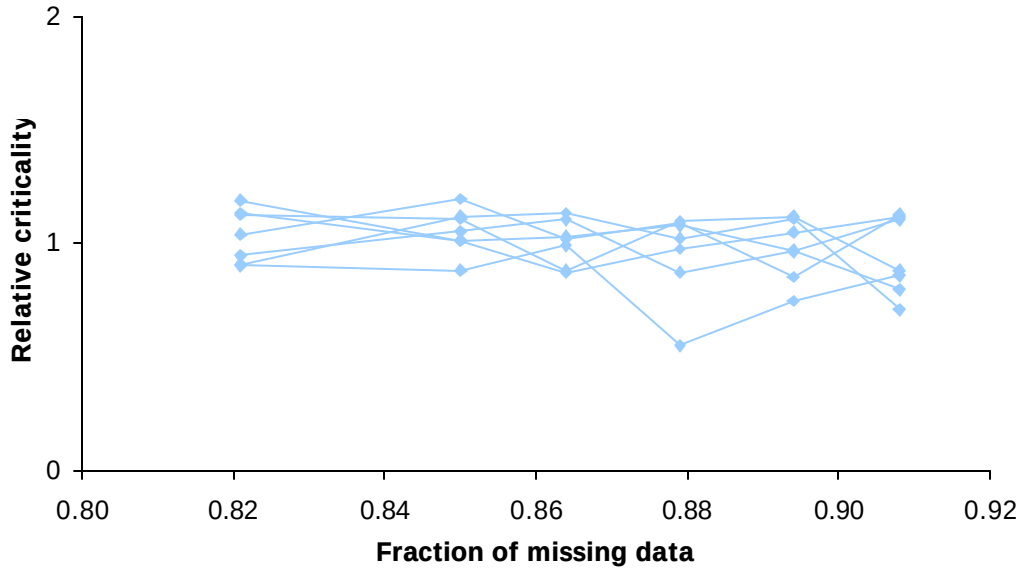

Figure 6.12 Criticality bias, crit(β_1,β_2)/crit(1.5,1.5), for estimates obtained with PMPL estimation. Compares with Figure 6.8.

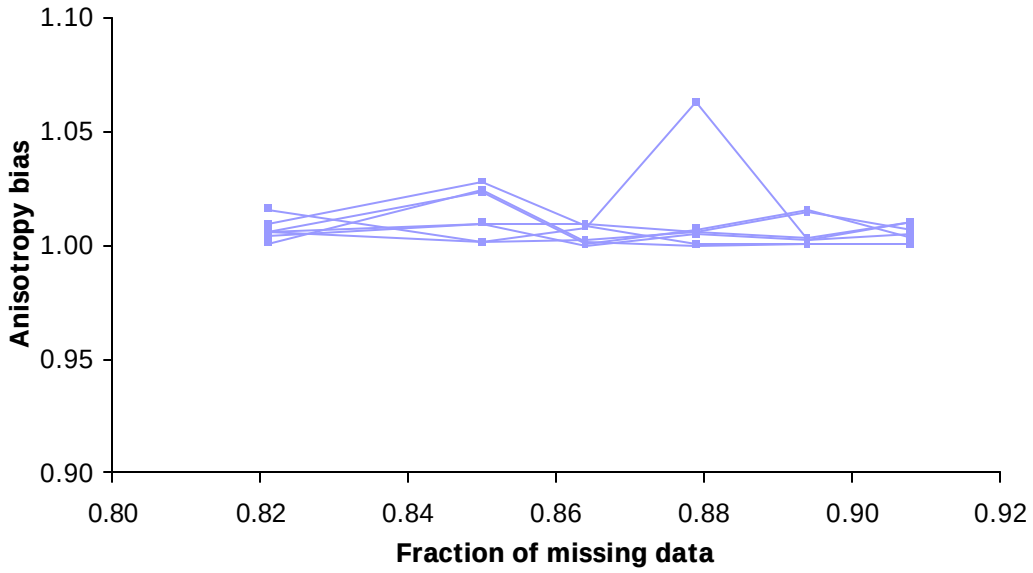

Figure 6.13 Anisotropy bias for PMPL estimates, measured by max($|\beta_1/\beta_2|$, $|\beta_2/\beta_1|$). Compares with Figure 6.9.

Tables 6.3 and 6.4 underline the qualitative observations made in Figures 6.10 - 6.13; the PMPL estimates have consistently higher precision and less bias than the MPL estimates, in particular when the fraction of missing values is approaching 90%. It is surmised that the PMPL method will provide consistent estimates for fractions greater than 90% as well, which will be needed in the following sections.

Figures 6.14 and 6.15 depict the values of precision and bias given in Tables 6.3 and 6.4.

Table 6.3 A comparison of precision measured by standard deviations of estimates for the MPL and the PMPL methods.

fraction of missing values	α		β_1		β_2	
	MPL	PMPL	MPL	PMPL	MPL	PMPL
0	0.055	0.054	0.041	0.041	0.039	0.039
0.821	0.596	0.269	0.324	0.127	0.336	0.110
0.85	0.581	0.244	0.292	0.092	0.589	0.160
0.864	0.620	0.242	0.347	0.086	0.244	0.067
0.879	0.436	0.292	0.595	0.098	0.892	0.226
0.894	1.626	0.331	0.580	0.098	0.765	0.121
0.908	17.818	0.392	9.385	0.140	17.634	0.136

Table 6.4 A comparison of bias measured by averages of absolute differences to the true values for the MPL and the PMPL methods.

fraction of missing values	α		β_1		β_2	
	MPL	PMPL	MPL	PMPL	MPL	PMPL
0	0.040	0.040	0.032	0.031	0.027	0.027
0.821	0.539	0.221	0.312	0.104	0.287	0.081
0.85	0.746	0.210	0.260	0.085	0.603	0.158
0.864	0.746	0.188	0.227	0.079	0.418	0.069
0.879	0.520	0.200	0.541	0.084	0.599	0.146
0.894	1.189	0.262	0.473	0.085	0.822	0.099
0.908	12.585	0.277	5.885	0.122	9.877	0.108

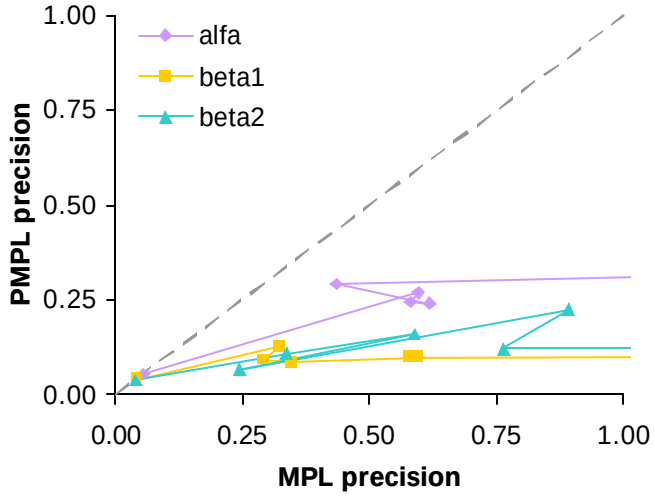

Figure 6.14 PMPL precision versus MPL precision for the thinning experiment. The dotted line indicates the y = x line, where the precisions are identical. Highly inflated MPL values are not depicted, cf. Table 6.3.

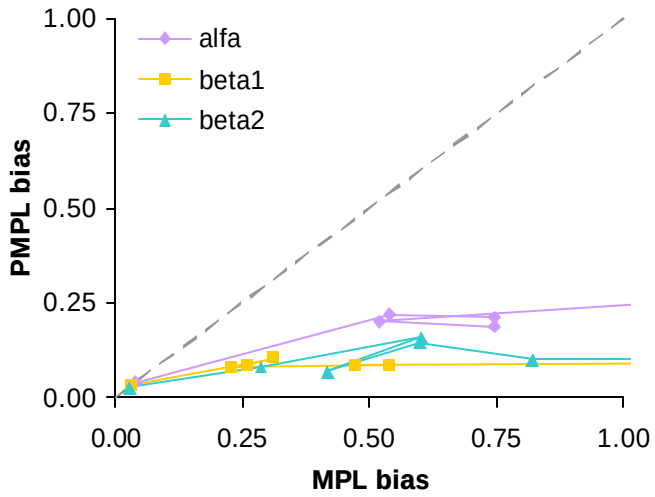

Figure 6.15 PMPL precision versus MPL precision for the thinning experiment. The dotted line indicates the y = x line, where the biases are identical. Highly inflated MPL values are not depicted, cf. Table 6.4.

The SAS/IML code for the PMPL algorithm is inserted in appendix D.

6.3.3 MCMC approximated ML estimation

This subsection describes an interesting and elegant piece of mathematical statistics aimed at the approximative calculation of a complex likelihood function. The idea is to rewrite the likelihood function in the form of log likelihood ratios in a fashion that allows approximations of the partition function, based on simulations, to enter the expression of the function and its derivatives. This so-called Monte Carlo Likelihood (MCL) method provides a richer and more elegant framework for solving the problem of estimating the Ising model under presence of huge amounts of missing data, than does the PMPL method presented in the subsection above.

MCL has one problem, though: It is highly non-linear, and leads to many calls of exponential functions with arguments like 100 or 1000, which it was experienced that even contemporary computers dislike. Thus, this subsection might be skipped, as the implementation presented abounding numerical difficulties due to these massively non-linear expressions and successful estimations were not executed. The presentation is included due to the niceties of the theory and as a documentation of work carried out during the studies. Some hints are given at the end on how to overcome the troubles encountered here. The presentation is an adaptation of pieces of theory for spatial point processes (Geyer, 1998; 1999) to the particularities of the Ising model and relies on Guttorp (1995) as well.

Details of the method as applied to a full observation x (an image), i.e. containing no missing data, are given first and then the interesting case of images with missing data is dealt with. The theory detailed in the sequel is described in (Geyer, 1999).

Definitions

Some formal definitions are needed first. Let (Ω,A,μ) be a measure space and h a non-negative real function on Ω. Then

$$f(x) = 1/c\ h(x), \quad x \in \Omega$$

defines a probability density f with respect to μ of a measure P, given that $c = \int h(x)\ \mu(dx)$ is finite and nonzero. The following terms are usually applied

- h is *an unnormalised density* of P with respect to μ.
- f is *the normalised density* of P with respect to μ.
- c is the *normalising constant* for h.

Parametric statistical models are introduced into this framework by extending the concept of h(x) to a family of densities described by a parameter space Θ. Let $H = \{ h(\theta), \theta \in \Theta \}$ be a *family of unnormalised densities* with respect to μ. Thus,

$$f(x;\theta) = 1/c(\theta)\, h(x;\theta), \quad x \in \Omega$$

defines a probability density $f(x;\theta)$ with respect to μ of a measure P_θ, given that the *normalising function* $c(\theta) = \int h(x;\theta)\, \mu(dx)$ is finite and nonzero for all $\theta \in \Theta$. The normalising function is equivalent to the partition function for the Ising model. Then $\Pi = \{P_\theta, \theta \in \Theta\}$ is a statistical model specified by the *family of probability densities* $F = \{f(x;\theta), \theta \in \Theta\}$ with respect to μ.

MCL without missing data

Assuming that an observation x of the stochastic variable X and a model P_θ of X with parameter θ is given, the aim is to compute a maximum likelihood estimate (MLE) of θ. Using the above separation of $f(x;\theta)$ the log likelihood ratio for an observation x against a fixed point $\psi \in \Theta$ is

$$l(\theta) = \log h(x;\theta)/h(x;\psi) - \log c(\theta)/c(\psi)$$

where the first term containing the unnormalised densities is known in closed form whereas the second term containing the normalising functions is not. That is, the ratio $h(x;\theta)/h(x;\psi)$ is readily calculated using the observation x, whereas an approximation of the ratio $c(\theta)/c(\psi)$ can be derived by use of MCMC. This is the basic principle in MCL, hence it is yielding an MCMC based approximation to the ML estimate of θ. The rationale of the approach can be described as follows.

It is assumed that $h(x;\theta) = 0$ whenever $h(x;\psi) = 0$. Then

$$\begin{aligned} c(\theta)/c(\psi) &= 1/c(\psi) \int h(x;\theta)\, \mu(dx) \\ &= \int h(x;\theta)/h(x;\psi)\, h(x;\psi)/c(\psi)\, \mu(dx) \\ &= \int h(x;\theta)/h(x;\psi)\, f(x;\psi)\, \mu(dx) \\ &= E_\psi\, [h(X;\theta)/h(X;\psi)]. \end{aligned}$$

Using the model P_ψ it is possible to obtain n quasi-independent samples $X_1, \ldots, X_n$ by use of MCMC and approximate $E_\psi\, [h(X;\theta)/h(X;\psi)]$ by $1/n\, \Sigma_i\, h(X_i;\theta)/h(X_i;\psi)$ leading to an MCMC approximation of the likelihood ratio

$$l_n(\theta) = \log h(x;\theta)/h(x;\psi) - \log(1/n\, \Sigma_i\, h(X_i;\theta)/h(X_i;\psi)),$$

which can be maximised to give an MCMC approximation θ_n to the MLE θ which maximises $l(\theta)$.

In order to maximise this by computer, an optimisation subroutine should be used that can be called in optimising step no. i with the current value of $l_n(\theta_i)$ and the gradient $\nabla l_n(\theta_i)$ for a fixed set of n simulated observations from P_ψ. The gradient of $l_n(\theta)$ is

$$\begin{aligned} \nabla l_n(\theta) &= \nabla(h(x,\theta)/h(x,\psi))/(h(x,\theta)/h(x,\psi) - \nabla(1/n\, \Sigma_i\, h(X_i;\theta)/h(X_i;\psi)) \,/\, (1/n\, \Sigma_i\, h(X_i;\theta)/h(X_i;\psi)) \\ &= \nabla h(x,\theta)/h(x,\theta) - 1/n\, \Sigma_i\, [\nabla h(X_i;\theta)/\, h(X_i;\theta))\, (h(X_i;\theta)/h(X_i;\psi)] \,/\, (1/n\, \Sigma_i\, h(X_i;\theta)/h(X_i;\psi)) \\ &= \nabla \log h(x,\theta) - 1/n\, \Sigma_i\, \nabla \log h(X_i;\theta)\, w(X_i), \end{aligned}$$

where

$$w(x) = [h(x;\theta)/h(x;\psi)] \,/\, (1/n\ \Sigma_i\ h(X_i;\theta)/h(X_i;\psi)). \qquad (6.11)$$

The Hessian is

$$\nabla^2 l_n(\theta) = \nabla^2 \log h(x;\theta) - 1/n\ \Sigma_i\ w(X_i)\ \nabla^2 \log h(X_i;\theta) - 1/n\ \Sigma_i\ \nabla w(X_i)\ \nabla \log h(X_i;\theta),$$

where

$$\nabla w(x) = w(x)\ [\ \nabla \log h(x,\theta) - 1/n\ \Sigma_j\ \nabla \log h(X_j;\theta)\ w(X_j)\ ].$$

The formulas are easy to apply to the family of exponential densities here, cf. the Ising model definition, yielding

$$h(x;\theta) = \exp \langle t(x),\theta \rangle,$$

and thus

$$\begin{aligned} \log h(x;\theta) &= \langle t(x),\theta \rangle, \\ \nabla \log h(x;\theta) &= t(x), \\ \nabla^2 \log h(x;\theta) &= 0. \end{aligned}$$

MCL for images with missing data

Assume that x is missing data and y is observed data for a model specified by an unnormalised density $h_\theta(x,y)$, i.e. the image (x,y) or "x+y" consists of the missing pixels x and the data pixels (transect data) y, giving "+" the proper geometric interpretation. The likelihood of θ given y is

$$L(\theta) = c(\theta|y)/c(\theta),$$

and the log likelihood ratio against a fixed point ψ is

$$\begin{aligned} l(\theta) &= \log L(\theta)/L(\psi) = \log c(\theta|y)/c(\theta) - \log c(\psi|y)/c(\psi) \\ &= \log c(\theta|y)/c(\psi|y) - \log c(\theta)/c(\psi). \end{aligned}$$

The fact that

$$c(\theta)/c(\psi) = E_\psi\ [h_\theta(X)/h_\psi(X)] \qquad (6.12)$$

is applied as well as

$$c(\theta|y)/c(\psi|y) = E_\psi\ [h_\theta(X,Y)/h_\psi(X,Y)\ |\ Y=y]. \qquad (6.13)$$

As before, the right hand sides of (6.12) and (6.13) can be approximated by MCMC. Thus, the model P_ψ is used to obtain n quasi-independent samples (X_1,Y_1), …. (X_n,Y_n) from the unconditional density of the images by use of MCMC, and approximate $E_\psi\ [h(X;\theta)/h(X;\psi)]$ by $1/n\ \Sigma_i\ h(X_i;\theta)/h(X_i;\psi)$. Secondly, n quasi-independent samples $(X_1{*},y)$, ..., $(X_n{*},y)$ conditional on the observed part of the image, y, are simulated. A combination of the two simulated sequences is leading to an MCMC approximation of the likelihood ratio

$$l_n(\theta) = \log h(x;\theta)/h(x;\psi) - \log(1/n\ \Sigma_i\ h(X_i;\theta)/h(X_i;\psi)),$$

which can be maximised to give an MCMC approximation θ_n of the MLE θ which maximises $l(\theta)$, as above.

The end result is a Monte Carlo approximated likelihood $l_n(\theta)$:

$$l_n(\theta) = \log 1/n \Sigma \exp<t(x_i*+y),\theta-\psi> - \log 1/n \Sigma \exp<t(x_i+y_i),\theta-\psi>,$$

where x+y denote the image composed of the known data pixels y and the unknown missing data pixels x. Again, in order to maximise this by computer, an optimisation subroutine should be used that can be called in optimising step no. i with the current value of $l_n(\theta_i)$ and the gradient $\nabla l_n(\theta_i)$ for a fixed set of n simulated observations from P_ψ.

Thus, an algorithm implementing the MCL approach to maximum likelihood in the presence of missing data could look like the sketch given in Table 6.5.

Table 6.5 MCL algorithm.

1. Obtain a rough initial estimate of θ (using e.g. PMPL).
2. Simulate a sequence of quasi-independent Ising model realisations using θ conditional on the data, y.
3. Calculate their sufficient statistics $t_C = (t_1, t_2, t_3)'$, where index C denotes conditional statistics.
4. Simulate a sequence of quasi-independent Ising model realisations using θ.
5. Calculate their sufficient statistics $t = (t_1, t_2, t_3)'$.
6. Use the sequences $\{t_{Ci}\}$ and $\{t_i\}$ in a computer optimisation routine given the function and the gradient described above.

One of the points of the MCL algorithm is the separation between the simulations and the optimisation. After running two Ising field samplers using the partial decoupling algorithm (step 2 - 5 in Table 6.5), two series of sufficient statistics $t_1,..,t_N$ and $t_{1C},.., t_{NC}$ have been derived that summarise all the information needed from the simulations in the optimisation step 6.

This works well as long as the so-called importance weights, w(x), (6.11) do not become divergent, which they do when the steps $\Delta\theta = \theta_{i+1}-\theta_i$ in the optimisation routine get too big. This poses a grave restriction on the optimisation algorithm, as it needs to take very small steps, and the initial guess must be rather close to the final estimate for this to work. To see how the weights get to diverge, we fill in the expressions for the Ising model in (6.11) using a certain sequence of $t(x_i) = t_i$ in the above notation:

$$\begin{aligned} w(x_i) &= [h(x_i;\theta)/h(x_i;\psi)] \,/\, (1/n \,\Sigma_i\, h(x_i;\theta)/h(x_i;\psi)) \\ &= \exp<t(x_i),\theta-\psi> \,/\, (1/n \,\Sigma_i \exp<t(x_i),\theta-\psi>), \end{aligned}$$

which works as long as all the t_i's are about equal. However, that is seldom the case, more often a few will deviate from the others, causing one or a few weights to divide the weighting mass summing approximately to 1 between themselves and leaving the rest of the weights to be virtually zero.

Several tricks were tried to remedy the situation, including linear scaling of the t_i's and setting boundaries on the stepsize $\Delta\theta$ for the optimisation algorithm; as it is pointed out in Geyer (1992) and in Geyer's contribution to Wilks, Richardson & Spiegelhalter (1996), it is possible to use a trust region to restrict the movement of the algorithm. However, this solution implies that the algorithm given in Table 6.5 becomes a step in a surrounding master algorithm, necessitating that the simulations in steps 2 - 5 be repeated using the latest value of θ_i whenever

the border of the current trust region is reached. The optimisation must be repeated within the trust region of the new starting guess and so on iteratively until, hopefully, an optimum is reached. This solution lacks the elegance and simplicity benefits that were are the assets of MCL, and to this author's experience it was not simple to obtain convergence using this method.

If this author should need to use MCL estimation in another context, he would go for some of the alternative solutions to overcome the numerical difficulties. Some of these are mentioned by Geyer (1998) and Higdon (1994); preferably the inverse logistic regression method could be selected. The inverse logistic regression method sets out by estimating the partition function $c(\theta)$ for a small set M of selected values intended to cover the region of θ values containing the maximising θ. The estimates $c^*(\theta_k)$, $\theta_k \in M$ are prepared by use of MCMC and then an interpolation function $c^{\#}(\theta)$ is estimated for the partition function. The approximated partition function $c^{\#}(\theta)$ is then used in the optimisation and the Ising field samplers need only be run once.

6.4 Estimation and simulation of an Ising model for the study area

This section returns to the application aspect and describes the estimation of an Ising model for the core part of test area 1 in 1997 using the PMPL method described in section 6.3.2. The estimated Ising model is used to simulate samples of the mussel distribution maps conditional on the transect data, and the resulting measures of variability of the distribution areas are evaluated.

6.4.1 Dataset for the core part of test area 1, 1997

To illustrate the use of the Ising model on the echo sounder data, the core part of test area 1, 1997, is used. This dataset was also used for the geostatistical simulation studies in chapter 5 and using the same area for the two random field models will make it easy to compare them. To use a discrete image model the dataset must be discretised accordingly. The transect data were classified using the feature space classification rules derived in chapter 3 and given a simple binary interpretation of being either mussels or non-mussels by merging the sand and reject classes. Thus, using a basic square pixel size of 1 m², the data pixels in the image were given values of mussels (~ 1) or non-mussels (~ 0), assigning a third value to all pixels not observed. Where several observations were attributed to the same pixel simple majority was used to decide the coding and an electronic coin was flipped in case of ties. The resulting data image having 120 x 120 pixels is depicted in Figure 6.16.

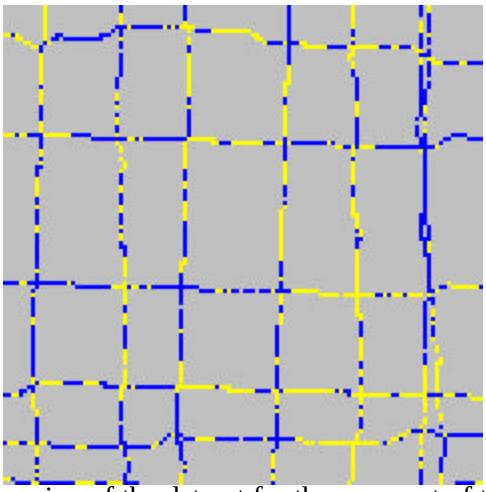

Figure 6.16 A discretised version of the dataset for the core part of test area 1, 1997, with classified observations posted on the transects. Darker pixels belong to the mussel class, lighter pixels belong to the non-mussels class and grey pixels were not observed.

6.4.2 PMPL estimation for the Ising model

There are $1286/120^2 = 8.9\%$ data pixels in the image, the rest of the pixel values are unknown, i.e. the fraction of missing data is 91.1%, which is just above the range studied in the thinning experiment in section 6.3.1. The fraction of mussel pixels in the image is 0.6932, which corresponds to a log odds ratio (OR) of 0.8151.

Based on the semivariogram estimations documented in chapter 3, the values of the correlation, r(1), between logE1 and logE2 for pixels one metre apart were derived. These values are given in Table 6.6. As we are in a local part of test area 1, where mussels and sand are dominating, it is expected that the β_1 and β_2 values will reflect the r(1) values for mussels and sand, i.e. correspond to correlations at approx. 0.70. The corresponding β value is approx. 1.75 found by graphical inspection of Figure 3.7 in Carstensen (1992). Using the OR we get an expected value for $\alpha = -(\beta_1+\beta_2)+\log OR = -4.32$. Thus, the following value of θ can be used as a starting value for the PMPL estimation:

$$\theta_0 = (-4.32, 1.75, 1.75)'.$$

Table 6.6 Derivation of correlation coefficients for 1x1 m² pixels

	testarea 1		**mussels**		**sand**	
	logE1	**logE2**	**logE1**	**logE2**	**logE1**	**logE2**
c0	0.0001	0.0001	0.0018	0.0009	0.0010	0.0002
c1	0.1142	0.0479	0.0363	0.0203	0.0191	0.0387
R	17.00	18.78	8.75	11.64	6.29	10.98
r(1)	0.8377	0.8515	0.6762	0.7390	0.5895	0.7570

The MPL maximisation was implemented in a SAS/IML program using the Gauss-Newton optimisation routine NLPQN. The source code is listed in appendix D. A good introduction to multivariate optimisation and the mechanics of Gauss-Newton methods is given in Press *et al*. (1992). The resulting estimate of θ is

$$\theta^*_{PMPL} = (-2.3138, 1.4038, 1.4415)',$$

which corresponds to a mean fraction of $\mu = \text{logit}^{-1}(<\theta,1>) = \text{logit}^{-1}(0.5315) = 0.6298$. The resulting mean fraction derived from the estimated parameters is not too far away from the value derived from the pixel counts at 0.6932. These figures also compare reasonably well with the specific areas found with the geostatistical methods, which yielded 0.711 for the kriging based estimate and 0.676 for the MPM estimate based on 10 samples of geostatistical simulation. The diagonal trace of the Fisher information matrix is (1.1081, 0.7179, 0.7369), reflecting the uncertainty of the estimates when 91.1% of the image contains unknown pixels.

The MCL method adapted from Geyer (1998) was used subsequently to try to polish the estimated θ. However, the results were not encouraging and comprised inexorable numerical difficulties as mentioned above.

6.4.3 Ising model simulations of mussel distribution maps

Having obtained an estimate of the θ parameter vector for the Ising model we can proceed to produce samples from the distribution $\pi(\theta)$ of the mussel beds in the study area and eventually arrive at a standard deviation for the specific areas found in the samples. The simulations were carried out by use of the partial decoupling sampler to condition the simulations on the data image depicted in Figure 6.16. In Figure 6.17 the 12 samples are depicted, they were interspaced by 500 sweeps to make them quasi-independent.

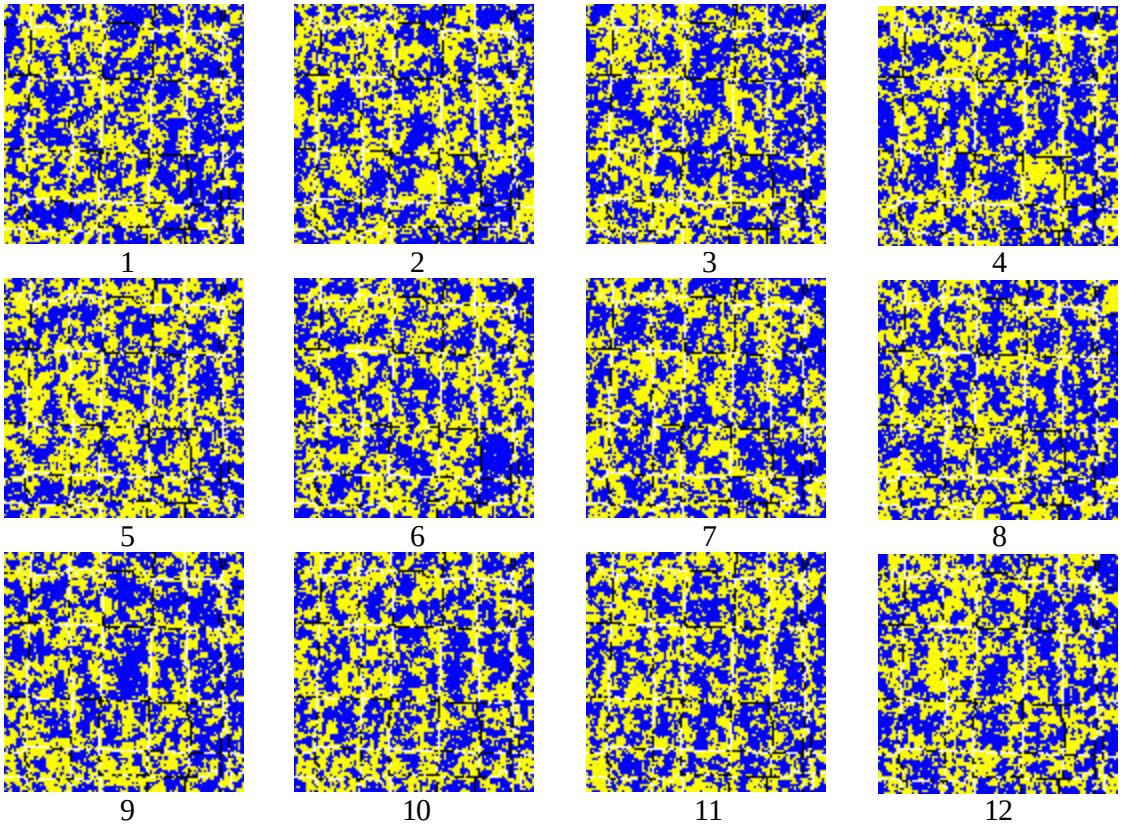

Figure 6.17 12 simulations of the mussel coverage in the core part of test area 1, 1997. Simulated mussel pixels are blue, simulated non-mussels are yellow, data pixels classified as mussels are black and data pixels classified as non-mussels are white. These images compare with the geostatistical equivalents depicted in Figure 5.7.

Table 6.7 The mean fractions for the 12 samples depicted in Figure 6.17, having an average at 49.26% and a standard deviation at 1.81%.

1	0.5205	7	0.4931
2	0.4819	8	0.5008
3	0.5049	9	0.5130
4	0.5129	10	0.4845
5	0.4591	11	0.4822
6	0.4825	12	0.4765

The mean fractions calculated for the 12 sample images depicted in Figure 6.17 are shown in Table 6.7. These mean fractions compare satisfactorily with the corresponding values for the geostatistical simulations. The standard deviation found here at 1.81% is in accordance with the standard deviation for the geostatistical simulations at 1.12%. The average at 49.26% is less

than the corresponding values for the geostatistical simulation at 59.87%. Furthermore, a comparison of Figures 6.17 and Figure 5.7 reveals that first- and second-order moments of the images are very crude measures of similarity due to the marked deviations between the two types of images. The data geometry, i.e. the net-shape formed by the transects is visible in the MRF based images, which is surmised to be an artefact produced by the simulation method. Furthermore, the clusters of mussel pixels are smaller and have a more sporadic pattern in Figure 6.17. This might indicate that the estimated interaction coefficients are too small, but it could also point to the fact that the Ising model is a very simple model, that might not be able to grasp the relevant properties of the mussel beds in the data in a fully satisfactory way.

To investigate the former explanation MPL estimates were calculated for the 10 images produced by geostatistical simulation and depicted in Figure 5.7. The resulting estimates are listed in Table 6.8 and indicate that this is not the case; on the contrary, the interaction coefficients given in Table 6.8 are consistently smaller than the PMPL estimate produced for the discretised transect data at (-2.3138, 1.4038, 1.4415)'. A visual inspection of the images in Figure 5.7 shows that they contain rather large clusters that would be expected to yield values of β at approx. 1.5 - 1.7 to this author's experience provided a constant external field is assumed. Thus, it is likely that the estimation can be improved successfully by allowing data to induce an external field $\alpha(s_i)$ that reflects spatial trends or large scale variation in the images.

Applications of this approach are reported in e.g. Higdon (1994). Use hereof would make the estimated interaction coefficients given in Table 6.8 more reasonable, and would probably allow simulation results to be improved as well. The external field could be derived from e.g. the kriged values, which would have the smooth large scale variation needed, and this would provide a good direction for integrating the geostatistical and the MRF approaches in a model that reflects large scale as well as small scale variation.

Table 6.8 MPL estimates of θ for the 10 geostatistically simulated images depicted in Figure 5.7.

no	α	β_1	β_2
1	-2.3125	1.1811	1.2337
2	-2.4885	1.2853	1.2190
3	-2.4813	1.2749	1.2047
4	-2.2641	1.1780	1.1569
5	-2.3602	1.1992	1.2055
6	-2.4123	1.2257	1.2199
7	-2.4078	1.2147	1.2414
8	-2.4198	1.1612	1.2762
9	-2.4192	1.1985	1.2828
10	-2.3361	1.1829	1.2259

Finally, using a higher order random field might allow the simulations to emulate the mussel bed patterns in a more realistic way.

6.5 Discussion

It has been illustrated how a simple model in an MCMC setting applies as a general tool to obtain a p.d.f. description of a distribution area based on one sample. First-order Markov random fields are very simple, but they provide a first approximation as illustrated in Figure 6.17. However, a comparison of the resulting maps with similar images obtained by geostatistical simulation points to the latter as the best bid for a simulation method as it has a better mimicry of the expected mussel sea bed texture.

Several pathways can be followed to enhance the results. The links to geostatistics can be improved using hybrid approaches where the two are blended. The first steps towards combining the paradigms of geostatistical modelling with Markov random field modelling have been made in e.g. Rathbun & Cressie (1994) and Diggle, Tawn & Moyeed (1998).

As regards more elaborate models, one could employ fractal models (Guillaudeux & Maillard, 1998; Snover & Commito, 1998) of the mussel patterns, or go to the theoretically more satisfying reaction-diffusion models (Paine & Levin, 1981; Murray 1993). Such models of spatial patterns of benthic communities are discussed in chapter 8. Before commencing to that subject, a short presentation of the work carried out on side-scan sonar data is given in the next chapter.

7 Side-scan sonar and data fusion

This chapter describes work that was carried out in close collaboration with Associate Research Professor Allan Aasbjerg Nielsen, IMM. The first section introduces the side-scan sonar data and the selection and pre-processing of datasets. The second section describes a study made to investigate the possible gains from combining the echo sounder and the side-scan sonar data to improve the results of sea bottom classification, and a short discussion is given.

7.1 Side-scan sonar data

During the field campaigns in 1996 and 1997 a range of side-scan sonar datasets were recorded using the Geoacoustics side-scan sonar device at 100 kHz and 500 kHz, and processed into digital files by use of the EOSCAN system. The processing and geocoding of the Geoacoustics images was executed with black-box proprietary software, and several attempts made to convert the datasets into an open readable format failed. The Geoacoustics side-scan sonar images were supposedly *geocoded* with the aforementioned proprietary software, i.e. converted into images having pixel positions reflect geographical positions located in the UTM coordinate system. An example mosaic of geocoded Geoacoustics side-scan images is shown in Figure 7.1.

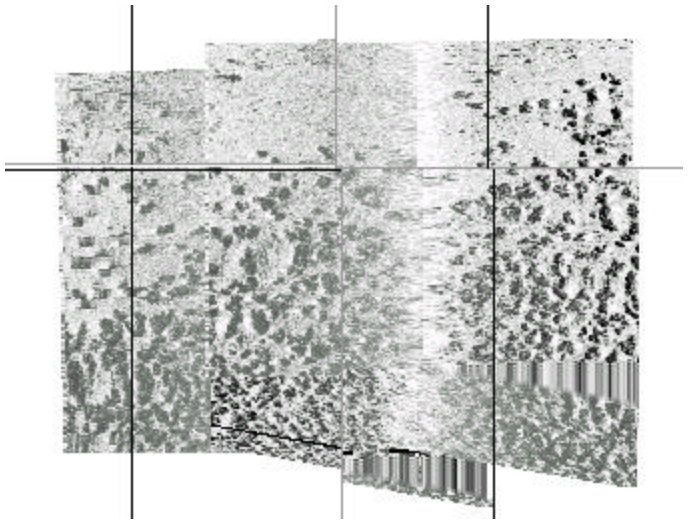

Figure 7.1 A mosaic composed of Geoacoustics side-scan sonar images from the *Posidonia oceanica* bottom type area at Cabo de Palos, 1996.

Unfortunately, it was not possible to fully verify the geocoding of the Geoacoustics data. Furthermore, the closed data format prohibited further insight in the datasets and their properties and caused the datasets to lack flexibility for further data processing. Therefore, it was decided to supplement the data material with another type of side-scan sonar data known to provide the

necessary readability and flexibility of the data format. Thus, during the 1997 field campaign in Øresund side-scan sonar data were recorded using the Isis side-scan sonar at 100 kHz and 384 kHz, and the datasets were stored in the Q-MIPS format, for which good documentation ensuring the readability exists (Triton Elics, 1998).

7.1.1 Pre-processing and geocoding of Isis side-scan sonar data

The geocoding and pre-processing of Q-MIPS data were based on the descriptions provided in Blondel & Murton (1997) and Bolinder (1995). The pre-processing and geocoding algorithms were implemented in SAS, and are therefore fully portable.

During the development of the algorithms it turned out that quite a lot of the positioning data were either missing or sampled at a frequency substantially lower than the frequency of the ping recordings. Furthermore, it was found that the recorded heading angles were very noisy and hard to interpret and therefore it was decided to derive the heading angles from the interpolated and recorded UTM coordinates. The recorded altitudes (vertical distance from the tow fish carrying the side-scan sonar device to the sea bottom) to be used for the slant-range to ground-range corrections were rather noisy too and had to be smoothed. A Gaussian filter was used for this purpose, cf. Figure 7.2, and also for a necessary smoothing of the derived heading angles.

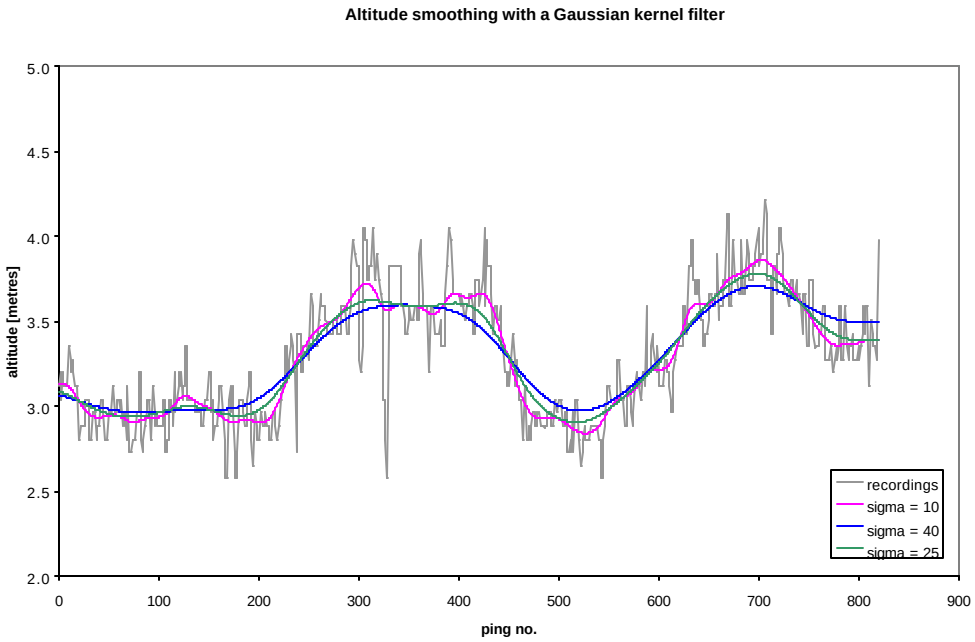

Figure 7.2 An illustration of the effect of the Gaussian kernel filtering of the altitude measurements for a ping sequence recorded in the mussel bottom type area in 1997 in Øresund.

After being pre-processed the Q-MIPS datasets were geocoded yielding side-scan sonar images like the example shown in Figure 7.3. Further details of the pre-processing and geocoding of the side-scan sonar data are given in appendix C.

7.1.2 Classification of Isis side-scan sonar images

Because of the time variable gain and manual changes in the setting of the gain in the side-scan sonar equipment discrimination between bottom types cannot be based on the recorded values themselves, but must be based on derived features that do not depend on the level. Such features can be based on higher order statistics, e.g. features calculated from gray-level co-occurrence

matrices, so-called GLCMs. GLCM methods are introduced in e.g. Haralick, Shanmugam & Dinstein (1973) and Carstensen (1992).

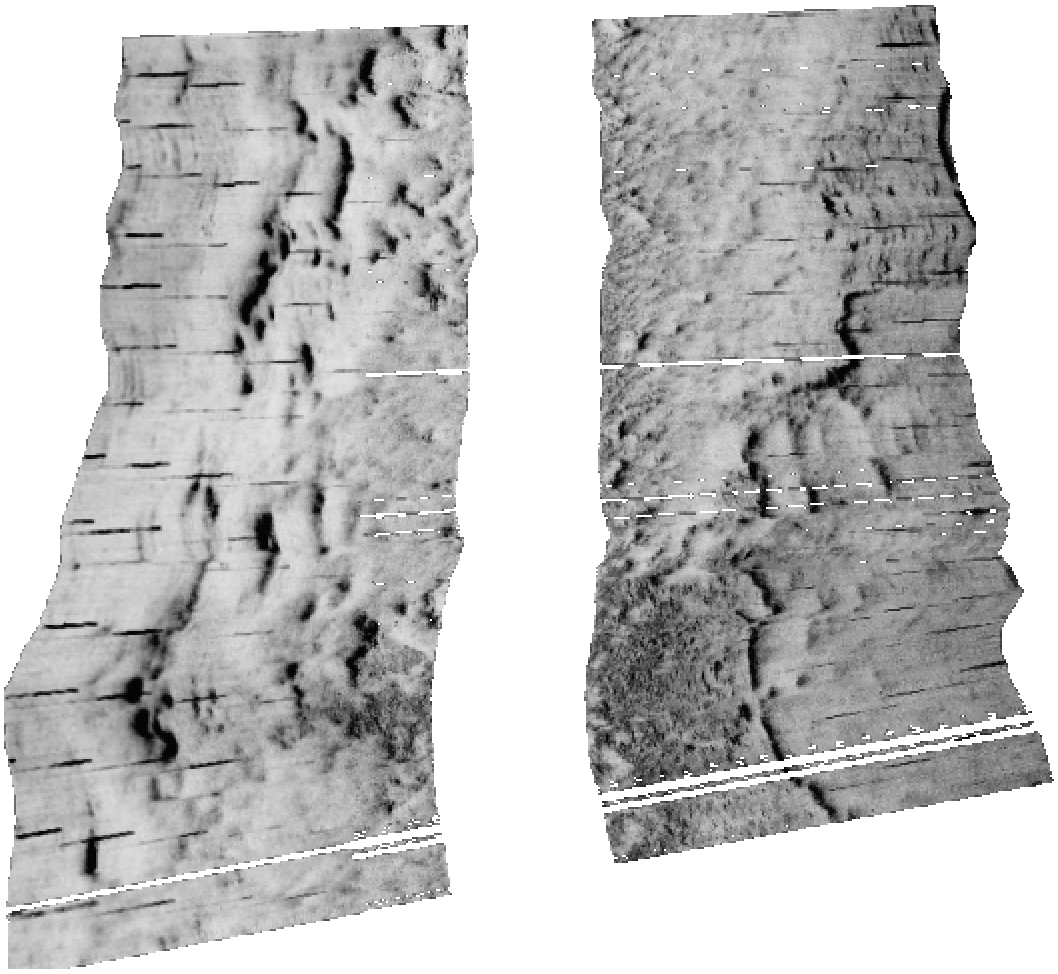

Figure 7.3 Resulting side-scan sonar image obtained from transect no. 23 in the Eelgrass bottom type area, 1997. (Gray levels have been inverted).

A discrimination based on global image features was carried out, for which 100 kHz and 384 kHz side-scan sonar images from the three bottom type areas were selected; 3 images were selected from the eelgrass bottom type area, and 2 images from the mussels and sand bottom type areas, respectively. Based on the GLCMs for the selected side-scan sonar images 15 global image features were derived: Energy, entropy, maximum probability, correlation, diagonal moment, kappa, difference energy, difference entropy, inertia, inverse difference moment, sum energy, sum entropy, sum variance, cluster shade, and cluster prominence. Analyses of variance (ANOVA) were performed on these 15 features and revealed that the 100 kHz images did a better job in the discrimination than the 384 kHz images, which was in accordance with the impression of a visual inspection of the data.

Subsequently, geocoded images were classified by means of higher order local moments calculated in a 7x7 filter window, and it was found that the discriminatory power resides mainly

with the second and third order moments (variance and skewness). Further details about the use of local moments for classification are given in the next section. One example of a classification is shown in Figure 7.4, based on a resampling of the 0.25 x 0.25 m² pixels in the original images into 1 x 1 m² pixels.

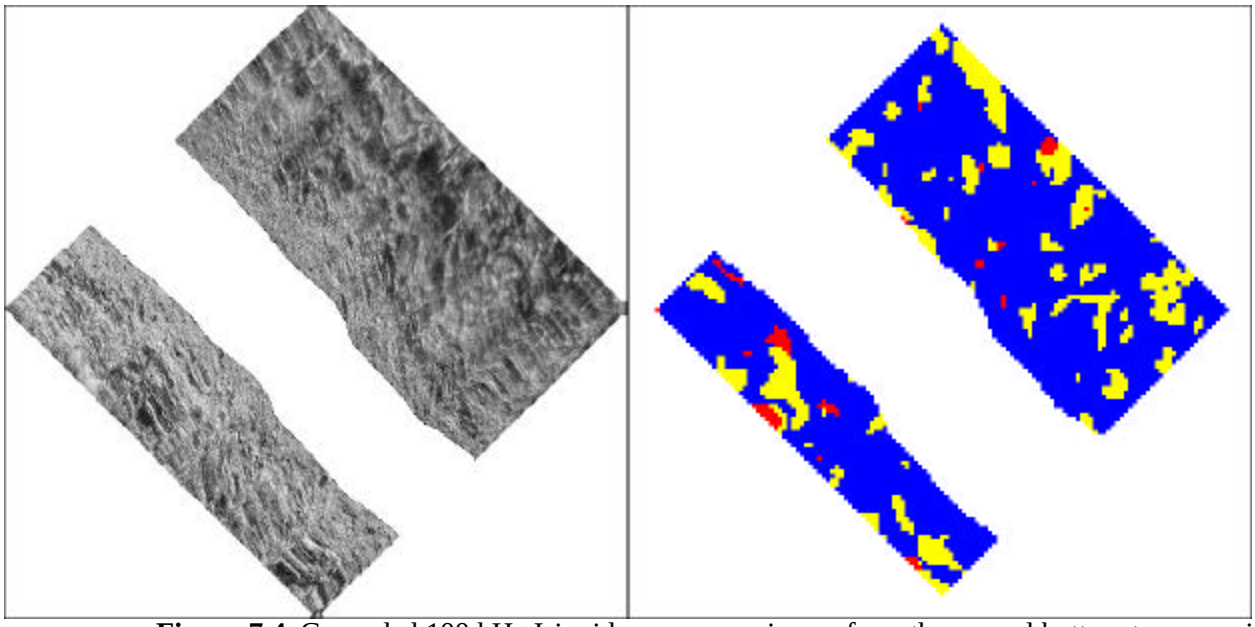

Figure 7.4 Geocoded 100 kHz Isis side-scan sonar image from the mussel bottom type area in Øresund, 1997, and a segmentation hereof based on higher order local moments. Blue is mussels, yellow is sand and red is reject/other. The region covered by the images is 100 m by 100 m.

7.2 Data fusion studies

The data fusion carried out was aimed at the classification of the joint kriged echo sounder data from RoxAnn and side-scan sonar images. Side-scan sonar data entered into the classifications only via features derived from them. These are the abovementioned local second and third order moments calculated in a 7x7 filter window. RoxAnn echo sounder data were kriged to a 1 m grid. Only 100 kHz side-scan sonar images were used, as these seem to have the higher discriminatory power.

For the data fusion study to example datasets were chosen, namely the side-scan sonar ping sequence no. 103 from the mussel bottom type area, and the ping sequence no. 114 from the sand bottom type area. The echo sounder data consists of the datasets described in chapter 3 and appendix B. The full side-scan sonar images (103) and (114) are shown in Figure 7.5 and Figure 7.6. For the classification the images were cropped to the specification areas applying to the echo sounder data as well.

Two spatial resolutions were used, 25 cm and 1 meter. In the 25 cm case the mussel area image covers 560 x 568 pixels and the sand area image covers 400 x 400 pixels.

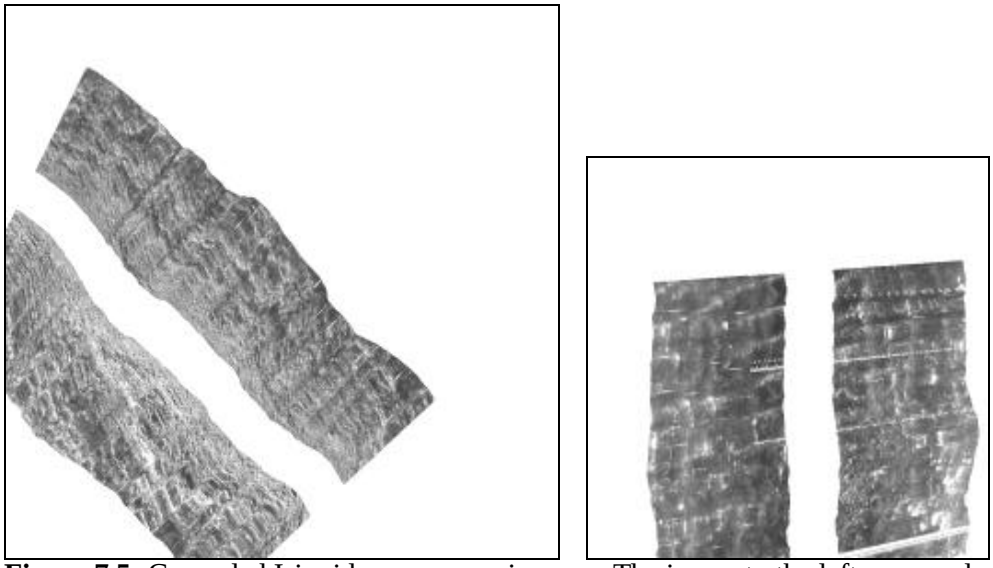

Figure 7.5 Geocoded Isis side-scan sonar images. The image to the left was produced from the ping sequence 103, recorded at the location of the mussel bottom type area, and has an original size of 1200 x 1200 pixels. The image to the right was produced from the ping sequence 114, recorded at the location of the sand bottom type area, and has an original size of 800 x 800 pixels.

All classifications described in the sequel were made by means of ordinary quadratic maximum likelihood (ML) discriminant analysis, the same method as described in section 3.2. In all cases statistics for the classifications were calculated only where all data, i.e. both echo sounder and side-scan sonar, have non-missing values. The results are shown as the classified images and the resubstitution confusion matrices. In the Figures 7.6 - 7.11 the mussels area is shown on the left and the sand area on the right. Missing data are coded white, mussels are blue, sand is yellow and rejects (beyond the 95% percentile in the χ^2 distribution for the Mahalanobis distance) are red.

RoxAnn data alone

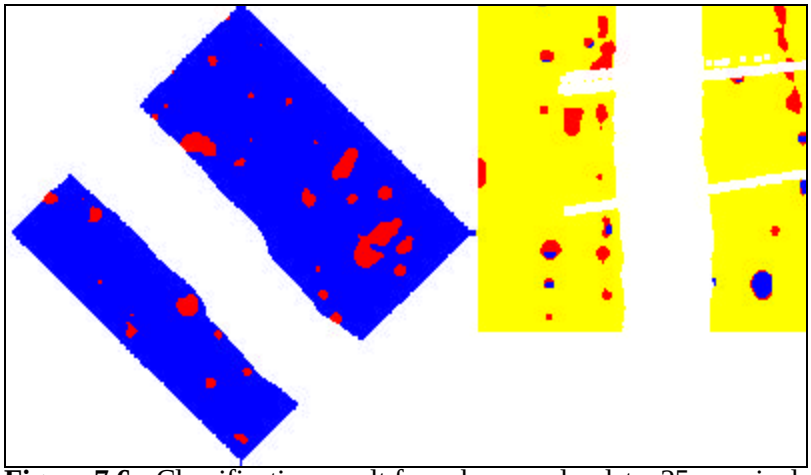

Figure 7.6 Classification result for echo sounder data, 25 cm pixels. The mussel bottom type area is depicted to the left and the sand bottom type area to the right, Øresund 1997. Blue is mussels, yellow is sand and red is reject class.

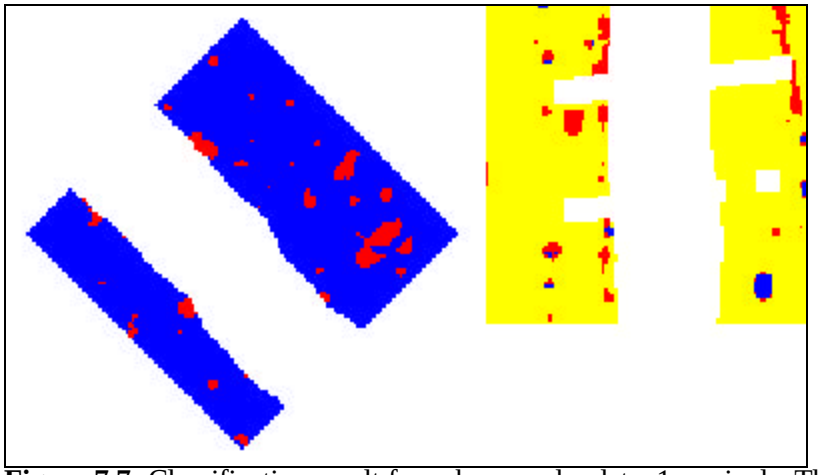

Figure 7.7 Classification result for echo sounder data, 1 m pixels. The mussel bottom type area is depicted to the left and the sand bottom type area to the right, Øresund 1997. Blue is mussels, yellow is sand and red is reject class.

Table 7.1 Resubstitution confusion matrix for echo sounder data, 25 cm pixels.

	Reject	Mussels	Sand	Total
Mussels	5.90%	94.08%	0.02%	100%
Sand	4.76%	1.06%	94.19%	100%
Total	5.34%	48.32%	46.34%	100%

Table 7.2 Resubstitution confusion matrix for echo sounder data, 1 m pixels.

	Reject	Mussels	Sand	Total
Mussels	6.29%	93.71%	0.00%	100%
Sand	5.25%	1.10%	93.65%	100%
Total	5.75%	45.69%	48.56%	100%

Side-scan Sonar data alone

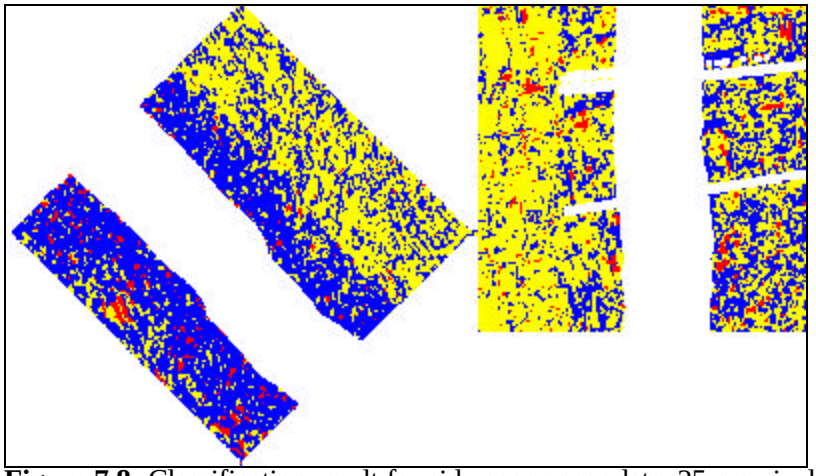

Figure 7.8 Classification result for side-scan sonar data, 25 cm pixels. The mussel bottom type area is depicted to the left and the sand bottom type area to the right, Øresund 1997. Blue is mussels, yellow is sand and red is reject class.

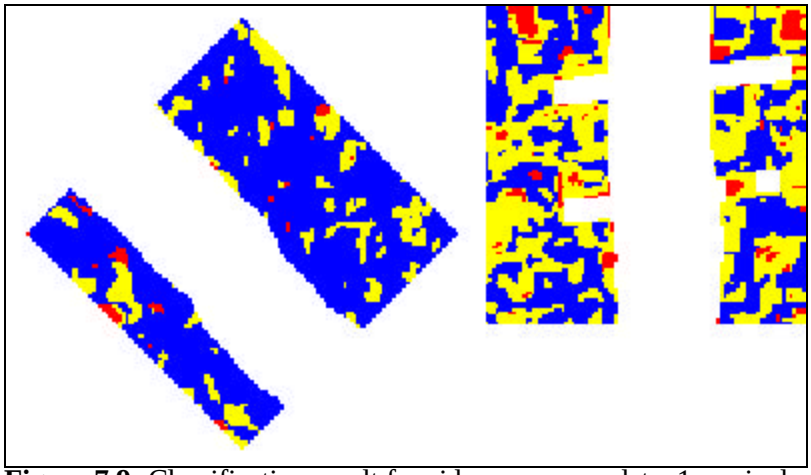

Figure 7.9 Classification result for side-scan sonar data, 1 m pixels. The mussel bottom type area is depicted to the left and the sand bottom type area to the right, Øresund 1997. Blue is mussels, yellow is sand and red is reject class.

Table 7.3 Resubstitution confusion matrix for side-scan sonar data, 25 cm pixels.

	Reject	Mussels	Sand	Total
Mussels	4.08%	58.44%	37.48%	100%
Sand	5.16%	30.65%	64.19%	100%
Total	4.61%	44.77%	50.62%	100%

Table 7.4 Resubstitution confusion matrix for side-scan sonar data, 1 m pixels.

	Reject	Mussels	Sand	Total
Mussels	1.87%	80.68%	17.45%	100%
Sand	6.46%	44.49%	49.06%	100%
Total	4.25%	61.92%	33.84%	100%

Combined RoxAnn and SSS data

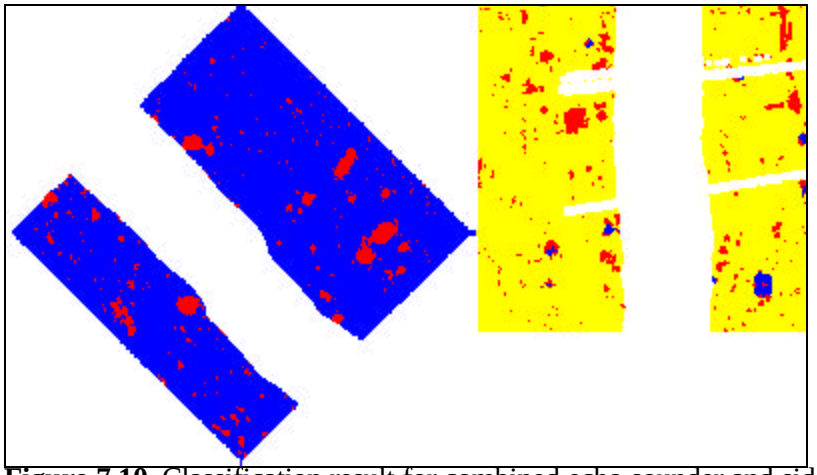

Figure 7.10 Classification result for combined echo sounder and side-scan sonar data, 25 cm pixels. The mussel bottom type area is depicted to the left and the sand bottom type area to the right, Øresund 1997. Blue is mussels, yellow is sand and red is reject class.

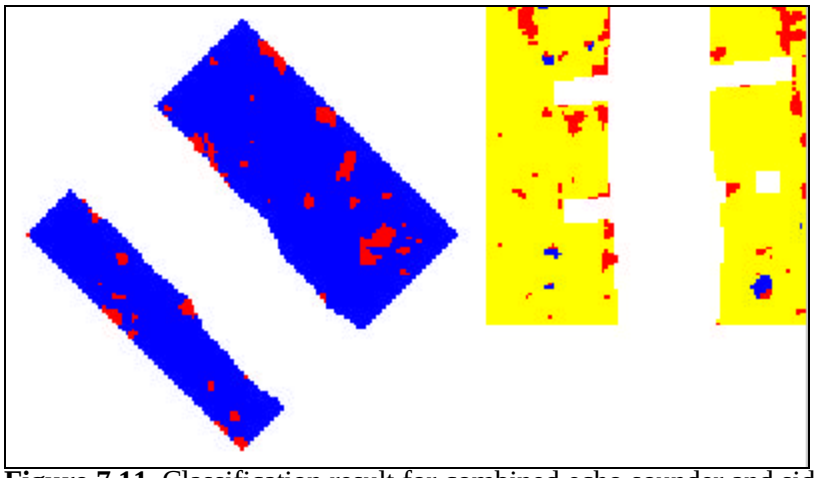

Figure 7.11 Classification result for combined echo sounder and side-scan sonar data, 1 m pixels. The mussel bottom type area is depicted to the left and the sand bottom type area to the right, Øresund 1997. Blue is mussels, yellow is sand and red is reject class.

Table 7.5 Resubstitution confusion matrix for combined echo sounder and side-scan sonar data, 25 cm pixels.

	Reject	Mussels	Sand	Total
Mussels	6.52%	93.46%	0.02%	100%
Sand	6.25%	0.89%	92.86%	100%
Total	6.39%	47.92%	45.69%	100%

Table 7.6 Resubstitution confusion matrix for combined echo sounder and side-scan sonar data, 1 m pixels.

	Reject	Mussels	Sand	Total
Mussels	6.95%	93.05%	0.00%	100%
Sand	6.81%	1.02%	92.17%	100%
Total	6.88%	45.33%	47.79%	100%

On the 1 m scale the satisfactory classification results are largely governed by the RoxAnn data, whereas for the 25 cm scale the finer resolution of the side-scan sonar data is conspicuous in the resulting image.

7.3 Discussion

Other surveyors and researchers have seemingly had similar experiences when comparing side-scan sonar to echo sounder based classification of the sea floor. Bornhold, Collins & Yamanaka (1999) conclude that side-scan images can provide a full coverage with good topographic detail and substrate information of varying quality, while the echo sounder data (QTC View in their case) can provide detailed substrate classifications over a wide range of bottom types.

It remains an open problem to devise good recipes for the utilisation of side-scan sonar in classification of smooth sea bottom textures like those formed by mussels and *Cymodocea nodosa*. For sea bottom textures containing objects at a scale making them clearly visible in the side-scan sonar images it is a more unproblematic task to classify the sea bed types, cf. the *Posidonia oceanica* patches present in Figure 7.1.

8 Models of spatial patterns

This chapter investigates the options for elaborating models of the spatial patterns formed by benthic communities. The first section introduces relevant methods and pieces of theory, in particular the Boolean model, and mentions some alternative frameworks for modelling of spatial patterns. The second section describes how basic assumptions lead to the formulation of a Boolean model for mussels, and outlines the same process for seagrasses. In the third section a new method for the estimation of non-stationary Boolean models is proposed, and the method is illustrated for a side-scan sonar image of *Posidonia oceanica*.

8.1 Introduction

This chapter gives some short bits and pieces regarding relevant fields like mathematical morphology, scale-space theory and stochastic geometry, and gives a short introduction to Boolean models. A short summary of other modelling frameworks for spatial patterns is given.

8.1.1 Mathematical morphology

This subsection contains a short introduction to the basic operators used in mathematical morphology. The presentation relies on Serra (1982), Cressie (1991) and, in particular in this section, on Vincent (1999).

The basic morphological operators are defined based on the concept of a structuring element, which is a particular set $B \in \mathbf{R}^2$, usually small and of a simple shape like e.g. a disk, square or a line segment. The structuring element is translated over images X and its relationships with X are studied at each location. An *origin* is supplied with the specification of the structuring element B indicating the point in the B, which is used to position B in the image during translations. An example of a square structuring element with the origin in the lower left corner is depicted in Figure 8.1.

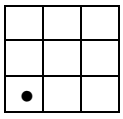

Figure 8.1 A simple 3x3 square structuring element.

From B the *transposed* set $\breve{B}$ can be derived:

$$\breve{B} = \{-b \mid b \in B\}$$

$\breve{B}$ is derived by rotating B by 180^o about the origin O, which typically belongs to B. The translation of B by x is denoted by B_x:

$$B_x = \{b + x | b \in B\}$$

The *dilation* of a set $X \subseteq \mathbf{R}^2$ by structuring element *B*, denoted $d_B(X)$, is the set of points $x \in \mathbf{R}^2$ such that the translation of *B* by *x* has a non-empty intersection with set *X*:

$$d_B(X) = \{x \in \mathbf{R}^2 \mid X \cap B_x \neq \emptyset\}$$

It can be shown that the dilation of *X* by *B* is equal to the Minkowski Addition of *X* and $\check{B}$, denoted $X \oplus \check{B}$:

$$d_B(X) = X \oplus \check{B} = \{x + b | x \in X, b \in \check{B}\}$$

The morphological dilation is defined as a Minkowski addition by some authors, in particular in the U.S. (Sternberg, 1986), however without any transposition of the structuring element, while the former definition is used by the French school (Serra, 1982). In practice, this distinction is mostly academic, since useful structuring elements B are typically symmetric: $\check{B}$ = B.

The *erosion* of *X* by a structuring element *B*, denoted $\varepsilon_B(X)$, is the set of points $x \in \mathbf{R}^2$ such that the translation of *B* by *x* is included in *X*:

$$\varepsilon_B(X) = \{x \in \mathbf{R}^2 \mid B_x \subseteq X\}$$

This definition of the erosion of *X* by *B* corresponds to the Minkowski subtraction of *X* and $\check{B}$:

$$\varepsilon_B(X) = X \ominus \check{B} = \{x \in \mathbf{R}^2 \mid \forall b \in \check{B},\ x - b \in X\}$$

In popular terms the dilation operator tends to "grow" sets while the erosion "shrinks" them. Through dilation, different components of a set *X* can be connected and some holes and gaps can be filled, whereas with erosion holes become bigger, and objects (i.e. connected components) can vanish. More formally, these operations are equipped with a number of fundamental properties, which will not be detailed here.

From the erosion and dilation operators, two other useful morphological transformations can be derived as follows:

The *opening* of *X* by *B*, denoted by $g_B(X)$, is given by:

$$g_B(X) = d_{\check{B}}(e_B(X))$$

The opening of *X* by *B* is often denoted by $(X)_B$, or $X \circ B$.

The *closing* of *X* by *B*, denoted by $f_B(X)$, is given by:

$$f_B(X) = e_{\check{B}}(d_B(X))$$

In the literature, the closing of *X* by *B* is sometimes denoted by $(X)^B$ or $X \bullet B$.

Openings and closings tend to smooth the boundary of the original set *X*, but each in a different manner. The opening tends to remove the small protrusions in which the structuring element

cannot fit, whereas the closing fills in the gaps that cannot hold the structuring element. The opening also shrinks the original set whereas the closing makes it bigger. More formally, one can state the following properties:

1. Openings and closings are increasing operators.
2. Openings are anti-extensive, closings are extensive.
3. Openings and closings are duals of each other.
4. Openings and closings are *idempotent.*

A thorough exposition of mathematical morphology is given in Serra (1982), and a more recent introduction to mathematical morphology is given by Vincent (1999).

8.1.2 Scale-space theory

Scale-space theory deals with the problem of finding proper scales for processing of images with regard to some stipulated objectives. The scale is found by investigating the scale-space over an image, which consists of all smoothed versions of the image for a specified smoothing kernel and a smoothing parameter, t, denoting the position in scale-space. Usually a Gaussian kernel is used to generate the Gaussian scale-space over an image, and the scale parameter, t, can be defined as $t = \sigma^2$ where σ^2 is the variance parameter entering the Gaussian kernel. Thus, for an image I given by I: $\mathbf{R}^2 \rightarrow \mathbf{R}$, the scale-space above it parameterised by t is given by

$$L(t) = g(t) \otimes I,$$

where L: $\mathbf{R}^2 \times \mathbf{R} \rightarrow \mathbf{R}$ maps an image I into scale-space by smoothing it with the Gaussian kernel g(t), and $\otimes$ is the convolution operator.

One of the points of Gaussian scale-space theory is that it makes the use of geometric operators like differential operators very handy due to the properties of the Gaussian kernel. A good introduction to scale-space theory can be found in Lindeberg (1996).

8.1.3 Boolean models

Boolean models are composites made by combining every point in a sample generated by a homogeneous spatial Poisson point process with a compact set, which can be deterministic or drawn from some distribution; the Boolean model then consists of the union of the compact sets. In the terminology of Boolean models the points, s, from the spatial Poisson process D are *germs* and the compact sets, Z, assigned to the germs are *grains.* The Boolean model, X, is then given by

$$X = \cup \{Z_i \oplus s_i \mid s_i \in D\},$$

where the Minkowski addition $Z_i \oplus s_i$ of the compact set Z_i and the point s_i implies that Z_i is translated to have its origin located on s_i. The Poisson process is described by its intensity, λ, and the distribution of grains can be characterised by the expectation of the grain areas, $E(|Z|)$, and e.g. the mean perimeter, $E(P(Z))$.

The mathematical treatment of Boolean models makes substantial use of the *hitting function* defined by

$$T_X(K) = P\{X \cap K \neq \varnothing\}$$

and its complement

$$Q_X(K) = 1\text{-}T_X(K) = P\{X \cap K = \varnothing\}$$

where K can be interpreted as a structuring element. If K is a point, i.e. K = {s}, then the measure $q = Q_X(\{s\}) = 1 - P\{s \in X\}$ is called the *porosity* of the Boolean model. The porosity is the probability that a point belongs to the complement of the Boolean model X. It can be shown, that

$$q = \exp(-\lambda E(|Z|)),$$

which is known as the coverage property of the Boolean model.

Introductions to Boolean models are given in Hall (1988), Cressie (1991) and Molchanov (1999).

8.1.4 Other frameworks for modelling of spatial patterns

Deterministic spatial models could be established based on biogeochemical properties of the benthic community in question, i.e. using dynamics of biota behaviour at the scale of individuals or at some aggregated scale to simulate temporal development and stability of spatial patterns that might emerge. For example, a mussel pattern model might be formulated using a settling of larvae as an initial event and then applying simple rules guiding the movements of the growing mussels at the sea bed like e.g. substrate preferences and tendencies to cluster. Simulating such a model over a sufficient time span might reveal patterns that could provide insight in the real world phenomena of mussel beds.

Reaction-diffusion models (Murray, 1993) based on Turing diffusion (Barrio *et al.*, 1999) or some other diffusion mechanism would be a strong alternative. These models are able to capture a broad scope of pattern phenomena, ranging from the formation of spots on a leopard to the spatial patterns of epidemic outbreaks (Murray, 1993). Although stochastic diffusion models seem to be good candidates for modelling of spatial patterns, they were not used here due to their complexity, especially in regard to estimation (Guttorp, 1995).

A successful application of a diffusion model to the development and structure of tidal mussel patches is described in Paine & Levin (1981). However, the spatial aspect of the mussel patches is not included in that model.

Snover & Commito (1998) apply a fractal model to sea floor photos of mussels to obtain estimates of fractal dimensions of mussel patches and they obtain seemingly good and reasonable results. Stoyan (1994) recommends caution when fractal models are imposed on natural phenomena perceived as point processes and demonstrates how second-order characteristics of some point processes that are not self-similar can behave exactly as second-order characteristics for self-similar point patterns. A good introduction to the practical application of fractals in the study of natural phenomena is given in Hastings & Sugihara (1993). Guillaudeux & Maillard (1998) used fractal models to simulate seabed textures and produced ripple simulations that are visually adequate.

Exotic alternatives include the use of artificial life models. An artificial life model might apply making use of internal states of individuals and the resulting actions-reactions to the environmental conditions and other individuals, including the clumping of individuals.

In the sequel the presentation is focused on simple stochastic models of spatial patterns like the Boolean model.

8.2 Models of spatial patterns for mussels

This section outlines the steps in deriving a model of spatial patterns for mussels, and demonstrates some of the data material that might eventually be used to estimate such models.

8.2.1 Basic formulation of a spatial pattern model for mussels

Contemplating a little on the basic elements of the process under consideration, namely the mussels, a description of a set of mussels can be given by

$$M = \{m_i \mid i=1..N\},$$

where

$$m_i = (s_i,p_i),\ s_i \in \mathbf{R}^4$$

and the i'th mussel, m_i, is given by its position s_i and property vector p_i = (size, orientation, …). The set M will normally describe mussels within a certain local region, given by e.g. the UTM coordinates of the corner points.

Leaving out all elements of the property vector but the size of the mussels, M can be projected onto $\mathbf{R}^2 \times \mathbf{R}$, i.e.

$$M \rightarrow M' = \{((x,y)_i, r_i) \mid i=1..N\},$$

keeping the geographical location (x,y)' and leaving out altitude and temporal dynamics, and representing the size of the mussel by a canonical measure like the length along the major axis of the shell, r. A grown *Mytilus edulis* measures 5 – 7 cm in the longer direction, and has a not entirely symmetric shape, however the deviation from symmetry is quite small and the spatial contour of a mussel might well be modelled by an ellipse. Yet, to simplify matters it is chosen to regard mussels as circular items in the following.

Assuming positions s_i to be members of a homogeneous Poisson process, M' is a Boolean model of the spatial mussel pattern, where the mussel contours are the grains and their positions are the germs. For general usage the assumption of a homogeneous Poisson process is not tenable (above a certain small scale), and therefore models must be found that allow the intensity of the point process to fluctuate. Within mussel beds a Boolean model based on a Poisson cluster process (Neyman-Scott process) might be an appropriate model at the fundamental scales.

Recent developments in models for spatial processes to be considered include the area-interaction model (Kendall, 1998) and the continuum random-cluster model. However, not restricting the scope unnecessarily, it is simply assumed here that the intensities can fluctuate and exhibit spatial trends, and therefore a non-stationary Boolean model is suggested as a proper model for spatial patterns of mussels.

Spatial models for seagrasses

The same elaboration as made above for mussels can be made for neptune grass leading to a non-stationary Boolean model too. However, there is a slight difference, as the grains for the Posidonia model would consist of neptune grass patches, which consist of one or several plants and therefore not necessarily of individuals.

The video strip-charts depicted in Figure 8.2 are included for their visual appeal and their future potential for estimating models of spatial patterns for benthic communities at the fundamental scales.

Figure 8.2 Video strip-charts from the field campaigns in Øresund.

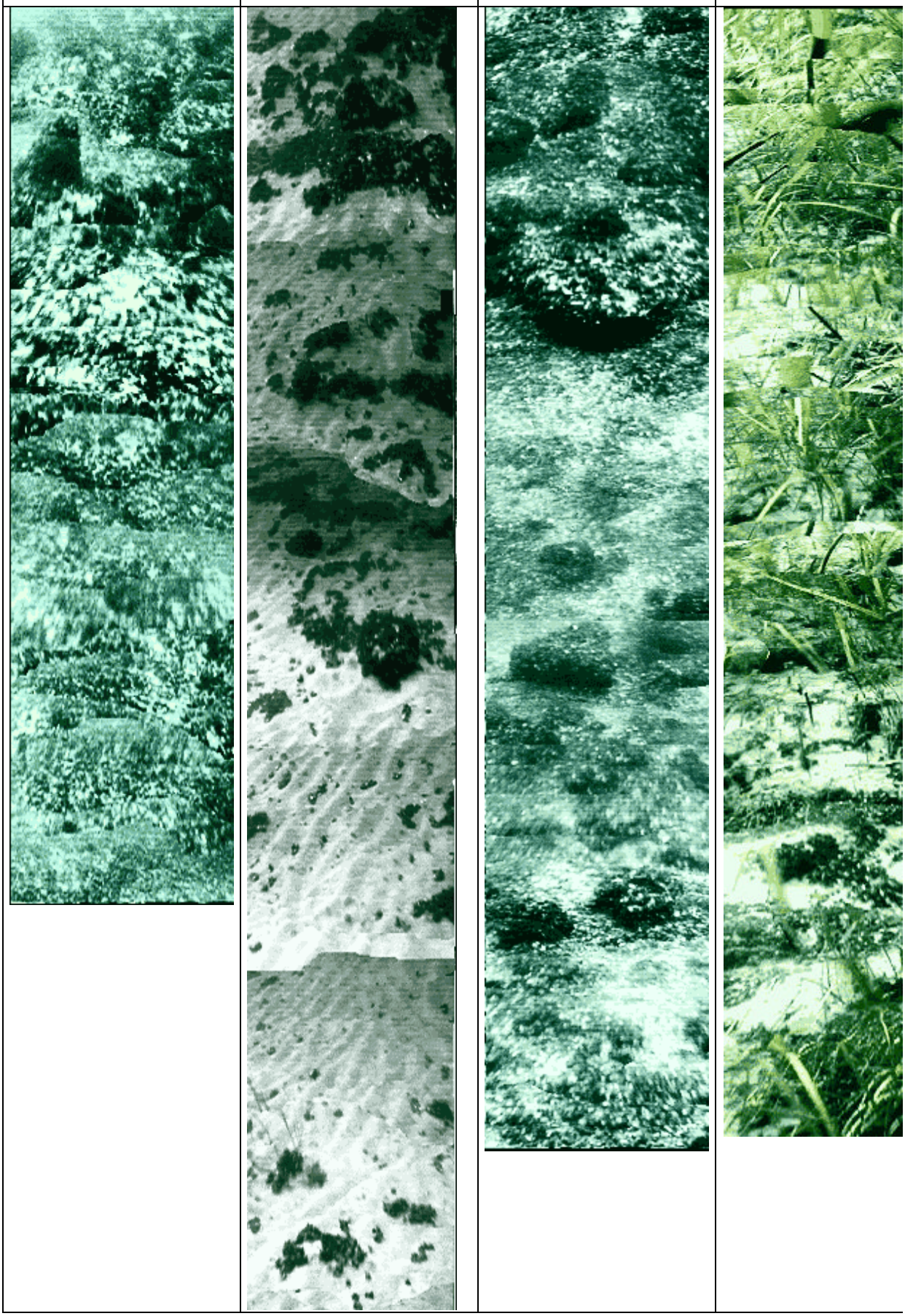

8.3 Estimation of non-stationary Boolean models

This section applies a kernel smoothing method to a sequence of images dilated with squares of increasing side length using a scale-space approach to derive filtered images at t = {10, 25, 50, 100, 400}. The kernel smoothing produces weighted and localised measures of porosities that enter a quadratic regression yielding localised estimates of intensities of the germ process as well as localised estimates of mean area and perimeter for the grains, using the method-of-moments (Cressie, 1991). With the intention of using the Boolean model in a future up-scaling approach, it is of interest to sketch large-scale variability of the basic instationary properties like intensity and expectations of area and perimeter.

8.3.1 Introduction

The object is to estimate Boolean models with varying or non-stationary intensities. Having an image of non-stationary intensities at hand provides opportunities for e.g. segmentation by use of differential operators within a scale-space framework to separate areas of relatively high and low intensity. The kernel smoother introduced for this purpose applies as a windowing device.

Until recently non-stationary Boolean models have not been studied very much since Hanisch (1980) introduced germ-grain models as generalisations of Boolean models, mainly because of the difficulties involved in estimation and inference hereof. Contributions to the theory of non-stationary Boolean models are contained in Schmitt (1997), Chiu & Quine (1997) and Molchanov & Chiu (1999).

8.3.2 Basic theory

Cressie (1991) illustrates the *method-of-moments*, first introduced in Serra (1982), by which estimates of the intensity, λ, and the expectations of the grain area and grain perimeter, $E(|Z|)$ and $E(P(Z))$, can be obtained by quadratic regression based on measured porosities in a sequence of dilations, $d = \{0,...,D\}$, of the studied image using a simple structuring element. Using a square structuring element with increasing side length d, it is possible to use the relation

$$-\log Q_X(dK) = \lambda E(|Z|) + (4\lambda E(P(Z)) / \pi)\cdot d + 4\lambda d^2, \qquad (8.1)$$

or for data

$$-\log q_i = \beta_0 + \beta_1 d_i + \beta_2 d_i^2, \quad d_i \in \{0,..,D\},$$

leading to the estimation of the β vector by quadratic regression and calculation of estimates of λ, $E(|Z|)$, and $E(P(Z))$ based hereon, using the relations

$$\lambda = \beta_2/4,$$

$$E(|Z|) = 4\cdot\beta_0/\beta_2,$$

and

$$E(P(Z)) = 4/\pi\cdot\beta_1/\beta_2.$$

The porosities, q(d), are simply estimated by counting pixels not contained in X, i.e.

$$q(d_i) = 1 - \#\{si \in X\}/N = 1 - \Sigma_X I[s_i \in X]/N, \qquad (8.2)$$

and the β vector $(\beta_0, \beta_1, \beta_2)'$ can be estimated by the o.l.s. estimator

$$\beta^* = (T'T)^{-1}T'Y,$$

where T is the matrix containing D row vectors $(1, d_i, d_i^2)$ and Y holds negative logarithms of the observed porosities, q_i.

The method-of-moments can be extended to non-stationary Boolean models by calculating a localised value of the porosities, $q_i(s)$, in every image pixel, s, thereby replacing the global measures q_i in (8.1) by localised weighted sums, where the weights stem from a Gaussian kernel applied to the dilated image sequence. The kernel smoothing of the porosities is illustrated in Figure 8.3, and can be expressed as

$$q(s;d_i) = 1 - \Sigma_X\, g(s_i\text{-}s)\cdot I[s_i \in X]/N, \qquad (8.3)$$

where

$$g(\Delta,t) = (4\pi t)^{-1/2} \exp(-\Delta^2/4t),$$

and $t = \sigma^2$ is the scale-space parameter. Thus, in every point, s, in the image the following modified version of the relation (8.1) is applied

$$-\log Q_X(dK;s) = \lambda(s)E(|Z|;s) + (4\lambda(s)E(P(Z);s) / \pi)\cdot d + 4\lambda d^2, \quad s \in \text{image}, \qquad (8.4)$$

and the object is to estimate the images reflecting $\lambda(s)$, $E(|Z|;s)$ and $E(P(Z);s)$.

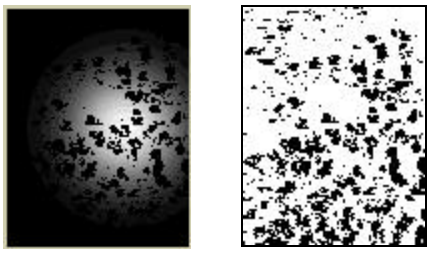

Figure 8.3 An illustration of the kernel smoothing. To the right, the global image is depicted reflecting the constant weights employed when forming a global porosity measure. To the left, the weights applied to the pixel at (60,40) by a Gaussian kernel with a $\sigma = 10$ is illustrated.

Other estimation methods for non-stationary Boolean models reported in recent literature include use of a certain combination of two structuring elements (Schmitt, 1997) and a another method based on kernel smoothing of measures derived by the method of intensities (Molchanov & Chiu, 1999).

8.3.3 Illustration of the estimation method for *Posidonia oceanica*

A subset of a mosaic for *Posidonia oceanica* was extracted and classified manually by thresholding gray levels into binary pixels having the black representing Posidonia patches and white being sand, cf. Figure 8.4.

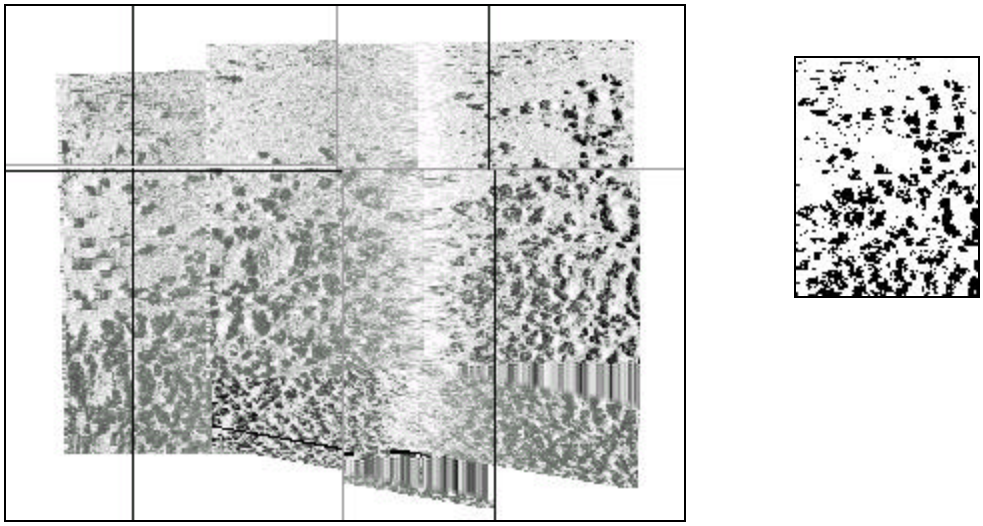

Figure 8.4 A mosaic composed of Geoacoustics side-scan sonar images from the *Posidonia oceanica* bottom type area at Cabo de Palos, 1996. The thresholded subimage depicted to the right contains 119 x 91 pixels, and was extracted from the upper right corner of the mosaic.

A series of dilated images were produced for d = {0,...,5}, cf. Figure 8.5. These images were used to produce localised porosity estimates using scales t at 10, 25, 50, 100, and 400. Because $t = \sigma^2$ these values approximate the use of 3x3, 5x5, 7x7, 10x10 and 20x20 windows, respectively. The sequence of porosities for t = 100 are depicted in Figure 8.6. Subsequently, the porosity image sequences were used for quadratic regression in every pixel as implied by the method-of-moments described above to arrive at images depicting intensities, mean area and mean perimeter.

However, instabilities occurred when the images for d = 5 were included leading to non-convex curves for the $q_i(s;d)$ relation, and the problem was remedied by simply discarding this last column of images in the regressions. The resulting images depicting intensities, mean areas and mean perimeters are shown in Figure 8.7.

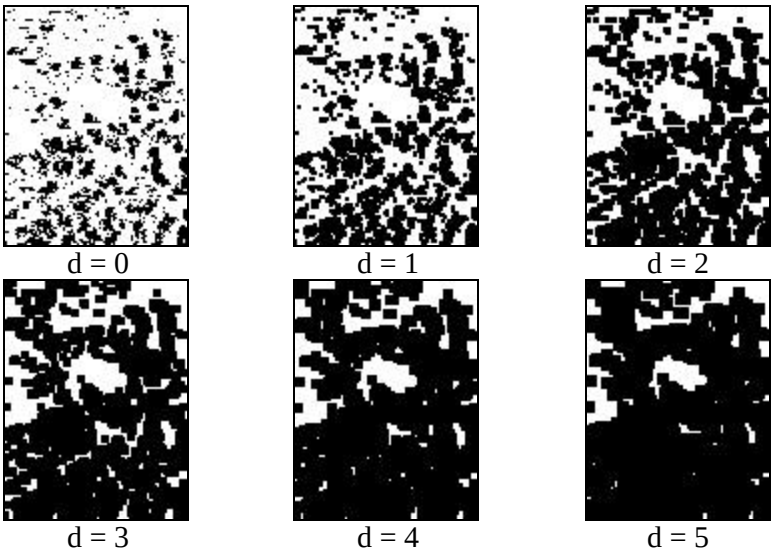

Figure 8.5 The sequence of increasingly dilated images derived from the neptune grass image.

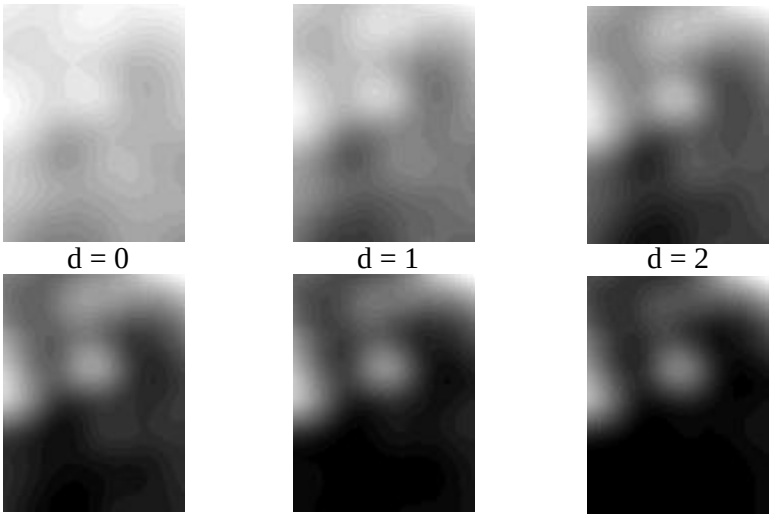

Figure 8.6 The sequence of increasingly smoothed porosity images estimated by Gaussian kernel smoothing with a parameter t = 100 of the increasingly dilated neptune grass images.

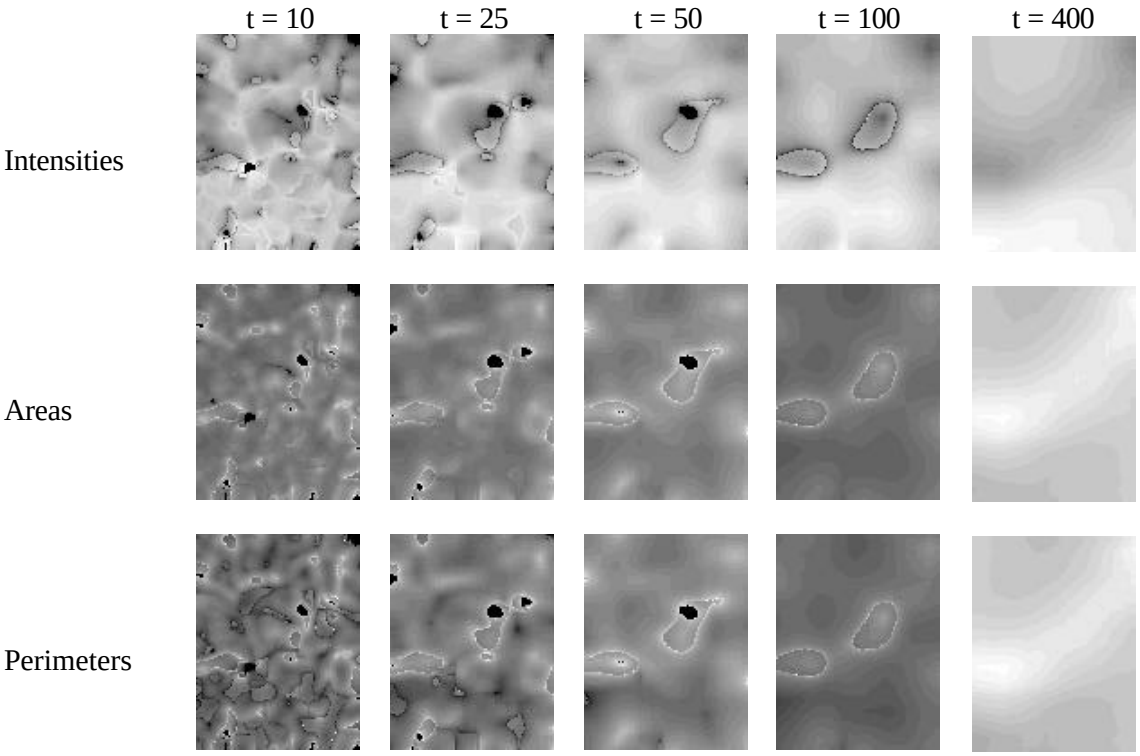

Figure 8.7 The resulting images of intensities, areas and perimeters for the scale parameters t used in the Gaussian kernel smoothing. The black holes in the images indicate regions of singularity in the o.l.s. estimator for the quadratic regression.

The results shown in Figure 8.7 indicate that the smoothing scale has to be sufficiently high to exclude local singularities. Furthermore, they show traces of resonance patterns around sharp thresholds in the data image, cf. the two ellipse-shaped contours that prevails up to t = 100 in the images. Yet for t = 400 corresponding approx. to a 20x20 smoothing window the resulting images are stable and give good indications of the spatial trends in intensities of the germs and the shape distribution for the grains, cf. Figure 8.4.

The method proposed here might pose some challenges in terms of interpretability, on the other hand it provides a high degree of resolution and detail, and therefore provides a good foundation for the further use of spatial trends of the parameters in the non-stationary Boolean models.

For example, these models could be employed in the distribution mapping by means of up-scaling (Schneider *et al.*, 1997) and kriging of the intensity field, possibly as an elaboration of the approach taken in Rathbun & Cressie (1994).

9 Summary and conclusions

This chapter contains a brief summary of the results and findings of the present study.

Chapter 3 outlined and detailed the necessary geostatistical data processing steps to prepare distribution maps based on echo sounder data. Based on exploratory spatial data analyses summarised in appendix B, this chapter demonstrated the feasibility of conducting classification of feature spaces of echo sounder measurements and arrived at a hybrid block kriging method providing mussel coverage rates that were subsequently used to prepare spatial distribution maps. Chapter 4 applied the algorithms developed and presented for mussels (*Mytilus edulis*) to the mapping of neptune grass (*Posidonia oceanica*) and *Cymodocea nodosa* in the Mediterranean and demonstrated that the method worked satisfactorily for the latter, which has a smooth texture.

Chapter 5 demonstrated how geostatistical simulations could be used to assess the variability of mussel distribution maps and the derived distribution areas of mussels. Chapter 6 demonstrated an alternative approach to the assessment of variability based on the use of Markov random fields. Due to large amounts of missing data inherent in the transect based images an adjusted method for Ising model estimation called penalised maximum pseudo-likelihood (PMPL) were proposed. A synthetic image thinning experiment demonstrated the feasibility of the method and, in particular, its ability to control inflation of estimates caused by the large amount of missing data. Subsequently, it was demonstrated how the Ising field could be simulated to assess distribution map variability, and the results were compared to those obtained with the geostatistical simulations.

Chapter 7 gave a short presentation of the use of side-scan sonar data and the fusion hereof with echo sounder data.

Chapter 8 discussed the formulating of models of spatial patterns formed by benthic communities and developed a new method to estimate localised parameters for non-stationary Boolean models based on a combination of scale-space theory and the so-called method-of-moments for stationary Boolean models. The use of the proposed method was illustrated for the spatial patterns of *Posidonia oceanica*.

9.1 Conclusions

Here is a short discussion of the degree of fulfilment attained for the objectives of this Ph.D. study as they were outlined in section 1.1:

1) *To determine the feasibility and applicability of hydroacoustic measurements in the form of echo sounder recordings and side-scan sonar images for preparation of distribution maps of benthic communities.*

It has been shown that mussels can be quantified based on echo sounder measurements, provided a sufficiently elaborate methodology for the preparation of distribution maps is used involving bottom type areas and groundtruth data to allow proper feature space classification.

For side-scan sonar data the use of higher order local moments (local standard deviations and local skewness) enabled classification and quantification for mussels, in particular when used jointly with echo sounder data.

2) To develop statistically sound data processing methods for preparation of distribution maps on the basis of hydroacoustic measurements.

This is demonstrated and discussed in chapters 3 and 4.

3) To develop statistical methods for assessment of the uncertainty of distribution maps, in particular of derived coverage area estimates.

Two approaches has been illustrated and their properties discussed in chapters 5 and 6, namely geostatistical simulation and the use of Markov random fields in an MCMC setting, the latter exemplified by the use of an Ising model.

4) To suggest and estimate stochastic models of the spatial patterns of the selected benthic communities.

The case has been made that non-stationary Boolean models would provide a good starting point regarding stochastic models of spatial patterns for benthic communities, and a new estimation method has been proposed for such models.

9.2 Outlook and perspectives

Some issues of further research and development within the field of hydroacoustic marine biology are briefly mentioned here.

- Multi-beam echo sounder and multi-beam sonar data are highly interesting and might turn out to be the primary instrumentation to use in the sea floor mapping in shallow waters.

- Up-scaling methods aimed at the combination of data sources (with different scales of support and modelling regimes) into coherent distribution maps would be very interesting to apply to the methodologies and fields touched upon in this thesis.

The up-scaling could be based on a unified view of the spatial statistical methods, which is hinted at in the following table:

Framework	**Instantiation / subfield / example**	**Smooth / Mean**	**Rough / Covariance descriptors**
Geostatistics	Ordinary kriging	Gaussian mean field, μ	Variograms, $\gamma(h)$
Markov random fields	Ising model	logit mean field, α	Energy coefficients, β
Stochastic geometry	Boolean model	Intensity field, λ	Point and set covariance functions, C(h)

10 References

Adler R. (1981): The geometry of random fields. Wiley, New York.

Augustin J.M., le Suave R., Lurton X., Voisset M., Dugelay S. & Satra C. (1996): Contribution of the multibeam acoustic imagery to the exploration of the sea-bottom. Marine Geophysical Researches, Vol. 18, pp. 459-486.

Augustin N.H., Mugglestone M.A. & Buckland S.T. (1998): The role of simulation in modelling spatially correlated data. Environmetrics, Vol. 9/2, pp. 175-196.

Balestri E., Piazzi L. & Cinelli F. (1998): Survival and growth of transplanted and natural seedlings of *Posidonia oceanica* (L.) Delile in a damaged coastal area. Journal of Experimental Marine Biology and Ecology, Vol. 228, pp. 209-225.

Barnes R.S.K. & Mann K.H. (1991): Fundamentals of aquatic ecology. 2. edition, Blackwell Scientific Publications Ltd., Oxford.

Barrio R.A., Varea C., Aragón J.L. & Maini P.K. (1999): A two-dimensional numerical study of spatial pattern formation in interacting turing systems. Bulletin of mathematical biology, Vol. 61, pp. 483-505.

Basford D.J., Eleftheriou A., Davies I.M., Irion G. & Soltwedel T. (1993): The ICES North Sea Benthos Survey: The Sedimentary Environment. ICES Journal of Marine Science, Vol. 50, pp. 71-80.

Beauchemin S.S. & Barron J.L. (1995): The computation of optical flow. ACM Computing Surveys, Vol. 27/3, pp. 433-467

Berkhout R.J., Chessa A.G. & Martinius A.W. (1996): A Statistical Adjustment of Haldorsen's Conditioned Boolean Simulation Algorithm. Mathematical Geology, Vol. 28/6, pp. 791-810.

Besag J. (1974): Spatial interaction and the statistical analysis of lattice systems (with discussion). Journal of the Royal Statistical Society, Vol. 2, pp. 192-236.

Besag J. (1989): Towards Bayesian image analysis. Journal of Applied Statistics, Vol. 16/3, pp. 395-407.

Besag J., Green P., Higdon D. & Mengersen K. (1996): Bayesian computation and stochastic systems. Preprint.

Blondel P. & Murton B.J. (1997): Handbook of seafloor sonar imagery. Wiley, Chichester.

Blondel P., Parson L.M. & Robigou V. (1998): TexAn: Textural analysis of sidescan sonar imagery and generic seafloor characterisation. Proceedings of the IEEE Oceans '98 Conference, pp. 419-423.

Bolinder A. (1995): Geographic rectification and mosaicking of side-scan sonar imagery. Ph.d. thesis, Department of Naval Architecture and Ocean Engineering, Chalmers University of Technology, Göteborg, Sweden.

Bornhold B.D., Collins W.T. & Yamanaka L. (1999): Comparison of seabed characterisation using sidescan sonar and acoustic classification techniques. Canadian Coastal Conference, Victoria, British Columbia, Canada.

Bozzano R., Mantovani R., Siccardi A. & Castellano L. (1998): Acoustic backscattering from marine vegetation. Proceedings of the IEEE Oceans '98 Conference, pp. 1017-1021.

Brinke W.B.M ten, Augustinus P.G.E.F. & Berger G.W. (1995): Fine-grained Sediment Deposition on Mussel Beds in the Oosterschelde (The Netherlands), Determined from Echosoundings, Radio-isotopes and Biodeposition Field Experiments. Estuarine, Coastal and Shelf Science, Vol. 40, pp.195-217.

Buckland S.T. (1982): A note on the Fourier series model for analysing line transect data. Biometrics, Vol. 38, pp. 469-477.

Burns D.R. (1992): Acoustic and elastic scattering from seamounts in three dimensions – A numerical modeling study. J. Acoust. Soc. Am., Vol. 92/5, pp. 2784-2791.

Burns D., Queen C.B. & Chivers R.C. (1985): An ultrasonic signal processor for use in underwater acoustics. Ultrasonics, July 1985, pp. 189-191.

Caccia D.C. (1998): Analyzing exact fractal time series: Evaluating dispersional analysis and rescaled range methods. Masters thesis, Statistics Department, University of Washington.

Carstensen J.M. (1992): Description and simulation of visual texture. Ph.d. thesis, Department of Mathematical Modelling, Technical University of Denmark.

Cervenka P., Herzfeld U.C. & de Moustier C. (1994): Accuracy of the spatial representation of the seafloor with bathymetric sidescan sonars. Marine Geophysical Researches, Vol. 16, pp. 407-425.

Chauvaud S., Bouchon C. & Manières R. (1998): Remote sensing techniques adapted to high resolution mapping of tropical coastal marine ecosystems (coral reefs, seagrass beds and mangrove). Int. Journal of Remote Sensing, Vol. 19/18, pp. 3625-3639.

Cherry S. (1997): Non-parametric estimation of the sill in geostatistics. Environmetrics, Vol. 8, pp 13-27.

Chiu S.N. & Quine M.P. (1997): Central limit theory for the number of seeds in a growth model in 3^d ith inhomogeneous Poisson arrivals. The Annals of Applied Probability, Vol. 7/3, pp. 802-814.

Chivers R.C. & Burns D. (1991): Remote acoustic sensing of the seabed. Proceedings of the IV International School and Physical Acoustics, pp. 343-353, edited by A. Alippi. World Scientific Publishers, Singapore.

Chivers R.C., Burns D. R. & Sisk H. (1989): Analysis of echo-sounder signals for sea-bed characterization. Ultrasonic International 89 Conference Proceedings.

Chivers R.C., Emerson N. & Burns D.R. (1990): New acoustic processing in underway surveying. The Hydrographic Journal, Vol. 56, pp. 9-17.

Cochran W.G. (1983): Planning and Analysis of Observational Studies. New York: John Wiley & Sons.

Cohen J. (1988): Statistical power analysis for the behavioral sciences. 2^{nd} ed., Lawrence Erlbaum Associates.

Collins W.T. & McConnaughey R.A. (1998): Acoustic classification of the sea floor to address essential fish habitat and marine protected area requirements. Canadian Hydrographic Conference 1998, CHS, Victoria, British Columbia, Canada.

Collins W.T., Gregory R. & Anderson J. (1996): A Digital Approach to Seabed Classification. Sea Technology, August 1996.

Conradsen K. & Carstensen J.M. (1998): Markov random fields. Course notes for 04351: Statistical Image Analysis. Department of Mathematical Modelling, Technical University of Denmark.

Conradsen K. (1984): An Introduction to Statistics; Vol 1A, 1B, 2A & 2B. Department of Mathematical Modelling, Technical University of Denmark.

Constantine A.G. & Hall P. (1994): Characterizing surface smoothness via estimation of effective fractal dimension. J.R. Statist. Soc., Vol. 56/1, pp 97-113.

Cox D.D., Cox L.H. & Ensor K.B. (1997): Spatial sampling and the environment: some issues and directions. Environmental and Ecological Statistics, Vol. 4, pp. 219-233.

Cox D.R. & Miller H.D. (1965): The theory of stochastic processes. London, Chapman & Hall.

Cressie N. & Zimmerman D.L. (1992): On the stability of the geostatistical method. Mathematical Geology, Vol. 24/1, pp. 45-59.

Cressie N.A.C. (1991): Statistics for spatial data, John Wiley and Sons, Inc., New York, 900 pp.

Deutsch C.V. & Journel A.G. (1998): GSLIB, Geostatistical Software Library and User's Guide, second edition, Oxford University Press.

Diggle P.J, Tawn J.A. & Moyeed R.A. (1998): Model-based geostatistics (with discussion). Applied Statistics, Vol. 47/3, pp. 299-350.

Dolmer P. (1998): The interactions between bed structure of *Mytilus edulis* L. and the predator *Asterias rubens* L. Journal of Experimental Marine Biology and Ecology, Vol. 228, pp. 137-150.

Duarte C.M. & Sand-Jensen K. (1990): Seagrass colonization: Patch formation and patch growth in *Cymodocea nodosa.* Mar. Ecol. Progr. Ser., Vol. 65, pp. 193-200.

Dunning J.B, Stewart D.J., Danielson B.J., Noon B.R., Root T.L., Lamberson R.H.& Stevens E.E. (1995): Spatially explicit population models: Current forms and future uses. Ecological Applications, Vol. 5/1, pp. 3-11.

Ersbøll B.K: (1989): Transformations and classifications of remotely sensed data - theory and geological cases. Ph.d. thesis, Department of Mathematical Modelling, Technical University of Denmark.

Fabricius-Bjerre, F. (1981): Textbook of Geometry, I: Analytical geometry and linear algebra. 6th edition. In Danish. Polyteknisk Forlag.

Fismen M. (1997): Exact simulation using Markov chains. Master thesis, Norwegian University of Technology and Science, Trondheim, Norway.

Foley J.D., van Dam A., Feiner S.K. & Hughes J.F. (1990): Computer graphics, principles and practice. 2. ed., Addison-Wesley, Reading, MA.

Foote K.G. & Stefánsson G. (1993): Definition of the problem of estimating fish abundance over an area from acoustic line-transect measurements of density. ICES Journal of Marine Science, Vol. 50, pp. 369-381.

Fox C.G. (1996): Objective classification of oceanic ridge-crest terrains using two-dimensional spectral models of bathymetry: Application to the Juan de Fuca Ridge. Marine Geophysical Researches, Vol. 18, pp. 707-128.

Geman S. & Geman D. (1984): Stochastic relaxation, Gibbs distributions and the Bayesian restoration of images. IEEE Transactions on Pattern Analysis and Machine Intelligence, Vol. 6, pp. 721-741.

Gensane M. (1989): A statistical study of acoustic signals backscattered from the sea bottom. IEEE Journal of Oceanic Engineering, Vol. 14/1, pp. 84-93.

Geyer C.J. & Thompson E. (1992): Constrained Monte Carlo maximum likelihood for dependent data (with discussion). Journal of the Royal Statistical Society, series B, Vol. 54/3, pp. 657-699.

Geyer C.J. (1998): Likelihood inference for spatial point processes. Preprint.

Geyer C.J. (1999): Likelihood Inference for Spatial Point Processes. In Stochastic Geometry: Likelihood and Computation, eds. W. Kendall, O. Barndorff-Nielsen and M. N. M. van Lieshout, London: Chapman and Hall/CRC, pp. 141-172.

Gilks W.R., Richardson S. & Spiegelhalter D.J. (1996): Markov chain Monte Carlo in practice. Chapman & Hall.

Glasbey C.A. & Mardia K.V. (1998): A statistical framework for image warping. Preprint.

Goff J.A. & Jordan T.H. (1988): Stochastic modeling of seafloor morphology: Inversion of sea beam data for second-order statistics. Journal of Geophysical Research, Vol. 93/B11, pp. 13589-13608.

Green P.J. & Murdoch D.J. (1998): Exact sampling for Bayesian inference: towards general purpose algorithms. Bayesian Statistics, Vol. 6, Oxford University Press (Preprint).

Green P.J. (1998): Slides from a presentation outlining MCMC at the Strathclyde Conference, 1998.

Green P.J. (1998a): Penalized likelihood. Preprint.

Green R. (1989): Power analysis and practical strategies for environmental monitoring. Environmental research, Vol. 50, pp. 195-205.

Guilladeux S. & Maillard E. (1998): Seabed simulations with fractal techniques. Proceedings of IEEE Oceans '98 Conference, Vol. 1, pp. 433-437.

Guttorp P., Meiring W. & Sampson P.D. (1994): A space-time analysis of ground-level ozone data. Environmetrics, Vol. 5, pp. 241-254.

Guttorp P. (1995): Stochastic Modeling of Scientific Data. Chapman & Hall / CRC.

Hall P. (1988): Introduction to the Theory of Coverage Processes. Wiley, New York.

Hanisch K.H. (1980): On classes of random sets and point process models. Elektronische Informationsverarbeitung und Kybernetik, Vol. 16, pp. 409-412.

Haralick R.M., Shanmugam K. & Dinstein I. (1973): Textural featurs for image classification. IEEE Transactions on Systems, Man and Cybernetics, Vol. 3/6, pp. 610-621.

Hastings H.M. & Sugihara G. (1993): Fractals, a user's guide for the natural sciences. Oxford University Press.

Hastings W.K. (1970): Monte Carlo sampling methods using Markov chains and their applications. Biometrika, vol. 57, pp. 97-109.

Hawrot R.Y. & Niemi G.J. (1996): Effects of edge type and patch shape on avian communities in a mixed conifer-hardwood forest. The Auk, Vol. 113/3, pp. 589-598.

Heald G.J. & Pace N.G. (1996): An analysis of 1st and 2nd backscatter for seabed classification. Proceedings of the 3rd European Conference on Underwater Acoustics. Heraklion, Crete, Greece. Ed. J. S. Papadakis.

Hellequin L. (1998): Statistical characterization of multibeam echosounder data. Proceedings of the IEEE Oceans '98 Conference, pp. 228-233.

Herzfeld, U.C., and Higginson C.A. (1996): Automated Geostatistical Seafloor Classification – Principles, Parameters, Feature Vectors, and Discrimination Criteria. Computers and Geoscience, Vol. 22, No. 1, pp. 35-52.

Higdon D.M. (1994): Spatial applications of Markov chain Monte Carlo for Bayesian inference. Ph.D. Dissertation, Statistics Department, University of Washington.

Hinkley D.V. (1988): Bootstrap methods. J. R. Statist. Soc. B, Vol. 50/3, pp. 321-337.

Hoelscher-Hoebing U. & Kraus D. (1998): Unsupervised image segmentation and image fusion for multi-beam/multi-aspect sidescan sonar images. Proceedings of the IEEE Oceans '98 Conference, pp. 571-576.

Hughes Clarke J.E., Mayer L.A. & Wells D.E. (1996): Shallow-water imaging multibeam sonars: A new tool for investigating seafloor processes in the Coastal Zone and on the Continental Shelf. Marine Geophysical Researches, Vol. 18, pp. 607-629.

Hughes J.P. & Guttorp P. (1994): Incorporating spatial dependence and atmospheric data in a model of precipitation. Journal of Applied Meteorology, Vol. 33, pp. 1503-1515.

Huseby R.B., Milvang O., Solberg A.S. & Bjerde K.W. (1993): Seabed classification from multibeam echosounder data using statistical methods. Proceedings of the IEEE Oceans '93 Conference, pp. 229-233.

Isaaks E.H. & Srivastava R.M. (1989): An introduction to applied geostatistics. Oxford University Press, New York, 561 pp.

ISO 5725-2 (1994): Accuracy (trueness and precision) of measurements methods and results - Part 2: Basic method for the determination of repeatability and reproducibility of a standard measurement method. International Organization for Standardisation, Geneva.

Jiang M., Stewart W.K. & Marra M. (1993): Segmentation of seafloor sidescan imagery using Markov Random Fields and neural networks. Proceedings of the IEEE Oceans '93 Conference, Vol. III, pp. 456-461.

Journel A. & Rossi M. (1989): When do we need a trend model in kriging? Mathematical Geology, Vol. 21/7, pp. 715-739.

Journel A.G. & Huijbregts C. (1978): Mining geostatistics. Academic Press.

Kaiser G. (1994): A Friendly Guide to Wavelets. Birkhäuser, Boston.

Kendall W. (1998): Perfect Simulation for the Area-Interaction Point Process. Preprint.

Kitanidis P.K. & Vomvoris E.G. (1983): A geostatistical approach to the inverse problem in groundwater modeling (steady state) and one-dimensional simulations. Water Resources Research, Vol. 19/3, pp. 677-690.

Kleinbaum D.G. (1994): Logistic regression: A self-learning text. Springer-Verlag, New York.

Kostylev V., Erlandsson J. & Johannesson K. (1997): Microdistribution of the polymorphic snail *littorina saxatilis* (Olivi) in a patchy rocky shore habitat. Ophelia, Vol. 47/1, pp 1-12.

Larsen R., Conradsen K. & Ersbøll B.K. (1998): Estimation of dense image flow fields in fluids. IEEE Transactions on Geoscience and Remote Sensing, Vol. 36/1, pp.256-264.

Laslett G.M. (1994): Kriging and splines: An empirical comparison of their predictive performance in some applications. Journal of the American Statistical Association, Vol. 89/426, pp. 391-400.

Lindeberg T. (1996): Scale-space: A framework for handling image structures at multiple scales. Proceedings of Seminar at the CERN School of Computing, Egmond aan Zee, The Netherlands, 8-21 September, 1996.

Little S. A. & Smith D.K. (1996): Fault scarp identification in side-scan sonar and bathymetry images from the Mid-Atlantic Ridge using wavelet-based digital filters. Marine Geophysical Researches, Vol. 18, pp. 741-755.

Lyngby J.E. & Sørensen P.S. (1994): Growth dynamics of eelgrass in Øresund and assessment of impact of shading on eelgrass growth. Doc. No. 94/173/0E. Report to Øresundskonsortiet prepared on behalf of VKI.

Magorrian B.H., Service M. & Clarke W. (1995): An acoustic bottom classification survey of Strangford Lough, Northern Ireland. J. Mar. Biol. Ass. U.K., Vol. 75, pp. 987-992.

Malinverno A. (1989): Testing linear models of sea-floor topography. Pure and Applied Geophysics, Vol 131, pp. 139-155.

Malladi R., Sethian J.A. & Vemuri B.C. (1994): Evolutionary fronts for topology-independent shape modeling and recovery. Proceedings of Third European Conference on Computer Vision (ECCV'94), Stockholm, Sweden, May 1994, pp. 3-13.

Mallet Y., Coomans D. & de Vel O. (1996): Recent developments in discriminant analysis on high dimensional spectral data. Chemometrics and Intelligent Laboratory Systems, Vol. 35, pp. 157-173.

Maravelias C.D. & Haralabous J. (1995): Spatial distribution of herring in the Orkney/Shetland area (Northern North Sea): A geostatistical analysis. Netherlands Journal of Sea Research, Vol. 34/4, pp. 319-329.

Marbá N., Duarte C.M., Cebrián J., Enríquez S., Gallegos M.E., Olesen B., Sand-Jensen K. (1996): Growth and population dynamics of Posidonia oceanica on the Spanish Mediterranean coast: elucidating seagrass decline. Marine Ecology Progress Series, Vol. 137, pp. 203-213.

Martin E.B. & Scott E.M. (1995): The detection of change in spatial processes. Environmetrics, Vol. 6., pp. 141-154.

Martin-Löf A. (1973): Mixing properties, diferentiability of the free energy and the central limit theorem for a pure phase in the Ising model at low temperature. Comm. Math. Phys., Vol. 32, pp. 75-92.

MAS3-CT95-0026 (1997): "Scientific Report for Year 1 of the BioSonar Project". Report prepared by the BioSonar project partners to the MAST Office of the European Union.

MAS3-CT95-0026 (1998): "Scientific Report for Year 2 of the BioSonar Project". Report prepared by the BioSonar project partners to the MAST Office of the European Union.

MAS3-CT95-0026 (1999): "Final Scientific Report of the BioSonar Project". Report prepared by the BioSonar project partners to the MAST Office of the European Union.

MAS-CT-0026 (1995): Technical annex to Sonar technology for monitoring and assessment of benthic communities. Prepared by the BioSonar project proposal group.

Messieh S.N., Rowell T.W., Peer D.L. & Cranford P.J. (1991): The effects of trawling, dredging and ocean dumping on the eastern Canadian continental shelf seabed. Continental Shelf Research, Vol. 11, Nos 8-10, pp. 1237-1263.

Molchanov I.S. (1999): Random closed sets. Chapter 7 contributed to *Stochastic Geometry, Likelihood and Computation*, edited by Barndorff-Nielsen, Kendall & van Lieshout, Chapman & Hall.

Molchanov I.S. & Chiu S.N. (1999): Smoothing techniques and estimation methods for non-stationary Boolean models with applications to coverage processes. Technical report, Department of Statistics, University of Glasgow.

Montgomery D.C: (1991): Design and analysis of experiments. 3rd edition, Wiley & Sons.

Murray J.D. (1993): Mathematical Biology. 2nd ed., Biomathematics Texts, Vol. 19, Springer-Verlag.

Myers D.E, Begovich C.L., Butz T.L. & Kane V. (1982): Variogram Models for Regional Groundwater Geochemical Data. Mathematical Geology, Vol. 14, pp. 629-644.

Myers D.E. (1999): Book review: *GSLIB, Geostatistical software library and user's guide, second edition; Clayton V. Deutsch and Andre G. Journel; Oxford University Press, 1998, x + 369 pages, ISBN 0-19-510015-8.* Computers & Geosciences, vol 25, pp. 309-312.

Nielsen A.A. (1994): Analysis of regularly and irregularly sampled spatial, multivariate, and multi-temporal data. Ph.d. thesis, Department of Mathematical Modelling, Technical University of Denmark.

Nielsen A.A. (1996): Introduction to Geostatistics. Course notes to 8829: Geographical Information Systems. Department of Mathematical Modelling, Technical University of Denmark.

Nielsen A.A. (1997): Linear unmixing. Research notes, Department of Mathematical Modelling, Technical University of Denmark.

Nielsen M. & Deriche R. (1996): Binocular dense depth reconstruction using isotropy constraint. Proceedings of the 9th Scandinavian Conference on Image Analysis, pp. 49-56, Uppsala, Sweden, June 6-9 1995.

Nielsen M. (1998): Course notes for Statistical Image Analysis. Technical University of Denmark, Spring 1998.

Nielsen M., Maas R., Niessen W.J., Florack L.M.J. & ter Haar Romey B.M. (1999): Binocular stereo from grey-scale images. Journal of Mathematical Imaging and Vision, Vol. 10/2, pp 103-122.

O'Driscoll R.L. (1998): Description of spatial pattern in seabird distributions along line transects using neighbour *K* statistics. Marine Ecology Progress Series, Vol. 165, pp. 81-94.

Onsager L. (1944): Crystal statistics, I. A two-dimensional model with an order-disorder transition. Phys. Rev., Vol. 65, pp. 117-149.

Pace N.G. & Dyer C.M. (1979): Machine classification of sedimentary sea bottoms. IEEE Transactions of Geoscience Electronics, Vol. GE-17/3, pp. 52-56.

Paine R.T. & Levin S.A. (1981): Intertidal landscapes: Disturbance and the dynamics of pattern. Ecological Monographs, Vol. 51/2, pp. 145-178.

Parsons T.R., Takahashi M. & Hargrave B. (1977): Biological oceanographic processes. 2nd edition, Pergamon Press, Oxford.

Parthiot F, Cervenka P. & Ollivier F. (1995): Seafloor spatial representation and bathymetry data quality. IEEE Oceans '95 Conference Proceedings, Vol. 3, pp. 1922-1927.

Phillips D.L., Henry Lee E., Herstrom A.A., Hogsette W.E. & Tingey D.T. (1996): Use of auxiliary data for spatial interpolation of ozone exposure in Southeastern forests. Environmetrics, Vol. 8, pp. 43-61.

Phinn S., Franklin J., Hope A., Stow D. & Huenneke L. (1995): Biomass distribution mapping using airborne digital video imagery and spatial statistics in a semi-arid environment. Journal of Environmental Management, Vol. 47, pp. 139-164.

Pican N., Trucco E., Ross M., Lane D.M., Petillot Y. & Tena Ruiz I. (1998): Texture analysis for seabed classification: Co-occurrence matrices vs self-organizing maps. Proceedings of the IEEE Ocens '98 Conference, Vol. 1, pp. 424-428.

Pollock K.H. & Kendall W.L. (1987): Visibility bias in aerial surveys: A review of estimation procedures. Journal of Wildlife Management, Vol. 51/2, pp. 502-510.

Porteiro C., Carrera P. & Miquel J. (1996): Analysis of Spanish acoustic surveys for sardine, 1991-1993: abundance estimates and inter-annual variability. ICES Journal of Marine Science, Vol. 53, pp. 429-433.

Prager B.T., Caughey D.A. & Poeckert R.H. (1995): Bottom classification: operational results from QTC view. IEEE Oceans '95 Conference Proceedings, Vol. 3, pp. 1827-1835.

Pratson L.F. & Edwards M.H. (1996): Introduction to advances in seafloor mapping using sidescan sonar and multibeam bathymetry data. Marine Geophysical Researches, Vol. 18, pp. 601-605.

Press W.H., Teukolsky S.A., Vetterling W.T. & Flannery B.P. (1992): Numerical Recipes in C: The Art of Scientific Computing. 2. edition, Cambridge University Press.

Priebe R., Chotiros N.P., Walter D.J. & Lambert D.N. (1995): Sea Floor Classification by Wavelet Decomposition of Fathometer Echoes. IEEE Oceans '95 Conference Proceedings, Vol. 3, pp. 1814-1821.

Rathbun S.L. & Cressie N.A.C. (1994): Space-time survival point processes: Longleaf pines in southern Georgia. Journal of the American Statistical Association, Vol. 89, pp. 1164-1174.

Rathbun S.L. (1998): Spatial modelling in irregularly shaped regions: Kriging estuaries. Environmetrics, Vol. 9/2, pp. 109-130.

Ripley B. (1988): Statistical inference for spatial processes. Cambridge University Press, New York, 1988.

Roberts E.A. (1993): Seasonal Cycles, Environmental Change and BACI Designs. Environmetrics, Vol. 4/2, pp. 209-231.

Rosholm A. (1997): Statistical methods for segmentation and classification of images. Ph.D. thesis, Department of Mathematical Modelling, Technical University of Denmark.

Rossi R.E., Mulla D.J., Journel A.G. & Frannz E.H. (1992): Geostatistical tools for modeling and interpreting ecological spatial dependence. Ecological Monographs, Vol. 2/2, pp. 277-314.

Sabol B.M. & Burczinski J. (1998): Digital echo sounder system for characterizing vegetation in shallow-water environments. Proceedings of the Fourth European Conference on Underwater Acoustics, edited by A. Alippi & G.B. Cannelli, Rome, 1998.

Sabol B.M., Shaffer D.J. & Melton jr. E. (1996): Mapping seagrasses for dredging operations. US Army Corps of Engineers. Vol D-96-1.

Sampson P.D. & Guttorp P. (1992): Nonparametric estimation of nonstationary spatial covariance structure. Journal of the American Statistical Association, Vol. 87, pp. 108-119.

Schlagintweit G.E.O. (1993): Real-time acoustic bottom classification for hydrography – a field evaluation of RoxAnn. Proceedings of the IEEE Oceans '93 Conference, Vol. III, pp. 214-219.

Schlese-Heidelbaugh W. & Nelson W.G. (1995): A power analysis of methods for assessment of change in seagrass cover. Aquatic Botany, Vol. 53, pp. 227-233.

Schmitt M. (1997): Estimation of intensity and shape in a non-stationary Boolean model. Proceedings of the International Symposium "Advances in Theory and Applications of Random sets", October 9-11, 1996, Fontainebleau, France.

Schneider D.C., Walters R., Thrush S. & Dayton P. (1997): Scale-up of ecological experiments: Density variation in the mobile bivalve *Macomona liliana*. Journal of Experimental marine Biology and Ecology, Vol. 216, pp. 129-152.

Schultz N. & Ersbøll A. (1998): Meditteranean Rox Ann data. Data report, Department of Mathematical Modelling, Technical University of Denmark.

Schultz N. (1995): Segmentation and classification of biological objects. Ph.d. thesis, Department of Mathematical Modelling, Technical University of Denmark.

Schultz N. (1998): A Nonparametric deformable template classifier. Preprint.

Schultz N. (1999): Using a Nonparametric Deformable Template Classifier for Sea Floor segmentation. Preprint.

Serra J. (1982): Image Analysis and Mathematical Morphology. Academic Press London.

Settle J.J. & Drake N.A. (1993): Linear mixing and the estimation of ground cover proportions. Int. Journal of Remote Sensing, Vol. 14/6, pp. 1159-1177.

Snover M.L. & Commito J.A. (1998): The fractal geometry of *Mytilus edulis L.* spatial distribution in a soft-bottom system. Journal of Experimental Marine Biology and Ecology, Vol. 223, pp. 53-64.

Sørensen P.S. (1994a): Sample sizes and power considerations for the Marine Monitoring Programme. Report no. 94/126/0E to Øresundskonsortiet prepared on behalf of VKI.

Sørensen P.S. (1994b): The statistical basis for use of RoxAnn measurements to prepare distribution maps. Doc. No. 94/160/0E. Report to Øresundskonsortiet prepared on behalf of VKI.

Sørensen P.S. (1995): Study of RoxAnn as a basis for mapping of mussel beds, Doc. no. 95/109/1E. Report to Øresundskonsortiet prepared on behalf of VKI.

Sørensen P.S., Madsen K.N., Nielsen A.A., Schultz N., Conradsen K. & Oskarsson O. (1998): Mapping of the benthic communities Common mussel and Neptune grass by use of hydroacoustic measurements. 3rd European Marine Science & Technology Conference, Session report of Seafloor characterisation session, European Commission.

Sotheran I.S., Foster-Smith R.L. & Davis J. (1997): Mapping of marine benthic habitats using image processing techniques within a raster-based geographic information system. Estuarine, Coastal and Shelf Science, Vol. 44/A, pp. 25-31.

Spencer S., Smith D.K., Cann J.R., Lin J. & McAllister E. (1997): Structure and stability of non-transform discontinuities on the Mid-Atlantic Ridge between 24° N and 30° N. Marine Geophysical Researches, Vol. 19, pp. 339-362.

Sternberg S.R. (1986): Grayscale morphology. *Computer Vision, Graphics, and Image Processing*, Vol. 35/3, pp. 333-355.

Stoyan D. (1982): A remark on the line transect method. Biom. J. Vol. 24/2, pp. 191-195.

Stoyan D. (1994): Caution with "fractal" point patterns! Statistics, Vol 25, pp. 267-270.

Sullivan P.J. (1991): Stock abundance estimation using depth-dependent trends and spatially correlated variation. Can. J. Fish. Aquat. Sci., Vol. 48, pp. 1691-1703.

Swendsen R.H. & Wang, J.S. (1987): Nonuniversal critical dynamics in Monte Carlo simulations. Physical Review Letters, Vol. 58/2, pp. 86-88.

Switzer P. & Green A.A. (1984): Min/max autocorrelation factros for multivariate spatial imagery. Tech. rep. 6, Stanford University. 10 pp.

Tamsett D. (1992): Sea-bed characterisation and classification from the power spectra of side-scan sonar data. Marine Geophysical Researches, Vol. 15, pp. 43-64.

Tassan S. (1994): Local algorithms using SeaWiFS data for the retrieval of phytoplankton, pigments, suspended sediment, and yellow substance in coastal waters. Applied Optics, Vol 33/12, pp. 2369-2378.

Theisen B.F. (1977): Feeding rate of *Mytilus edulis* L. (Bivalvia) from different parts of Danish waters in the water of different turbidity. Ophelia, Vol. 16/2, pp. 221-232.

Theisen B.F. (1982): Variation in size of gills, labial palps, and adductor muscle in Mytilus edulis L. (Bivalvia) from Danish waters. Ophelia, Vol. 21/1, pp. 49-63.

Thompson S.K. (1992): Sampling. John Wiley & Sons Inc.

Triton Elics Inc. (1998): Q-MIPS Data format description. Preprint.

Tukey J. (1977): Exploratory Data Analysis. Addison Wesley, Reading, MA.

Vincent L. (1999): Current topics in applied Morphological Image Analysis. Chapter 6 contributed to *Stochastic Geometry, Likelihood and Computation*, edited by Barndorff-Nielsen, Kendall & van Lieshout, Chapman & Hall.

Weaver W. (1982): Lady Luck: The theory of probability. Dover edition, Dover Publications Inc., New York.

Wen R. & Sinding-Larsen R. (1997): Image filtering by factorial kriging - sensitivity analysis and application to Gloria side-scan sonar images. Mathematical Geology, Vol. 28/4, pp. 433-468.

Williamson N.J. & Traynor J.J. (1996): Application of a one-dimensional geostatistical procedure to fisheries acoustic surveys of Alaskan pollock. ICES Journal of Marine Science, Vol. 53, pp. 423-428.

Zietz S. & Elicker C. (1995): Modeling and analysis of sonar backscatter intensity for ocean bottom classification. Proceedings of the IEEE Oceans '95 Conference, pp. 1836-1839.